THÈSE POUR OBTENIR LE GRADE DE DOCTEUR DE L'UNIVERSITÉ DE MONTPELLIER

En Physique

École doctorale : Information, Structures et Systèmes (166)

Unité de recherche : Laboratoire Charles Coulomb

En partenariat international avec l'Université d'État de Saint-Pétersbourg, RUSSIE

Electron and nuclear spin dynamics in nanostructures based on n-CdTe

Dynamique du spin électronique et nucléaire dans les nanostructures à base de n-CdTe

Présentée par Boris GRIBAKIN
le 29 novembre 2024

Sous la direction de Denis SCALBERT et Kirill KAVOKIN

Devant le jury composé de

M Régis ANDRÉ, DR	Président du jury
Mme Maria CHAMARRO, PR	Rapporteure
M Loïc LANCO, PR	Rapporteur
M Dmitry SMIRNOV, CR	Examinateur
M Denis SCALBERT, DR	Directeur de these
M Kirill KAVOKIN, DR	Directeur de these
M Steeve CRONENBERGER, MCF	Co-encadrant
Mme Maria VLADIMIROVA, DR	Membre invité



Contents

Acknowledgements i

Abstract ii

Introduction iii

1 Electron and nuclear spins in CdTe 1
- 1.1 Electron properties . . . 1
  - 1.1.1 Band structure . . . 1
  - 1.1.2 Defects and doping . . . 2
  - 1.1.3 Optical transitions and selection rules . . . 3
- 1.2 Electron spin properties . . . 4
  - 1.2.1 Optical orientation . . . 4
  - 1.2.2 Electron spin relaxation . . . 5
  - 1.2.3 Spin-exchange scattering . . . 11
  - 1.2.4 Electron spin transport and diffusion . . . 12
- 1.3 Nuclear spin system . . . 15
  - 1.3.1 Hyperfine interaction . . . 16
  - 1.3.2 Effective hyperfine fields . . . 17
  - 1.3.3 Nuclear spin-spin interactions and the local field . . . 18
  - 1.3.4 Spin temperature . . . 20
- 1.4 Dynamic nuclear polarization . . . 21
  - 1.4.1 Dynamic nuclear polarization and spin temperature . . . 21
  - 1.4.2 Adiabatic demagnetization . . . 22
  - 1.4.3 Spin temperatures obtained in semiconductors . . . 23
  - 1.4.4 Nuclear spin relaxation and warm-up . . . 24
  - 1.4.5 Nuclear spin diffusion . . . 26
  - 1.4.6 Dynamic polarization of electron spins by a cold nuclear spin system . . . 27
  - 1.4.7 Nuclear spin diffusion barrier . . . 28
- 1.5 Experimental approaches to electron spin dynamics . . . 29
  - 1.5.1 Time-resolved techniques . . . 29
  - 1.5.2 Continuous-wave techniques . . . 31
  - 1.5.3 Spin noise spectroscopy . . . 32
- 1.6 Experimental approaches to nuclear spin dynamics . . . 36
  - 1.6.1 Readout of the nuclear spin state . . . 36
- 1.7 Conclusions . . . 39

2 Conduction band hops of localized electron spins in n-CdTe 40
2.1 Introduction . . . 40
2.2 Effects of spin motion on the spin noise lineshape . . . 42
2.3 Two-state model . . . 46
2.4 Spatiotemporal spin noise power spectrum . . . 48
2.4.1 Solving the advanced two-state model . . . 49
2.4.2 Results . . . 56
2.5 Experimental . . . 59
2.5.1 Experimental setup . . . 59
2.5.2 Samples & experiments . . . 64
2.6 Results and discussion . . . 65
2.6.1 Modeling details . . . 65
2.6.2 Probe power and effective sample temperature . . . 72
2.6.3 Spin noise lineshapes and linewidth dispersion . . . 73
2.6.4 Electron spin relaxation time as a function of doping density and temperature . . . 80
2.7 Conclusions . . . 82

3 Interplay of nuclear spin relaxation and diffusion in wide n-CdTe QWs 83
3.1 Introduction . . . 83
3.2 Experimental . . . 86
3.2.1 Samples and characterization . . . 86
3.2.2 Setup and experiments . . . 88
3.2.3 Main experimental results . . . 89
3.3 Modeling and discussion . . . 91
3.3.1 Donor-bound electrons (Sample A) . . . 91
3.3.2 Free electrons (Sample B) . . . 97
3.4 Conclusions . . . 101

4 Conclusions and perspectives 103

A Calculation of the local and kinetic local fields 104
A.1 Local field . . . 104
A.2 Kinetic local field . . . 105

B Faddeeva function 107

Acknowledgements

I express my deepest gratitude to my supervisors, Kirill Kavokin and Denis Scalbert, for their unwavering support, guidance, and patience throughout the entirety of this thesis. The success of this thesis is also indebted to Steeve Cronenberger and Masha Vladimirova, who have helped me a great deal during the course of this work. I thank my principal co-authors M. Kotur, V. Litvyak, and D. Yakovlev, as well as colleagues who have also made significant contributions to the presented research, namely H. Boukari, R. André, E. Khramtsov, G. Karczewski, E. Zhukov. Special thanks are owed to the members of the thesis jury: Maria Chamarro, Loïc Lanco, Régis André, and Dmitry Smirnov. Last but not least, I could not have possibly succeeded in this difficult endeavor without the support of my family and friends.

Finally, I acknowledge the support of the Government of France through the Vernadskii Scholarship, which allowed this co-directed thesis to persist in spite of the tragic political events that came to transpire during the course of the thesis.

Abstract

The electron and nuclear spin properties of nanostructures based on n-CdTe are studied experimentally and theoretically.

Spatiotemporal electron spin dynamics in epitaxial n-CdTe are revealed by the newly developed angle-resolved spin noise spectroscopy (AR-SNS), which provides direct access to electron spin fluctuations with wavevectors up to 10 µm^{-1} via goniometric homodyne detection. Experiments reveal that spin correlations between localized and delocalized electrons have a profound impact on the spin relaxation of localized electrons even at temperatures that are low compared to the binding energy. A theoretical two-state model based on Bloch equations is in quantitative agreement with the entire body of acquired experimental data, where spatiotemporal electron spin noise spectra are measured as functions of temperature and donor density, faithfully reproducing all the experimentally observed spectra.

The nuclear spin system of n-CdTe is investigated in two distinctive samples containing wide single quantum wells by a multistage technique combining optical pumping and Hanle effect-based detection, accompanied by theoretical modeling. In the presence of neutral donors, applying weak fields of the order and in excess of the local field leads to the inhibition of nuclear spin diffusion due to the onset of a nuclear spin diffusion barrier, which is shown to be afforded by the combination of strong neutron donor localization, sparse nuclear spin system, and small local field found in CdTe. An opposite picture is observed when the electron structure of the sample is dominated by dilute electron gas puddles, with essentially field-independent nuclear spin relaxation following a Korringa-like relaxation process.

Résumé

Les propriétés de spin électronique et nucléaire des nanostructures basées sur n-CdTe sont étudiées expérimentalement et théoriquement.

La dynamique spatiotemporelle du spin électronique dans le n-CdTe épitaxié est révélée par la nouvelle technique de spectroscopie de bruit de spin résolue en angle (AR-SNS), qui permet un accès direct aux fluctuations du spin électronique avec des vecteurs d'onde allant jusqu'à 10 µm^{-1} par une détection homodyne goniométrique. Les expériences montrent que les corrélations de spin entre les électrons localisés et délocalisés ont un impact profond sur la relaxation du spin des électrons localisés, même à des températures inférieures à l'énergie de liaison. Un modèle théorique à deux états basé sur les équations de Bloch est en accord quantitatif avec l'ensemble de données expérimentales acquis, où les spectres de bruit de spin électronique spatiotemporels sont mesurés en fonction de la température et de la densité de donneurs, reproduisant fidèlement tous les spectres observés expérimentalement.

Le système de spin nucléaire du n-CdTe est étudié dans deux échantillons contenant de larges puits quantiques à l'aide d'une technique combinant pompage optique et détection basée sur l'effet Hanle, accompagnée d'une modélisation théorique. En présence de donneurs neutres, l'application de champs faibles de l'ordre du champ local ou supérieurs conduit à l'inhibition de la diffusion du spin nucléaire en raison de l'apparition d'une barrière de diffusion du spin nucléaire, qui est montrée comme étant due à la combinaison d'une forte localisation des donneurs neutres, d'un système de spin nucléaire clairsemé, et d'un champ local faible trouvé dans le CdTe. Une image opposée est observée lorsque la structure électronique est dominée par des flaques de gaz électronique dilué, avec une relaxation du spin nucléaire essentiellement indépendante du champ, suivant un processus de relaxation de type Korringa.

Introduction

Magnetism as a phenomenon has been known to mankind for a very long time. Indeed, it has been used to advance civilization long before its physical origin was well-understood; a great example would be the compass, which permitted us to reliably traverse the oceans before metal ships, global positioning, and instant on-demand communication. In modern times, multiple information storage technologies based on magnetism have been developed and are used concurrently, such as magnetic tape and disk drives, which still benefit from steady incremental improvements. Other technologies have already been outclassed, such as floppy disks, core memory, and drum memory. Finally, new spin-based technologies are in development, with the hope that they will provide impoved access speed, information density, or both [1–3].

Spin physics in solids has a rich and entertaining history. As early as 1927, when Sommerfeld incorporated the then-recently developed Fermi-Dirac distribution into his free electron model [4], it became clear that the implications of spin go far beyond just the magnetic properties of materials. Spin provides an additional degree of freedom that can be studied and perhaps exploited with the end goal of developing new devices that are simultaneously high-performing, energy-efficient, and reconfigurable. Direct manipulation of non-equilibrium electron spin instead of or in conjunction with electric charge constitutes the foundational principle of spintronics, and the central problem in this field is the limited coherence times and general fragility of spin systems [5]. Electron spin physics is deeply intertwined with that of nuclear spins, which introduces additional challenges to preserve electron spin coherence: one must either manage to suppress decoherence due to spin-spin interactions with nuclei [6], or use them as an integral part of the device [7], but ignoring them is typically not an option. Therefore, studies of electron and nuclear spin relaxation time is a frequent goal of condensed matter research. Ultimately, the measured electron and nuclear spin relaxation times result from a complex interplay of interactions which is determined by the choice of materials, sample structure, applied fields, temperature etc. — the list of variables is inexhaustible. The rich parameter space ensures that despite decades of focused research, there is still plenty of room for new discoveries to be made, even in the most widely studied materials.

In semiconductors, electron spin can be manipulated optically via selection rules, and the hyperfine interaction enables optical manipulation of nuclear spin as well. The impetus for research in this area can be traced back to the work of Kastler on optical pumping [8]. This was adapted to semiconductors almost twenty years later by Lampel [9], who managed to register the optical orientation of electron spins through the nuclear spin system via the Overhauser effect. For some years after that, optical studies of electron-nuclear spin physics in semiconductors were continued most productively in two centers: the Paris school at École Polytéchnique, and the St. Petersburg school at the Ioffe Institute. Many of the results obtained during that time are summarized in Ref. [10], which is still a must-read for any specialist in this field.

Since then, research on semiconductor spin physics has benefitted from the proliferation of time-resolved techniques, and ultrafast studies of spin dynamics have become routine [11]. The focus of the state-of-the-art has gradually shifted from bulk semiconductors onto quantum

wells, quantum dot ensembles, and eventually single quantum dots in the 90s and 00s [12]. Finally, contemporary condensed matter spin physics is often devoted to nanostructures based on emerging materials, such as transition metal dichalcogenides [13] and perovskites [14, 15]. Though conventional semiconductors (Si, GaAs, GaN, CdTe etc.) and the respective nanostructures are no longer considered to be on the cutting edge of materials science, they have not lost their appeal either, as the perfected sample growth technologies and the large body of established properties permit the more subtle effects to be studied.

Though considerably less prevalent than Si and GaAs, CdTe has occupied its own niches in industry and research. Currently, the most important application is in photovoltaics, where CdTe-based solar panels have become the dominant thin-film technology, comprising several percents of global production [16]. CdTe photovoltaics have a smaller carbon footprint and a shorter energy payback time compared to many other technologies [17]. The material is also used for infrared windows and lenses, and in electro-optic modulators due to the large electro-optic constants; alloys with mercury and zinc are utilized in infrared, X-ray and gamma-ray detectors. In basic research, CdTe and CdTe-based nanostructures are attractive due to the high structural quality which can be achieved by molecular beam epitaxy. As a testament to this, negative trions were first detected in a CdTe multiple quantum well structure with modulation doping [18]. Spontaneous quantum degeneracy of polaritons was also first observed in a CdTe-based microcavity, foreshadowing the direct observation of exciton polariton Bose-Einstein condensation [19, 20]. Fabrication centers located in Grenoble and Warsaw are known to produce very high-quality samples based on II-VI semiconductors [21–25]. Indeed, Refs. [18, 19] also used nanostructures grown in Grenoble. The epitaxial n-CdTe samples discussed in Chapter 2 and the 30 nm-wide quantum well structure of Chapter 3 were grown by H. Boukari and R. Andrè of Insitut Nèel, Grenoble, respectively; the 20 nm-wide quantum well studied in Chapter 3 was grown at the Institute of Physics, Polish Academy of Sciences, Warsaw under G. Karczewski.

This thesis concludes three years of studies and research performed with and under the supervision of Dr. K. V. Kavokin (Spin Optics Laboratory, St. Petersburg State University) and Dr. D. Scalbert (Laboratoire Charles Coulomb, Université de Montpellier). Chapter 1 serves to introduce the properties of electron and nuclear spin systems in CdTe that will be relevant to the original part of the work. An overview of optical properties is followed by the description of various electron spin relaxation and transport mechanisms. We then consider the properties of the CdTe nuclear spin system, and the interactions between electron and nuclear spin, which lead to dynamic nuclear polarization, dynamic polarization of electrons by nuclei, and the nuclear spin diffusion barrier. We conclude by discussing various experimental approaches that can be used to probe electron and nuclear spins.

Chapter 2 is devoted to the "electron" part of the thesis directed by D. Scalbert and performed entirely at Laboratoire Charles Coulomb, in which we discuss an original experimental technique, angle-resolved spin noise spectroscopy. The technique is applied to a series of insulating epitaxial n-CdTe layers. Angle-resolved spin noise spectroscopy makes use of goniometric homodyne collection of spin-flip scattered light to attain previously unreachable wavevectors of spin fluctuations, permitting an in-depth study of the spatiotemporal electron spin noise spectra at various doping densities, temperatures, and magnetic fields. A two-state theoretical model based on Bloch equations, which reached its current advanced state largely due to the persistence and passion of S. Cronenberger, is used to consistently interpret the entire body of experimental data, highlighting the previously underappreciated impact of conduction electrons on the spin fluctuations of neutral donors in various regimes. We definitively show that a complete picture of donor-bound electron spin dynamics in CdTe and similar materials is

impossible without considering the effects of indirect spin jumps through the conduction band accompanied by Dyakonov-Perel relaxation, even when nearly all electrons are localized. The findings of this work have been accepted to Physical Review Research and are to be published as a regular article under the title "Angle-resolved spin noise spectroscopy in semiconductors: Two-state theory and experiments" in 2025 [26].

Chapter 3 constitutes the "nuclear" part of the thesis directed by K. V. Kavokin with additional help from M. Vladimirova. We work with experimentalists from the Spin Optics Laboratory at Saint Petersburg State University and from Technische Universität Dortmund to study the nuclear spin system of n-CdTe in vastly different electronic environments provided by two nanostructures containing wide CdTe quantum wells with unintentional n-doping. The nuclear spin dynamics, obtained in multistage dynamic nuclear polarization experiments with Hanle effect-based detection, are recorded in weak-to-moderate magnetic fields, revealing a strong variation of the magnetic field dependence of nuclear spin relaxation in relation to electron localization. By constructing a phenomenological model with few fitting parameters, we show that neutral donors provide sufficient localization of electron spins to provoke the formation of a nuclear spin diffusion barrier, which inhibits nuclear spin diffusion towards the donor, thereby slowing nuclear spin relaxation by an order of magnitude in fields of the order of 2 mT as compared to zero field. Conversely, in absence of strong localization, no magnetic field dependence of nuclear spin relaxation is observed; furthermore, the presence of a low-density two-dimensional electron gas that is inhomogeneously distributed in the quantum well plane leads to the interplay of Korringa-like nuclear spin relaxation and a spin diffusion flow from electron-free areas, which results in a long-lived signal that persists for thousands of seconds. The principal findings showcased in Chapter 3 are published as a regular article in Physical Review B [27].

Chapter 1

Electron and nuclear spins in CdTe

In this Chapter, we cover the basic physics that act as a foundation for the main body of work presented in Chapters 2 and 3. As a zinc-blende semiconductor, CdTe shares many similarities with other popular materials such as GaAs, with the differences being mostly quantitative, not qualitative. We nevertheless attempt to retain a certain degree of generality where possible, underlining relevant differences and similarities with GaAs as needed. Below, we give a brief overview of the band structure of bulk CdTe as well as that of CdTe nanostructures, along with the resulting optical properties. We then discuss the electron and nuclear spin properties of CdTe, including electron-nuclear interactions which can be exploited to achieve dynamic nuclear polarization. Finally, we discuss modern experimental approaches to electron and nuclear spin studies in semiconductors.

1.1 Electron properties

1.1.1 Band structure

It is well-known that the discrete levels of individual atoms coalesce into bands when a crystal is formed [28]. Atomic spectra are generally degenerate, and as such their transformation into quasi-continuous bands depends on the symmetry of crystalline fields, which are determined by the lattice symmetry. Zinc-blende semiconductors feature a direct bandgap. The conduction band (c) is simple, while the valence band includes three contributions: the heavy-hole (hh) and light-hole (lh) subbands, followed by the split-off subband. The energy separation between the conduction band and the valence band is given by the bandgap E_g. It has a weak temperature dependence due to thermal expansion. In CdTe at liquid helium temperatures $E_g = 1.6$ eV [29].

The spin-degenerate conduction band is described by an s-type Bloch function. The hole subbands are described by p-type Bloch functions, and are four-fold degenerate at the Γ point of the Brillouin zone, i.e., when the crystal momentum is zero $k = 0$. The degeneracy is lifted at finite values of k, where we have two separate hh and lh branches corresponding to total orbital momentum projections $J_{z,hh} = \pm 3/2$ and $J_{z,lh} = \pm 1/2$, respectively; each branch is doubly degenerate. In nanostructures, the hh and lh degeneracy at $k = 0$ is also usually lifted due to different quantum confinement energies of heavy and light holes. As an example, in the 20 nm-wide quantum well studied in Chapter 3, the difference is more than 5 meV [30]. At the Γ point, the split-off band is separated by the spin-orbit splitting Δ_{SO}, which is due to spin-orbit interaction. In materials composed of rather heavy atoms, Δ_{SO} is comparable to the bandgap: in GaAs $\Delta_{\mathrm{SO}} = 0.3$ eV [31], while in CdTe $\Delta_{\mathrm{SO}} = 0.9$ eV [32]. Therefore, the effects of split-off band admixture on the hole states and interband transitions can often be neglected.

Nevertheless, its relative importance is determined not only by the magnitude of Δ_{SO}, and it can be particularly important for forbidden transitions, e. g., in spherical quantum dots [33].

In the simplest spherical approximation, the extrema of the bands are parabolic. They can then be thought of as energy spectra of free particles with certain effective masses. Usually, the effective masses are smaller than the electron mass m_0. The effective mass approximation is normally valid near the bottom of the conduction band, where we have electrons with mass m_e. In CdTe, $m_e \approx 0.10 m_0$ [29, 34]. The valence subbands can also be described by isotropic effective masses, but in this case the approximation is considered more crude, as the bands can be noticeably non-spherical, which is reflected by the inclusion of additional terms into the Luttinger Hamiltonian [35]. This introduces a warping of the isoenergetic surfaces, and in this case the effective mass must be described by a tensor. There are many other peculiarities that have to do with the valence band; for example, the light and heavy holes tend to be mixed rather strongly by perturbations, such as magnetic fields. However, in what follows, we mostly focus on low temperatures and electrons, so a more detailed understanding of the valence band is not necessary.

1.1.2 Defects and doping

The introduction of lattice defects, most importantly n- or p-doping, leads to the appearance of additional levels in the energy spectrum of the crystal. This can be shown most effectively by considering the very simple Kronig-Penney model [36], e. g., by introducing a vacancy defect. In practice, the effective mass approximation often provides acceptable accuracy in describing donors and acceptors [28]. Within this approximation, an electron localized on an isolated donor site can most simply be described via the hydrogen atom Hamiltonian

$$\hat{\mathcal{H}}_{\mathrm{loc},e} = \frac{\hbar^2 \hat{\mathbf{k}}^2}{2m_e} - \frac{1}{4\pi\varepsilon\varepsilon_0}\frac{e^2}{r}, \tag{1.1}$$

where $\hat{\mathbf{k}}$ is the crystal momentum operator, ε is the dielectric constant of the material, and r is the distance from the donor center. In the energy spectrum of the crystal, the ground state of the neutral donor appears as a discrete level below the bottom of the conduction band, separated from it by the (Rydberg) binding energy

$$E_b = \frac{\hbar^2}{2m_e}\frac{1}{a_{\mathrm{B}}^2}, \tag{1.2}$$

where $a_B = 4\pi\varepsilon\varepsilon_0\hbar^2/m_e$ is the hydrogen Bohr radius for an electron in CdTe. Compared to GaAs, CdTe has a rather large neutral donor binding energy, $E_b \approx 14$ meV [37] ($E_b \approx 5$ meV in GaAs). As the doping density is increased, the assumption of isolated donors gradually becomes less valid. Interactions between neutral and/or ionized donor sites can be viewed as charge or spin jumps, though a more accurate quantum mechanical description would be the gradual formation of an impurity band [38]. This can be seen most clearly by referring to the Hubbard model [39]. When the doping density becomes high enough that the impurity band merges with the conduction band, the semiconductor's electron structure becomes metallic. This occurs when the average distance between donors approaches the neutral donor Bohr radius.

A typical donor in II-VI compounds is Al, while halogens such as Cl and I act as acceptors. Unintentional doping can easily occur, as it is very difficult to eliminate all contaminants affecting the growth process [27, 40]. The carriers can be spatially separated from the region

containing the dopant atoms through a technique called modulation doping. Using quantum well structures as an example, one may dope the barriers, leaving the well itself defect-free. This can be done intentionally or unintentionally [18, 41, 42],

1.1.3 Optical transitions and selection rules

In many common semiconductors the bandgap energy is within or near the visible spectrum. In CdTe $E_g = 1.6$ eV, which is in the near infrared. This feature of semiconductors is the primary reason for their widespread use in optical devices, such as light-emitting diodes, lasers, and photovoltaic technology. The introduction of widely tunable continuous-wave and pulsed lasers has opened the floodgates for optical studies of semiconductors, which deepened our knowledge of their physics tremendously and acted as a catalyst for the steady development of applications that we enjoy today, such as compact and efficient electronics and fiber-optic communication.

When a photon with an energy close to E_g is absorbed by a semiconductor, an electron-hole pair is created according to energy and momentum conservation. Angular momentum is also conserved, and the spin state of the photocreated electron-hole pair depends on the polarization of the photon through what is called the selection rules. These may be directly obtained by analyzing the dipole transition matrix elements, taking into account the symmetry of electron and hole Bloch functions near band extrema [10, 43]. The resulting optical transitions are illustrated in Fig. 1.1 for a bulk zinc-blende semiconductor, and in Fig. 1.2 for a zinc-blende semiconductor nanostructure using the electron representation [43][1]. In the latter, the four-fold degeneracy of the heavy-hole and light-hole subbands at $k = 0$ is lifted due to different confinement energies of heavy and light holes, enabling more selective excitation. At sufficiently low temperatures and excitation energies smaller than the *lh*-*c* transition, the effects of light holes can typically be neglected in nanostructures, provided that the *hh*-*lh* splitting is significantly greater than the linewidths.

Eventually, we must consider also the exciton effect, which can be described as the binding of a photocreated electron-hole pair due to Coulomb attraction. A free exciton has a binding energy that is slightly smaller than the neutral donor binding energy due to finite hole mass (see Section 1.1.2). Excitons possess angular momentum that is determined by the angular momenta of the electron and hole. In zinc-blende semiconductors, excitons formed by electrons and heavy holes can have total angular momentum projection $J_z = \pm 1, \pm 2$ depending on the spin projection of the electron and the total angular momentum projection of the heavy hole. The $|\pm 1\rangle$ excitons can be created (destroyed) via single photon absorption (emission), and have a short radiative lifetime; hence, they are said to be "bright". The $|\pm 2\rangle$ excitons are "dark" as the respective optical transition is dipole-forbidden. These two pairs of exciton states are also split due to short-range electron-hole exchange, but the splitting is very small, of the order of 1 µeV [44], which is much smaller than typical temperatures, as well as *hh*-*lh* splittings in nanostructures. In quantum wells, another type of "dark" exciton is any exciton with a crystal momentum that is outside the light cone. Such an exciton cannot fulfill momentum conservation in the event of photon emission, and as such, these excitons have a lifetime of the order of ns, around two orders of magnitude longer than that of excitons within the light cone [45, 46]. This type of "dark" exciton is specifically a feature of quantum wells due to the fixed value of out-of-plane exciton momentum, dictated by the width of the quantum well. Consequently, the energy-momentum conservation requirements are stricter, leading to longer radiative lifetimes.

[1] To convert to the electron-hole representation, one must invert the signs of the orbital momentum projections of the hole states.

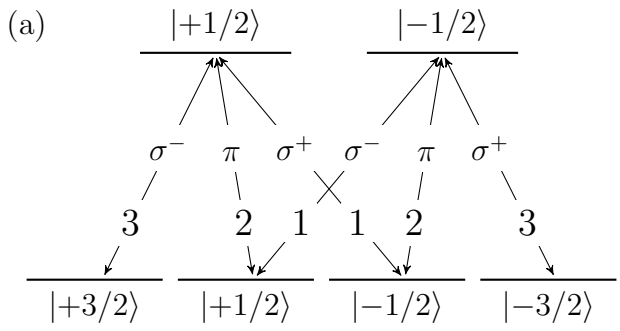

Figure 1.1: Near-bandgap optical transitions in a bulk zinc-blende semiconductor such as CdTe. The heavy- and light-hole subbands are degenerate near $k = 0$. σ^+ and σ^- denote the two orthogonal circular polarizations, π is a linear polarization. The numbers quantify the relative probability ratio for the corresponding transitions. The maximum average electron spin that can be achieved by optical pumping is limited to 0.25.

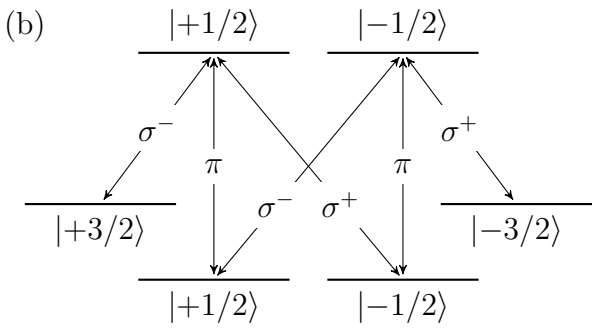

Figure 1.2: Near-bandgap optical transitions in a nanostructure based on a zinc-blende semiconductor. The heavy- and light-hole subbands are split due to different quantum confinement energies, enabling the optical pumping of the $|\pm 3/2\rangle - |\pm 1/2\rangle$ transition. Optical orientation is then more efficient, and the average electron spin may reach 0.5.

Excitons can bind to neutral and ionized donors before they recombine. Additionally, they can form complexes with resident charge carriers, creating positive or negative trions, which occur in quantum wells in the presence of an electron gas, as well as in charged quantum dots. In the bulk, trion binding energies are typically more than 10 times smaller [47], which is why they are a feature of nanostructures. In CdTe nanostructures, where they were first discovered [18], these complexes are characterized by binding energies that are quite small, of the order of several meV [41, 48, 49][2]. Nevertheless, they can easily be observed in low-temperature photoluminescence (PL) spectra. They serve as indicators for the presence and type of doping, and the relative intensities of trion and free exciton peaks can give an idea of the charge carrier density in quantum wells. Positive and negative trions have similar binding energies, hence additional measurements are usually required to reliably determine their type. This is typically done, e. g., via polarization-resolved luminescence measurements in magnetic field [40, 52].

1.2 Electron spin properties

1.2.1 Optical orientation

Coming back to Figs. 1.1 and 1.2, we can see that the level structure permits selective excitation of specific spin states, depending on the polarization of light. For example, in bulk zinc-blende semiconductors, pumping with σ^--polarized light creates more $|+1/2\rangle$ electrons than $|-1/2\rangle$, along with various kinds of holes. This is what forms the basis of the optical orientation technique [10]. For nanostructures, the selectivity is enhanced compared to the bulk case. Here, directing σ^--polarized along the growth direction of the sample, we only promote electrons from the $|+3/2\rangle$ valence band state to the $|+1/2\rangle$ conduction band state. In the hole representation,

[2] In GaAs, the trion binding energies are of the same order of magnitude, but smaller [50, 51].

we say that we create $|+1/2\rangle$ electrons and $|-3/2\rangle$ holes [43]. This spin selectivity introduces more possibilities for experiments and also increases the theoretical upper bound for the average electron spin to 0.5.

In the ground state, there are no electrons in the conduction band (at zero temperature). Optically or electrically excited electrons recombine within their radiative lifetime. Their spin state may change during the lifetime, before recombination. Indeed, the spin relaxation time can be very different from the lifetime; typically, it is much longer. In doped semiconductors, spin flips with resident electrons are often observed, which makes it possible to study the spin state of resident carriers optically. The eventual recombination of the electron-hole pairs results in luminescence, the polarization of which reflects the ratio of the recombination rate and the spin relaxation rates of electrons and holes. If there is no spin relaxation, the PL should be polarized exactly as the pumping beam; conversely, if the spin lifetime is shorter than the recombination time, the PL must be unpolarized. This topic was initially thoroughly studied via optical orientation of minority carriers in bulk materials such as p-GaAs [10], though eventually the studies evolved to cover a broad spectrum of semiconductor nanostructures, including quantum dots and various devices [53, 54].

The idea of utilizing the spin component of charge carriers instead or in conjunction with the charge has been around for some time, and optical methods continue to be the tool of choice to shed light on the spin physics of charge carriers in semiconductors. The end goal of such studies is usually the spin relaxation time, which tells us how long the spin remembers its initial state. It is directly influenced by various spin flip mechanisms, but also, less directly, by the spatial dynamics of spins. We will concern ourselves mostly with electron spins since they are directly relevant to this work. It is often the case that electrons have longer spin relaxation times than holes. This is especially true in the bulk due to the strong mixing between heavy and light holes. Below, we cover some features expected of spatiotemporal electron spin dynamics.

1.2.2 Electron spin relaxation

In modern physics, spin relaxation is most often described within the framework of Bloch equations, which describe the behavior of the longitudinal and transverse components of the magnetization of a paramagnet [55]. Originally derived for nuclear spins in nuclear magnetic resonance (NMR) conditions (i. e., a strong field $\mathbf{H}_z$ is applied, accompanied by a weak oscillating field in the orthogonal direction), they are usually valid for typical electron and nuclear spin dynamics experiments. Assuming the strong field $\mathbf{H}_z$ is directed along the z axis, the magnetization vector $\mathbf{M} = (M_x, M_y, M_z)$ is described by the set of Bloch equations

$$\dot{M}_z = T_1^{-1} (M_0 - M_z), \tag{1.3}$$

$$\dot{M}_x = \gamma [\mathbf{M} \times \mathbf{H}_z]_x - T_2^{-1} M_x, \tag{1.4}$$

$$\dot{M}_y = \gamma [\mathbf{M} \times \mathbf{H}_z]_y - T_2^{-1} M_y. \tag{1.5}$$

In the above, $\dot{M}$ denotes the derivative of M, γ is the gyromagnetic ratio, and M_0 is the stationary magnetization linked to H_0 via the Curie susceptibility χ as $M_0 = \chi H_0$. The longitudinal (or spin-lattice) relaxation time T_1 describes the relaxation to the stationary magnetization M_0. This process requires energy exchange between the paramagnet and other energy reservoirs, most notably the lattice, since states with different magnetization are ascribed different energies by the field H_0. The transverse (or spin-spin) relaxation time T_2 does not require energy exchange, because the relevant magnetization components are orthogonal to $\mathbf{H}_z$. Essentially, it describes the decoherence of the precession of individual spins within the paramagnet. Most importantly, this decoherence is caused by energy-conserving spin-spin interactions.

Since energy relaxation is not required, T_2 can be much shorter than T_1. For instance, in nuclear spin systems, T_1 is typically of the order of seconds or longer, while T_2 is limited to around 10^{-4} s by magnetic dipole-dipole interactions between the nuclei [55]. In systems with an inhomogeneous distribution of g-factors (or if an inhomogeneous magnetic field is applied), there is a natural distribution of precession frequencies, which leads to the eventual decay of transverse magnetization even in the absence of any spin-spin interactions. Though this process is really only a dephasing[3], it influences the observed transverse relaxation time. To highlight this fact, the observed transverse relaxation time can be denoted $T_2^* \leq T_2$, while T_2 describes the "true" relaxation time that is only due to spin-spin interactions. Often the distinction is not made, since there is practically no way to measure T_2 directly, although there are ways to get very close, notably by using spin echo [56, 57].

A typical spin dynamics experiment provides T_2^*. The effect of g-factor distribution can be eliminated by performing field-dependent measurements of T_2^* and extrapolating to zero field [58, 59]. However, the resulting transverse relaxation time is still only an approximation of T_2, primarily because of the random nuclear fields experienced by the spin ensemble. These can be more or less important depending on the efficiency of the hyperfine interaction, but for strongly localized charge carriers at sufficiently low temperatures they become the dominant source of electron spin relaxation. A more accurate estimate of T_2 can be obtained via spin echoes [11]: the nuclear spins are nearly frozen during the time between pulses, hence the phases of all electron spins can be reversed almost completely [56, 57]. Another solution is to study single spins, e. g., single quantum dots [60]. Nevertheless, most experimental approaches reveal T_2^* that includes dephasing via nuclear spins, but possibly accounting for g-factor inhomogeneity. We are mostly interested in T_2^*, and this will be the default relaxation time we are referring to.

Finally, we note that the Bloch equations shown above can be extended to describe the spatial distribution of the time-dependent magnetization, taking into account spin diffusion which can be either continuous [61] or mediated by individual jumps [62].

Fluctuating effective fields and spin relaxation

Let us now discuss spin relaxation that contributes to the "real" T_2. In classical terms, spins always precess in an effective magnetic field. The fundamental mechanism of any type of spin relaxation is then the systematic interruption of stable spin precession. This can be modeled by assuming the presence of a magnetic field component that fluctuates in magnitude and/or in direction. To estimate the spin relaxation time τ_s, one might distinguish two aspects of the fluctuating field: its root-mean-square value $\langle\Omega\rangle$, and its correlation time τ_c, i. e., the time during which it may be considered constant. In this case, we may say that after time τ_c, the squared angle of rotation of the spin due to precession is $(\langle\Omega\rangle\tau_c)^2$. Over a time t, the total angle is $(\langle\Omega\rangle\tau_c)^2 t/\tau_c$. Finally, the initial spin orientation can be considered lost when the total angle becomes of the order of unity, hence

$$\tau_s^{-1} \approx \langle\Omega\rangle^2 \tau_c. \tag{1.6}$$

The above reasoning is correct in the short correlation time approximation, that is $\tau_s \gg \tau_c$ [35]. In the opposite limit, $\tau_s \propto \tau_c$. It is important to note that for electrons, τ_c may be limited not by the local properties of the fluctuating field, but by the time that an electron spends at a given site. The latter may lead to an effect called motional narrowing, where increasing motion in an inhomogeneously broadened system leads to increased lifetimes and narrower spectral

[3] This dephasing is not only formally, but experimentally reversible via four-wave-mixing (see Section 1.5.1)

resonance lines. Originally observed in an NMR study by Bloembergen and coworkers [63], it has been shown to be a ubiquitous effect across many physical systems, including emerging materials such as perovskites [14] and transition metal dichalcogenides [64]. It is worth noting that different kinds of spins experience different kinds of fluctuating effective magnetic fields, with different τ_c. This is most evident for the effective hyperfine field experienced by localized and free electron spins, see Chapter 3.

The problem of spin relaxation is then reduced to identifying possible sources of fluctuating fields and determining their correlation times τ_c. We will now discuss the electron spin relaxation mechanisms that are relevant in zinc-blende semiconductors.

Dyakonov-Perel relaxation

In Section 1.1.1, we stated that the conduction band is doubly degenerate. In fact, this is only true at $\mathbf{k} = 0$ (and in zero magnetic field). Everywhere else in the Brillouin zone this degeneracy is normally lifted by the so-called spin-orbit coupling, that is, the coupling between the spin of an electron and its velocity. This relativistic effect leads to a momentum-dependent splitting which is equivalently described by the spin-orbit Hamiltonian as electron spin precession in an effective magnetic field $\mathbf{\Omega}_{\mathrm{SO}}(\mathbf{k})$, given by [35]:

$$\hat{\mathcal{H}}_{\mathrm{SO}} = \hbar \mathbf{\Omega}_{\mathrm{SO}}(\mathbf{k}) \cdot \hat{\mathbf{S}}, \tag{1.7}$$

where $\hat{\mathbf{S}}$ is the electron spin operator. The character of the momentum dependence is determined by the crystal symmetry. In non-centrosymmetric semiconductors, such as CdTe, $\mathbf{\Omega}_{\mathrm{SO}}(\mathbf{k})$ is qubic in momentum, as shown by Dresselhaus in Ref. [65]. In quantum wells, a linear contribution is also present [66].

The Dyakonov-Perel spin relaxation process is a consequence of the spin-orbit interaction and may be understood as follows. The electron momentum in the conduction band is conserved between scattering events, which can be caused by, e. g., phonons, charged impurities, or other electrons. The scattering can be described by a momentum relaxation time τ_p. Between collisions, electron momentum is conserved, and its spin precesses in a certain effective magnetic field $\mathbf{\Omega}_{\mathrm{SO}}(\mathbf{k})$. However, upon each collision, $\mathbf{k}$ changes, and the electron spin experiences a slightly different effective field. Essentially, τ_p plays the role of the fluctuating field correlation time. The Dyakonov-Perel mechanism is graphically illustrated in Fig. 1.3. If τ_p is much larger than $\mathbf{\Omega}_{\mathrm{SO}}^{-1}$, then the process results in efficient spin relaxation. Conversely, if collisions are so frequent that the electron never manages to perform a full rotation, spin relaxation is suppressed (motional narrowing). Therefore, the Dyakonov-Perel spin relaxation rate ν_{DP} is directly proportional to the momentum scattering time τ_p. For a nondegenerate electron gas, it is calculated as [10, 67]

$$\nu_{\mathrm{DP}} = Q \tau_p \alpha_{\mathrm{so}}^2 \frac{(k_B T)^3}{\hbar^2 E_g}, \tag{1.8}$$

where E_g is the bandgap, k_B is the Boltzmann constant, T is the temperature, α_{so} is the spin-orbit constant, and Q is a numerical factor of the order of unity that depends on the scattering mechanism.

This mechanism is accepted to be dominant in samples with doping densities above the Mott transition, as most resident electrons are free [68, 69]. In this regime, ν_{DP} decreases with doping density due to motional narrowing. In Chapter 2, we show that the Dyakonov-Perel relaxation rate plays an important role even in weakly doped samples at reasonably low temperatures. This is due to the long τ_p experienced by the small amount of thermally excited free electrons in the conduction band.

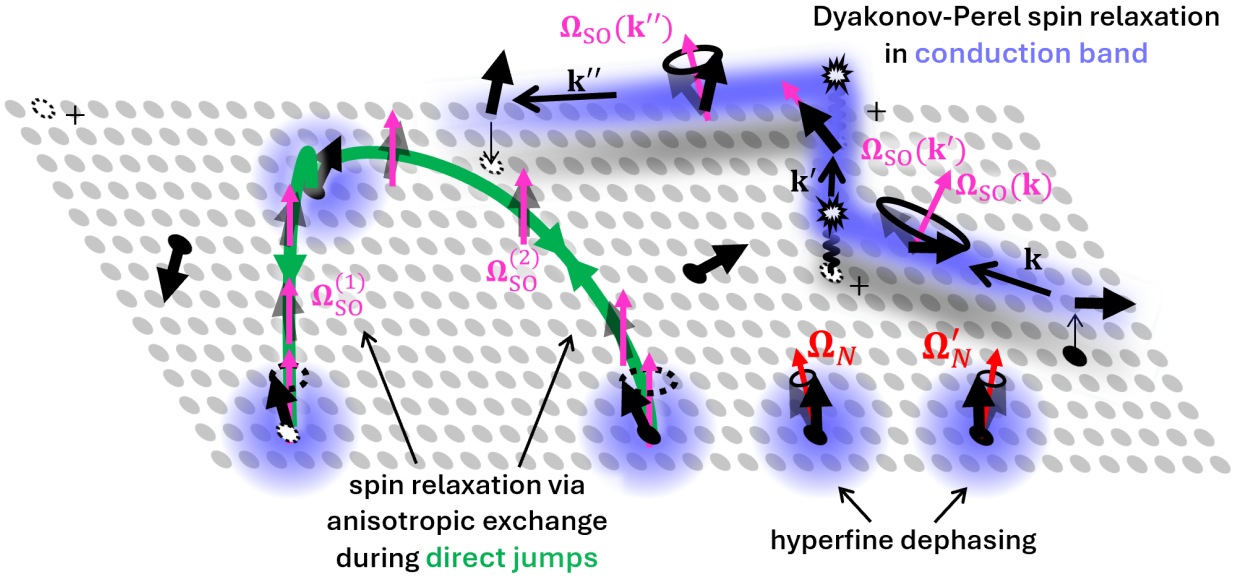

Figure 1.3: Illustration of relevant low-temperature spin relaxation mechanisms characteristic of n-CdTe and other zinc-blende semiconductors. In the upper right, the Dyakonov-Perel mechanism proceeds via scattering by ionized donors. Green lines signify spin tunneling to empty sites and mutual spin flips between donor-bound electron spins, both accompanied by spin relaxation. $\mathbf{\Omega}_{\mathrm{SO}}^{(1,2)}$ are effective spin-orbit fields leading to spin rotation proportional to the jump length. Finally, in the bottom right, ensemble-wide spin dephasing due to static random hyperfine fields is illustrated.

Anisotropic exchange

The spin-orbit splitting of the conduction band influences the spin dynamics of localized electrons as well, as their wave functions are largely built of conduction band states with very little admixture of valence band states (at least for shallow donors). This affects mutual spin flips that occur between neutral donors through what is called the anisotropic exchange interaction [70, 71]. The spin undergoes a rotation due to spin-orbit interaction while it is tunneling to a different site, therefore the exchange interaction couples spins that are slightly tipped, with an angle that is determined by the spin-orbit constant. Consequently, every mutual-spin flip brings about relaxation, as the z-projection of spin is not conserved.

In fact, the effect of the spin-orbit field can be described without considering the precise mechanism of interelectron interaction. This has been shown using the WKB (Wentzel-Kramers-Brillouin [72]) approximation in Ref. [73] for weak spin-orbit fields. Starting from a hydrogen atom Hamiltonian with a spin-orbit term, one arrives at an asymptotic electron wave function far from the donor

$$\Psi(r) \sim \exp\left(-\frac{r}{a_{\mathrm{B}}}\right) \exp\left[i\boldsymbol{\gamma}_{\mathrm{SO}}(r)\cdot\hat{\mathbf{S}}\right], \tag{1.9}$$

where a_{B} is the Bohr radius, $\hat{\mathbf{S}}$ is the electron spin operator, and $\boldsymbol{\gamma}_{\mathrm{SO}}(r)$ is the distance-dependent angle of spin rotation around the spin-orbit field. The second exponential in the above equation is simply a rotation operator. Therefore, in the event of the spin tunneling to a different site, it is this tilted spin that will occupy the new site. This consideration enables us to conclude that the relaxation mechanism must be the same for both mutual spin-flips and

jumps to unoccupied sites. The only important thing then is the jump length, as the rotation angle is proportional to distance. This mechanism is illustrated in Fig. 1.3 for both tunneling spin jumps and mutual spin flips.

The rotated spin $\mathbf{S}'$ can be represented by $\mathbf{S}' = \hat{R}(\boldsymbol{\gamma}_{\mathrm{SO}})\mathbf{S}$, where the matrix $\hat{R}(\gamma_{\mathrm{SO}})$ describes the rotation around the vector $\boldsymbol{\gamma}_{\mathrm{SO}}$ by the angle γ_{SO}. It can be expressed via the Rodrigues formula [74, 75]:

$$\hat{R}(\boldsymbol{\gamma}_{\mathrm{SO}}) = \hat{1} + \sin(\gamma_{\mathrm{SO}})\hat{Q} + 2\sin^2\left(\frac{\gamma_{\mathrm{SO}}}{2}\right)\hat{Q}^2 = \exp\left(\gamma_{\mathrm{SO}}\hat{Q}\right), \tag{1.10}$$

where the matrix $\hat{Q}$ describes the cross-product of the spin vector $\mathbf{S}$ and the unit vector describing the direction of the spin-orbit field $\boldsymbol{\gamma}_{\mathrm{SO}}/\gamma_{\mathrm{SO}}$, i. e., $\hat{Q}\mathbf{S} \equiv [\boldsymbol{\gamma}_{\mathrm{SO}} \times \mathbf{S}]/\gamma_{\mathrm{SO}}$. Averaging the formula over the direction of the field, we arrive at the scalar expression

$$R(\gamma_{\mathrm{SO}}) = 1 - \frac{4}{3}\sin^2\left(\frac{\gamma_{\mathrm{SO}}}{2}\right) \approx 1 - \frac{\gamma_{\mathrm{SO}}^2}{3}, \tag{1.11}$$

which describes spin relaxation due to a single average jump. The approximation $\gamma_{\mathrm{SO}} \ll 1$ is normally very good, as typically $\gamma_{\mathrm{SO}} \sim 10^{-2}$, at least in GaAs and CdTe [71]. It can be calculated via

$$\gamma_{\mathrm{SO}} = r\sqrt{\frac{m_e}{2E_{\mathrm{b}}}}\Omega_{\mathrm{SO}}(\mathbf{k}_0), \tag{1.12}$$

where m_e^* is the electron mass, E_{b} is the electron binding energy, and $\mathbf{k}_0 = \frac{\mathbf{r}}{r}\left(\frac{2mE_{\mathrm{b}}}{\hbar^2}\right)^{1/2}$ [73]. Since γ_{SO} is proportional to the distance away from the donor r, it is usually given in terms of the spin-orbit length $\gamma_{\mathrm{SO}} = r/l_{\mathrm{SO}}$. For example, in GaAs $l_{\mathrm{SO}} \approx 5$ µm [73], while interdonor jumps cover submicron lengths even at very low doping.

Hyperfine interaction

Another source of a fluctuating magnetic field is represented by the nuclear spin system, which we discuss in more detail in Section 1.3. The stochastic behavior of individual nuclear spins due to spin-spin interactions leads to a random distribution of nuclear spins which evolves with a characteristic time of the order of 10^{-4} s [35]. The straightforward relaxation of a stationary single spin due to precession in the randomly evolving effective field determines the contribution to T_2. It is normally very weak, occurring on the timescale of $10 - 100$ µs in GaAs quantum dots [57, 76]. A much stronger effect has to do with ensemble-wide dephasing that is due to the inhomogeneity of the nuclear field as shown in Fig. 1.3. The phase differences between different carrier spins caused by this dephasing are much greater than the phase changes incurred directly by nuclear spin fluctuations [76, 77], that is, $T_2^* \ll T_2$. This is clearly demonstrated in spin echo experiments [56, 57, 78].

In zinc-blende semiconductors, spin relaxation due to nuclear spins is usually neglected for holes due to weak hyperfine interaction; it is also insignificant for free electrons, as the movement of the electron produces very strong motional narrowing. In contrast, it becomes the dominant relaxation mechanism for localized electrons in the low temperature limit [35, 68]. However, even at temperatures much lower than the donor activation energy, the motional narrowing effect significantly reduces the hyperfine contribution to electron spin relaxation, as we will show in Chapter 2.

Effect of magnetic fields on spin relaxation

In the simplest picture, applying an external magnetic field slows down the relaxation of the spin component parallel to the field (longitudinal spin relaxation), and does not affect the relaxation of the transverse component (transverse spin relaxation). This is evident if one considers a rotating frame [35], since only the transverse component of the fluctuating fields is suppressed. Efficient suppression occurs when the Larmor frequency Ω in the longitudinal field is much greater than the inverse correlation time τ_c^{-1}. This can be used to estimate τ_c [68], which seems to range from 10^{-10} s to 10^{-8} s in weakly doped n-GaAs at liquid helium temperatures. Such suppression of spin relaxation in a longitudinal field is fairly ubiquitous, having been observed in various bulk semiconductors as well as nanostructures such as quantum dots (e. g., see Refs. [15, 79]). A frequent complication comes in the form of an inhomogeneous g-factor distribution. In this case, spin dephasing is enhanced as the magnetic field is increased, leading to a reduction of T_2^*. Reference [80] provides good examples of both these field-dependent behaviors.

A deeper look reveals the complexity of the subject, as spin relaxation mechanisms themselves may be field-dependent. For example, it has been shown theoretically that in asymmetric quantum wells based on zinc-blende semiconductors, Larmor precession and cyclotron motion can suppress Dyakonov-Perel relaxation or not depending on the interplay of linear-in-$\mathbf{k}$ spin-orbit terms [81]. Further complications arise if interactions other than the hyperfine must be taken into account. In particular, the electron-phonon interaction becomes relevant in fields of the order of 1 T and leads to a relaxation rate $\propto B^{-\nu}$, where $\nu \approx 3-4$ [82].

The spin components that are transverse to the external field experience no improvement in spin coherence, as for them the fluctuating fields are directed along the external field, and hence are not suppressed. However, in systems with significant inhomogeneous broadening, such as quantum dot ensembles and deep CdTe/CdMgTe quantum wells, a broad distribution of g-factors leads to faster decoherence when a magnetic field is applied [41, 83]. A similar effect can be produced if the precession frequencies are different for different states visited by the spin. This "frequency mismatch broadening" effect is more thoroughly discussed in Section 2.6.3 regarding indirect hops between neutral donors in the presence of a finite nuclear spin polarization, which leads to different effective g-factors for localized and free states.

Electron spin relaxation, donor density, and temperature

The dependence of the electron spin relaxation rate on donor density is well-studied at low temperatures in n-GaAs, notably in Refs. [68, 80]. Due to their overall similarity, qualitatively, these results should apply to n-CdTe as well. In zero (or weak) magnetic field, the shape of the dependence is such that the longitudinal relaxation time is shorter at doping that is much lower or higher than the Mott transition, while a maximum is reached at doping density around the Mott transition. The current understanding of the physical origins of such behavior is as follows. At low doping and sufficiently low temperature, the electrons are "glued" to the donors, and the ensemble of electron spins experiences the full dephasing effect of the random hyperfine field. In the metallic phase, the effect of nuclei is unimportant due to strong motional narrowing, but frequent scattering in the conduction band leads to increasing Dyakonov-Perel relaxation as the doping density rises. The spin relaxation time reaches its peak just below the Mott transition, where the effect of the nuclear field is already small due to motional narrowing brought about by jumps between closely-spaced donors, but the electron density in the conduction band is not yet enough for Dyakonov-Perel relaxation to be significant.

The shape of the curve can be altered by applying a magnetic field, since it suppresses the

effect of nuclear spin fluctuations, as we have mentioned above. Indeed, in n-GaAs at liquid helium temperatures, a magnetic field of 1 T can enhance the energy relaxation time T_1 by more than two orders of magnitude [80]. On the other hand, this decreases T_2^* due to g-factor inhomogeneity.

Temperature affects electron spin relaxation in the regime where temperature changes lead to significant ionization of localized states. For GaAs, this seems to correspond to temperatures of around 10 K [80, 84]. One would expect the corresponding temperatures to be about twice as high in CdTe due to the higher binding energy. The magnetic field effects mentioned in the previous paragraph are strongest when all electrons are localized. The relaxation-suppressing effect of the magnetic field gradually disappears as the temperature is increased due to decreasing occupancy of donor sites, while the zero-field relaxation is prolonged due to motional narrowing. The decrease of spin coherence is not as temperature-dependent, on the other hand [80]. A thorough study of temperature-dependent electron spin relaxation in n-GaAs has been performed in Ref. [84], where the hyperfine and Dyakonov-Perel contributions to the relaxation rate were weighted by the fractions of electrons occupying the corresponding states to reach near-perfect agreement with the experimental data. This implies that spin mixing between the localized and delocalized electrons is much faster than their individual spin relaxation rates.

1.2.3 Spin-exchange scattering

An efficient spin-exchange scattering process between itinerant and free electrons is frequently proposed in the literature to describe the underlying mechanisms of experimental phenomena, namely the fast equilibration of localized and delocalized spins [73, 84–92]. Originally proposed in Ref. [85], the mechanism was invoked to explain several properties of their experiments on GaAs using optically detected NMR, namely i) the observation of an NMR signal through optical resonances corresponding to delocalized states, and ii) the simultaneous depolarization of all lines observed in an optical nuclear magnetic resonance experiment. The former seems to be a stronger argument due to the drastically different Overhauser fields experienced by localized and delocalized electrons. A mutual spin-flip during such a scattering event generally conserves the total energy, and therefore has a high probability compared to other processes, such as re-excitation of localized electrons via Auger processes, and trapping-and-release of a delocalized electron on an excited donor state, as the analysis of Ref. [85] shows. The final result of the exchange process is the equilibration of the average values of the localized spins $\langle S_{\mathrm{loc}} \rangle = \langle S_{\mathrm{free}} \rangle$, and the spin ensembles follow the same spin dynamics.

This result is important for studies of both nuclear and electron spin systems. In optical studies of nuclear spin dynamics, it ensures that information on the nuclear spin system can be extracted from virtually any electron resonance, since the average spin is shared by all electron states. The effect of efficient spin mixing on the electron spin system is primarily the weighting of the contributions of conduction band and localized spin relaxation mechanisms by the respective equilibrium electron populations, as the modeling of Refs. [84, 90] shows.

For the mechanism to be efficient enough to induce the experimentally observed cross-relaxation, i. e., make the localized and delocalized electrons share the same spin relaxation times, it must be faster than all spin relaxation mechanisms. In the literature, not many calculations exist for the rate of this spin exchange. In the seminal Ref. [85], the exchange rate is estimated to be around 1×10^{11} s^{-1} in n-GaAs with doping density $n_{\mathrm{d}} = 10^{15}$ cm^{-3} at $T = 10$ K, and is proportional to the density. For this density, the order-of-magnitude estimate of Ref. [87] yields 1×10^{9} s^{-1} at $T = 5$ K, while the more involved calculation of Mahan and Woodworth [88] results in around 5×10^{11} s^{-1} at 4 K. Finally, the calculation of Kavokin [73]

predicts a rate of around 10^{10} s^{-1} at the same doping density.

These times are fast enough that all electron states share the effect of the Overhauser field on localized spins, since nuclear spin relaxation is many orders of magnitude slower. We use this conclusion in Chapter 3 to justify tracking the Overhauser field felt by neutral donors via an excited state of a free exciton. For electrons, the spin relaxation times are typically of the order of nanoseconds, which is still slower than most of the estimates for localized-delocalized spin exchange, but one can expect that at sufficiently low temperatures the spin-exchange mechanism may become inefficient enough for cross-relaxation to disappear. In Chapter 2, our experiments are described without accounting for this exchange mechanism to satisfying agreement.

1.2.4 Electron spin transport and diffusion

From Section 1.2.2, it is evident that the observed electron spin relaxation cannot be fully understood without considering the full spatiotemporal spin dynamics, provided that spin transfer between states is faster than the spin relaxation rate. The following treatment is quite general, though we stress that localized (trapped) electrons are understood as electrons bound to neutral donors (traps) in CdTe, while delocalized (free, itinerant) electrons are electrons with energies above the bottom of the conduction band and move freely throughout the crystal. Assuming these are the only types of electrons that can occur in principle, one may envision two main types of spin hops: direct hops between donors via tunneling or mutual exchange spin-flips, or indirect hops through the conduction band. The latter can be the result of thermal ejection followed by re-trapping by an ionized donor, or they can be mediated by mutual spin-flips between localized and itinerant electrons. The mutual spin-flip mechanism is usually assumed to be very efficient as we have discussed in the previous Section, but both are thermally activated.

Any type of spin motion leads to motional averaging of the fluctuating hyperfine field. However, different types of jumps are in principle accompanied by different types of relaxation. Case in point, in semiconductors without inversion symmetry, direct jumps induce spin relaxation via anisotropic exchange, while during indirect jumps via the conduction band the spins undergo Dyakonov-Perel relaxation. The exact contribution of either depends on the importance of the relevant transport mechanism. In general, conduction band electron spin dynamics are reflected in the spin dynamics of localized states, which is well-demonstrated in the previously mentioned Ref. [84] (see also Ref. [93]). In Chapter 2, we present a thorough study of the complex interplay of localized and delocalized spin relaxation mechanisms in the spin noise signal of neutral donors, including the resulting spatiotemporal spin noise spectra. To facilitate the discussion of delocalized spin behavior in Chapter 2, below we give a brief overview of various phenomenological release, diffusion, and trapping mechanisms, with estimates made for bulk insulating n-CdTe crystals.

Release to itinerant state

Generally, the release of particles from trapped states is described by the empirical Arrhenius equation, i. e.,

$$\nu_\mathrm{r} = \nu_{\mathrm{r},\infty} \exp\left(\frac{-E_\mathrm{A}}{k_\mathrm{B}T}\right), \tag{1.13}$$

where $\nu_{\mathrm{r},\infty}$ is the attempt-to-escape frequency, E_A is the activation energy, k_B is the Boltzmann constant, and T is the temperature. Historically, the approach was frequently applied in analyses of thermally stimulated conductivity and thermally stimulated photoluminescence

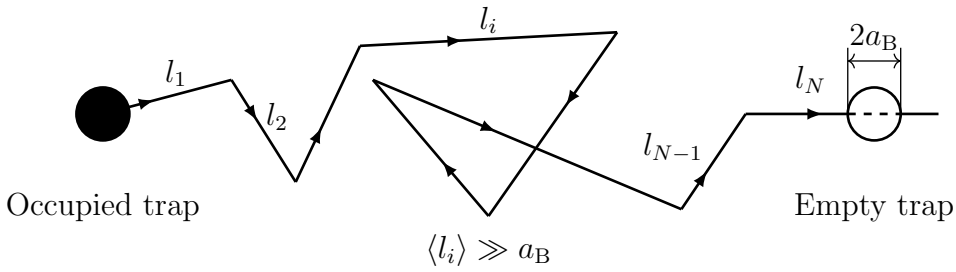

Figure 1.4: Illustration of diffusion-assisted ballistic trapping. Only a small fraction of space is occupied by traps, and the average distance between traps is much greater than the mean free path the particle in the itinerant state $\langle l_i \rangle$. The mean free path of is much greater than the size of individual traps, estimated here by a_B. Hence, transport in the itinerant state is generally diffusive, but trapping is ballistic.

experiments [94]. The equation applies also to shallow donors in CdTe [95], where the attempt-to-escape frequency is estimated as $\nu_{r,\infty} \sim 3 \times 10^{11}$ s^{-1} [96].

Transport between traps: diffusive vs. ballistic

The two extremes of transport between traps in the presence of scattering centers are represented by diffusive and ballistic motion. The former occurs if the momentum scattering rate τ_p^{-1} is much greater than the trapping rate ν_t: $\tau_p \nu_t \ll 1$, that is, the mean free path is much smaller than the displacement between the initial and final sites. Then, multiple scattering events occur before trapping finally occurs. Conversely, if the momentum scattering time is much greater than the spin lifetime in the free state $\tau_p \nu_t \gg 1$, then ballistic transport is expected.

In CdTe, at doping below the Mott transition ($n_{Mott} = 2 \times 10^{17}$ cm^{-3}) with reasonably low compensation, the well-known Brooks-Herring formula [97] predicts an ionized impurity scattering rate $\tau_i \approx 10^{-13} - 10^{-11}$ s at temperatures in the range between 5 K and 25 K. At these low temperatures, ionized impurity scattering is the dominant momentum scattering mechanism, so we let $\tau_p = \tau_i$. To estimate the trapping rate, we use the diffusion coefficient $D \equiv \nu_t l_s^2$, where l_s is the scattering length of itinerant electrons which can be estimated directly from experiments presented in Chapter 2. If the diffusion is governed by the momentum scattering time τ_p, we may also write

$$D_{\tau_p} = \frac{k_B T}{m_e^*} \tau_p, \tag{1.14}$$

where m_e^* is the electron effective mass. Taking $l_s^{-2} \approx 10^{13}$ m^{-2}, we estimate $\nu_t^{-1} \approx 10^{-9} - 10^{-11}$ s. Analysis shows that a regime where the ratio $\tau_p \nu_t \ll 1$ does not strictly hold can be expected in very weakly n-doped samples with $\lesssim 1\%$ compensation. In conclusion, one expects low temperature spin transport to be largely diffusive in n-CdTe, even at very low donor densities.

We add that spin-flip exchange scattering, though very efficient, does not alter the aforementioned dynamics, as energy conservation requires that the conduction electron stay in the same state.

Trapping: diffusive vs. ballistic

The general problem of diffusion in the presence of traps is in fact a separate subject that has been extensively investigated for hopping or continuous diffusion in the presence of regularly

or randomly distributed static or dynamic traps [98–102]. It is doubtless that more involved approaches yield deeper insight. However, simple continuous diffusion with an effective diffusion coefficient D has the advantage of having a clear physical meaning. Hence, we will be focusing on this more empirical approach.

Electron spin trapping by donors is determined by the relationship between two length scales: the neutral donor Bohr radius a_B, and the mean free path of the itinerant state. Diffusive trapping occurs when the size of the trap is large compared to the mean free path defined by the thermal velocity and momentum scattering rate. If the trap is much smaller than the mean free path, then the trapping is expected to be ballistic. In this case, one expects

$$\nu_t \propto v_{th} n_{d+}, \tag{1.15}$$

as first shown by Maxwell [103]. In the above, n_{d+} is the density of ionized impurities, and the thermal velocity is given by $v_{th} = \sqrt{k_B T / m_e^*}$. In the diffusive trapping regime, we have rather $\nu_t = \alpha D n_{d+}$ [100, 104], where D is the diffusion coefficient on the scale of a single trap, and α is a constant with the dimension of length. Since $D \propto v_{th}^2$, we may equivalently write

$$\nu_t \propto v_{th}^2 n_{d+}. \tag{1.16}$$

Recalling that $D = \nu_t l_s^2$ by definition, one expects $l_s^{-2} = \alpha n_{d+}$, where α is the same coefficient as above.

Based on the τ_p estimate made above, we estimate the mean free path $\tau_p v_{th}$ to be roughly between a_B and $100 a_B$ in CdTe at low temperatures, depending on the doping. Therefore, the trapping is unquestionably ballistic when τ_p is on the longer side, corresponding to low to moderate doping densities. Incidentally, this doping regime is where itinerant electrons should be expected to make the greatest contribution to spin relaxation. At higher doping, direct hops between donors are much more efficient at low temperatures [105], and spin transport is governed by tunneling between donor sites instead of free electron propagation.

To conclude, in insulating n-CdTe at low temperatures one should almost always expect a combination of diffusive transport and ballistic trapping, which is illustrated in Fig. 1.4. Transport may become ballistic only in very pure weakly doped samples, and trapping may should acquire diffusive characteristics near the Mott transition.

Trapping: rate equations

Quoting Ref. [101], let us write a rate equation for the trapped state populated by:

$$\frac{\partial n_{tr}^*}{\partial t} = \nu_t^* n_u^* - \nu_r n_{tr}^*, \tag{1.17}$$

where n_{tr}^* is the particle density inside traps, i. e., it is the number of trapped particles divided by the total volume of the traps[4], and n_u^* is the particle density outside traps defined as the number of free particles divided by the total volume (the total volume of traps is comparatively small and can be neglected here). Applied to spin dynamics, these are the average spin densities in the localized and delocalized states. Evidently, at low temperatures $\nu_t^* \gg \nu_r$. Note that it is also possible to write the equation above in terms of occupations, but we prefer to deal with

[4]Trap volume can only be defined in a straightforward way for traps with well-defined borders. On a more fundamental level, the traps are described by wave functions. However, in the simple approach described in this section, it should be sufficient to use the characteristic linear size and volume of the wave functions. As a pertinent example, for hydrogen-like traps, one may take the Bohr radius as the characteristic linear size.

densities as in Ref. [101] as this approach is more applicable to spin dynamics, in particular the theoretical model introduced in Chapter 2.

Though there is particle exchange between localized and delocalized states, the total number of particles must stay the same in the absence of spin relaxation. It can be shown that in this case, the release and trapping rates must be renormalized for the itinerant state:

$$\frac{\partial n_u^*}{\partial t} = D\Delta n_u^* + \kappa\left(\nu_\mathrm{r} n_\mathrm{tr}^* - \nu_\mathrm{t}^* n_u^*\right), \tag{1.18}$$

where Δ is the Laplacian. Introducing the trap volume V_0 and their number density ν, the fraction of space occupied by traps κ can be written as

$$\kappa = V_0\nu, \tag{1.19}$$

assuming $\kappa \ll 1$ which is consistent with the estimates we have made above. The explicit appearance of κ is essentially due to the fact that the equations are written for densities, not particle populations. However, by an appropriate choice of new variables, κ can be eliminated from the equations. The rate ν_t^* can be redefined to include the κ factor, $\nu_\mathrm{t} = \kappa\nu_\mathrm{t}^*$, and we can also replace either $n_\mathrm{tr} = \kappa n_\mathrm{tr}^*$ or $n_u = \kappa^{-1} n_u^*$. Using the new definitions, we write

$$\frac{\partial n_\mathrm{tr}}{\partial t} = \nu_\mathrm{t} n_u - \nu_\mathrm{r} n_\mathrm{tr}, \tag{1.20}$$

$$\frac{\partial n_u}{\partial t} = D\Delta n_u + \nu_\mathrm{r} n_\mathrm{tr} - \nu_\mathrm{t} n_u, \tag{1.21}$$

Within this convention, if the itinerant state is nearly empty, then $\kappa^{-1}\nu_\mathrm{t} \gg \nu_\mathrm{r}$, and $\kappa^{-1} n_\mathrm{tr} \gg n_u$. Therefore, ν_t and ν_r (n_tr and n_u) can be of the same order of magnitude even though the itinerant state is nearly empty, provided that traps are distributed sparsely. Indeed, without additional considerations regarding the values of the trapping and release rates, if the average values of n_tr and n_u in the steady state are equal, then necessarily $\nu_\mathrm{r} = \nu_\mathrm{t}$, though for electron spins in CdTe the equality can be evoked without this constraint as we discuss in Chapter 2.

1.3 Nuclear spin system

As we mentioned in Section 1.2.2, the nuclear spin system contributes to electron spin relaxation. Indeed, the nuclear spins are frequently considered as simply another source of electron spin decoherence, especially in quantum dots [6, 108]. However, they can also act inversely, increasing the electron spin lifetime in the regime of dynamic nuclear polarization. For example,

Table 1.1: Various parameters of the CdTe nuclear spin system. x_α are the natural abundances, A_α are the hyperfine constants, and γ_α are the nuclear gyromagnetic ratios. Throughout the work, we neglect the ^{123}Te isotope, as its natural abundance is less than 1%. Data are taken from Refs. [42, 106, 107].

Isotope	x_α	A_α (μeV)	γ_α (10^7 rad s^{-1} T^{-1})
^{111}Cd	0.128	-37.4	-5.698
^{113}Cd	0.122	-39.1	-5.960
^{123}Te	0.009	-	-7.059
^{125}Te	0.071	-45	-8.511

the feedback from the nuclei can be used for frequency focusing of electron spin precession in quantum dots [7], and there is a growing body of encouraging research on the topic of hybrid quantum registers employing nuclear spins as long-lived quantum bits [109–113]. As nuclear spins do not interact directly with light, they can be controlled either directly by radiofrequency (rf) fields in NMR conditions, or indirectly via hyperfine interaction with electrons. The latter is typically achieved through resonant or nonresonant optical pumping, with protocols of increasing complexity, alone or in combination with rf pulses [111, 114–116].

In non-enriched CdTe, most isotopes possess zero spin $I = 0$, i. e., they are non-magnetic. The stable isotopes with nonzero spin (magnetic nuclei) are ^{111}Cd, ^{113}Cd, ^{123}Te, and ^{125}Te. All these isotopes possess spin $I = 1/2$. Their natural abundances are shown in Table 1.1. The combination of these factors make the CdTe nuclear spin system particularly interesting, as other semiconducting materials consisting of only $I = 1/2$ magnetic nuclei are scarce. The only other examples are CdSe, which is very similar in terms of nuclear spin, and silicon, which only has around 5% of magnetic nuclei. For comparison, the nuclear spin system of GaAs, which is the most-studied among semiconductors, is composed of nuclei with $I = 3/2$. This fact lends itself to generally stronger spin-spin interactions, which is due both to the smaller average distance between nuclear spins and the larger value of I (the gyromagnetic ratios are similar between GaAs and CdTe [106]).

Despite the rather low density of magnetic nuclei in CdTe, they still contribute to electron spin relaxation in weakly n-doped samples, as we show in Chapter 2. Additionally, this sparsity of the nuclear spin system leads to interesting effects in dynamic nuclear spin polarization experiments, which are described in Chapter 3.

Below we briefly recall the properties of nuclear spin systems that are relevant in this work. We begin by analyzing the various interactions that occur in systems of nuclear spins.

1.3.1 Hyperfine interaction

In a broad sense, the hyperfine interaction is the interaction of nuclear multipole moments with various electromagnetic fields created by electrons. For the electron spin, it becomes important in semiconductors with low n-doping at low temperature as a source of electron spin relaxation [68, 84, 105], and in the case of strong nuclear spin polarization, leading to an Overhauser shift [10, 35, 117]. For the nuclear spin system, it is the primary channel of interaction with the environment at low temperatures [118]. The greatest contribution to the hyperfine interaction comes from the magnetic dipole, and the secondary contribution is due to electric quadrupole terms. The quadrupole effects are absent for nuclei with spin $I \leq 1/2$, but they can significantly alter the behavior of the nuclear spin system in weak magnetic fields in other cases [119, 120]. The dipole moment of a nucleus is determined by its spin, and the hyperfine Hamiltonian is written as [118]

$$\hat{\mathcal{H}}_{\text{hf}} = \hbar^2 \gamma_e \gamma_N \hat{\mathbf{I}} \cdot \left[\frac{\hat{\boldsymbol{l}}}{r^3} - \frac{\hat{\mathbf{s}}}{r^3} + 3\frac{\mathbf{r}(\hat{\mathbf{s}} \cdot \mathbf{r})}{r^5} + \frac{8\pi}{3}\delta(\mathbf{r})\hat{\mathbf{s}} \right], \tag{1.22}$$

where $\gamma_{e(N)}$ is the electron (nuclear) gyromagnetic ratio, $\hat{\mathbf{s}}$ and $\hat{\mathbf{I}}$ are the electron and nuclear spin operators, $\hat{\boldsymbol{l}}$ is the electron orbital momentum, $\mathbf{r}$ is the coordinate of the electron with respect to the nucleus, and $\delta(\mathbf{r})$ is the Dirac delta function. The first term in $\hat{\mathcal{H}}_{\text{hf}}$ is the interaction with the electron orbital momentum, the second and third terms constitute the dipole-dipole interaction with the electron spin, and the fourth term is the Fermi contact interaction. In zinc-blende semiconductors, the conduction band is formed from s-type atomic states with orbital

quantum number $l = 0$, therefore there is no field created by the orbital motion of the electron. Furthermore, due to spherical symmetry of the s-type Bloch wave, the classical magnetic dipole terms average to zero, and only the Fermi contact term remains:

$$\hat{\mathcal{H}}_{\text{hf}} = \hbar^2 \gamma_e \gamma_N \frac{8\pi}{3} \delta(\mathbf{r}) \hat{\mathbf{I}} \cdot \hat{\mathbf{s}} = A \nu_0 \delta(\mathbf{r}) \hat{\mathbf{I}} \cdot \hat{\mathbf{s}}, \tag{1.23}$$

where A is the hyperfine constant, and ν_0 is the elementary cell volume.

Regarding holes, in zinc-blende semiconductors the valence band is formed from p-type orbitals, with $l = 1$. This creates hole subbands with total momenta $j = \pm 3/2$ (heavy holes) and $j = \pm 1/2$ (light holes). The p-type character of the hole states leads to the weakness of the contact term. On the other hand, nonzero orbital momentum results in the other terms being non-zero. In GaAs, they amount to about 10% of the coupling strength of the electron contact interaction in absence of *hh*-*lh* mixing [121]. Though nonzero *hh*-*lh* mixing enhances hyperfine interactions with holes, the relaxation times are still much longer than that with electrons [122]. Hence, hyperfine interaction with holes is typically neglected in zinc-blende materials [35]. On the other hand, the weakness of the hyperfine interaction for holes leads to longer spin relaxation times when it is the dominant relaxation mechanism [123]. In perovskites, the situation is reversed somewhat because it is the valence band that is characterized by an s-type Bloch function, while the conduction band is of p-type. As a result, it is the hole spins that are efficiently coupled to the nuclear spin system (for implications in optical orientation, see, e. g., Ref. [15]).

1.3.2 Effective hyperfine fields

In conventional semiconductors, the area of carrier localization is typically large enough to cover thousands of nuclei and cannot be made much smaller. In this case, the electron cannot distinguish between one nucleus or another, i. e., it interacts with the total, or average, nuclear spin, which may be described classically. This is the fundamental reason for introducing effective magnetic fields to facilitate the description of the hyperfine interaction.

We introduce the effective nuclear field (the Overhauser field) $\mathbf{B}_N$ acting on an electron spin,

$$\mathbf{B}_N = \frac{\nu_0 \sum_i A_i |\psi(\mathbf{r}_i)|^2 \mathbf{I}_i}{g_e \mu_{\text{B}}} = \frac{\sum_\alpha A_\alpha \mathbf{I}_\alpha}{g_e \mu_{\text{B}}} \approx \frac{A \langle \mathbf{I} \rangle}{g_e \mu_{\text{B}}} = b_N \langle I \rangle / I, \tag{1.24}$$

where b_N is the nuclear field in the case of complete polarization, i numbers magnetic nuclei, and α denotes the different nuclear species. In GaAs, owing to the small electron g-factor and $I = 3/2$, $b_N = 5.3$ T [35]. In CdTe, due to the low density of magnetic nuclei, b_N is much smaller at ≈ -70 mT [27]. Evidently, the Overhauser field $\mathbf{B}_N$ is a measure of nuclear spin polarization.

Unless the nuclear spins are completely polarized, there is a fluctuating component of the nuclear field that causes electron spin relaxation. The magnitude of this component is inversely proportional to the square root of the number of nuclei interacting with the electron [6]. It is usually described by the parameter δ_e, which in Ref. [6] is calculated as

$$\delta_{\text{e}}^2 = \frac{16 I(I+1)}{3 N_{\text{L}}} \frac{\sum_j A_j^2}{(\mu_{\text{B}} g_{\text{e}})^2}, \tag{1.25}$$

where N_{L} is the effective number of nuclei that the electron interacts with. The distribution of nuclear spin fluctuations is then taken into account via the Gaussian probability density

$\mathcal{F}(\mathbf{\Omega}) = (\sqrt{\pi}\delta_e)^{-3}\exp(-\Omega^2/\delta_e)$, where Ω is the electron precession rate in the effective hyperfine field. The Overhauser field $\mathbf{B}_N$ acts in much the same way as a regular magnetic field. For instance, it affects the luminescence polarization via the Hanle effect, which is often used to measure $\mathbf{B}_N$ to this day, despite the technique being a good 40 years old [10]. It also leads to Zeeman splitting of the electron spin states, which permits direct spectroscopic measurement of $\mathbf{B}_N$ even for single quantum dots [53, 124]. A more involved discussion of experimental techniques that can be employed to measure $\mathbf{B}_N$ is provided in Section 1.6.

The counterpart of the Overhauser field that is produced by the electron spin is the Knight field

$$\mathbf{B}_e(\mathbf{r}) = \frac{\nu_0\langle A\rangle|\psi(\mathbf{r})|^2\langle\mathbf{S}\rangle}{\hbar\gamma_N} \equiv b_e\frac{\langle\mathbf{S}\rangle|\psi(\mathbf{r})|^2}{S|\psi(\mathbf{r})|^2\Big|_{\max}}, \tag{1.26}$$

which acts on the nuclei under the electron orbit. It is proportional to the average electron spin $\langle\mathbf{S}\rangle$ ($S = 1/2$ is the maximum value of $\langle\mathbf{S}\rangle$). The spatial distribution of the Knight field follows the electron probability distribution $|\psi(\mathbf{r})|^2$; this is also why the field exerted by localized electrons is much greater than that of free ones. The Knight field averaged over the electron wave function is given by $b_e \ll b_N$. For neutral donors in GaAs, $b_e \approx 100$ mT, while in CdTe, $b_e \approx 160$ mT due to enhanced electron localization.

The total field felt by the nuclear spin system is the sum of $\mathbf{B}_e$ and the external field $\mathbf{B}$. Therefore, an estimate of the amplitude of $\mathbf{B}_e$ may be obtained via the Hanle effect or by measuring the field dependence of the hyperfine shift [125, 126]. The fluctuating component of the Knight field essentially determines the hyperfine nuclear spin relaxation rate.

1.3.3 Nuclear spin-spin interactions and the local field

Though the spin-spin interactions of nuclei are weak compared to typical electron energies, they turn out to be very important for the description of both nuclear spin physics, and electron-nuclear spin interactions in the case of high nuclear spin polarization and low external field. The magnetic dipole-dipole coupling of nuclear spins is virtually inescapable in crystalline matter, since most known isotopes possess nonzero spin[5]. The spins occupy a rigid lattice, which determines the overall scale of the interaction, together with the gyromagnetic ratios. The Hamiltonian of this interaction can be written as

$$\hat{\mathcal{H}}_{\rm dd} = \hbar^2\gamma_N\gamma_N'\left[\frac{\hat{\mathbf{I}}\cdot\hat{\mathbf{I}}'}{r^3} - 3\frac{(\hat{\mathbf{I}}\cdot\mathbf{r})(\hat{\mathbf{I}}'\cdot\mathbf{r})}{r^5}\right], \tag{1.27}$$

where γ_N and γ_N' are the gyromagnetic ratios of nuclei with spins $\hat{\mathbf{I}}$ and $\hat{\mathbf{I}}'$, respectively, separated by the displacement $\mathbf{r}$ ($r = |\mathbf{r}|$). It can also be written as $\hat{\mathcal{H}}_{\rm dd} = \hat{\mathbf{I}}\,\hat{D}\,\hat{\mathbf{I}}'$, where the matrix $\hat{D}$ is traceless. The strength of the interaction is determined by the coupling constant $\hbar^2\gamma_N\gamma_N'I^2r_{\rm nn}^{-3}$, where $r_{\rm nn}$ is the distance between nearest neighbors. The magnetic dipole-dipole interaction is considered the default nuclear spin-spin interaction. In the Zeeman basis, it permits mutual spin-flips that conserve total spin as well as single and double spin flips which change the total spin of the pair by one or two quanta of angular momentum [118]. In other words, the magnetic dipole-dipole interaction does not conserve the total spin of the system,

[5] An interesting exception is silicon with only 5% magnetic nuclei, and in particular isotopically purified silicon, where $I \neq 0$ nuclei can constitute as little as 10^{-4} % of the nuclei [127]. The nuclear spin systems of CdTe and CdSe are also rather atypical in that less than half of the nuclei have spin, but this still necessitates accounting for the magnetic dipole-dipole interaction.

only the energy. Most studies of semiconductor nuclear spin systems are conducted in the presence of strong fields. In a strong magnetic field, when the total projection of spin on the axis of the field is a good quantum number, only transitions that conserve total spin are allowed. This is normally the case in NMR conditions, and in most studies of semiconductor nuclear spin systems. The spin-conserving terms of the Hamiltonian (1.27) are collectively referred to as its secular part and represent the truncated dipole-dipole Hamiltonian.

If the nuclei possess also nonzero quadrupole moments, then quadrupolar effects may become relevant, especially in low external fields. In an ideal cubic crystal, quadrupole interactions are suppressed due to symmetry. Nevertheless, they can be activated by an electric field gradient brought about by lattice deformation, charged or neutral impurities, or by an external electric field (e. g., from surface charges). For example, in GaAs, where every nuclear spin has $I = 3/2$, even comparatively weak strain, e. g., that which is brought about by gluing the sample to the sample holder of a cryostat, may increase the local field by a factor of five relative to what one would expect from magnetic dipole-dipole interactions alone [119]. An interesting aspect of the quadrupolar interaction as opposed to the Zeeman or Fermi contact interaction is that it leads to a non-equidistant spectrum. Since it is also inhomogeneous, strong quadrupolar effects may decrease the rate of energy transfer through the nuclear spin system, thereby improving electron spin coherence [128]. In CdTe, all nuclei with nonzero spin have $I = 1/2$, and therefore have zero quadrupolar momenta, which simplifies the study of its nuclear spin system considerably.

As opposed to these direct interactions, there exist also indirect spin-spin interactions that are mediated by electrons [118, 129, 130], also referred to as the J-coupling. The relevant Hamiltonian is denoted as $\hat{\mathcal{H}}_{\text{ind}}$. In semiconductors, these interactions are mediated by conduction band electrons through what is referred to as the Ruderman-Kittel-Kasuya-Yoshida (RKKY) interaction [131], or via excited electron states in insulators [132]. First direct experimental evidence to their existence was obtained in liquids, where certain nuclear resonance lines were observed as multiplets. This could only be due to an interaction characterized by nonvanishing trace, which ruled out the dipolar interaction and led to the introduction of an indirect coupling which has the bilinear form $J\,\hat{\mathbf{I}}\cdot\hat{\mathbf{I}}'$ [118, 131, 133]. It appears to be similar in magnitude to the direct magnetic dipole-dipole interaction in semiconductors, as exemplified by GaAs and CdTe [130]. Apart from the exchange-like J-coupling, it is sometimes necessary to consider the indirect pseudodipolar interaction [134]. The relevant Hamiltonian has the symmetry of the dipole-dipole interaction, i. e., it is traceless. In GaAs, the indirect interactions are known to be largely of opposite sign with respect to the direct dipolar interaction, reducing the total interaction considerably [135, 136]. In CdTe, they work together with the dipolar one [130].

The local field

The above interactions form the nuclear spin-spin Hamiltonian

$$\hat{\mathcal{H}}_{\text{SS}} = \hat{\mathcal{H}}_{\text{dd}} + \hat{\mathcal{H}}_{\text{ind}}. \tag{1.28}$$

To evaluate the strength of internuclear coupling as compared to the external and hyperfine fields it is convenient to define so-called (thermodynamic) local field, which is given by the trace of $\hat{\mathcal{H}}_{\text{SS}}^2$ per nuclear spin of the nuclear spin ensemble, i. e., $B_L^2 \propto \text{Tr}\left\{\hat{\mathcal{H}}_{\text{SS}}^2\right\}/N$ [118]. Assuming all nuclei possess the same gyromagnetic ratio γ_N, it may be calculated as [136]

$$B_L^2 = \frac{\text{Tr}\left\{\hat{\mathcal{H}}_{\text{SS}}^2\right\}}{\text{Tr}\left\{\hat{\mathcal{M}}_z^2\right\}} = \frac{1}{N}\frac{3}{I(I+1)}\frac{1}{\hbar^2\gamma_N^2}\text{Tr}\left\{\hat{\mathcal{H}}_{\text{SS}}^2\right\}, \tag{1.29}$$

where $\hat{\mathcal{M}}_z$ is a component of the magnetization of the nuclear spin ensemble, N is the number of nuclear spins in the ensemble.[6] It is typically of the order of 0.1 mT, or 1 G. In GaAs, since quadrupole effects contribute to the effective local field, it may significantly deviate from the theoretical minimum value 0.08 mT (no quadrupole contribution, indirect interactions fully compensate dipolar interaction) up to values of the order of 1 mT (strong quadrupolar effects), and even more near neutral donors due to the inhomogeneous electric field produced by localized electrons [136, 138].

Calculation of the local field in CdTe

In CdTe, the indirect nuclear spin-spin interactions have the same sign as the dipole-dipole interaction. Therefore, the local field is actually not that much smaller than in GaAs, despite the relative sparsity of the nuclear spin system and smaller spin. A calculation of B_L assuming a coupling with the symmetry of the magnetic dipole-dipole interaction is presented in Appendix A.1. Using the parameters for the dipole-dipole and pseudodipolar couplings presented in Refs. [129, 130], we learn that the dipole-dipole interaction leads to a local field of about 0.02 mT, while the inclusion of pseudodipolar and exchange terms brings it up to about 0.03 mT. Nevertheless, the absence of any kind of quadrupole effects simplifies the treatment of the nuclear spin system tremendously.

1.3.4 Spin temperature

Spin-lattice relaxation times (T_1) are generally quite long for nuclear spins, of the order of seconds [35, 118]. This is around three orders of magnitude slower than the precession rate of nuclear spins in the local field, which defines the T_2 of the nuclear spin system. Therefore, it is often the case that the nuclear spin system reaches internal equilibrium nearly instantly as compared to its energy exchange with the lattice. This fact is often used to justify the introduction of nuclear spin temperature, which can be orders of magnitude smaller in absolute value than the temperature of the lattice. In GaAs, which is a frequent platform for nuclear spin polarization experiments, spin temperatures of several microkelvins can be obtained with the thermal bath held at liquid helium temperatures [120]. In fields much greater than B_L, when the Zeeman term is much greater than nuclear spin-spin interactions, the concept of spin temperature is unnecessary, as the energy of the nuclear spin system is uniquely determined by the polarization. In contrast, it is essential when describing the physics in fields of the order of the local field or less [118].

The concept of spin temperature is not universally applicable. A rigorous theoretical review of the subject can be found in Ref. [118]. Generally, spin temperature can only be introduced if $T_2 \ll T_1$. Subsystems of different isotopes are routinely described by different spin temperatures in high fields, and in some cases, the quasi-equilibrium may fail to establish entirely [139]. This is because the establishment of a spin temperature is permitted by a relatively efficient spin-spin coupling. The rate of energy exchange between nuclear spins can be substantially reduced, as is the case in Ref. [139], where strong strain-related quadrupolar interactions forbid the thermalization of nuclear spin populations due to their spatial inhomogeneity and non-equidistant energy levels. This is, however, a rather rare occasion, and typically one expects the spin temperature approach to work [138]. In systems with $I = 1/2$, such as CdTe, quadrupolar

[6] In the above, we follow a frequently encountered convention in nuclear spin physics where the trace operation is defined to include a normalizing factor to ensure that the trace of the density matrix is unity [137]. For a density matrix written for one spin, the factor is $1/(2I+1)$, for two spins it is $1/(2I+1)^2$ etc.

interactions are absent, and we can confidently assume that the spin temperature hypothesis holds.

The nuclear spin system can be considered paramagnetic. In fact, in conventional non-magnetic semiconductors such as GaAs and CdTe, the spin-spin interactions are so weak that the high-temperature approximation is applicable down to spin temperatures < 0.1 µK. The spin susceptibility, governed by the Curie law, is then inversely proportional to temperature. Therefore, if the spin temperature is made low enough, even relatively weak external fields bring about significant nuclear spin polarization, much greater than the equilibrium value corresponding to lattice temperature.

A straightforward way of obtaining low spin temperatures is the adiabatic demagnetization process, which has been applied to metals to reach nanokelvin temperatures not just in the nuclear spin system, but in the entire sample due to the efficient spin-lattice coupling observed in metals [140]. The demagnetization approach requires a specialized experimental setup (dilution refrigerator, initial field as strong as possible), tightly controlled conditions, and finally a lot of room. Semiconductors present us with the opportunity of reaching microkelvin nuclear spin temperatures at liquid helium lattice temperature, using a magnetic field of the order of 1 mT and optical pumping.

1.4 Dynamic nuclear polarization

In classic optical orientation conditions (see Section 1.2.1), a constant electron spin polarization is maintained by continuous-wave optical pumping with circularly polarized light. The scalar nature of the contact hyperfine interaction allows for spin-conserving electron-nuclear mutual spin flips, since $\hat{\mathbf{I}} \cdot \hat{\mathbf{s}} = \hat{I}_z \hat{s}_z + (\hat{I}_+ \hat{s}_- + \hat{I}_- \hat{s}_+)/2$, where the $+$ $(-)$ subscript denotes the raising (lowering) operator. Therefore, the electron spin polarization supported by the pump can be partly transferred to the nuclei through what is called dynamic nuclear polarization (DNP) [10, 35]. The magnitude and spatial profile of the resulting nuclear spin polarization are determined by nuclear spin diffusion, applied magnetic field, the presence or absence of quadrupole effects, lattice temperature, pump power and wavelength, and the electronic structure of the sample (doping type and density, electron occupancies, wave functions) [27, 53, 120, 141]. DNP is commonly exploited to improve electron spin coherence in various implementations of qubits and quantum registers [111, 142].

The pumping stage is generally performed in an external magnetic field in Faraday geometry [10]. The magnetic field is necessary to stabilize the non-equilibrium nuclear spin, and to introduce the Zeeman energy reservoir. The latter ensures that nuclear spin flips are associated with significant changes in the total energy of the nuclear spin system, which eventually leads to its cooling. Such experimental conditions will henceforth be referred to as DNP conditions. In certain cases, the nuclei can be efficiently polarized even in zero external magnetic field. This requires an intrinsic effective magnetic field that would provide stabilization of nuclear spin instead of the external field; this can be the Knight field of a localized electron spin [125, 126], or a static quadrupole field [143].

1.4.1 Dynamic nuclear polarization and spin temperature

Assuming the validity of the spin temperature approach described in Section 1.3.4, it is evident that DNP is accompanied by a cooling of the nuclear spin system, since the observed nuclear spin polarization can be orders of magnitude higher than that which would result solely from the external field at lattice temperature. Indeed, the nuclear spin temperature θ_N can be inferred

from the field dependence of B_N via the Curie law:

$$B_N = \frac{\hbar\gamma_N I(I+1)b_N}{3k_B\theta_N}B, \tag{1.30}$$

where B is the external field. Strictly speaking, the establishment of a single spin temperature for all species of nuclei is only a feature of DNP in weak fields. In high fields, the energy differences between Zeeman levels of different types of nuclei may become greater than the energy of spin-spin interactions [10, 144]. Then, different subsystems of nuclei are characterized by their own spin temperatures as a result of DNP. In weak fields and if quadrupole interactions are not very strong, mutual spin flips between all nuclei are possible, and hence a common spin temperature is established.

To obtain high nuclear spin polarization $B_N \approx b_N$, the nuclear spins are often cooled below lattice temperature, as deeply as possible. In these experiments, DNP occurs as a result of optical pumping with circularly polarized light in Faraday geometry. Additional cooling of the nuclear spin system is reached by adiabatic demagnetization to zero field, which can be performed in the laboratory or rotating frame [145]. This procedure has been used for near half a century since its inception [144, 146].

1.4.2 Adiabatic demagnetization

The spin temperature can be further reduced by adiabatic demagnetization, i. e., switching off the external field during a time much longer than the nuclear spin T_2. In adiabatic conditions, the temperature of the nuclear spin ensemble depends on the magnetic field:

$$\theta_N \propto \sqrt{B_L^2 + B^2}. \tag{1.31}$$

The Zeeman energy of the system changes with B, and because the nuclear spins are isolated, the changes in energy cannot be dissipated, leading to changes in spin temperature. A detailed treatment of the problem is given in the seminal work of Abragam and Proctor [147] (see also the textbook [118]). In high fields $B \gg B_L$, the distance between the equidistant levels scales proportionally to B, but the populations of the Zeeman energy levels of the nuclear spin system are conserved if the field passage is slow compared to T_2, hence the temperature describing the probability distribution also changes. This type of process is called adiabatic in the quantum mechanical (or Ehrenfest) sense. In low fields $B \approx B_L$, the treatment is more complicated because the energy levels are no longer equidistant, and quantum adiabaticity is in contradiction with the expectation of a persistent Boltzmann distribution. Suffice it to say that demagnetization to such low fields is often still completely reversible, and it is rather that specific measures should be taken to prepare experiments that show a lack of irreversibility [147, 148] (i. e., preparing the subsystems of different isotopes at different spin temperatures, then sweeping the field to zero and back to arrive at a single spin temperature).

Assuming the field sweep is reversible, only the pair (θ_N, B) contains information on the physical state of the nuclear spin system, and it is useful to introduce the nuclear spin temperature in zero external field $\theta_N^{(0)} = \theta_N(B)|_{B=0}$ as a measure of the entropy of the nuclear spin ensemble [138, 147, 149]. Using Eqs. (1.30) and (1.31), we plot in Fig. 1.5 the dependence of the Overhauser field and nuclear spin temperature on the external field that is varied adiabatically. The field-dependent behavior of θ_N is such that it is proportional to B when $B \gg B_L$, and near-constant when $B \ll B_L$, assuming that the field is changed adiabatically in the quantum mechanical sense [35].

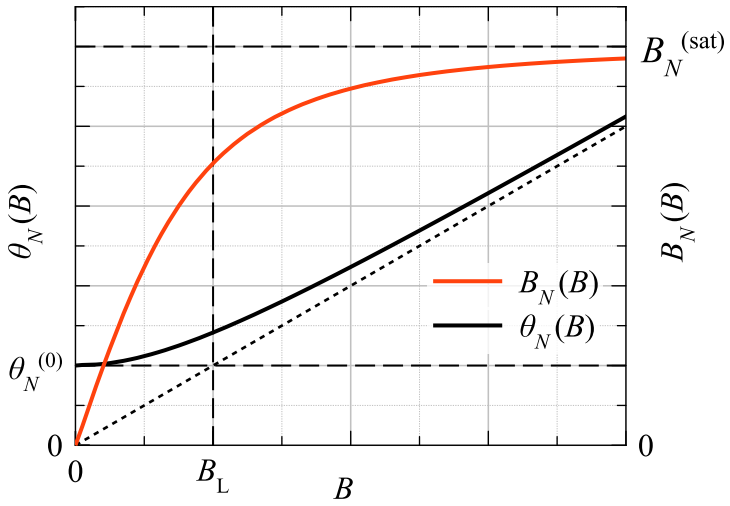

Figure 1.5: Nuclear spin temperature (black solid line, left vertical axis) and the Overhauser field (red solid line, right vertical axis) plotted as functions of the adiabatically varied external magnetic field B, assuming the Curie law holds. The black dotted line is the $\theta_N(B)$ dependence for $B_L = 0$. The Overhauser field saturates at $B_N^{(\mathrm{sat})} = B_L b_N \hbar \gamma_N I(I+1)/(3k_\mathrm{B}\theta_N^{(0)})$, i. e., it is inversely proportional to the nuclear spin temperature at zero field $\theta_N^{(0)}$, which itself is a measure of the entropy of the nuclear spin system. The curves are calculated following Eqs. (1.30) and (1.31).

1.4.3 Spin temperatures obtained in semiconductors

Spin temperatures of the order of tens of µK are routinely obtained in DNP experiments on GaAs [119, 120, 149, 150], resulting in nuclear polarizations much higher than the equilibrium value at lattice temperature. The simplicity and robustness of the approach is remarkable, and the resulting spin temperatures have not changed much since the technique was first introduced in the second half of the XX century [10], hovering around 1 µK in GaAs. Performing DNP in high fields (around several T) leads to even greater p_N, but this does not affect $\theta_N^{(0)}$ significantly. For example, $p_N = 74\%$ for ^{75}As nuclei in $B = 4.5$ T at $\theta_N = \pm 1.3$ mK in Ref. [151]. Renormalizing this temperature to $B = 0$ and accounting for the large quadrupole contribution to the local field (~ 5 mT) gives $\theta_N^{(0)} \sim \pm 1$ µK, along the lines of other experiments.

Though GaAs is normally the semiconductor of choice for DNP experiments, CdTe is also suitable and is perhaps more interesting due to the small B_L, which leads one to expect lower spin temperatures. In Chapter 3, $\theta_N^{(0)} = 0.3$ µK under neutral donor orbits in bulk CdTe corresponds to local nuclear spin polarization $p_N = B_N/b_N \approx 3\%$ in the very weak field $B = 0.1$ mT. To give perspective, the thermal polarization at lattice temperature (typically around 4 K) would be smaller in proportion to the temperature ratio, which is 7 (*sic*) orders of magnitude. Larger values of nuclear spin polarization can also be achieved in more optimized pumping conditions. For example, as we report in Chapter 3, $p_N > 10\%$ is measured on a QW sample in $B = 10$ mT.

Finally, dynamic nuclear polarization is often an unwanted effect in experiments on electron spin dynamics. Even weakly elliptical light can polarize the nuclear spins if there is a longitudinal magnetic field component. Non-normal incidence of linearly polarized light can also lead to small DNP which can result, among other things, in an asymmetric spin noise spectrum (see

Section 2.6.3). Therefore, care must be taken to avoid unintentional DNP. This is typically done by modulating the polarization of the incident light between two orthogonal modes at a frequency of around 50 kHz [10].

1.4.4 Nuclear spin relaxation and warm-up

DNP is a strictly nonequilibrium phenomenon. Therefore, any nuclear spin polarization has a tendency to relax to the equilibrium value at a given lattice temperature and external field once pumping is stopped. The process is typically described in terms of the longitudinal relaxation time T_1. In strong fields $B \gg B_L$, this relaxation can be equivalently described as a warm-up of the nuclear spin system, though it is not required. When dealing with nuclear spin relaxation in weak fields $B \lessapprox B_L$, and zero field in particular, the spin temperature approach is indispensable.

As discussed in Section 1.3.4, the rate of energy exchange between the nuclear spins and the lattice is quite slow, of the order of seconds. Since the spin polarization of cold nuclear spins is induced by the external field, setting $B = 0$ leads to the disappearance of B_N on the timescale of T_2 defined by B_L ($\sim 10^{-4}$ s). However, so long as the process can be considered adiabatic, i. e., no significant warm-up has time to occur, B_N largely recovers upon reapplication of B during T_2. This actually constitutes one of the most elegant and classic spin temperature experiments [10, 118, 152]. This type of experiment favors the warm-up interpretation, since the process of energy exchange is not strongly affected by the presence or absence of the external field. Nevertheless, if we start increasing the wait time before reapplying B, we will eventually notice that the recovered nuclear spin polarization is smaller compared to the case where the field was kept constant. This is because the warm-up rate of the nuclear spin system is fundamentally field-dependent due to spin-spin interactions [118].

Field dependence of nuclear spin warm-up rate

The weak-field relaxation rate is linked to that in the limit $B \gg B_L$ via

$$T_1^{-1}(B) = T_1^{-1}(B')\Big|_{B' \gg B_L} \frac{\mathrm{Tr}\left\{\sum_p \left[\hat{\mathcal{H}}_{\mathrm{SS}}, \mathbf{I}_p\right]^2\right\}}{2\mathrm{Tr}\left\{\hat{\mathcal{H}}_{\mathrm{SS}}^2\right\}}, \tag{1.32}$$

where $\hat{\mathcal{H}}_{\mathrm{SS}}$ is the Hamiltonian of the nuclear spin system [118]. The above equation can be rewritten in terms of external and local magnetic fields, with

$$T_1^{-1}(B) \propto \frac{(3/2)B_{LK}^2 + B^2}{B_L^2 + B^2}, \tag{1.33}$$

where the local field B_L is defined in Eq. (1.29), and the kinetic local field B_{LK} is given by

$$B_{LK}^2 = -\frac{1}{N}\frac{3}{I(I+1)}\frac{1}{\hbar^2\gamma_N^2}\mathrm{Tr}\left\{\left[\hat{\mathcal{H}}_{\mathrm{SS}}, \mathbf{I}\right]^2\right\}, \tag{1.34}$$

where $\mathbf{I}$ is the total spin of all nuclei participating in $\hat{\mathcal{H}}_{\mathrm{SS}}$, and N is their number. Since scalar interactions such as the exchange interaction or the secular part of the dipole-dipole interaction conserve the total spin, they do not contribute to the commutator in Eq. (1.34). Calculations show that the warm-up rate is 2-3 times faster in zero field than at $B \gg B_L$ for a spin Hamiltonian containing dipole-dipole and exchange interactions, depending on the

degree of coherence between the local fields experienced by any pair of nuclear spins [118]. The weak-field warm-up rate may be further affected if there are other terms in the nuclear spin Hamiltonian apart from the Zeeman and dipole-dipole contributions. For example, in GaAs quadrupolar effects lead to comparatively faster warm-up in near-zero field than what would be expected from the dipolar spin-spin coupling alone [119, 153]. Conversely, if pseudodipolar interactions are present, the effect may be reversed. For example, the exchange interaction in CdTe significantly contributes to the local field B_L, but not to the kinetic local field B_{LK}. As a consequence, B_{LK} and B_L differ by a factor of about 1.1, and the warm-up rate is nearly independent of the external field. A calculation of B_{LK} in CdTe can be found in Appendix A.2.

Nuclear spin relaxation via hyperfine interaction with electrons

The processes that induce nuclear spin warm-up and determine T_1 in fields $B > B_L$ are typically discussed in terms of nuclear spin relaxation. Spin relaxation via spin-flips with electrons on the Fermi surface (Korringa mechanism [154]) is usually typical of metals [118], but can also be observed in semiconductors such as GaAs [153, 155, 156] and CdTe [27, 141, 157] if there is an electron gas present. The defining feature of Korringa relaxation is the relationship

$$T_{1,\mathrm{K}}^{-1} \propto k_\mathrm{B} T, \tag{1.35}$$

that is, the Korringa relaxation rate $T_{1,\mathrm{K}}^{-1}$ is proportional to the lattice temperature. A generalization for low-dimensional systems can be made, in which case

$$T_{1,\mathrm{K}}^{-1} \propto k_\mathrm{B} T |\psi_{e,\mathrm{free}}(\mathbf{r})|^4, \tag{1.36}$$

where $\psi_{e,\mathrm{free}}(\mathbf{r})$ is the envelope wave function of the electron gas in question [155, 158]. Spin relaxation via spin-flips with an electron gas that has a Fermi level near the bottom of the conduction band is treated in Chapter 3, we refer to it as Korringa-*like* relaxation.

In semiconductors, notably GaAs, the most common mechanism of nuclear spin relaxation is mediated by fluctuating Knight fields of localized electrons [91], as mentioned in Section 1.3.2. The process can also be described as a dynamical spin-flip process, with the localized electron spins acting as a heat pipe between the nuclear spin system and the lattice. The corresponding relaxation rate is [159]

$$T_{1,\mathrm{loc}}^{-1}(\mathbf{r}) \propto |\psi_{e,\mathrm{loc}}(\mathbf{r})|^4. \tag{1.37}$$

That is, it is spatially inhomogeneous, following the square of the localized spin probability density given by the square of the wave function $|\psi_{e,\mathrm{loc}}(\mathbf{r})|^2$. There is no simple temperature dependence in this case, because the exact rate is influenced by the correlation time, i. e., the time that an electron spends at a given site, which is difficult to estimate theoretically. In the limit of short correlation time, one may write for the center of the donor

$$T_{1,\mathrm{loc}}^{-1}(0) = \Omega^2 \tau_\mathrm{c}, \tag{1.38}$$

where Ω is the nuclear spin precession rate in the root-mean-square value of the fluctuating Knight field, and τ_c is the correlation time.

Quadrupole coupling to fields produced by slowly fluctuating charges can also contribute to nuclear spin relaxation [153]. The injection of energy into the nuclear spin system can also be performed on-demand with rf fields, which is done in classic and zero-and-ultra-low-field (ZULF) NMR [130].

1.4.5 Nuclear spin diffusion

The apparent nuclear spin dynamics, particularly in the case of strongly localized relaxation centers, often require analysis of the spatial characteristics of nuclear spin polarization due to the effect of nuclear spin diffusion, which is another important consequence of the spin-spin coupling in nuclear spin systems. It is a classical description of the complex quantum behavior of inhomogeneously polarized nuclear spins. First suggested by Bloembergen [134], it has been observed in model NMR materials such as CaF_2, but also in semiconductors such as GaAs [153, 156, 159–161], CdTe [27], ZnSe [162] etc. Particularly profound fundamental studies have been carried out on CaF_2 [163, 164] which has an especially simple nuclear spin system. A theoretical introduction into the topic can be found in Ref. [118] (see also Ref. [165]). The result is that as long as the polarization does not vary strongly between nearest-neighbor nuclear spins, the nuclear spin polarization p_N follows the diffusion equation

$$\frac{\partial p_N}{\partial t} = D_N \Delta p_N + \dots \,, \tag{1.39}$$

where Δ is the Laplacian, and D_N is the nuclear spin diffusion coefficient determined by spin-spin interactions. The ellipsis stands for other mechanisms that might affect nuclear spin polarization, such as pumping and relaxation mediated by the hyperfine interaction. In the above, p_N describes the distribution of average nuclear spin polarization with spatial resolution of the order of the lattice constant. Applying the Curie law, we may rewrite the equation to describe the inverse spin temperature, which has the advantage of describing energy transfer through the nuclear spin system in zero external field, when $p_N \equiv 0$, i. e.,

$$\frac{\partial \beta_N}{\partial t} = D_N \Delta \beta_N + \dots \,, \tag{1.40}$$

where $\beta_N = 1/(k_B \theta_N^{(0)})$. The spin temperature picture is particularly useful when discussing nuclear spin dynamics in zero field, when spin temperature may be inhomogeneously distributed even though there is no nuclear spin polarization. Finally, diffusion can also be directly incorporated into the Bloch equations for the spatially variable magnetization, as first shown by Torrey [61].

The value of the nuclear spin diffusion coefficient D_N is determined by the rate of spin flips between nearest neighbors. A simple nearest-neighbor estimate is $D_N = W(r) r^2$, where $W(r)$ is the spin-flip rate between two spins separated by r [134]. For a dipole-dipole coupling, $W(r) \propto r^{-6}$ [134, 166]. Since $r \propto n^{-1/3}$, where n is the spin density, we conclude that $D_N \propto n^{4/3}$. D_N can only be considered constant if all nuclear spins are in the same conditions (i. e., homogeneous magnetic field, absence of random quadrupolar shifts). If a mutual spin flip of neighboring nuclei is forbidden by energy conservation, it is necessarily reflected in the value of D_N. As an example, in sufficiently strong fields, the difference between Zeeman energies of different isotopes can become greater than the characteristic energy of the spin-spin interactions quantified by B_L. Crudely, the process can be imagined as the gradual separation of NMR lines with increasing field. For a pair of isotopes with gyromagnetic ratios γ_1 and γ_2, assuming the linewidths are of the order of B_L, this occurs approximately when

$$B \gtrsim B_L \frac{1}{2} \frac{\gamma_1 + \gamma_2}{|\gamma_1 - \gamma_2|}. \tag{1.41}$$

As an example, in CdTe, due to the small value of $B_L = 0.04$ mT, mutual spin flips between ^{111}Cd and ^{113}Cd become forbidden when $B \gtrsim 1$ mT, and diffusion between Cd and Te subsystems is forbidden already at $B \gtrsim 0.1$ mT, though the latter is perhaps not expected to produce

a significant effect due to the comparatively small abundance of magnetic Te atoms. For another example, we turn to GaAs-based quantum dots, where random strain-related quadrupolar shifts can be quite large. Naively, one might expect diffusion to be forbidden altogether if the quadrupole shifts are greater than the Zeeman splitting in the local field. In experiments, however, diffusion is occasionally observed, leading to the hypothesis of a percolation-like mechanism [161]. In Chapter 3, we show how a field dependence of nuclear spin diffusion manifests itself in optical experiments.

It is important to address nuclear spin diffusion in the context of DNP studies, notably when nuclear spin polarization and relaxation are essentially mediated by donor-bound electrons (or any other paramagnetic centers). Nearby nuclear spins are strongly coupled to the paramagnetic center, while farther nuclei experience virtually no direct interaction with the localized spin. It is then spin diffusion that serves as an indirect coupling between far-away nuclear spins and the localized spin, and it can lead to their polarization or depolarization, depending on the conditions. In typical detection methods, one studies the nuclear spins through their effect on electron spins via the nuclear field B_N [see Eq. (1.24)]. Hence, only the spatially averaged nuclear spin polarization (weighted by the electron probability density) is measured. This creates uncertainty as to the cause of any reduction in nuclear spin polarization over time, as irreversible warm-up induced by the hyperfine interaction and energy-conserving spin diffusion are difficult to separate, especially considering that both processes can be field-dependent. To that end, an elegant experiment was introduced in the seminal work of Paget [159], where the pump polarization was changed to erase the nuclear spin polarization in the center of a neutral donor. A reflux of the signal was observed, indicating that nuclear spin diffusion strongly affects nuclear spin diffusion near neutral donors in n-GaAs. The experiment was repeated in Ref. [161] for single InGaAs quantum dots to prove the existence of spin diffusion between the quantum dot and its surroundings.

In general, precise spatial characteristics of the temporal evolution of the nuclear spin system are difficult to obtain. Direct observations are really only possible in purposely organized experiments such as those of Refs. [163, 164]. The problem is compounded if multiple spin-spin interactions are known to be pertinent for the description of the nuclear spin system, e. g., electric quadrupole interactions in GaAs [153].

1.4.6 Dynamic polarization of electron spins by a cold nuclear spin system

Conceptually, it is not difficult to imagine that the same coupling that permits DNP could, at least in some cases, lead to dynamic electron polarization by cold nuclei. However, the magnitude of the effect and the conditions where it could have a strong effect are not clear. In diluted magnetic semiconductors, the exchange coupling between the localized magnetic impurity and conduction electrons is well-known to lead to the formation of antiferromagnetic polarons via mutual feedback [167]. It has been suggested by Merkulov [168] that if the nuclear spin system is made cold enough, nuclear spin polarons will form unless the spin temperatures of electrons and nuclei are of different sign. Though the nuclear spin polaron is yet to be observed experimentally, it should be possible to confirm the decrease of nuclear spin correlation length near the phase transition via spin noise spectroscopy because the electron spin relaxation time should decrease due to less efficient motional narrowing [169]. After the onset of the polaron state, it should normally be accompanied by a spontaneous electron spin splitting in zero field, similarly to the analogous effect in diluted magnetic semiconductors [167].

In the DNP regime, the average electron spin $\langle S \rangle$ and the average nuclear spin $\langle I \rangle$ are

generally bound by [118, 170] (see also Ref. [144])

$$\frac{\langle I\rangle}{I(I+1)} = \frac{T_1}{T_{1e}}\frac{\langle S\rangle}{S(S+1)}. \tag{1.42}$$

This applies as long as the magnetic fields are not too strong, so that the equilibrium values of electron and nuclear spin polarization can be safely neglected and $\langle I\rangle \ll 1$. In the above, T_{1e}^{-1} is the contribution to energy relaxation of nuclear spins due to hyperfine interaction with electrons. The pumping conditions, the electronic structure of the sample, and electron spin relaxation determine $\langle S\rangle$, while any nuclear spin relaxation besides hyperfine influences $\langle I\rangle$ via $T_1^{-1}T_{1e}$. In GaAs, this can be, e. g., quadrupole interaction with fields created by slowly varying spatiotemporal charge fluctuations [150, 153]. In the case of n-doped CdTe, unless there are other relaxation centers present and nuclear spin diffusion is strong enough for the nuclear spin polarization to reach them, one should assume $T_1 = T_{1e}$ [144].

The expression (1.42) is often used to describe the average nuclear spin $\langle I\rangle$ produced by a given average electron spin $\langle S\rangle$, which is itself maintained externally via optical pumping. However, it can be shown that the equation works both ways, describing the link between the average values of electron and nuclear spin with or without illumination [169]. Indeed, if equilibrium electron spin polarization is not neglected, a more rigorous variant of Eq. (1.42) can be used to predict various collective ordered states of the electron-nuclear spin system. This includes a previously unknown dynamic nuclear spin ferromagnet state, as well as the already discussed nuclear spin polaron, as shown in Ref. [169].

For our purposes, it is enough to recognize that even in absence of optical pumping, electron spins are polarized by nuclei if $B_N \neq 0$. This was observed directly in Ref. [91]. The extent is determined by the degree of nuclear spin polarization, which is a function of nuclear spin temperature and external field. The polarization can be achieved in a straightforward way, by optically cooling the nuclear spin system and applying a small external magnetic field.

1.4.7 Nuclear spin diffusion barrier

In Section 1.4.5, we posited that spin diffusion is suppressed if mutual spin flips between nearest neighbors are forbidden by energy conservation. A sufficient difference in Zeeman energies of two unlike spins can be brought about by a sufficiently strong external field. For like nuclei, the only way to suppress spin flips is to apply a field that would be inhomogeneous enough that

$$\Delta B \gtrsim B_L, \tag{1.43}$$

where ΔB is the difference between the magnetic fields experienced by the two nuclei. A practical way of producing a magnetic field that would be inhomogeneous on an atomic scale is to use paramagnetic impurities or neutral donors in a semiconductor. If the localized spin is polarized, then it exerts a radially inhomogeneous Knight field on the nuclear spins. Provided that this field is made strong enough, spin diffusion becomes suppressed within a certain radius, and the so-called diffusion barrier is formed, as first suggested by Bloembergen [134], and later directly observed by Wolfe [171]. A somewhat dated but comprehensive review of the subject can be found in Ref. [165].

In a sample with several nuclear species, the inhomogeneity of the Knight field may occasionally be compensated by the difference of gyromagnetic ratios. Thus, spin flips that would be forbidden for like spins can be allowed for unlike ones, and even if the Knight field is increased, some transitions become forbidden while others become allowed [166], potentially leading to a very permeable diffusion barrier, if any [161]. The resulting interplay of mechanisms is complex

and not easily described, which may be the cause of conflicting reports in the literature regarding diffusion barriers in semiconductors. Some evidence exists for their formation in GaAs quantum dots at high magnetic fields [160, 166]. However, there is also recent evidence to the contrary [161, 172].

To obtain more favorable conditions for the observation of a nuclear spin diffusion barrier, one must look for systems where: (i) the local field B_L is small, (ii) the inhomogeneity of the Knight field ΔB can be made large, and (iii) the nuclear spin system comprises as few nuclear species as possible. Preferably, all nuclear spin species should have $I = 1/2$ to avoid dealing with quadrupolar effects which one would expect to increase the permeability of the barrier. A straightforward way of increasing ΔB is to look for stronger Knight fields, so one might explore systems where electrons are strongly bound to donors, or very deep quantum dots. ΔB is also proportional to the average distance between nearest-neighbor nonzero-spin nuclei, which can be appreciably greater than the regular nearest-neighbor separation in dilute nuclear spin systems such as those of Si, CdSe, and CdTe. Incidentally, dilute systems of nuclear spins are also typically characterized by smaller local fields. Although quantum dots provide strong spin localization, the nuclear spin systems of GaAs and InGaAs quantum dots are characterized by local fields of at least 0.2 mT [173], and potentially up to 300 mT due to strain [139]. Additionally, the random quadrupolar shifts in these materials may make it difficult to suppress all spin flips. Silicon boasts a very dilute nuclear spin system, which is largely composed of one isotope, ^{29}Si with $I = 1/2$. It is a very appealing material due to applications, but its indirect band structure does not facilitate optical experiments, DNP in particular. CdTe and CdSe are more interesting options in this regard, with the former being a frequent platform for quantum wells [41, 42, 174, 175], and the latter for quantum dots [176, 177]. In Chapter 3, we present experimental and theoretical evidence to the formation of a nuclear spin diffusion barrier near neutral donors in a wide CdTe quantum well with small unintentional doping.

1.5 Experimental approaches to electron spin dynamics

Modern spin physics often employs time-resolved methods based on the pump-probe technique. Time-resolved setups offer great flexibility and potentially deeper insights into relaxation processes [35]. For example, Rabi fluctuations of level occupancies can be measured directly for the bandgap transition [178] or for Zeeman-split states [12]. However, continuous-wave experiments, such as those based on the Hanle effect, have their advantages and remain in active use. In particular, spin noise spectroscopy provides direct access to spin relaxation, and can help uncover both temporal and spatial information on resident spin dynamics [22, 179–181]. We will discuss spin noise spectroscopy in depth after we briefly introduce the other approaches.

1.5.1 Time-resolved techniques

Time-resolved optical response

Time-resolved (TR) photoluminescence (PL) is a natural evolution of the steady-state optical pumping technique mentioned above. A circularly polarized pump pulse from a mode-locked laser generates electrons and holes in certain spin states according to the dipole selection rules. Then, changes in the circular polarization of the PL are monitored via a streak camera [182]. When performed in Voigt geometry, this type of experiment can permit measurements of the electron g-factor via direct observation of Larmor precession in the dynamics, and can even

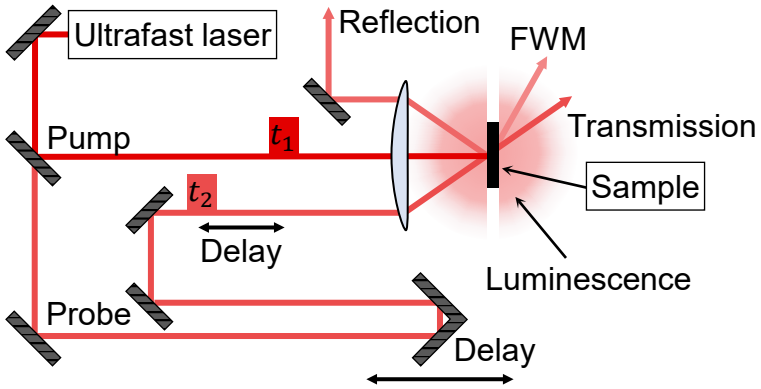

Figure 1.6: Illustration of a typical two-beam degenerate pump-probe experimental setup. The ultrafast (fs or ps) laser is separated into two components, with one acting as the pump impinging on the sample at time t_1, and the other as the probe arriving at t_2. The spot of the probe beam on the sample is usually required to be more stable than that of the pump. Hence, in practice, the probe beam is usually fixed, and instead the path of the pump beam is tuned to select the delay. The setup permits extracting time-resolved reflection, transmission, and four-wave-mixing signals, as well as photoluminescence.

yield the sign [183]. The obvious drawback of using TRPL to measure spin dynamics is that the observable spin relaxation times are limited by the timeframe of electron-hole recombination (of the order of ps), and longer spin dynamics are inaccessible.

Pump-probe spectroscopy

Experiments based on a straightforward pump-probe scheme with a variable delay between the two pulses offer access to relaxation times up to ~ 10 ns, which is limited by the pulse repetition rate (typically $70-90$ MHz for Ti-Sapph lasers). This can be very useful, as a nontrivial optical response may be revealed long after photocarriers created by the pump pulse have recombined, as is the case for the nonradiative exciton reservoir in GaAs quantum wells [46]. In the domain of spin physics, for example, resident electrons in quantum dots and wells can be polarized by resonant excitation of the negative trion due to optical selection rules if hole-in-trion spin relaxation is fast [12].[7] As a result, a signal may be observed on a timescale of the order of nanoseconds, if not tens or hundreds [184].

In pump-probe spin dynamics experiments one usually tracks the Kerr- or Faraday rotation as they give direct information about the (pump-induced) sample magnetization.[8] Pump-probe Kerr- and Faraday rotation (PPKR and PPFR, respectively) are the go-to tools in modern studies of semiconductor spin dynamics [186]. The difference between the two lies only in experimental geometry: PPKR is performed in reflection, while PPFR is performed in transmission. In Voigt geometry, the temporal evolution of the signal reflects the decay of spin coherence, which is modulated at the relevant (typically, electron) Larmor frequency due to spin precession in the transverse field. Two-color PPKR can be an indispensable tool to

[7] This is similar to spin pumping of majority carriers in n-GaAs, where electrons are optically oriented due to the replacement of unpolarized carriers with polarized ones [10].

[8] The Faraday effect consists in the polarization rotation of a linearly polarized light beam as it passes through a magnetized medium. The angle of rotation is proportional to the magnetization and the distance travelled within the medium [185]. The Kerr effect has the same physical origin.

identify the spin coherence times of resident and photocreated carriers [187].

Spin relaxation times can be much longer then 10 ns, particularly in n-GaAs, where electron spins are known to reach lifetimes of 100 ns in moderately doped bulk samples at cryogenic temperatures [68]. The range of spin relaxation rates accessible by PPKR (PPFR) can be extended by resonant spin amplification (RSA) [188]. If a spin undergoes an integral number of precession cycles between adjacent pump pulses, then the precession produced by the next pulse is in phase with the preceding one. As a result, leftover polarizations from previous pulses add up constructively, and significant amplification of the Faraday rotation signal is achieved. This leads to increased sensitivity to long spin decoherence times, potentially up to 5 µs. Another approach to extend the temporal range of pump-probe is to select only some pulses produced by the laser (pulse picking) which has been performed, e. g., in Refs. [15, 92, 189].

Four-wave-mixing

Four-wave-mixing (FWM) generally involves sending three coherent laser pulses to the sample with various relative delays, which elicits a fourth pulse – the nonlinear optical response of the system. The most common variation of the technique is degenerate FWM, which is based on two pulses only. If the second pulse arrives within the optical coherence time of the system after the system is initialized by the first pulse, then a polarization grating is formed, which self-diffracts the second pulse. The output is then formed along the phase-matching direction [11]. Depending on the polarization of pulses, FWM may permit the measurement of longitudinal and transverse spin relaxation times, as well as the g-factor and its inhomogeneity [174, 190]. A variation of technique, transient spin grating, can yield information on charge and spin diffusion in the sample [191, 192].

In systems with significant inhomogeneous broadening, the second pulse can be chosen in a way that flips the phases acquired by all the individual systems, reversing the effects of pure dephasing. The output signal then presents itself in the form of echoes, the amplitude of which reflects the decay of coherence that could not be reversed by the second pulse. Thus, FWM is noticeably different from all other measurement techniques we list: it can be used to directly reverse the effects of spin dephasing. This is particularly interesting for single quantum dots, where electron transverse spin relaxation times of the order of 100 µs can be observed since the main source of dephasing – the nuclear spins – can be dynamically decoupled via elaborate pulse sequences, such as the Carr-Purcell-Meiboom-Gill pulse sequence [57, 78].

When used to stimulate a coherent Raman process (achieved by a certain choice of pulse polarizations), FWM can permit the resolution of sub-µeV differences between the Zeeman splittings of electron spins localized on donors and potential fluctuations [193]. Despite yielding similar information to PPKR (PPFR) in certain configurations, FWM is a more versatile technique. In particular, the mechanism of signal formation is different in FWM. This can be exploited to extract information on the spatiotemporal dynamics of resident carriers and estimate the electron correlation time τ_c, as shown in Ref. [59].

1.5.2 Continuous-wave techniques

Hanle depolarization

A classic technique in studies of spin dynamics is based on the Hanle effect, i. e., depolarization of luminescence in a transverse magnetic field. The polarization degree of luminescence is proportional to the spin projection along the direction of optical pumping. Therefore, spin depolarization in a transverse field is also referred to as the Hanle effect. Although the effect

was discovered and explained more than a century ago [194], it continues to be the go-to tool for studies of electron spin relaxation due to its simplicity and versatility [105, 175]. This is unsurprising, as measuring spin depolarization as a function of transverse magnetic field (the Hanle curve) yields both the electron lifetime τ and spin relaxation time τ_s [10]. The strength of the technique lies also in the very wide range of relaxation times that are accessible, since the width of the curve is determined by the effective relaxation rate $\tau_*^{-1} = \tau^{-1} + \tau_s^{-1}$, and this usually corresponds to electron Larmor precession rates in fields of the order of 1 mT, but possibly up to several T. The method is particularly well-suited for long spin relaxation times, which can be difficult to access in pump-probe experiments without pulse-picking or resonant spin amplification due to the short pulse repetition rate.

In fact, Hanle spin depolarization can be probed by a variety of methods, not only luminescence. For example, the Kerr effect can be used to yield the Hanle curve in a two-beam setup (Hanle-MOKE) [195]. Notably, using scanning Kerr-rotation microscopy to locally probe Hanle depolarization can yield information on the spatial behavior of spins along with the spin relaxation time [196]. Under pulsed pumping, one may obtain a series of Hanle curves in differential transmission centered around fields corresponding to resonance between the Larmor precession frequency and pulse repetition rate; this is somewhat similar to the resonant spin amplification method but using a single beam [175].

Polarization recovery curve method

Similarly to how spin polarization decreases if a transverse magnetic field is applied, it increases in a longitudinal field due to partial suppression of depolarization due to fluctuating fields. Tracing the spin polarization as a function of applied longitudinal field, one obtains the polarization recovery curve (PRC). The width of the PRC can coincide with the Hanle curve when both are determined by hyperfine interactions [197], but it can also be significantly larger in a number of situations. We will not list them here, but a thorough theoretical review of the behavior of PRC in various regimes with comparisons to experiments can be found in Ref. [198]. In conclusion, PRCs can be very useful, both alone and in conjunction with Hanle depolarization measurements.

1.5.3 Spin noise spectroscopy

The approach used in this work to study spatiotemporal electron spin dynamics is based on spin noise spectroscopy. First realized by Alexandrov and Zapasskiy in sodium vapors in 1981 [199], more than 20 years had passed until spin noise spectroscopy could be applied to semiconductors, which was done by Oestreich *et al.* [200]. Later, the same group was the first to measure the spin noise of a single hole spin in a quantum dot [201]. Spin noise spectroscopy has now become a frequently used tool in condensed matter physics, and new variations of the technique continue to appear in the literature. Interesting possibilities include Z-scan tomography [202], two-color SNS [203], two-beam SNS [180, 204, 205], and spatiotemporal spin noise spectroscopy [181]. In this Section, we recall the theoretical foundations of spin noise spectroscopy, and discuss various experimental implementations. We conclude by briefly introducing a further extension of SNS which we refer to as angle-resolved spin noise spectroscopy (AR-SNS). A detailed description is presented in Chapter 2 along with results obtained on a series of n-doped bulk CdTe samples.

Fluctuation-dissipation theorem

The foundational principle of SNS is the fluctuation-dissipation theorem. Applied to systems with resonance, it states that in thermal equilibrium, a system will exhibit stronger noise around the resonance frequencies. In fact, if it is easy to drive the system at a certain frequency by applying an external perturbation at said frequency, then it is unsurprising that the response to white-noise thermal fluctuations is also greater at that frequency. In mathematical terms, the classical version of the theorem can be written as

$$S_x(\omega) = \frac{2k_B T}{\omega} \mathrm{Im}[\chi_x(\omega)], \tag{1.44}$$

where T is the temperature, ω is the frequency, $S_x(\omega) = \langle \hat{x}(\omega)\hat{x}^*(\omega) \rangle$ is the power spectral density of the stochastic process described by $x(t)$, $\hat{x}(\omega) = \mathcal{F}[x(t)]$ is the Fourier transform. $\mathrm{Im}[\chi_x(\omega)]$ is the imaginary component of the susceptibility (linear response function) of the system; in other words, it is the absorption spectrum. The theorem can be used to link together phenomena such as drag and Brownian motion, electrical resistance and Johnson-Nyquist noise, light absorption and thermal radiation [206]. For example, an object moving through a fluid experiences drag, but undergoes Brownian motion when stationary, with both effects being produced by the internal physics of the fluid.

In this work, the fluctuation-dissipation theorem is most interesting in its implications for the measurement of electron spin dynamics. Broadly speaking, it suggests that if we were to record the temporal spin fluctuations, their Fourier transform would be equivalent to an absorption spectrum.

Spin noise spectroscopy

At equilibrium, the spin ensemble in a semiconductor is characterized by zero net angular momentum. However, due to thermal fluctuations, the root-mean-square (RMS) value of the net angular momentum is not zero, even in zero magnetic field. In fact, for a given number of spins N, the spin fluctuation is proportional to $\sqrt{N}$ [179]. This spin noise produces a fluctuating magnetization, which induces a fluctuating circular dichroism in the sample.

Let us now direct a beam of linearly polarized light at the sample. Once the beam passes through the sample, the plane of its polarization will also fluctuate, following the magnetization in accordance with the Faraday effect. The technique of SNS is completed by detecting the polarization fluctuations and performing a spectral analysis. Detection is most often accomplished by using a balanced detector, which rejects most of the noise, such as unwanted intensity fluctuations. In this approach, a polarizing beam splitter is used to form two beams that are cross-polarized but equal in intensity. These are then sent onto the photodiodes of the detector. The output signal of the detector is the difference of the two photocurrents, which typically achieves common mode rejection of more than 50 dB with modern equipment [207]. A single photodiode can also be used for hetero- or homodyne detection [208]; in this case, care must be taken to achieve sufficient extinction of the probe beam and Rayleigh-scattered light.

The spectral analysis was the preeminent problem for the application of SNS to semiconductors, as the spin noise signal is much weaker in semiconductors than in alkali metal vapors, and more measurements are required to average out the photon shot noise and electrical noise in the detection scheme [209]. In Ref. [200], a single spin noise spectrum recorded with a sweeping spectrum analyzer took about 20 hours, which made the result academic rather than practical at the time. However, improvements in signal processing, namely, the proliferation of acquisition cards with field programmable gate arrays (FPGAs), allow much more efficient

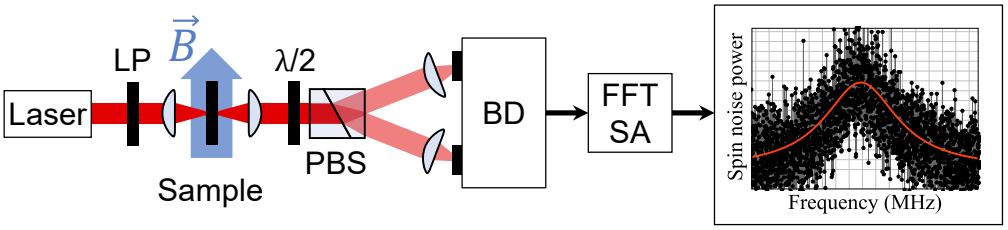

Figure 1.7: An illustration of a typical spin noise spectroscopy setup. The off-resonance laser beam is passed through a linear polarizer (LP) before being focused on the sample, which is held in the magnetic field **B** applied in Voigt geometry. The combination of a half-wave plate ($\lambda/2$) and a polarizing beam splitter (PBS) permits the separation of the beam into two parts with near-equal intensities. The balanced detector (BD) outputs a difference signal which contains the relevant fluctuating component. The signal is recorded as a function of time, and Fourier-transformed in real-time by the FFT spectrum analyzer (FFT SA), revealing the spin noise spectrum.

accumulation of spin noise data. Indeed, switching from a sweeping spectrum analyzer to a fast Fourier transform (FFT) analyzer, one can decrease the measurement time by 2-3 orders of magnitude [209]. Currently, FFT analyzers are the standard spectral analysis tool in SNS. A typical setup for SNS measurements in Voigt geometry summarizing the above considerations is shown in Fig. 1.7.

Spin noise spectroscopy and spin-flip Raman scattering

Shortly after the first demonstration of SNS in Ref. [199], it was understood that there is an intimate link between spin-flip Raman spectroscopy (SFRS) and SNS [210, 211]. Indeed, this was apparent, since the connection between Faraday rotation and Raman scattering was already known at the time [185]. Essentially, the polarization fluctuations that are measured in spin noise spectroscopy are the result of coherent Raman scattering of the probe beam in the forward direction, with heterodyning provided by the probe beam functioning as the local oscillator. In fact, SNS and SFRS differ only in the method of detection: in SFRS, the spectrum of the light field is measured; in SNS, it is the spectrum of the light intensity. This leads to some interesting properties of SNS, which are normally found only in nonlinear optical techniques. For example, if we increase the power density of the probe while keeping the total power the same, the signal will be increased in inverse proportion with the beam area [211]. This exact feature became the foundation for the Z-scan tomography of Ref. [202]. Conversely, if we increase the spot size while maintaining the total power, we will observe a decrease in signal.

Notably, the spin-flip-scattered light is not emitted in any specific direction, similarly to luminescence. Therefore, in principle, nothing prevents the collection of this light from an arbitrary direction, provided that the signal is sufficiently amplified. For example, one may use homo- or heterodyne detection, whereby one could secure all benefits of spin noise spectroscopy while evading certain disadvantages of the conventional technique, such as detector bandwidth limitations and necessity of increasing probe power to improve the signal [208].

Spatiotemporal spin noise spectroscopy

In a seminal paper, Van Hove showed that in the Born approximation, the differential scattering cross-section is factorized into two terms, one containing the parameters of scattering particles and the Fourier transform of their interaction with the system, and the other containing information about the system under study [212]. Spin noise spectroscopy, though not entirely unperturbative, is typically performed off-resonance, where absorption is weak. Therefore, the Born approximation, and hence the results of Ref. [212], are directly applicable. In the case of scattering of electromagnetic waves, the interaction potential is essentially the electron density. For localized electrons, the Fourier transform of the probability density is largely independent of wavevector in the range corresponding to the CdTe bandgap (near-infrared). Therefore, the differential cross-section, that is, the angular distribution of spin-flip scattered light intensity, directly gives the Fourier transform of the pair distribution function of spin fluctuations.

In Ref. [180], it was understood that spin fluctuations with nonzero wavevector could be probed in a two-beam setup, the wavevector corresponding to the angle between the beams. An approach based on the idea of recovering the spin-flip-scattered light itself was experimentally developed in Ref. [181], where wavevector-resolved spin fluctuations were studied in a single-beam setup by means of optical homodyne detection. The measurement was implemented by using a local oscillator beam that would impinge on the detector at an angle, thereby selectively amplifying only spin fluctuations with a given wavevector. Then, the integration of the power spatial distribution carried out by the detector would effectively produce an analog spatial Fourier transform of the spin fluctuations. This allowed the authors to avoid passing a second beam through the sample, which would inevitably lead to greater perturbation of the spin system. Effectively, a series of measurements would yield a spatiotemporal spectrum of spin fluctuations, which is why the technique is referred to as spatiotemporal spin noise spectroscopy (ST-SNS). A serious limitation of the technique is the restricted wavevector range, as the accessible wavevectors are limited by the numerical aperture of the fixed imaging system. In Ref. [181] this led to the wavevector-cutoff effect starting from q around several μm^{-1}, which would not only decrease the signal power, but would also affect the observed linewidth at larger wavevectors.

The application of ST-SNS, supplemented by measurements in reflection geometry (backscattering, $q \approx 50\ \mu m^{-1}$ in CdTe) to combat the limited wavevector range, to weakly n-doped epitaxial CdTe uncovered the jump character of electron spin diffusion, as described in Ref. [22]. It was shown that the spatial dynamics of localized spins can be described by a single temperature-independent jump length, at least at cryogenic temperatures. This jump length was found to be very large, 3 µm, an order of magnitude greater than the average interdonor distance. In fact, the nature of these long-ranged spin jumps was not quite understood in the work. Additionally, the inaccessible range between the wavevectors of ST-SNS measurements and the backscattering wavevector left room for interpretation. Nevertheless, ST-SNS was shown to be a remarkable tool that permitted the extraction of both temporal and spatial characteristics of spin fluctuations.

Angle-resolved spin noise spectroscopy

The aforementioned issue of restricted wavevector range can be amended by choosing an objective with a greater numerical aperture. This largely translates to smaller working distances and focus lengths. Very small working distances may be an option in modern cryostats where the objective is also kept at low temperature. Otherwise, the working distance cannot be made much smaller than several centimeters due to the vacuum shroud, and in this case, few things

can be done to access wavevectors larger than several μm^{-1} (assuming the laser wavelength corresponds approximately to the CdTe bandgap). If a broader range of wavevectors is required, a better alternative is to abandon the fixed imaging system of ST-SNS in favor of a goniometric setup which would enable measurements in a wider wavevector range. It is worth mentioning here Ref. [213], where angular resolution was attained via rotating the probe beam with a fixed collection arm. In Ref. [213], the signal decay was probably due to changes in the reflective index with the angle of probe incidence. The spin fluctuations themselves are distributed isotropically in space, meaning that in a homogeneous sample of spherical shape (preferably in a vacuum) one would observe no signal deterioration. In any case, to preserve the conditions of the experiment, namely the incident power, it is preferable to scan the direction of collection. Then, virtually no wavevector-dependent signal loss is introduced by the measurement procedure itself, although some signal power will inevitably be lost due to angle-dependent Fresnel coefficients and signal absorption in the substrate.

The practical application of angle-resolved spectroscopy to a range of n-doped CdTe samples is discussed in Chapter 2.

1.6 Experimental approaches to nuclear spin dynamics

A typical experiment addressing nuclear spin dynamics generally consists of three well-defined stages: i) preparation; ii) evolution of the nuclear spin system; iii) readout of the nuclear spin state. Naturally, more complicated protocols can be used to probe various properties of the nuclear spin system [111, 114–116, 159, 161].

In semiconductors, DNP is most conveniently attained via optical orientation of carriers, which then transfer their angular momentum to nuclei via hyperfine interaction. Further cooling of the nuclear spins can be achieved by adiabatic demagnetization to zero field. We have already briefly described the process in Section 1.4. The evolution of the nuclear spin system can proceed in a magnetic field [27, 141, 153], or rf fields can be applied in nuclear warm-up spectroscopy experiments [119]. Arguably, the most interesting aspect of DNP experiments is the detection, which can be performed in many different ways.

1.6.1 Readout of the nuclear spin state

In the seminal work of Lampel [214], conventional electrically detected nuclear magnetic resonance (NMR) was used to observe DNP in semiconductors for the first time. However, since the NMR signal is proportional to the number of contributing nuclei, it is not a very sensitive technique in nanostructures [35]. This makes Lampel's result all the more impressive, especially considering that experiments were performed on Si, which has a low density of magnetic nuclei as well as an indirect bandgap. An additional drawback of conventional NMR is that it relies on high external fields for a large population difference to be created. Let us briefly discuss some of the more efficient optical methods, all of which make use of the strong back-action the nuclear spins exert on the electrons.

Direct measurement of Overhauser shift

This method consists in spectroscopically measuring the Overhauser shift of a line in the PL spectrum. In semiconductors, this has only been applied to single quantum dots, where it has become a standard technique [53, 124, 215]. Due to the smallness of the spectral shift, strong external fields of the order of 1 T are usually required to achieve measurable nuclear

polarization, although more modest fields of around 0.1 T can be enough [60]. Even then, the shifts typically do not exceed 100 µeV [53], which is why the technique can only be applied to systems with long lifetimes and no inhomogeneous broadening, i. e., single quantum dots. The requirement of strong external fields allows this method of detection to pair well with NMR studies. As an example, selective excitation of nuclear hyperfine transitions permits independent and precise determination of hyperfine constants, which are otherwise difficult to measure accurately [151].

Hanle luminescence depolarization

The techniques described above, though powerful, do not permit the study of DNP in weak fields of the order of B_L, that is, when the spin-spin reservoir is not eclipsed by the Zeeman one. The weak-field physics of nuclear spin systems are fascinating from a fundamental point of view; additionally, strong field requirements are generally undesirable for applications. Hence, one requires methods to study the nuclear spin system in the weak-field regime.

One classic weak-field technique relies on the Hanle effect, which is sensitive to Overhauser fields arising in a cold nuclear spin system in external fields of the order of B_L [10]. In this method, the sample is illuminated by circularly polarized light in Voigt geometry. One measures the Hanle curve obtained in absence of nuclear polarization, that is, in conditions when the polarization of the pumping beam is modulated between σ^+ and σ^- polarized light at a frequency of around 50 kHz. This is fast enough for the nuclei to not acquire any spin polarization, but slow enough for the electron spin dynamics to remain unaffected. A second Hanle curve is measured under optical pumping by circularly polarized light after the nuclei have been cooled down by DNP. In the latter case, the nuclear field acts together with the external transverse field, and the nuclear field B_N can be measured by comparing the two Hanle curves. Despite being used with little modification since the dawn of optical orientation studies, the technique has aged very well: it has been recently used to great success in studies of spin-spin interactions in GaAs and CdTe [27, 119, 120, 136, 141].

The drawbacks of the Hanle method include limited knowledge of the signal formation process. *A priori*, one probes B_N as experienced by the electron state corresponding to the detection energy. On the other hand, the localized-itinerant spin exchange seems to be very efficient, as first evidenced for GaAs by Paget [85]; in this case, the electron spin polarization should be at least qualitatively the same for all occupied electron states. Since the complete electron wave function is never known, one must make assumptions regarding the electron states that predominantly contribute to the resulting signal. For example, in Ref. [136], the authors had to use a fitting parameter to describe the relative contribution of localized electrons to the mean electron spin under pumping. An additional drawback of using luminescence is that it constitutes a destructive measurement. Effectively, this requires a pump-probe approach for measurements of nuclear spin dynamics. As a result, one is obliged to perform potentially very long experiments, up to ≈ 1000 s per measurement [27].

We make use of this method in the original part of this work devoted to nuclear spin dynamics, see Chapter 3.

Spin noise spectroscopy

In SNS, the fluctuating nuclear field can be observed in zero field as a low-frequency peak, provided that the correlation time is long enough [62, 181, 216]. A finite Overhauser field affects the spin noise spectrum both in Faraday and Voigt geometry [217]. The shift of the electron Larmor frequency in Voigt geometry provides the most straightforward way to measure

the Overhauser field with SNS [218, 219]. The technique is sensitive even at very low external fields, provided the nuclear spins are sufficiently cold. For example, in bulk n-CdTe, typical electron spin noise linewidths are of the order $10 - 50$ MHz, which corresponds to fields of the order of 0.1 mT. Therefore, a nuclear field of several tenths of a millitesla can be registered easily. Another advantage of the technique is that the nuclear spin dynamics can be monitored in real-time: although spin noise spectroscopy is not completely unperturbative, no significant amount of photocarriers is created. This is in stark contrast to measurements via Hanle luminescence depolarization, where the nuclear spin system is warmed up by the measurement itself, so that a new realization of cooling has be performed to record another data point. As a disadvantage, the method requires a strong spin noise signal for the real-time measurements, which presupposes significant resident spin densities.

It is worth mentioning that in principle, nuclear spin noise can be measured directly, without the participation of electrons [220]. However, due to the existence of the hyperfine coupling and the desirability of optical experiments, measurements via electron spin noise are much more attractive in semiconductors.

Faraday rotation

The SNS approach relies on the presence of resident spins, the response of which allows one to spy on the nuclear spins. In contrast, the Zeeman splitting of the electron spin states induced by a finite nuclear field exists whether there are resident spins or not. Therefore, one is tempted to measure directly the Faraday rotation, which must be sensitive to nuclear fields everywhere, not only in the areas populated by resident spins. This has been done for bulk n-GaAs embedded in a $3\lambda/2$ cavity in Ref. [91]. The cavity is necessary to amplify the small Faraday rotation induced by the nuclear spins. Measurements of the Overhauser field via spin noise spectroscopy and Faraday rotation in the same experimental conditions (i. e., simultaneously) could provide further insights into the spatial distribution of nuclear spin polarization, which would expand our understanding of electron-nuclear spin interactions and nuclear spin diffusion.

Optically detected NMR

Arising as an evolution of regular NMR, classic optically detected NMR relies on tracking the luminescence polarization as the rf is swept [10, 159, 221]. Whenever the rf is resonant with a nuclear spin transition, it induces a transverse component of the nuclear field, and hence the average electron spin is depolarized according to the Hanle effect. The drop in polarization is directly related to nuclear spin population changes, permitting the estimation of B_N. Furthermore, a fully optical experiment can be realized if the circularly polarized light itself is rf-modulated [222]. The oscillating Knight field resulting from the modulated light replaces rf radiation as the energy source, and drives the nuclear spins when the frequency is resonant. These experiments lend themselves well to dynamic nuclear polarization, which softens the requirement of strong magnetic fields.

In very weak or even zero external field, the spin-spin interactions of the nuclear spin system can be probed directly, which constitutes the method of nuclear spin warm-up spectroscopy [119, 223], or zero-and-ultra-low-field (ZULF) NMR [130]. Following optical cooling, the nuclear spins are purposely warmed up by rf radiation of a given frequency. The resulting state of the nuclear spin system is described by a higher spin temperature than that directly after cooling. The efficiency of rf absorption reflects the energy spectrum of the nuclear spin system. The warm-up stage can be performed in any magnetic field, including zero field. After the warm-up step, the nuclear spins are probed by Hanle luminescence depolarization, which does require

an external magnetic field, though it can be made very small, of the order of the local field. In Ref. [119], the quadrupole reservoir of the GaAs nuclear spin system was studied via warm-up spectroscopy, yielding the parameters of the interaction, and in Ref. [130], the clustered nature of the CdTe nuclear spin system was observed.

Finally, we note that the NMR spectrum can also be measured using Faraday rotation or spin noise spectroscopy, which has been done in Refs. [91] and [138], respectively.

1.7 Conclusions

Electron spins are subject to different relaxation mechanisms, depending on their state. In particular, localized spin ensembles lose spin coherence due to the random hyperfine field, with direct hops between donors providing motional narrowing and anisotropic exchange relaxation simultaneously. For conduction band electrons in zinc-blende crystals, the typical relaxation mechanism is Dyakonov-Perel relaxation, while the hyperfine field is efficiently averaged out. Therefore, for a complete treatment of electron spin relaxation one must (i) account for spin promotion to the conduction band and (ii) consider the effects of spin transport, especially if the experimental regime is such that one must deal with both localized and free electrons. If the two states are coupled, relaxation rate composition laws can be sufficiently accurate to predict the temperature dependence of the electron spin relaxation rate [84]. Nevertheless, one expects that a more involved model may be required to correctly describe more subtle effects.

As for nuclear spins, we have discussed how low spin temperatures can be obtained by dynamic nuclear polarization. The relaxation (or warm-up) dynamics of nuclear spins is strongly affected by electron localization, and properly accounting for nuclear spin diffusion is just as important as for electrons. A magnetic field dependence of the nuclear spin relaxation rate in the regime of weak fields can arise naturally due to the intrinsic field dependence of the warm up rate, or it can be brought about by the formation of a nuclear spin diffusion barrier. Calculations of the local and kinetic local fields show that the former effect cannot be significant in CdTe, while the latter is not out of the realm of possibility.

In this Chapter, we have reviewed the spin properties of electrons and nuclei in semiconductors, devoting particular attention to CdTe, and we have covered the state-of-the-art in experimental electron and nuclear spin physics of zinc-blende semiconductors and nanostructures based on them. We are therefore well-equipped to proceed to the original results presented in Chapters 2 and 3.

Chapter 2

Conduction band hops of localized electron spins in n-CdTe

This chapter is devoted to the experimental implementation and application of angle-resolved spin noise spectroscopy (AR-SNS), as well the two-state spatiotemporal spin dynamics model which we introduce to explain all the results obtained via AR-SNS. This new extension of SNS permits virtually non-perturbative access to the spatiotemporal spin noise spectra of donor-bound electrons over a much wider range than in Ref. [22]. We apply AR-SNS to a series of high-quality n-CdTe layers with various doping densities grown by molecular beam epitaxy. The doping and temperature dependence of the spatiotemporal spin dynamics allows us to observe various regimes of localized spin dynamics. Long-ranged jumps are confirmed to be the dominant mechanism for spin transport between localization sites at low doping and temperature, and are shown to proceed via the conduction band even at temperatures much lower than the activation energy. The experiments are interpreted with the help of a phenomenological two-state model for the localized and free electron spins which is based on Bloch equations coupled by temperature-dependent release and trapping rates. The findings of this work are published in Ref. [26].

2.1 Introduction

Donor-bound electron spins are widely studied in semiconductor physics, with the research mainly motivated by their prospects in the realm of quantum information processing [224]. The long coherence times of donor electrons make them excellent candidates for qubits [225], but perhaps a more promising application is found in the domain of spintronics [226, 227], where spin transport and its spatiotemporal characteristics are of great importance. The spin dynamics of donor-bound electrons is continually studied in conventional III-V and II-VI semiconductors [83, 84, 105, 228, 229], as well as emerging materials such as transition metal dichalcogenides [230]. Among conventional semiconductors, CdTe is an interesting choice due to the long transverse relaxation times given by the dilute nature of its nuclear spin system (see Section 1.3).

Though a plethora of various experimental techniques is used in electron spin physics, as explained in Section 1.5, very few strictly optical experiments can deliver both temporal and spatial information simultaneously (measurements directly incorporating microscopy are a notable exception, see, e. g., Ref. [196]). In this regard, spatiotemporal spin noise spectroscopy (ST-SNS) [22, 181] is a unique tool.

ST-SNS is an extension of spin noise spectroscopy (SNS). In its standard version, stochastic spin fluctuations at thermal equilibrium are mapped onto Faraday rotation fluctuations [206]. Progress was made by introducing homodyne detection, where the spin-flip scattered light is

optically mixed with a local oscillator beam [208, 231, 232]. It was then suggested that spatial resolution in SNS could be achieved either in direct or reciprocal space by introducing a two-beam arrangement [180, 204, 233]. ST-SNS was experimentally demonstrated in reciprocal space with a local oscillator beam not interacting with the sample [22, 181, 213]. Indeed, even in real space, that is to say in ordinary transmission geometry, changing the wavevector distribution, i. e., the size, of the local oscillator beam affects the measurements via changing time-of-flight [22, 181].

With this method it is vital to have access to the characteristic wavevectors of the spin fluctuations, which are of the order of ten inverse micrometers. However, the range of measurable wavevectors can be quite limited when exciting and collecting the scattered light with a fixed optical system [22, 181], and even when scanning the probe beam's angle of incidence as in Ref. [213]. The latter has the additional disadvantage of altering the excitation conditions via angle-dependent Fresnel coefficients. The problem of wavevector range is crucial when dealing with semiconductors that have bandgaps in the near-infrared, such as CdTe, even when ST-SNS measurements are supplemented with backscattering data. In this article, we address the wavevector range problem inherent in ST-SNS by employing a goniometric setup in the spirit of dynamic light scattering, where the detection arm is rotated, and the probe beam is fixed. This variant of spin noise spectroscopy, which we call hereafter Angle-Resolved Spin Noise Spectroscopy (AR-SNS), affords us an in-depth look at the spatiotemporal spin dynamics in n-doped bulk CdTe, ultimately revealing the shortcomings of the models used previously.

The jump character of spin diffusion in CdTe was revealed by the combination of photon echo and Kerr rotation experiments performed on a quantum well sample in Ref. [59], and by ST-SNS in a low-doped n-CdTe sample in Ref. [22]. However, the spatial characteristics of jumps were not discussed in the former, and the micrometer-long jumps observed in the latter were clearly not explainable in terms of direct hopping between donors. In this work, we solve this puzzle by introducing a two-state spin diffusion model which takes into account the long-ranged spin jumps between donors via electron spin diffusion in the conduction band. Experimentally, AR-SNS is applied to four samples with different levels of n-doping. The model explains all the experimental results remarkably well.

We demonstrate that ultimately, the wavevector dependence of the spin noise linewidth (linewidth dispersion) is determined by the interplay between two spin jump mechanisms: short-range nearest-neighbor hops vs. long-range conduction band jumps, the exact contributions of which are determined mainly by doping density and temperature. The model also successfully reproduces the shape of the spin noise line in various experimental conditions, including when the line is decidedly asymmetric or otherwise non-Lorentzian.

In the following Section we present several illustrative models of increasing complexity to outline the information that can be extracted from wavevector-resolved spin noise measurements. In Section 2.3 we introduce the complete phenomenological two-state model and outline its main features. Section 2.4 describes the model in greater mathematical detail. The treatment is quite general and can be applied to low-temperature electron spin relaxation in other semiconductors. The experimental setup, description of the studied samples, and an overview of the experiments are presented in Section 2.5, while the experimental results are discussed in Section 2.6 within the framework of the two-state model. Finally, we draw conclusions in Section 2.7.

2.2 Effects of spin motion on the spin noise lineshape

To understand how a spin noise spectrum may behave as a function of wavevector, it is worthwhile to consider two very simple models. Both are based on Bloch equations written for a macroscopic average spin density. Each includes a constant relaxation term and a spatial term that will describe either continuous diffusion or discrete jumps. A more rigorous calculation can be found, e. g., in a recent book by Glazov [54]. We stress that this approach is meant only to sketch out the main features, and here we do not account for the presence of an external field or the fluctuating nuclear fields which induce hyperfine relaxation, which are properly treated in the advanced two-state model (see Sections 2.3 and 2.4).

Let us first consider the case of continuous diffusion. This could apply, e. g., to a resident carrier gas. Following the spirit of Refs. [62, 234, 235] and disregarding magnetic fields, we write the Bloch equation for the z component $S_z(\mathbf{r},t)$ of the spin density $\mathbf{S}(\mathbf{r},t)$ as

$$\frac{\partial S_z(\mathbf{r},t)}{\partial t} - D\Delta S_z(\mathbf{r},t) + \nu_\mathrm{s} S_z(\mathbf{r},t) = 0, \tag{2.1}$$

where $\mathbf{r}$ is the continuous spatial coordinate, ν_s is a constant relaxation rate, D is the diffusion coefficient, and Δ denotes the Laplacian. We introduce the correlator

$$S_{zz} = \langle S_z(\mathbf{r},t) S_z(\mathbf{0},0)\rangle, \tag{2.2}$$

where the averaging is over the initial conditions. The correlations between the z-projections of $\mathbf{S}$ correspond to what is measured in a typical spin noise experiment. For now, we will neglect certain details, such as the introduction of fictitious Langevin forces describing thermal fluctuations, and the strict calculation of the spatiotemporal Fourier spectra. Naively, one expects $\partial/\partial t \to -i\omega$, and $\Delta \to -q^2$. Skipping to the result, the equation for the spatiotemporal Fourier transform of correlators satisfying Eq. (2.1) is

$$\hat{S}_{zz} \propto \frac{1}{-i\omega + \nu_\mathrm{s} + Dq^2}. \tag{2.3}$$

To obtain the spin noise spectrum, we must take the real part of Eq. (2.3), which is simply a Lorentzian curve with a wavevector-dependent width. The linewidth dispersion is shown by the dashed line in Fig. 2.1.

The above result can also be used to describe bound spins hopping between donors, provided that the wavevector is much smaller than the inverse jump length. Now, let us imagine that this condition is not met. We rewrite Eq. (2.1) for local spin densities $S_{i,z}(t)$, substituting the diffusion term with discrete instantaneous jumps to and from other sites

$$\frac{\partial S_{i,z}(t)}{\partial t} - \sum_j \left[W_{ij} S_{j,z}(t) - W_{ji} S_{i,z}(t)\right] + \nu_\mathrm{s} S_{i,z}(t) = 0, \tag{2.4}$$

where $W_{ij} = W(|\mathbf{r}_i - \mathbf{r}_j|)$ are the intersite jump rates that depend only on the distance between the sites. For simplicity, we have neglected spin relaxation occurring during jumps, for example due to the anisotropic exchange interaction, in the above. The sum $\sum_j W_{ij}$ is the average rate of spin jumps from a given site ν_j, $\sum_j W_{ij} = \nu_\mathrm{j}$. Rewriting for the correlators $S_{ik,zz}$,

$$\frac{\partial S_{ik,zz}(t)}{\partial t} - \sum_j W_{ij} S_{jk,zz}(t) + (\nu_\mathrm{j} + \nu_\mathrm{s}) S_{ik,zz}(t) = 0, \tag{2.5}$$

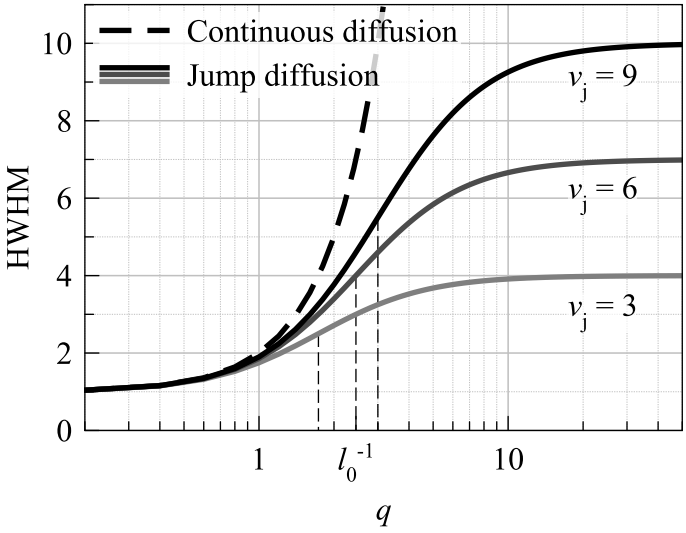

Figure 2.1: Spin noise linewidth dispersion shown for two toy models describing continuous (dashed line) and jump diffusion (solid lines). The dashed line corresponds to the real part of Eq. (2.3) with $D = 1$ (arb. un.). The solid lines are calculated as the real part of Eq. (2.7) assuming an exponential jump rate, and keeping $D = \nu_j l_0^2$ constant to preserve $D = 1$ at small wavevectors. $\nu_s = 1$ for all curves presented.

where $S_{ik,zz} = \langle S_{i,z}(t) S_{k,z}(0) \rangle$ and $S_{jk,zz} = \langle S_{j,z}(t) S_{k,z}(0) \rangle$ are the same function of distance between the i (j) site and the k site as long as all sites are equivalent. Applying the spatial Fourier transform $\hat{x}(\mathbf{q}) = \mathcal{F}[x_i] = N^{-1} \sum_i e^{i\mathbf{q}\mathbf{r}_i} x_i$ (N is the number of sites), we write

$$\frac{\partial \hat{S}_{zz}(\mathbf{q}, t)}{\partial t} - \sum_{ij} e^{i\mathbf{q}\mathbf{r}_i} W_{ij} S_{kj,zz} + (\nu_j + \nu_s) \hat{S}_{zz}(\mathbf{q}, t) = 0. \tag{2.6}$$

The Fourier transform of the convolution factorizes into $\hat{S}_{zz}(\mathbf{q}, t)$ and $N^{-1} \sum_{ij} W_{ij} e^{i\mathbf{q}(\mathbf{r}_i - \mathbf{r}_j)} \equiv W(q) = \nu_j F_q$, where F_q is the jump structure factor. Finally, applying the temporal Fourier transform, we arrive at the solution

$$\hat{S}_{zz} \propto \frac{1}{-i\omega + \nu_s + \nu_j (1 - F_q)}, \tag{2.7}$$

The spin noise power spectrum is once again described by a Lorentzian lineshape with wavevector-dependent linewidth. Recalling the definition of the Fourier transform, it becomes clear that

$$F_q\Big|_{q=0} = 1, \tag{2.8}$$

according to the definition of F_q [$W(q)|_{q=0} = \nu_j$], and

$$F_q\Big|_{q\to\infty} = 0, \tag{2.9}$$

meaning that jumps do not occur at arbitrarily small distances. Therefore, at $q = 0$ the spin motion is completely averaged out, and the linewidth is given by the intrinsic relaxation rate ν_s. At q that correspond to spatial frequencies higher than the inverse jump length the linewidth tends to $\nu_s + \nu_j$, which is the inverse lifetime of a spin on a given site, i. e., it is the correlation

time. One reasonable assumption for the jump rate is $W(r) \propto r\exp(-r/l_0)$, where l_0 is the characteristic jump length, then $F_q = 1/\left[1+(l_0 q)^2\right]$ [236]. This distribution of jumps rates is characteristic of the Singwi-Sjolander model [22, 236, 237]. The linewidth dispersion with such a jump distribution is shown in Fig. 2.1. At small wavevectors $q \ll l_0^{-1}$, we recover the quadratic linewidth dispersion, with $D = \nu_\mathrm{j} l_0^2$. This is to be expected, as small wavevectors mean poor spatial resolution, and therefore the discrete jumps behave like continuous diffusion. At larger wavevectors we observe a saturation of the linewidth, and eventually the broadening is given by the inverse lifetime of a spin on a given site.

We conclude that wavevector-resolved measurements of spin noise spectra contain information on the motion of spins. The limit of high spatial frequencies reveals the single-site dynamics, while the shape of the linewidth dispersion curve is determined by the spatial characteristics of the spin jumps. The jump length is easily determined from the linewidth dispersion curve, provided that the plateau is observed. An application of this approach to n-CdTe can be found in Ref. [22], where a single jump length is sufficient to explain the experimental data.

In Ref. [22], a one-state spin jump model was derived from older works concerned with molecular diffusion [236–239]. The resulting form of the linewidth dispersion was similar to that of Eq. (2.7), though their model also accounted for the inhomogeneous hyperfine broadening and the external magnetic field. The model permitted the extraction of important information regarding spatiotemporal spin dynamics in low-doped CdTe. In particular, it was observed that the jump lengths are very long, of the order of single microns, which is much greater than the interdonor distance in the studied sample. Looking ahead, the experiments conducted within the scope of this work have shown that the one-state model is insufficient, and does not describe experiments well enough. For instance, as more samples were studied, it became clear that the ensemble of data cannot be explained assuming a single jump length; indeed, that is the case only in the limits of low and high doping (near the Mott transition). From these considerations, one may hypothesize that the long-range spin jumps proceed through the conduction band, while short-range spin jumps occur directly between donors due to overlapping wave functions.

Equation (2.4) is easily generalized for multiple jump types governed by different rates ν_j and structure factors $W(\mathbf{q})$. Additionally, each type of jump can be accompanied by its own relaxation mechanism. This can be accomplished by introducing the tensor $\hat{R}_{ij}$ describing spin rotation due to random fields and replacing [240]

$$\sum_j W_{ij} S_{j,zz} \to \sum_j W_{ij} \hat{R}_{ij} S_{j,zz}. \tag{2.10}$$

For the sake of simplicity, let us approximate $\hat{R}_{ij}$ with a constant effective relaxation factor $\bar{R}$: $\bar{R} = 1$ if there is no spin rotation between jumps, otherwise $0 < \bar{R} < 1$. Finally, we obtain an expression similar to Eq. (2.7),

$$\hat{S}_{zz} \propto \frac{1}{-i\omega + \Gamma(q)}, \tag{2.11}$$

$$\Gamma(q) = \nu_\mathrm{s} + \nu_\mathrm{j} - \sum_\zeta \bar{R}^\zeta \nu_\mathrm{j}^\zeta F_q^\zeta, \tag{2.12}$$

where $\nu_\mathrm{j}^\zeta = \sum_j W_{ij}^\zeta$ is the escape rate for the mechanism ζ, F_q^ζ is the respective structure factor, and $\nu_\mathrm{j} = \sum_\zeta \nu_\mathrm{j}^\zeta$ is the total escape rate. An immediate result of accounting for relaxation during hops is that the linewidth at $q = 0$ is now given by

$$\nu_\mathrm{s} + (1 - \bar{R})\nu_\mathrm{j}, \tag{2.13}$$

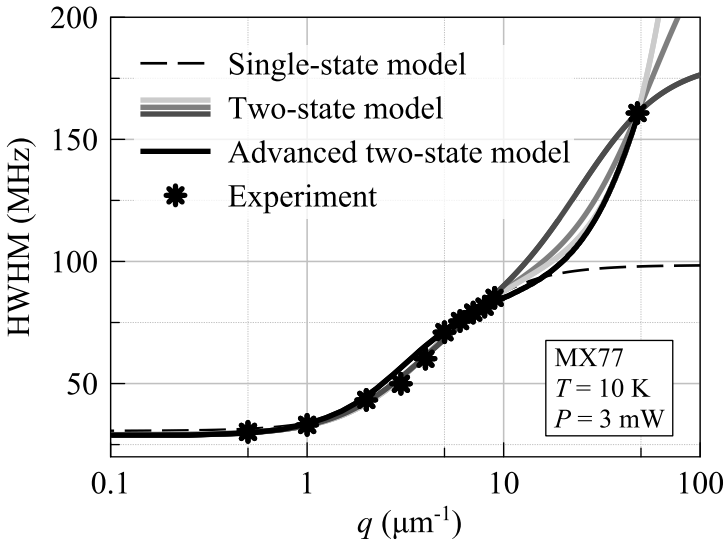

Figure 2.2: Linewidth dispersion obtained on the MX77 sample at 4.4 K modeled by various models. The one-state model (2.7) drastically underestimates the linewidth in backscattering. The simple two-state model (2.11) fits the experiment well, but additional theoretical considerations are required to constrain the fit parameters to the gap in experimentally accessible wavevectors. The advanced two-state model described in Sections 2.3 and 2.4 is also shown.

where $\bar{R}$ is averaged across all the mechanisms considered: $\bar{R} = \sum_{j\zeta} \hat{R}^{\zeta} \nu_{\mathrm{j}}^{\zeta} / \sum_{j\zeta} \nu_{\mathrm{j}}^{\zeta}$. That is, the jump dynamics affect the lineshape also in typical transmission geometry. Moreover, the relaxation that occurs during each jump would work against the motional narrowing effect that serves to reduce the influence of fluctuating nuclear fields. If relaxation during jumps is relatively strong, one would expect at least a partial replacement of the inhomogeneous broadening induced by nuclear fields by the homogeneous relaxation during jumps, potentially leading to a Voigt-like lineshape with a significant Lorentzian component. This is indeed observed in experiments, as we will show later.

Figure 2.2 demonstrates experimental data obtained with AR-SNS on an n-CdTe sample with a low doping density of 4×10^{15} cm^{-3} (average distance between donors is of the order of 10 Bohr radii), fits with the simple one-state and two-state models we have described above, and also the result of fitting with the advanced model described in Sections 2.3 and 2.4. In the simple two-state model, a short-range mechanism is introduced to account for the large linewidth in backscattering. Evidently, the inclusion of a second jump mechanism achieves good agreement with experimental data, though the large gap between AR-SNS measurements and the backscattering point introduces considerable uncertainty in determining the escape rate and jump length of the short-range mechanism. Case in point, in the two gray curves in Fig. 2.2 largely overlap in the observable region and describe the data equally well, but the jump lengths and escape rates are quite different for the short-range mechanism: $\nu_{\mathrm{j}} = 1240$ MHz, $l_0 = 5$ nm for the lightest gray curve, and $\nu_{\mathrm{j}} = 100$ MHz, $l_0 = 40$ nm for the darkest gray curve. The longer-ranged mechanism that determines the broadening behavior at small q is well-constrained by the experimental points, with $\nu_{\mathrm{j}} = 65$ MHz, $l_0 = 0.25$ nm for the lightest gray curve, and $\nu_{\mathrm{j}} = 53$ MHz, $l_0 = 0.28$ nm for the darkest gray curve. The difference between the two latter estimates of l_0 can be considered a marker of the uncertainty.

To eliminate these uncertainties, a more involved theory is required, along with a body of experimental data that would permit tracking the changes in the linewidth dispersion as external

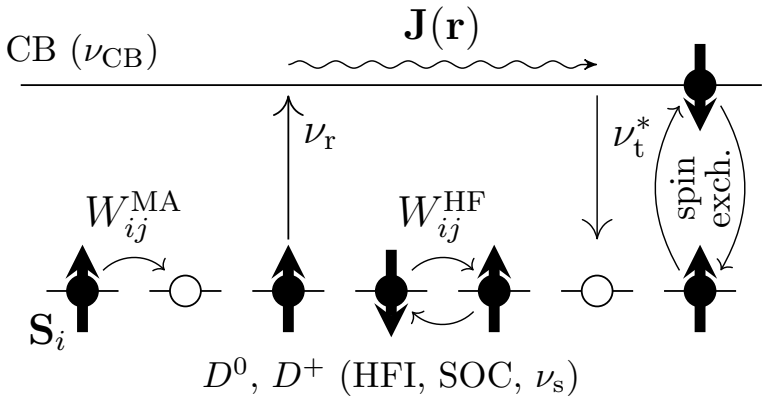

Figure 2.3: A diagram of the main features of the two-state spin jump model described by Eqs. (2.16-2.17): short-range spin jumps between nearest neighbors (HF and MA) and long-range jumps through the conduction band (CB). The model incorporates several relaxation mechanisms: hyperfine interaction with nuclei (HFI) and anisotropic exchange interaction between donors due to spin-orbit coupling (SOC) for bound electrons, and Dyakonov-Perel relaxation for CB electrons. A nonzero intrasite relaxation rate ν_{s} can be used to incorporate phonon-mediated spin relaxation in strong magnetic fields [82, 241].

parameters change. Additionally, so far we have not considered magnetic fields, including the hyperfine fields exerted by nuclei. These induce additional inhomogeneous spin dephasing and affect the spectral shape, and furthermore have a different effect on the localized and itinerant electrons. We respond to these problems by constructing a two-state model which describes the coupled localized and itinerant states.

2.3 Two-state model

In this Section, we construct a two-state model of localized electron spatiotemporal spin dynamics accounting for various types of relaxation and magnetic fields, including random hyperfine fields. The main goal of the model is to account both for short-ranged and long-ranged spin jumps, the former occurring largely within the localized state, and the latter via the conduction band. The model is applicable to a broad range of semiconductors, particularly those without inversion symmetry due to the importance of Dyakonov-Perel relaxation, which plays a central role in the theory. The mathematical approach is largely inspired by the work of Glazov [62], which itself is based on Bloch equations written for fluctuating localized electron spins.

To describe donor-bound electron spin dynamics, we start from essentially the same main equation as Ref. [62], assuming that the jumps between donors are governed by two main mechanisms: mutual exchange spin flips between occupied sites (the Herring-Flicker mechanism, HF [242]) and jumps between an occupied and a free site (the Miller-Abrahams mechanism, MA [243]). A similar equation is derived for the free conduction band (CB) electron state, where we assume that electron spins experience diffusive motion before eventually recombining. The equations must be coupled by electron trapping and release. They are governed by the rates ν_{t}^{*} and ν_{r}, respectively. The theory is completed by accounting for the following spin relaxation mechanisms: hyperfine interaction of bound electrons with nuclei (HFI), anisotropic exchange interaction between donors due to spin-orbit coupling (SOC) [70], and finally Dyakonov-Perel (DP) relaxation for CB electrons [67]. When applying our model, we treat the CB spin relaxation rate ν_{CB} as a fitting parameter, however the results agree very well with DP relaxation

due to ionized impurity scattering.

Long-ranged electron spin jumps are known to significantly affect the spin noise linewidth dispersion in n-CdTe at cryogenic temperatures [22]. A conceptually similar process is the spin-exchange scattering between localized and free states, which is often considered to be very efficient, as we have discussed in Section 1.2.3. In contrast to the long-ranged jumps, the process should act on the same characteristic length as the HF mechanism (i. e., it is short-ranged), should not induce any significant spin relaxation, and should have the same temperature dependence as electron CB jumps. It should act similarly to the HF and MA mechanisms in the spin noise linewidth dispersion, inducing a dispersion component that is parabolic in the observable range. In what follows, we do not explicitly consider this spin-exchange scattering.

We also consider an intrasite relaxation rate ν_s, similarly to the previous Section. Such intrasite relaxation can be due to the effects of spin-phonon interactions, which significantly affect spin relaxation when the Zeeman energy is greater than the thermal energy [54, 82, 241]. At temperatures of about 10 K, this corresponds to fields of the order of 10 T, which is far from our experimental conditions. Hence, we neglect these effects by setting $\nu_\mathrm{s} = 0$ in all fits, though all equations are derived for arbitrary ν_s. A diagram depicting the main features of the model is given in Fig. 2.3.

We write the coupled equations for the spin evolution as

$$\frac{\mathrm{d}\langle \mathbf{S}_{\mathrm{t},i}\rangle}{\mathrm{d}t} = \sum_j \left[W_{ij}\hat{R}^{ij}_\mathrm{SO}\langle \mathbf{S}_{\mathrm{t},j}\rangle - W_{ji}\langle \mathbf{S}_{\mathrm{t},i}\rangle\right] + \mathbf{\Omega}_{i\mathrm{d}}\times\langle \mathbf{S}_{\mathrm{t},i}\rangle + \nu_\mathrm{t}^* v_\mathrm{t} n_\mathrm{CB}\langle \mathbf{S}_\mathrm{c}(\mathbf{r}_i)\rangle - \nu_\mathrm{r}\langle \mathbf{S}_{\mathrm{t},i}\rangle - \nu_\mathrm{s}\langle \mathbf{S}_{\mathrm{t},i}\rangle, \tag{2.14}$$

$$\frac{\mathrm{d}\langle \mathbf{S}_\mathrm{c}(\mathbf{r})\rangle}{\mathrm{d}t} = D\nabla^2_\mathbf{r}\langle \mathbf{S}_\mathrm{c}(\mathbf{r})\rangle + \mathbf{\Omega}_\mathrm{c}\times\langle \mathbf{S}_\mathrm{c}(\mathbf{r})\rangle + \sum_j v(\mathbf{r}-\mathbf{r}_j)\left[\nu_\mathrm{r}(v_\mathrm{t}n_\mathrm{CB})^{-1}\langle \mathbf{S}_{\mathrm{t},j}\rangle - \nu_\mathrm{t}^*\langle \mathbf{S}_\mathrm{c}(\mathbf{r})\rangle\right] - \nu_\mathrm{CB}\langle \mathbf{S}_\mathrm{c}(\mathbf{r})\rangle, \tag{2.15}$$

where $\langle \mathbf{S}_{\mathrm{t},i}\rangle$ is the average spin on site i, and $\langle \mathbf{S}_\mathrm{c}(\mathbf{r})\rangle$ describes the average spin in the free state. These equations can be rewritten in terms of spin densities, with the local spin density $\mathbf{S}_i = v_\mathrm{t}^{-1}\langle \mathbf{S}_{\mathrm{t},i}\rangle$ and the spin density in the CB $\mathbf{J}(\mathbf{r}) = n_\mathrm{CB}\langle \mathbf{S}_\mathrm{c}(\mathbf{r})\rangle$:

$$\frac{\mathrm{d}\mathbf{S}_i}{\mathrm{d}t} = \sum_j \left[W_{ij}\hat{R}^{ij}_\mathrm{SO}\mathbf{S}_j - W_{ji}\mathbf{S}_i\right] + \mathbf{\Omega}_{i\mathrm{d}}\times\mathbf{S}_i + \nu_\mathrm{t}^*\mathbf{J}(\mathbf{r}_i) - \nu_\mathrm{r}\mathbf{S}_i - \nu_\mathrm{s}\mathbf{S}_i, \tag{2.16}$$

$$\frac{\mathrm{d}\mathbf{J}(\mathbf{r})}{\mathrm{d}t} = D\nabla^2_\mathbf{r}\mathbf{J}(\mathbf{r}) + \mathbf{\Omega}_\mathrm{c}\times\mathbf{J}(\mathbf{r}) + \sum_j v(\mathbf{r}-\mathbf{r}_j)\left[\nu_\mathrm{r}\mathbf{S}_j - \nu_\mathrm{t}^*\mathbf{J}(\mathbf{r})\right] - \nu_\mathrm{CB}\mathbf{J}(\mathbf{r}). \tag{2.17}$$

The rates W_{ij} describe spin jumps between donor sites i and j, with the average time between a jump to another donor given by $\nu_\mathrm{j} = \sum_k W_{ki}$. The $\hat{R}^{ij}_\mathrm{SO}$ matrix incorporates spin losses due to SOC [73]. In order to lighten the equations, the HF and MA mechanisms are not distinguished in Eq. (2.16), although their respective jump rates and spatial distributions differ. Nonetheless, this distinction is made in the following [see, e.g., Eq. (2.52)]. This turns out to be necessary to reproduce the temperature dependence of the linewidth dispersion in certain conditions, since at low temperature and compensation, the weak MA mechanism is thermally activated, while the more important HF mechanism is not. The dimensionless function $v(\mathbf{r})$ describes the volume occupied by the trap, $\int v(\mathbf{r})\mathrm{d}\mathbf{r} = v_\mathrm{t}$, where v_t has the meaning of trap volume. This function is necessary for dimensional consistency and spin conservation in the absence of relaxation [1]; it can be represented by a Dirac delta as $v(\mathbf{r}) = v_\mathrm{t}\delta(\mathbf{r})$ if ionized donors can be

[1] This is most evident from Eqs. (2.14) and (2.15), one only needs to integrate Eq. (2.15) around one trap i

considered small enough, and it can also be thought of as the probability distribution of the trap.

In the following Section, we show that ν_t^* enters the final spatiotemporal spin noise spectrum only as $\nu_\mathrm{t} = n_{\mathrm{d}+} v_\mathrm{t} \nu_\mathrm{t}^*$, where $n_{\mathrm{d}+}$ is the density of traps given by the ionized donor density. That is, ν_t^* is renormalized by the fraction of space occupied by traps, similarly to Ref. [101], as we have hinted at in Section 1.2.4. The physical meaning of ν_t is that it is the trapping rate as experienced by the population of electrons in the itinerant state. We continue the discussion in terms of ν_t only.

The free electron diffusion coefficient is determined by the thermal velocity and momentum scattering time τ_p: $D_{\tau_\mathrm{p}} = \tau_\mathrm{p} k_\mathrm{B} T / m_\mathrm{e}^*$. However, it is not obvious that this should be the diffusion coefficient D in Eq. (2.17), since in SNS we see the electron spin, not its charge, and spin exchange between free and localized electrons may eventually lead to spin diffusion that is substantially different from charge diffusion, especially considering that the spin exchange process is supposed to be very efficient [85, 88] For this reason, we introduce the CB scattering length l_s as a parameter, with the spin diffusion coefficient $D = l_\mathrm{s}^2 \nu_\mathrm{t}$. The physical meaning is that the spin diffusively travels a distance l_s during ν_t^{-1} before being trapped again. At low temperatures, when phonon scattering does not contribute significantly, ionized impurity scattering becomes the dominant mechanism of momentum relaxation [244], so τ_p may be approximated as τ_i, the ionized impurity scattering time, which we calculate via the Brooks-Herring formula [97, 245, 246]. It is used to calculate the Dyakonov-Perel relaxation rate ν_DP and D_{τ_p}.

The donor-bound electron spins precess in the total field with an angular frequency $\mathbf{\Omega}_{i\mathrm{d}} = \mathbf{\Omega}_i + \mathbf{\Omega}_\mathrm{d}$, where $\mathbf{\Omega}_i$ and $\mathbf{\Omega}_\mathrm{d}$ are the precession rates in the local nuclear field and in the external magnetic field, respectively. For the CB electron spins, we neglect the effect of random hyperfine fields because of efficient motional narrowing. Furthermore, the CB spins may precess at a slightly different angular frequency $\mathbf{\Omega}_\mathrm{c}$ due to different g-factor and/or because of local nuclear spin polarization. In Section 2.6.3, this is shown to have a significant impact in certain experimental conditions.

2.4 Spatiotemporal spin noise power spectrum

The aim of this section is to give an analytical expression of the wavevector dependent spin noise power spectrum for electron spins obeying the coupled Bloch Eqs. (2.16-2.17). The bulk of the mathematical work presented in this section was performed by S. Cronenberger, with D. Scalbert and the author providing small input, independently verifying the calculations as required, and performing preliminary fits of AR-SNS data.

We start from the theory developed in Ref. [62]. However, we keep track of the spatial dependence of the electron spin components throughout the calculations to eventually carry out a spatial Fourier transform of the solution, thus obtaining the spatiotemporal spin noise spectrum. A step-by-step near-analytical solution of the model is provided in Section 2.4.1, which is succeeded by Section 2.4.2, where we describe the most pertinent implications of the theory and useful approximations.

---

assuming $\Omega_\mathrm{c} = 0$, $D = 0$, $\nu_\mathrm{CB} = 0$, and compare to Eq. (2.14) setting $W_{ij} = 0$, $\Omega_{i\mathrm{d}} = 0$, and $\nu_\mathrm{s} = 0$. Replacing $\int_i \langle \mathbf{S}_\mathrm{c}(\mathbf{r}) \rangle \mathrm{d}\mathbf{r} = v_\mathrm{t} \langle \mathbf{S}_\mathrm{c}(\mathbf{r}_i) \rangle$, we verify that the two resulting rates are equal in magnitude but different in sign. The expression of the integral above is correct as long as $\mathbf{J}(\mathbf{r}) = \mathrm{const}$ on the scale of a single trap. In the next Section, we introduce this assumption and discuss its applicability.

2.4.1 Solving the advanced two-state model

We introduce the spatiotemporal correlation function,

$$S_{\alpha\beta}(r,t) = \langle \int_{-\infty}^{\infty} S_{\alpha}(r'+r,t'+t)S_{\beta}(r',t')dr' \rangle, \tag{2.18}$$

where $\mathbf{S}(r,t) = \sum_l \delta(r-r_l)\mathbf{S}_l(t)$, $\alpha,\beta = x,y,z$ enumerate Cartesian components, and the angular brackets denote averaging over t' at fixed t. Our aim is to calculate the spin noise power spectrum at a given wavevector q, that is to say, the space-time Fourier transform of (2.18)

$$\hat{S}_{\alpha\beta}(q,\omega) = \int_{-\infty}^{+\infty}\int_{-\infty}^{+\infty} S_{\alpha\beta}(r,t)e^{i(\omega t - qr)}\mathrm{d}r\mathrm{d}t. \tag{2.19}$$

Hereafter, we neglect explicitly depicting the vector nature of the coordinates r, r' for brevity, and the same applies to the wavevector q. At $q=0$, Eq. (2.19) reduces to Eq. (2) of Ref. [62], i. e., the usual spin noise power spectrum in transmission geometry. Substituting Eq. (2.18) into Eq. (2.19) we get

$$\begin{aligned}\hat{S}_{\alpha\beta}(q,\omega) &= \int_{-\infty}^{+\infty}\langle S_{\alpha,q}(t'+t)S_{\beta,-q}(t')\rangle e^{i\omega t}\mathrm{d}t \\ &= \sum_{l,l'}\int_{-\infty}^{+\infty} e^{-iqr_{ll'}}\langle S_{l,\alpha}(t'+t)S_{l',\beta}(t')\rangle e^{i\omega t}\mathrm{d}t \\ &= 2\mathrm{Re}\{\sum_{l,l'} e^{-iqr_{ll'}}\mathcal{C}^{(ll')}_{\alpha\beta}\},\end{aligned} \tag{2.20}$$

where $r_{ll'} = |\mathbf{r}_l - \mathbf{r}_{l'}|$. In the above, we have introduced the spatial Fourier transform $S_{\alpha,q}(t) = \sum_l S_{l,\alpha}(t)e^{-iqr_l}$, $S_{\alpha}(r,t) = \sum_q S_{\alpha,q}(t)e^{iqr}$, and the correlation functions

$$\mathcal{C}^{(ll')}_{\alpha\beta} = \int_0^{+\infty}\langle S_{l,\alpha}(t+t')S_{l',\beta}(t')\rangle e^{i\omega t}\mathrm{d}t. \tag{2.21}$$

For a system of N electron spin localization sites with hopping and hyperfine interaction, $\mathcal{C}^{(ll')}_{\alpha\beta}$ satisfy Eq. (4) of Ref. [62]. We modify their equations to take into account an additional channel of electron spin diffusion and relaxation which is mediated by the CB, as described by Eqs. (2.16-2.17). Assuming that the spin fluctuations are probed along the z axis, we are interested in $\hat{S}_{zz}(q,\omega)$. Hence, the calculations can be restricted to $\mathcal{C}^{(ll')}_{\alpha z}$. We rewrite the main Eqs. (2.16-2.17) for correlators similarly to Section 2.2, but properly accounting for the Langevin random forces this time [54]. Performing a temporal Fourier transform, we obtain

$$\tau_\omega^{-1}\mathcal{C}^{ll'}_{\alpha z} - \mathcal{M}^{(ml')}_{\alpha z} + \sum_{\alpha'\beta'}\epsilon_{\alpha\alpha'\beta'}\Omega_{\mathrm{ld},\beta'}\mathcal{C}^{ll'}_{\alpha' z} = \frac{1}{4N}\delta_{ll'}\delta_{\alpha z} + \nu_{\mathrm{t}}^{*}\mathcal{K}^{(l')}_{\alpha z}(r_l), \tag{2.22}$$

$$\left[-i\omega + \nu_{\mathrm{CB}} - D\nabla^2 + \nu_{\mathrm{t}}^{*}\sum_m v(r-r_m)\right]\mathcal{K}^{(l')}_{\alpha z}(r) + \sum_{\alpha'\beta'}\epsilon_{\alpha\alpha'\beta'}\Omega_{\mathrm{c}\beta'}\mathcal{K}^{(l')}_{\alpha' z}(r) = \nu_{\mathrm{r}}\sum_m v(r-r_m)\mathcal{C}^{(ml')}_{\alpha z}, \tag{2.23}$$

where $\tau_\omega^{-1} = (-i\omega + \nu_{\mathrm{s}} + \nu_{\mathrm{r}} + \nu_{\mathrm{j}})$, $\mathcal{M}^{(ml')}_{\alpha z} = \bar{R}\sum_m W_{lm}\mathcal{C}^{(ml')}_{\alpha z}$, and $\nu_{\mathrm{j}} = \sum_m W_{ml}$ as in Section 2.2. The on-site spin lifetime τ_ω is determined by the hopping rate ν_{j} and the intrasite spin relaxation rate ν_{s}. The release rate ν_{r} also limits the time that a spin is localized on a given site. $\Omega_{\mathrm{ld},\beta'} = \Omega_{l\beta'} + \Omega_{\mathrm{d}\beta'}$ is the total electron spin precession frequency given by the

random hyperfine fields $\Omega_{l\beta'}$ and the static effective field $\Omega_{\mathrm{d}\beta'}$. The latter includes the external magnetic field and the static effective field of nuclear fluctuations acting on localized electrons, respectively [2]; $\epsilon_{\alpha\alpha'\beta'}$ is the third-rank antisymmetric tensor. $\delta_{ll'}\delta_{\alpha z}$ assumes that there are no initial correlations neither between sites at different locations, nor between different polarization components (δ_{ab} is the Kronecker delta). The correlations are induced by spin precession in magnetic fields, as well as by hopping [$\mathcal{M}_{\alpha z}^{(ml')}$], release/trapping [terms proportional to ν_{r} and ν_{t}^{*} in Eqs. (2.22-2.23)] and CB diffusion [$D\nabla_r^2\mathcal{K}_{\alpha z}^{(l')}(r)$ in Eq. (2.23)].

We assume that the jump rate W_{lm} is homogeneous (same for all sites l) and isotropic. That is, $W_{lm} \equiv W(r_{lm})$, where r_{lm} is the distance between the l and m sites. This is well-justified as long as there are no donor clusters or significant anisotropy. Spin-orbit rotations occur at hops and are taken into account through a constant spatially averaged spin-orbit factor $\bar{R} = 1 - \frac{1}{3}\frac{\bar{l}^2}{L_{\mathrm{SO}}^2}$, where L_{SO} the spin orbit length and $\bar{l}$ the mean-square hopping distance. In writing the above equations, we do not distinguish between the HF and MA interdonor spin jumps for the sake of brevity; the inclusion of several interdonor jump mechanisms is straightforward, as outlined in Section 2.2.

The quantities $\mathcal{K}_{\alpha z}^{(l')}(r)$ are correlation functions that describe a spin that, being already correlated to a localized spin at position $r_{l'}$, is promoted in the CB through the release process at a rate ν_{r}:

$$\mathcal{K}_{\alpha z}^{(l')}(r) = \int_0^{+\infty} \langle J_\alpha(r, t+t') S_{l',\beta}(t') \rangle e^{i\omega t} \mathrm{d}t. \tag{2.24}$$

A rigorous calculation of spin fluctuations of a two-dimensional electron gas confined in a semiconductor quantum well at thermal equilibrium can be found in Ref. [248]. Here, in Eq. (2.23), the itinerant spin relaxation is described by a scalar CB spin relaxation rate, i. e., the Dyakonov-Perel process. The spin-orbit effective field in bulk CdTe is not strong enough to induce precession of the electron spin during diffusion as could be the case in strained bulk semiconductors or quantum wells [248], i. e., the CB spins never perform a full uninterrupted rotation in the spin-orbit field, hence oscillations of the correlation function can only be induced by external magnetic fields.

In Eqs. (2.17) and (2.23) we make a rough approximation by assuming continuous diffusion with spatially homogeneous loss and gain terms. As mentioned in Section 1.2.4, there exist more rigorous theoretical approaches to diffusion-assisted trapping. However, continuous diffusion with an effective diffusion coefficient D has the advantage of making the calculation more tractable, since the Fourier transform makes short work of the Laplacian involved in this approach. Moreover, as discussed in Section 1.2.4, estimates show that electron (spin) transport can be considered diffusive in practically all regimes that will be relevant to us.

[2] Generally, $\Omega_{c\beta'} \neq \Omega_{\mathrm{d}\beta'}$ if there is finite inhomogeneous nuclear spin polarization, e. g., under donor orbits. This is due to different probability densities of localized and free electron spins, which leads to different effective hyperfine fields experienced by the different electrons. For strongly localized states, the difference can also arise simply due to different g-factors of the two states, as it is known that the g-factor is energy-dependent [247].

Equation on the spatiotemporal correlator for bound spins

Let us consider an external magnetic field directed along the x axis. Equation (2.22) for $\alpha = z$ is rewritten as

$$\begin{aligned}\mathcal{C}_{zz}^{(ll')} =& \frac{\tau_\omega}{1+\tilde{\Omega}_l^2}\Bigg\{\left[\frac{\delta_{ll'}}{4N} + (\mathcal{MK})_{zz}^{(ll')}\right]\left(1+\tilde{\Omega}_{lz}^2\right) \\ &+ \left[\tilde{\Omega}_{lz}\left(\tilde{\Omega}_{lx}+\tilde{\Omega}_\mathrm{d}\right) - \tilde{\Omega}_{ly}\right](\mathcal{MK})_{xz}^{(ll')} \\ &+ \left[\tilde{\Omega}_{ly}\tilde{\Omega}_{lz} + \left(\tilde{\Omega}_{lx}+\tilde{\Omega}_\mathrm{d}\right)\right](\mathcal{MK})_{yz}^{(ll')}\Bigg\},\end{aligned} \tag{2.25}$$

where $\tilde{\Omega} \equiv \tau_\omega \Omega$ is used to denote dimensionless frequencies, and $(\mathcal{MK})_{\alpha z}^{(ll')} = \mathcal{M}_{\alpha z}^{(ll')} + \nu_\mathrm{t}^* \mathcal{K}_{\alpha z}^{(l')}(r_l)$. For $\alpha = x, y$, the results are very similar. We formally introduce the Fourier transforms $\hat{\mathcal{C}}_{zz}(q)$ as

$$\hat{\mathcal{C}}_{\alpha z}(q) = \sum_{ll'} e^{-iqr_{ll'}} \mathcal{C}_{\alpha z}^{ll'}, \tag{2.26}$$

$$\hat{\mathcal{K}}_{\alpha z}(q) = \sum_{ll'} e^{-iqr_{ll'}} \mathcal{K}_{\alpha z}^{l'}(r_l). \tag{2.27}$$

To obtain the spatiotemporal spin noise power spectrum $\hat{S}_{zz}(q,\omega)$, we must deal with the sums $\sum_{l,l'} e^{-iqr_{ll'}} (\mathcal{O})_l (\mathcal{MK})_{\alpha z}^{(ll')}$, where the coefficients $(\mathcal{O})_l$ contain the electron spin precession frequencies in the transverse external field and in the nuclear fields as they appear in Eq. (2.25). The latter sums can be rewritten as

$$\sum_{l,l'} e^{-iqr_{ll'}} (\mathcal{O})_l (\mathcal{MK})_{\alpha z}^{(ll')} = \sum_{q'} (\hat{\mathcal{O}})_{q'} \sum_{l,l'} e^{-i(q-q')r_l} e^{iqr_{l'}} (\mathcal{MK})_{\alpha z}^{(ll')} \tag{2.28}$$

using the Fourier transforms

$$(\mathcal{O})_l = \sum_q (\hat{\mathcal{O}})_q e^{iqr_l}, \tag{2.29}$$

$$(\hat{\mathcal{O}})_q = \frac{1}{N} \sum_l (\mathcal{O})_l e^{-iqr_l}. \tag{2.30}$$

Assuming that nuclear spin fluctuations are spatially uncorrelated, the power spectral density of the frozen nuclear spin fluctuations in reciprocal space is independent of q: $|(\hat{\mathcal{O}})_q|^2 = |\frac{1}{N}\sum_l (\mathcal{O})_l|^2$. Therefore, terms that satisfy $\sum_l (\mathcal{O})_l = 0$ do not contribute to Eq. (2.28). In contributions with nontrivial $\sum_l (\mathcal{O})_l$, though the magnitudes $|(\hat{\mathcal{O}})_q|$ are the same for all q, the wavevector-dependent phase is random due to the random distribution of localization sites, hence the sum over $q' \neq 0$ should average to 0. Equation (2.28) is then reduced to

$$\sum_{l,l'} e^{-iqr_{ll'}} (\mathcal{O})_l (\mathcal{MK})_{\alpha z}^{(ll')} = (\hat{\mathcal{O}})_{q'=0} \sum_{l,l'} e^{-iqr_{ll'}} (\mathcal{MK})_{\alpha z}^{(ll')}. \tag{2.31}$$

We consider the case of homogeneous and isotropic hopping, that is, W_{lm} depends only on r_{lm}, and we can make use of the convolution theorem to calculate $\sum_{l,l'} e^{-iqr_{ll'}} \mathcal{M}_{\alpha z}^{(ll')}$. We are then left with $\hat{\mathcal{K}}_{\alpha z}(q) = \sum_{l,l'} e^{-iqr_{ll'}} \mathcal{K}_{\alpha z}^{l'}(r_l)$, which also appears in the spatial Fourier transform of Eq. (2.23) (see discussion below). Hence, we end up with a new set of coupled equations. Assuming continuous diffusion in the CB, Eq. (2.22) transforms into:

$$\hat{\mathcal{C}}_{zz}(q)\left(1 - \bar{R}\nu_\mathrm{j} F_q \tau_\omega A_\omega\right) = \tau_\omega A_\omega \left[\frac{1}{4} + \nu_\mathrm{t}^* \hat{\mathcal{K}}_{zz}(q)\right] + \tau_\omega B_\omega \left[\nu_\mathrm{t}^* \hat{\mathcal{K}}_{yz}(q) + \bar{R}\nu_\mathrm{j} F_q \hat{\mathcal{C}}_{yz}(q)\right], \tag{2.32}$$

$$\hat{\mathcal{C}}_{yz}(q)\left(1 - \bar{R}\nu_\mathrm{j} F_q \tau_\omega A_\omega\right) = \tau_\omega A_\omega \nu_\mathrm{t}^* \hat{\mathcal{K}}_{yz}(q) - \tau_\omega B_\omega \left[\frac{1}{4} + \nu_\mathrm{t}^* \hat{\mathcal{K}}_{zz}(q) + \bar{R}\nu_\mathrm{j} F_q \hat{\mathcal{C}}_{zz}(q)\right], \tag{2.33}$$

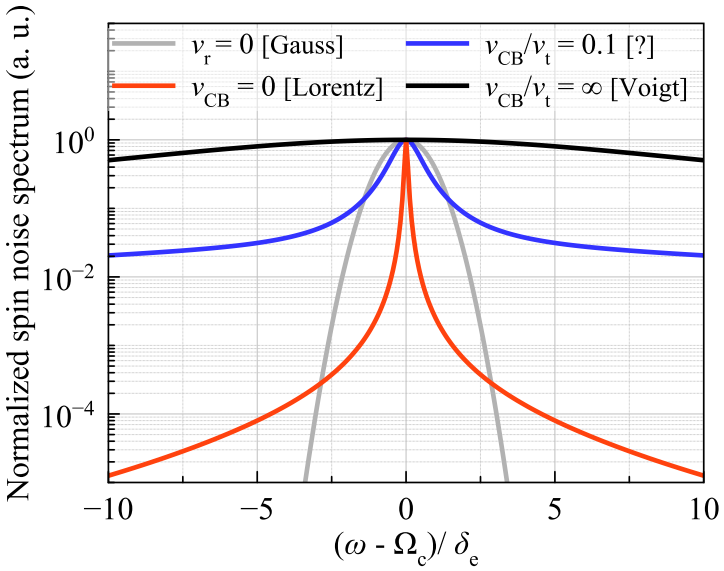

Figure 2.4: Theoretical spectra calculated with Eq. (2.42) for $\delta_e = 0.1$ ns^{-1}, $\nu_j = 0$, $\nu_t = nu_r = 1$ ns^{-1} (except for the gray line where $\nu_r = 0$), and normalized to unity amplitude. The ratio ν_{CB}/ν_t is indicated for each curve as well as the line profiles they can be accurately fitted with.

where $F_q = \sum_j W_{ij} e^{iqr_{ij}}/\nu_j$ is the structure factor of the hopping process as introduced in Section 2.2. The functions A_ω and B_ω are defined as in Ref. [62]:

$$A_\omega = \frac{1}{N} \sum_l \frac{1 + \tilde{\Omega}_{l,z}^2}{1 + \tilde{\Omega}_l^2}, \tag{2.34}$$

$$B_\omega = \frac{1}{N} \sum_l \frac{\tilde{\Omega}_{l,x} + \tilde{\Omega}_d}{1 + \tilde{\Omega}_l^2}. \tag{2.35}$$

Equation on the bound-free spatiotemporal correlator

For Eq. (2.23), the calculation is complicated by the functions $v(r - r_m)$ describing the traps location and spatial profile. The solution can be kept analytical as long as the trap size is much smaller than the spatial extent of the correlator $\mathcal{K}_{\alpha z}^{(l')}(r)$, and the traps do not overlap. The trap size can be estimated by a_B, while the characteristic length of $\mathcal{K}_{\alpha z}^{(l')}(r)$ is given by the smaller of two values: the scattering length l_s, and the distance that is traversed by a CB electron before decoherence $\nu_{CB}^{-1} v$, where $v \propto \sqrt{k_B T/m_e^*}$ is the thermal velocity. In our experiments, $a_B \ll l_s$ always, and $\nu_{CB}^{-1} v \gg l_s$. At low temperatures and n-doping below the Mott transition, $a_B \ll n_d^{-1/3}$, where n_d is the donor density. Therefore, the spatial profile of a trap can be approximated by a delta function: $v(r - r_m) = v_t \delta(r - r_m)$, where v_t is the effective trap volume. We now apply the continuous Fourier transform $f(r) \to \int_{-\infty}^{\infty} e^{-iqr} f(r) \mathrm{d}r$ to Eq. (2.23):

$$\left(-i\omega + \nu_{CB} + Dq^2\right) \int_{-\infty}^{\infty} e^{-iqr} \mathcal{K}_{\alpha z}^{(l')}(r) \mathrm{d}r + \Omega_c \sum_{\alpha'} \epsilon_{\alpha\alpha' x} \int_{-\infty}^{\infty} e^{-iqr} \mathcal{K}_{\alpha' z}^{(l')}(r) \mathrm{d}r$$
$$= -\sum_m \int_{-\infty}^{\infty} e^{-iqr} v(r - r_m) \left[\nu_t^* \mathcal{K}_{\alpha z}^{(l')}(r) - \nu_r \mathcal{C}_{\alpha z}^{(ml')}\right] \mathrm{d}r. \tag{2.36}$$

The integral on the right-hand side collapses to its value at $r = r_m$ factorized by v_t, provided that the characteristic size of the trap probability density function $v(r)$ is smaller than that of

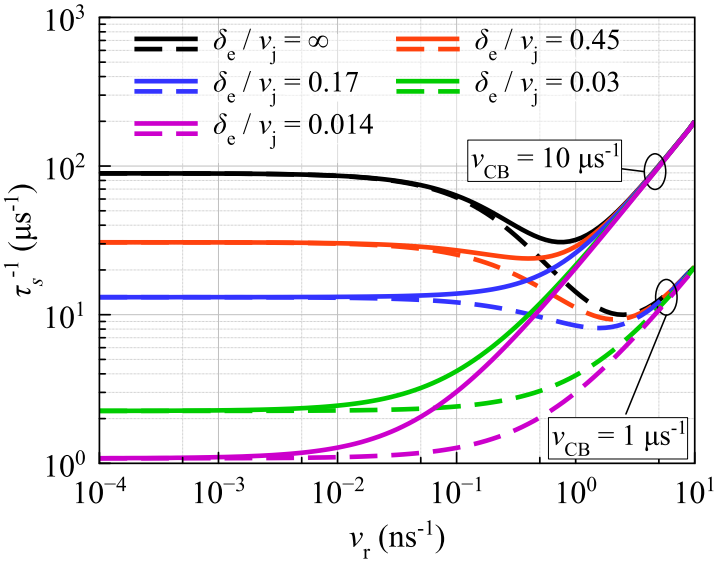

Figure 2.5: Spin relaxation rate calculated with Eq. (2.59) as a function of the release rate ν_r for several values of δ_e/ν_j indicated above each curve. The parameters ν_{CB} and ν_t are kept constant and equal to 10 μs^{-1} (1 μs^{-1} for dashed curves) and 2 ns^{-1}, respectively.

$\mathcal{K}^{(l')}_{\alpha' z}(r)$, which is defined by the CB jump length, and the traps do not overlap. These conditions are fulfilled in the experiments treated in this work. To express the integrals on the left-hand side as sums, we perform the standard substitution $\int e^{-iqr} f(r) \mathrm{d}r \to \sum_m n_{d+}^{-1} f(r_m)$, where n_{d+}^{-1} is the inverse number density of the traps, i. e., the volume-per-trap.[3] Recalling the definitions given in Eqs. (2.26-2.27), the transformed equation is written as

$$\sum_{\alpha'} \left[\left(-i\omega + \nu_{CB} + Dq^2 + n_{d+} v_t \nu_t^* \right) \delta_{\alpha\alpha'} + \Omega_c \epsilon_{\alpha\alpha' x} \right] \mathcal{K}_{\alpha z}(q) = n_{d+} v_t \nu_r \mathcal{C}_{\alpha z}(q), \tag{2.37}$$

where we have also multiplied Eq. (2.36) by $e^{iqr_{l'}}$ and summed over l'. Finally, a compact form of this result can be presented as

$$\hat{\mathcal{K}}_{zz}(q) = n_{d+} v_t \nu_r \mathrm{T}_{q,\omega} \hat{\mathcal{C}}_{zz}(q) + \Omega_c \mathrm{T}_{q,\omega} \hat{\mathcal{K}}_{yz}(q), \tag{2.38}$$

$$\hat{\mathcal{K}}_{yz}(q) = n_{d+} v_t \nu_r \mathrm{T}_{q,\omega} \hat{\mathcal{C}}_{yz}(q) - \Omega_c \mathrm{T}_{q,\omega} \hat{\mathcal{K}}_{zz}(q), \tag{2.39}$$

where $\mathrm{T}_{q,\omega}$ is the spin lifetime in the CB in analogy to τ_ω for localized states:

$$\mathrm{T}^{-1}_{q,\omega} = (-i\omega + \nu_{CB} + Dq^2 + n_{d+} v_t \nu_t^*). \tag{2.40}$$

The linear Eqs. (2.38-2.39) are solved easily:

$$\mathcal{K}_{zz}(q) = \nu_r \frac{n_{d+} v_t \mathrm{T}_{q,\omega}}{1 + \Omega_c^2 \mathrm{T}^2_{q,\omega}} \left[\hat{\mathcal{C}}_{zz}(q) + \mathrm{T}_{q,\omega} \Omega_c \hat{\mathcal{C}}_{yz}(q) \right], \tag{2.41}$$

and similarly for $\mathcal{K}_{yz}(q)$. Recalling Eqs. (2.32-2.33), one observes that $\hat{\mathcal{K}}_{\alpha z}(q)$ enters only with a coefficient proportional to ν_t^*. Indeed, ν_t^* is encountered only as part of the product $n_{d+} v_t \nu_t^*$

[3] This is an acceptable approximation as long as the CB scattering length l_s is much greater than the distance between localization sites, which we have already established. It is also worth clarifying that the density entering here is defined by the donor sites that contribute to the sum, i. e., those that are described by the rates ν_t^* and ν_r. Since the long-ranged jumps corresponding to l_s are due to electron jumps and are too long to be attributed to spin-exchange scattering, we use the ionized donor density n_{d+}.

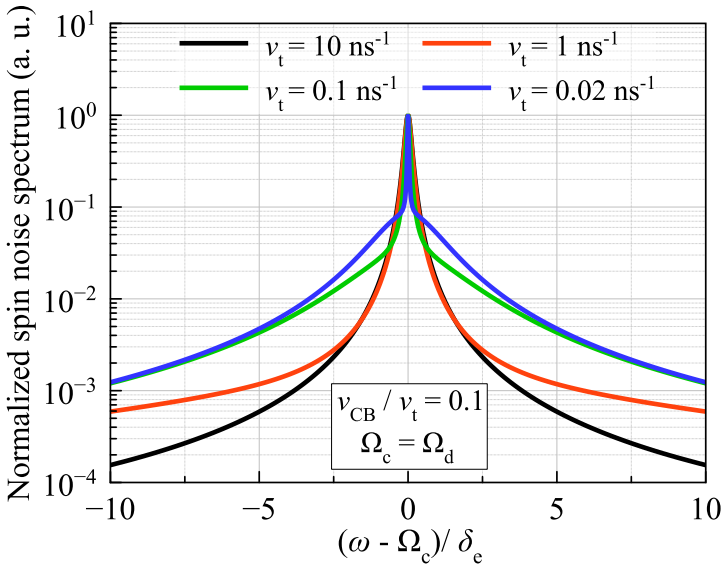

Figure 2.6: Theoretical spectra calculated with Eq. (2.42) for various values of the trapping rate ν_t, with $\delta_e = \nu_r = 10^8$ s^{-1}, $\nu_j = 0.17$ ps^{-1}, $\Omega_c = \Omega_d$, $\nu_{CB}/\nu_t = 0.1$, and normalized to unity amplitude. In the short trapping time regime $\Omega_c \nu_t^{-1} \ll 1$, the shape of the spin noise line depends only on the ratio ν_{CB}/ν_t and is Lorentzian. Increasing the trapping time eventually leads to a peculiar lineshape that resembles two superimposed Lorentzian curves.

in our model, hence it is the trapping rate $\nu_t \equiv n_{d+} v_t \nu_t^*$ that is observed in experiments. Effectively, the rate ν_t^* is renormalized by the fraction of space occupied by traps, in the spirit of Ref. [101]. Since ν_t is the quantity measured in experiments, we will focus on it instead of ν_t^*.

The spatiotemporal spin noise spectrum

Algebraically solving the linear system defined in Eqs. (2.32-2.33) and Eqs. (2.38-2.39) for $\hat{\mathcal{C}}_{zz}(q)$, we finally obtain the spin noise power spectrum

$$\hat{S}_{zz}(q,\omega) = \frac{1}{4} \frac{[\tau_\omega^{-1} - F(q,\omega)A_\omega]A_\omega - F(q,\omega)B_\omega^2}{[\tau_\omega^{-1} - F(q,\omega)A_\omega + f_{nd}(q,\omega)B_\omega]^2 + [F(q,\omega)B_\omega + f_{nd}(q,\omega)A_\omega]^2} + \text{c.c.} \tag{2.42}$$

where c. c. denotes the complex conjugate, and

$$F(q,\omega) = \bar{R}\nu_j F_q + \frac{\nu_r \nu_t \mathrm{T}_{q,\omega}}{1 + \Omega_c^2 \mathrm{T}_{q,\omega}^2}, \tag{2.43}$$

$$f_{nd}(q,\omega) = \nu_r \nu_t \Omega_c \mathrm{T}_{q,\omega}^2. \tag{2.44}$$

In the limit $\nu_r \to 0$ and $q \to 0$, Eq. (2.42) is equivalent to Eq. (13) of Ref. [62], disregarding the typographical error in the second term of the denominator therein. Inspection of relations (2.34) and (2.35) leads to the equality $B_\omega = iA_\omega$ at high magnetic field. In this case, maintaining $\nu_r = 0$, Eq. (2.42) is identical to the Eqs. (30) proposed in [22] for $R(\omega) = 2\tau_\omega A_\omega$.

There exist analytical forms of the functions A_ω and B_ω as defined by Eq. (2.34) and (2.35), provided that $N \to \infty$ and the fluctuating nuclear fields are described by a Gaussian distribution, $\mathcal{F}(\mathbf{\Omega}) = (\sqrt{\pi}\delta_e)^{-3} \exp(-\Omega^2/\delta_e^2)$, where the δ_e parameter describes the distribution of precession frequencies in the nuclear field [6]. In transverse external magnetic field A_ω and

B_ω are given by,

$$B_\omega = \frac{\sqrt{\pi}}{4\tilde{\Omega}_\mathrm{d}^2\tilde{\delta}_\mathrm{e}}\left[-\left(i\tilde{\delta}_\mathrm{e}^2+2\tilde{\Omega}_\mathrm{d}\right)w(iz^*)+\left(i\tilde{\delta}_\mathrm{e}^2-2\tilde{\Omega}_\mathrm{d}\right)w(iz)\right]+\frac{1}{\tilde{\Omega}_\mathrm{d}}, \tag{2.45}$$

$$A_\omega = \frac{\sqrt{\pi}}{8\tilde{\Omega}_\mathrm{d}^3\tilde{\delta}_e}\left[ir^*\left(\tilde{\Omega}_\mathrm{d},\tilde{\delta}_e\right)w(iz^*)-ir\left(\tilde{\Omega}_\mathrm{d},\tilde{\delta}_e\right)w(iz)\right]+\frac{\tilde{\delta}_e^2}{2\tilde{\Omega}_\mathrm{d}^2}, \tag{2.46}$$

where $\tilde{\delta}_e = \tau_\omega\delta_\mathrm{e}$, $z = \tilde{\delta}_\mathrm{e}^{-1}(1-i\tilde{\Omega}_\mathrm{d})$, $z^* = \tilde{\delta}_\mathrm{e}^{-1}(1+i\tilde{\Omega}_\mathrm{d})$ and

$$r(\tilde{\Omega}_\mathrm{d},\tilde{\delta}_e) = -\tilde{\delta}_e^4 - 2i\tilde{\delta}_e^2\tilde{\Omega}_\mathrm{d} + (\tilde{\delta}_e^3-\tilde{\delta}_e^2+4)\tilde{\Omega}_\mathrm{d}^2, \tag{2.47}$$

$$r^*(\tilde{\Omega}_\mathrm{d},\tilde{\delta}_e) = -\tilde{\delta}_e^4 + 2i\tilde{\delta}_e^2\tilde{\Omega}_\mathrm{d} + (\tilde{\delta}_e^3-\tilde{\delta}_e^2+4)\tilde{\Omega}_\mathrm{d}^2. \tag{2.48}$$

In the above, $w(z) = e^{-z^2}\mathrm{erfc}(-iz)$ is the Faddeeva function, the properties of which can be consulted in Appendix B. Without external magnetic field, $\Omega_\mathrm{d} = 0$, solutions described by Eqs. (2.45) and (2.46) are undefined, and the following analytical solutions can be used:

$$B_\omega = 0, \tag{2.49}$$

$$A_\omega = \frac{1}{3}+\frac{4}{3\tilde{\delta}_e^2}-\frac{4}{3}\frac{\sqrt{\pi}}{\tilde{\delta}_e^3}w(i\tilde{\delta}_e^{-1}). \tag{2.50}$$

Some spectra calculated with Eq. (2.42) in a low-doping regime where there is no short-range hopping ($\nu_\mathrm{j} = 0$) are shown in Fig. 2.4. The line profile becomes Gaussian if the release mechanism is turned off ($\nu_\mathrm{r} = 0$). In effect, this brings us back to Ref. [62]. If the release rate ν_r is large compared to the hyperfine relaxation measured by δ_e, and CB spin relaxation is neglected ($\nu_\mathrm{CB} = 0$), it becomes Lorentzian. The situation is analogous to motional narrowing induced by interdonor hops. Conversely, if CB spin relaxation is efficient to the point that spin coherence is completely lost during a single jump, the spin noise line takes the form of a Voigt profile. In intermediate regimes, the line profile deviates from these well-known spectral functions.

In Fig. 2.5, the spin relaxation rate τ_s^{-1} extracted from the spin noise linewidth is plotted as a function of the release rate ν_r for several values of $\delta_\mathrm{e}/\nu_\mathrm{j}$. At small values of ν_r, the spin relaxation rate is reduced by motional narrowing as ν_j increases. A narrowing of the spin noise line is also observed as ν_r increases, provided that direct hops are not very frequent (ν_j is small compared to δ_e). This is important, as increasing ν_r also leads to an increase of the CB contribution to spin relaxation. The behavior at asymptotically large release rates is such that the spin relaxation rate is equal to $\nu_\mathrm{r}\nu_\mathrm{CB}/\nu_\mathrm{t}$, provided that we are in the regime of short trapping time $\Omega_\mathrm{c}\nu_\mathrm{t}^{-1} \ll 1$, and spin relaxation in the CB is weak $\nu_\mathrm{CB}/\nu_\mathrm{t} \ll 1$.

In the short trapping time regime, the spin noise lineshape is Lorentzian and the spin relaxation time is inversely proportional to the linewidth. In this regime, increasing the trapping time does not affect the lineshape and linewidth so long as the ratio $\nu_\mathrm{CB}/\nu_\mathrm{t}$ is kept constant. Outside this regime, the shape of the spin noise line is determined not only by the ratio, but also by the trapping time itself. This is illustrated in Fig. 2.6, where spectra are calculated in a regime where short-range hopping leads to a significant motional narrowing of the spin noise line, and the linewidth is dominated by the CB contribution to spin relaxation (this corresponds to our measurements on samples MX77 and MX78, see Section 2.6.3). The black curve corresponds to the short trapping time regime, where the lineshape is Lorentzian. As ν_t increases, the line deviates from a Lorentzian shape via the appearance of wings. At very long trapping times, the spin noise line resembles two superimposed Lorentzian curves, though we stress that the parameters of a two-Lorentzian fit do not directly yield any relevant parameters.

2.4.2 Results

The spatiotemporal spin noise spectrum (2.42) has a complicated mathematical structure, though the physics behind it are quite clear. A compact approximate solution can be presented in the form

$$S_{zz}(q,\omega) = \frac{1}{\pi}\frac{R(\omega)}{1 - J(q,\omega)R(\omega)} + \text{c.c.}, \tag{2.51}$$

where c.c. denotes the complex conjugate. The solution normalized to unit area in the angular frequency domain. It has the mathematical form usually encountered for an interplay between hopping and hyperfine interaction [22, 62, 239, 240]. $J(q,\omega)$ is the dynamical jump structure factor,

$$J(q,\omega) = \sum_{\zeta} \bar{R}_{\zeta}\nu_{\text{j}}^{\zeta}F_q^{\zeta} + \nu_{\text{r}}\nu_{\text{t}}^{-1}\text{T}_{q,\omega}^{-1}T_B(q,\omega), \tag{2.52}$$

where ζ enumerates the different types of direct spin jumps between donors, and

$$T_B(q,\omega) = \left(1 + \Omega_{\text{c}}^2\text{T}_{q,\omega}^2\right)^{-1} - i\Omega_{\text{c}}\text{T}_{q,\omega}, \tag{2.53}$$

$$\text{T}_{q,\omega}^{-1} = -i\omega + \nu_{\text{CB}} + \nu_{\text{t}}l_{\text{s}}^2q^2 + \nu_{\text{t}}, \tag{2.54}$$

with $\text{T}_{q,\omega}^{-1}$ being the spin lifetime in the CB (2.40) assuming $D = \nu_{\text{t}}l_{\text{s}}^2$. The first term in Eq. (2.52) is the contribution from hopping between donors. We consider two terms indexed by ζ: spin-exchange between two occupied donors (ζ = HF), and electron hopping from an occupied donor to an unoccupied one (ζ = MA). The jump frequencies $\nu_{\text{j}}^{\zeta} = \sum_k W_{ki}^{\zeta}$ are the same for each site i. Spin relaxation induced by SOC at each hop is described by $\bar{R}_{\zeta} = 1 - \frac{1}{3}\frac{l_{\zeta}^2}{L_{\text{SO}}^2}$, where L_{SO} is the spin orbit length and l_{ζ} is the mean-square hopping distance of the ζ mechanism. F_q^{ζ} is the hopping structure factor, i. e., it is the normalized jump rate $W_{ik}^{\zeta}/\nu_{\text{j}}^{\zeta}$ in reciprocal space (discussed in more detail in Section 2.6). The second term in Eq. (2.52) is the contribution from jumps though the CB. Due to the finite time spent in it, contrary to the instantaneous hops between donors, it has the spectral signature $\text{T}_{q,\omega}$ of the CB electron spin dynamics.

Equation (2.51) is exact as long as there are no external magnetic field applied, $\Omega_{\text{d}} = \Omega_{\text{c}} = 0$. In this case

$$R(\omega) = \tau_{\omega}A_{\omega}, \tag{2.55}$$

where $\tau_{\omega}^{-1} = -i\omega + \nu_{\text{s}} + \nu_{\text{r}} + \nu_{\text{j}}$, and

$$A_{\omega} = \frac{1}{3} + \frac{4}{3(\delta_{\text{e}}\tau_{\omega})^2} - \frac{4}{3}\frac{\sqrt{\pi}}{(\delta_{\text{e}}\tau_{\omega})^3}w(i/\tau_{\omega}\delta_{\text{e}}). \tag{2.56}$$

The properties of this solution without accounting for CB diffusion are well-documented in Ref. [62]. Equation (2.51) also happens to be a very good approximation in transverse external fields much larger than the nuclear fields, $\Omega_{\text{d(c)}} \gg \delta_{\text{e}}$. Then, one must take

$$R(\omega) = \frac{\sqrt{\pi}}{\delta_{\text{e}}}w\left(i[\tau_{\omega}^{-1} + i\Omega_{\text{d}}]/\delta_{\text{e}}\right). \tag{2.57}$$

Equation (2.51) is then very useful for discussing the spin relaxation time τ_{s} of donor-bound electron spins, since it covers both experiments in zero field and in Voigt geometry. Following the definition of T_2^* by Bloembergen in Ref. [63] [4], we introduce the damping parameter Γ_q as

[4] This is not to be confused with the spin dephasing time, though in the original article [63], the T_2^* estimate through the amplitude of the area-normalized spectral function was indeed introduced to discuss all contributions to the line broadening.

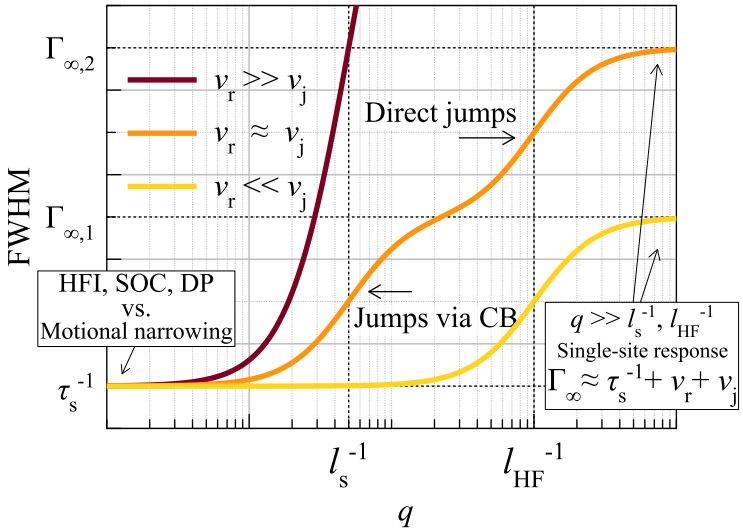

Figure 2.7: An illustration of the different types of linewidth dispersion in n-CdTe at low to moderate doping contained within the two-state spin jump model [Eqs. (2.16-2.17)]. The three theoretical curves correspond to different values of the release rate ν_r, which is thermally activated. At low temperatures, the role of conduction band (CB) jumps is subdued, and short-range hopping between donors is the dominant mechanism (yellow curve). In the opposite case, when temperature is relatively high, long-ranged jumps via the CB are more prevalent (dark red curve). In intermediate conditions, both mechanisms can be observed (orange curve). Different areas of the linewidth dispersion curve permit experimental determination of different model parameters. Near $q = 0$, the interplay between HFI, SOC, DP relaxation with motional narrowing determine the width and shape of the spin noise line. At $q \gg l_\mathrm{s}^{-1}, l_\mathrm{HF}^{-1}$, we have the single-site response [22], where every escape mechanism contributes to the broadening of the Lorentzian line. Our implementation of AR-SNS permits measuring spin noise spectra in CdTe up to $q > l_\mathrm{s}^{-1}$, enough to observe both the CB and direct contributions in the moderately-doped sample MX77.

a measure of the spin noise linewidth by departing from Eq. (2.52):

$$\begin{aligned}\Gamma_q =& \mathrm{Re}\left\{R^{-1}(\omega)\Big|_{\omega=\Omega_\mathrm{d}} - J(q,\omega)\Big|_{\omega=\Omega_\mathrm{c}}\right\} \\ =& \frac{\delta_\mathrm{e}}{\sqrt{\pi}}\left\{w\left(i[\nu_\mathrm{s}+\nu_\mathrm{r}+\nu_\mathrm{j}]/\delta_\mathrm{e}\right)\right\}^{-1} - \sum_\zeta \nu_\mathrm{j}^\zeta F_q^\zeta - \nu_\mathrm{r} \\ &+ \frac{1}{3}\sum_\zeta \frac{l_\zeta^2}{L_\mathrm{SO}^2}\nu_\mathrm{j}^\zeta F_q^\zeta + \nu_\mathrm{r}\frac{\nu_\mathrm{CB}\nu_\mathrm{t}^{-1} + l_\mathrm{s}^2 q^2}{1+\nu_\mathrm{CB}\nu_\mathrm{t}^{-1} + l_\mathrm{s}^2 q^2},\end{aligned} \tag{2.58}$$

assuming short trapping times $\Omega_\mathrm{c}\nu_\mathrm{t}^{-1} \ll 1$. For a Lorentzian lineshape, Γ_q is exactly equal to the half-width at half-maximum (HWHM). For a Gaussian lineshape, the parameter underestimates the HWHM by around 30% due to the faster decay of the wings. The linewidth dispersion curves implied by Eq. (2.58) in different regimes are illustrated in Fig. 2.7. The spin relaxation time

is given by $\tau_s = \Gamma_{q=0}^{-1}$, i. e.

$$\begin{aligned}\tau_s^{-1} =& \frac{\delta_e}{\sqrt{\pi}} w^{-1}\left(i[\nu_r + \nu_j + \nu_s]/\delta_e\right) - \nu_j - \nu_r \\ &+ \frac{1}{3}\sum_\zeta \frac{l_\zeta^2}{L_{SO}^2}\nu_j^\zeta + \frac{\nu_r}{\nu_t}\frac{\nu_{CB}}{1+\nu_{CB}\nu_t^{-1}}.\end{aligned} \tag{2.59}$$

In Eqs. (2.58-2.59), $\nu_j = \sum_\zeta \nu_j^\zeta$ is the total jump rate due to both HF and MA mechanisms. In Eq. (2.59), the first term corresponds to the ensemble average of individual sites and contains the broadening due to hyperfine interaction, spin jumps, and intrasite relaxation. It approaches $\delta_e/\sqrt{\pi}$ when the hyperfine relaxation dominates, i. e., $\delta_e \gg \nu_r + \nu_j + \nu_s$. In the opposite limit it simply tends to $\nu_r + \nu_j + \nu_s$. The second and third terms describe motional narrowing. The fourth and fifth terms are the broadening resulting from spin relaxation acquired during jumps via the SOC and DP mechanisms, respectively. Evidently, CB jumps with DP spin relaxation act in much the same way as hopping and SOC between donors, but at a different spatial scale, similarly to what was seen with the simple model in Section 2.2. These effects can narrow or broaden the spin noise line beyond the interplay of hopping and HFI. As the wavevector is increased, F_q varies from unity at $q = 0$ to zero at $q = \infty$. Hence, the broadening dispersion is given by $\Delta\Gamma(q) = \Gamma_q - \tau_s^{-1}$, and results from suppression of the dynamical averaging of the nuclear field.

It is made clear by Eq. (2.59) that the free state partly shares its spin relaxation with the localized state, in proportion to the "population ratio" given by ν_r/ν_t. We use the parentheses in reference to Section 2.4 (see also 1.2.4), where we have discussed in detail the renormalization of the trapping rate. That is to say, the ratio ν_r/ν_t can be far from zero if the traps are sparse, even if there are very few itinerant electrons. Efficient spin mixing and cross-relaxation between localized and itinerant states has been first proposed and experimentally evidenced by Paget [85], and the underlying mechanism is usually thought to be spin-exchange scattering [88]. If the spin mixing mediated by thermal fluctuations or spin-exchange scattering is fast enough, the average magnetization of each of the two states become equal, which is particularly relevant in measurements of DNP as discussed in Section 1.6.1. Additionally, the observed spin relaxation rate becomes the weighted average of the relaxation rates of the two states [84, 90, 105]. This assumption has been used in Ref. [93] to reproduce the temperature dependence of the short spin relaxation times measured by Sprinzl *et al.* [249] at $n_d = 4.9\times10^{16}$ cm^{-3} and high density of photo-excited carriers. Although the temperature dependence was quite well reproduced, the spin relaxation of the localized state was left as a fitting parameter. More recently, in n-type GaAs at doping densities around the MIT, weighting the relaxation rates of the free and localized states by the degree of free and localized electrons in the respective states has led to impressive quantitative agreement between calculations and measurements [84]. Depending on the different weight and relaxation rates, the spin relaxation time is shortened or extended as the temperature or doping changes. Such a weighting should no longer hold if there exists a spin relaxation mechanism that is faster than the spin mixing. Another complication arises if the dominant mechanism of line broadening is the hyperfine interaction, as in this case the weighting does not account for motional narrowing induced by a reduction of the correlation time via the spin release rate ν_r, as described by Eq. (2.59) and as interpreted in [86]. A more involved model, such as the one we present, could fill in these gaps.

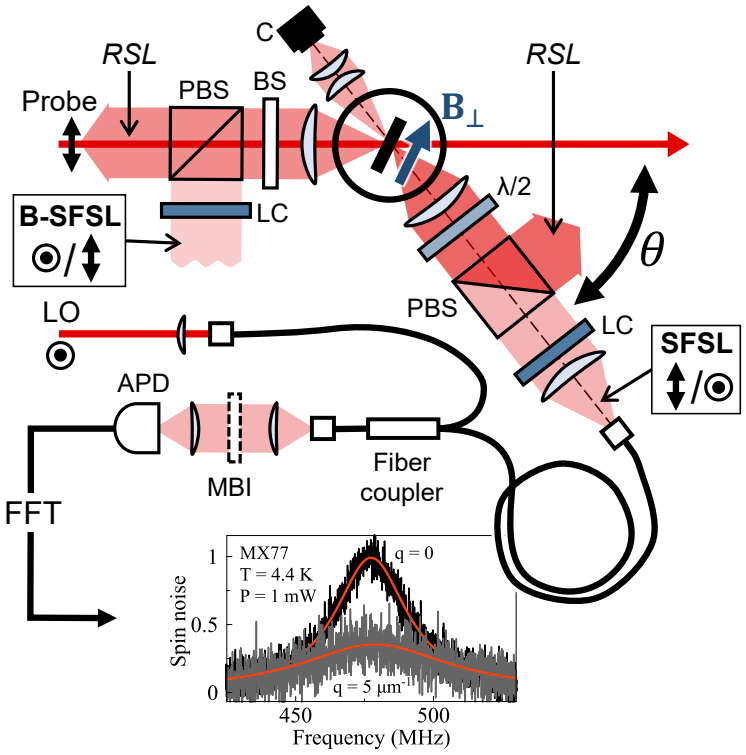

Figure 2.8: Experimental implementation of angle-resolved spin noise spectroscopy (AR-SNS) using a collection arm mounted on a rotation stage and homodyne detection. The spin flip-scattered light (SFSL) is collected at angle θ that determines the wavevector q of observed spin fluctuations. Backscattered SFSL (B-SFSL) is used to supplement the measurements with a single measurement at large q. The Rayleigh-scattered light (RSL) is filtered out using polarizing beamsplitters (PBS). Liquid crystal variable phase plates (LC) and the Babinet-Soleil compensator (BS) allow for polarization correction and modulation. Detection is performed by an avalanche photodiode (APD), after which the signal is digitized, Fourier transformed, and analyzed. The camera (C) and removable mirror for back illumination (MBI) permit efficient alignment of the probe beam and local oscillator (LO) on the sample.

2.5 Experimental

We are now well-equipped to discuss AR-SNS experiments, hence we will discuss the experimental implementation of this technique that we briefly mentioned at the end of Section 1.5.

2.5.1 Experimental setup

As shown by Gorbovitskii and Perel, the formation of the spin noise signal is microscopically a result of coherent spin-flip Raman scattering [210]. Therefore, SNS can be viewed as essentially another way of detecting spin-flip scattered light. In fact, it only differs from spin-flip Raman spectroscopy (SFRS) by the method of detection. SFRS is the spectroscopy of the light field amplitude, while SNS is the spectroscopy of the field intensity. This leads to some intriguing properties of SNS as compared to SFRS, which are well explained in Ref. [211]. Here, however, we are primarily interested in the enhanced frequency resolution afforded by the application of a fast Fourier transform (FFT) spectrum analyzer, which cannot be rivaled by optical SFRS.

The spin-flip scattered light (hereafter scattered light) is measured with a homodyne detec-

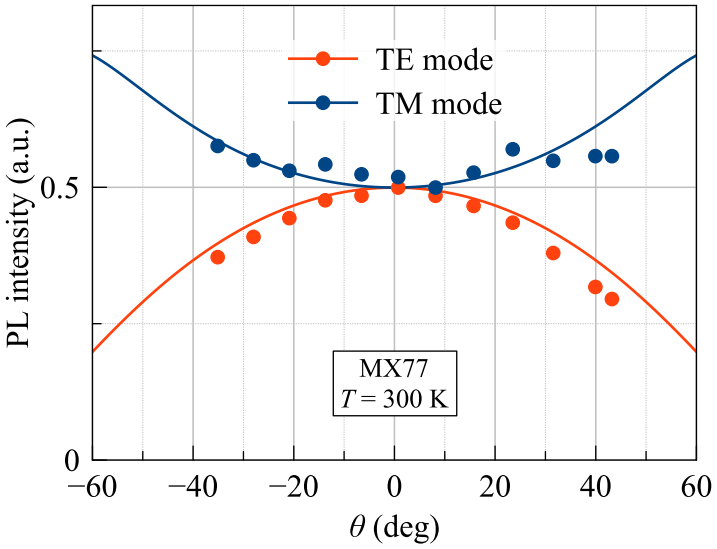

Figure 2.9: Dependence of PL intensity on the angle of detection shown for two orthogonal PL polarizations: TM is parallel to the plane of incidence of the PL ray, and TE is perpendicular. Overall, the luminescence is unpolarized, hence the two intensities coincide at $\theta = 0$. The angle dependence of PL transmission from within the sample is well-described by Fresnel equations written for the transmission of the two modes through the cryostat window (refraction index $n = 1.5$), and the sample-vacuum interface, assuming a refraction index $n = 3 + 5i$ for the sample.

tion scheme in Voigt geometry. A schematic representation of our setup is shown in Fig. 2.8. The linearly polarized beam from a Toptica DL Pro laser tuned to 782 nm is split into the probe beam and the local oscillator (LO). The wavelength is chosen so as to be below the neutral donor The probe is spatially filtered with a polarization-maintaining monomode fiber before being focused onto the sample by a lens with focal length 10 cm. For spin noise measurements without balanced detection, it is very important to ensure sufficient extinction of the probe. Imperfect extinction leads to uneven offsets in polarization modulation experiments, which makes the interpretation more difficult, especially when studying fine details such as the lineshape. Achieving good extinction by tuning a linear polarizer is complicated by the weak but inescapable birefringence of the sample. Therefore, a variable wave plate (Babinet-Soleil compensator, BS) is inserted before the sample, so that the polarization of the incident beam can be altered to compensate for the sample's birefringence. The collection arm is equipped with a cage system hosting an antireflective-coated lens (10 cm focal length) fixed to a translation stage with an adjustable mount, a polarizing beamsplitter to eliminate Rayleigh-scattered laser light, a liquid crystal phase modulator to enable polarization-modulated measurements, and a fiber port[5]. The scattered light is collected in a numerical aperture ~ 0.06 corresponding to a wavevector resolution of about 0.15 µm^{-1}.

The magnetic field $B \sim 20$ mT is applied by using permanent magnets mounted on a delay line to facilitate field modulation experiments, typically in Voigt geometry, i. e., the field is

[5]It is often the case that collecting light, especially scattered light, into a monomode fiber results in large losses. This is not true for the spin-flip scattered light in our case. The spatial mode on the sample is already obtained from the output of an essentially identical monomode fiber, and therefore matches the spatial mode of the collection fiber, resulting in efficient collection. This was checked by comparing the signal obtained by homodyne detection in free space, and that obtained by collecting the spin-flip scattered light into the monomode fiber. No noticeable signal loss was found.

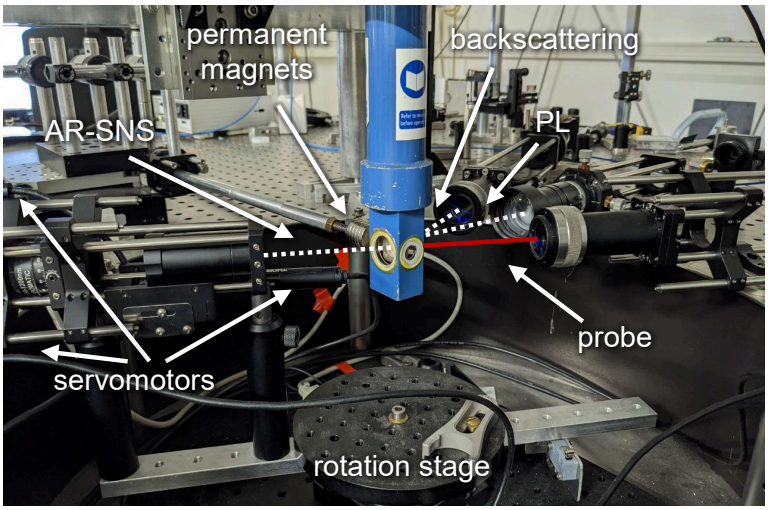

Figure 2.10: Photograph of a part of the experimental setup showing the sample in the cold finger cryostat, the permanent magnets used to subject the sample to a weak transverse field, and the optics that focus the probe beam onto the sample and allow the collection of photoluminescence and spin-flip scattered light. The angle of the AR-SNS collection arm with respect to the probe beam is adjusted by controlling the rotation stage. To ensure that AR-SNS measurements are obtained from the same point of the sample, servomotors are introduced to compensate for the imperfections of the rotation stage, see text.

normal to the incident probe beam. These were chosen for optimal stability, as resistive coils lead to undesirable thermal expansions which affect beam alignment. The field is calibrated by comparing to data obtained with a set of Helmholtz coils. The calibration loses accuracy over several beam realignments. Since precise g-factor measurements are outside the scope of this work, and electron spin relaxation is field-independent in such weak fields, the precision of this calibration is sufficient.

A cold finger cryostat is used to keep the sample at low temperature. The copper sample holder has a horizontal slit to permit transmission of scattered light. The sample is fixed onto the sample holder using silver paint, but it is glued only on one side of the slit to minimize strain. This has the drawback of significantly worsening thermal contact, which leads to lackluster thermalization of the sample lattice (see discussion in Section 2.6).

As explained previously, varying the incidence angle of the probe is not ideal for AR-SNS, as the intensity incident on the layer varies with the incidence angle for two reasons: the geometric factor arising from the changing spot size, and the angle-dependent Fresnel coefficients. To combat the former, the incidence angle is kept fixed, and the collection angle is varied. The effect of Fresnel coefficients is inescapable unless one is dealing with a spherical sample. For our planar samples, the magnitude of the effect is illustrated in Fig. 2.9 by the dependence of PL intensity on the angle of detection. One would expect the same picture for spin-flip scattered light, as it is also isotropically distributed. In experiments, the probe incidence is chosen to be as far from normal as possible. This ensures access to greater angles while varying only the angle of detection (see the illustration in Fig. 2.8), which leads to a broader range of accessible wavevectors. The spin-flip scattered light is gathered at an angle θ by a collection arm which is mounted on a rotation stage. The wavevector q of the probed spin fluctuations is related to θ by a simple formula, $q \approx \frac{4\pi}{\lambda}\sin(\theta/2)$. This provides a simple way to find the upper bound of the wavevector range accessible by AR-SNS. Setting $\lambda = 782$ nm and $\theta = \pi$, we find $q < 16\ \mu\text{m}^{-1}$. In reality, we have $q \lesssim 10\ \mu\text{m}^{-1}$, since the maximum angle between the

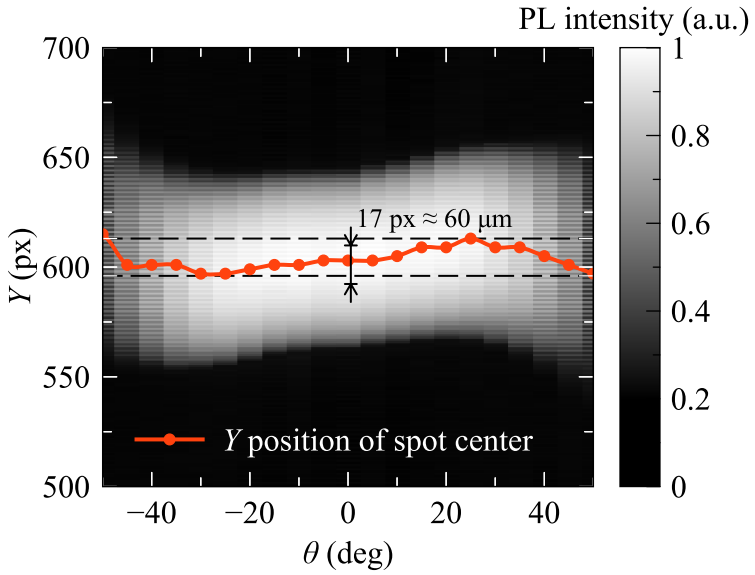

Figure 2.11: Colormap showing the horizontally integrated PL intensity as a function of vertical coordinate Y in pixels and incident angle θ, recorded with CS165MU camera (pixel size 3.45×3.45 µm^2). The probe beam is passed from a fiber fixed inside a cage system coupled to a rotation stage. Note the vertical "wobble" of the PL spot. The horizontal coordinate of the spot (the X position of the spot center) is stable.

probe and detection directions is limited by $\theta_{\max} \lesssim \pi/2$. This limitation is largely due to the geometry of the cryostat. A photograph of the setup is shown in Fig. 2.10, where the collection arm is set to $\theta = 0$. At $\theta = \theta_{\max}$, the collection arm is positioned with the same angle of incidence on the sample, but impinging from the other side.

The alignment for optimal collection of spin-flip scattered light is generally performed using PL produced by back-illumination, which is made to overlap with the probe beam on the sample. The impurity-related PL is collected through a notch filter centered at 820 nm, allowing the alignment to be carried out at the same probe wavelength as AR-SNS measurements. The PL is monitored in real-time with a CMOS camera, the linear spot size is around $20 - 25$ µm. In particular, the quality of the rotation stage was tested by placing the CMOS camera in place of the sample and tracking the position of the spot as a function of the incidence angle. The position of the spot was found to be stable along the X axis, while an oscillating behavior was observed for the Y coordinate. Integrating the images over the horizontal coordinate, we obtain the data presented in Fig. 2.11, showing significant "wobble" along the vertical axis. The "wobble" is greater than the spot size used in experiments. To compensate for this, i. e., to ensure that the scattered light is collected from the same spot on the sample, servomotors are mounted on the collection arm. For each value of the incident angle, the spot is recentered to the vertical coordinate at normal incidence, $\theta = 0$. The respective servomotor positions are recorded, spline-interpolated, and used automatically afterwards. A photograph of the central part of the experimental setup is shown in Fig. 2.10. For backscattering measurements, the detection path is different from the AR-SNS path shown in Fig. 2.8, and the scattered light and the LO are recombined in free-space. The wavevector resolution of these measurements is the same as for AR-SNS, about 0.15 µm^{-1}.

Homodyne detection of spin fluctuations is performed by an avalanche photodiode (APD, Menlo Systems APD210). The spin-flip scattered light collected at angle θ (wavevector q) is mixed with the LO on the surface of the detector, and the resulting signal from the APD is

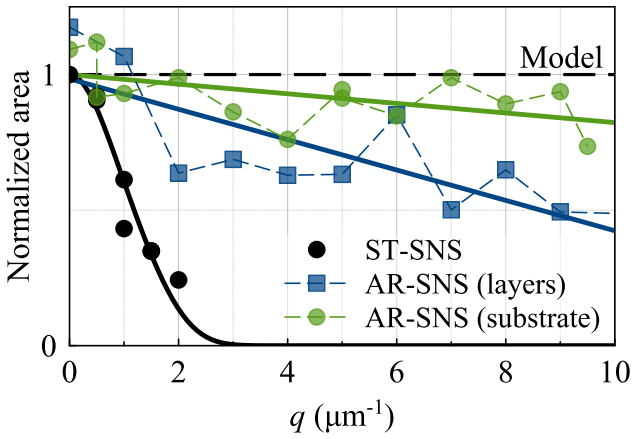

Figure 2.12: Signal amplitude dependence on wavevector in sample MX77 measured by homodyne detection, probe power 3 mW. Green circles: $T_e = 6$ K, probe impinges on substrate. Blue squares: $T_e = 4.4$ K, probe arrives directly at epitaxial layers. Black circles: $T_e = 10$ K, ST-SNS setup with fixed objective [181, 250]. Solid green and blue lines are linear regressions of the data, the solid black line is a fit taking into account the optical transfer function of the fixed objective. The two-state model predicts a wavevector-independent area (dashed black line). Data is normalized so that the fitted area is equal to unity at $q = 0$.

recorded and Fourier-transformed in real-time by an AC240 acquisition card. As a result, one obtains a spatiotemporal spin noise spectrum [22, 181]. Two types of spin noise measurements were implemented: polarization-modulated and field-modulated. In the former type, one acquires interlaced spin noise spectra with matching (S_{sn}) and orthogonal (S_{ref}) polarizations of spin-flip scattered light and the LO. The latter does not contain the spin noise contribution. The two spectra are subtracted from one another, normalized by their sum, and the result is averaged, thereby improving the signal-to-noise ratio. In Voigt geometry, the resulting polarization-modulated spectrum normally presents as a single peak at Larmor frequency. About 15 μW of LO power are incident on the detector, which is enough to overcome the intrinsic noise equivalent power of the APD. Nevertheless, electronic noise has a non-negligible effect on spin noise spectra. Before each series of measurements, a "dark" spectrum S_{dark} is taken, so that the resulting spin noise spectra could be normalized relative to the photon shot noise. In our experiments, the amplitude of the spin noise contribution is of the order of 1% in units of photon shot noise. The final spin noise spectra as presented in this work are calculated as $(S_{sn} - S_{ref}) / (S_{sn} + S_{ref} - 2S_{dark})$.

Field-modulated experiments are based on the same principle, but the difference spectrum is acquired using two different values of the transverse field. Such experiments are substantially slower because, though the field switching is automated, the permanent magnets are physically moved by an improvised translation stage (see Fig. 2.10), and each move takes several seconds. Nevertheless, it is a useful alternative in $q \approx 0$ experiments, as imperfect extinction often leads to a non-flat background in polarization-modulated experiments due to a part of the probe beam impinging on the detector. Field-modulated experiments result in spectra that contain a positive peak and a negative peak, their frequencies corresponding to the two field values chosen. All else being equal, polarization- and field-modulated experiments yield identical lineshapes.

2.5.2 Samples & experiments

Four bulk n-CdTe samples grown by molecular beam epitaxy were studied. The structure of the four samples is the same: the Al-doped CdTe layers are 10 µm thick, separated by a 40 nm CdTe buffer layer from the $Cd_{0.96}Zn_{0.04}Te$ substrate. The small density of Zn atoms is required to ensure high structural quality of the epitaxial CdTe, but leads to significant absorption of the signal in the substrate. The nominal doping densities are $n_d = 2\times10^{14}$ cm^{-3} (M3460), $n_d = 4\times10^{15}$ cm^{-3} (MX77), $n_d = 2\times10^{16}$ cm^{-3} (MX78) and $n_d = 1\times10^{17}$ cm^{-3} (MX79). In the four samples, the average distances between donors varies roughly between 4 Bohr radii to 32 Bohr radii. There is also unintentional p-doping across all samples. Though weak, it must be accounted for at low temperatures due to the importance of charged impurity scattering of electrons. The samples are non-metallic (the Mott density $n_{Mott} \approx 2\times10^{17}$ cm^{-3} in CdTe).

As mentioned previously, the probe beam is tuned to 782 nm, that is, several meV below the donor-bound exciton resonance D^0X (1.5926 eV), where absorption is weak but present. This ensures that the spin-flip scattered light is collected from localized spins. The sample transmission at this wavelength was typically about 30%. Throughout the experiments, the incident power from the probe was in the range between several tenths of a mW to several mW. In principle, without extrapolating to zero probe power, the measurements cannot be considered non-perturbative [251]. However, the main effect of the probe beam seems to be a slight heating of the sample, without noticeable qualitative changes in the spin relaxation (see 2.6.2).

In Refs. [22, 181], where a static imaging system was used, the primary cause of signal amplitude deterioration starting at $q \approx 1-2$ µm^{-1} was the wavevector cutoff effect, caused by the finite aperture of the static imaging system [181]. By employing a rotating collection arm to select light scattered at different wavevectors, we avoid this limitation, achieving a 5-fold increase of the accessible wavevector range. However, some variance in signal amplitude versus the angle of detection is inevitable. For example, it is impossible to eliminate the effects of angle-dependent Fresnel coefficients and absorption of signal in substrate, see Fig. 2.12 and the previous Section.

To mitigate substrate absorption, virtually all measurements on MX77 were performed with the probe impinging the layer side of the sample, otherwise the backscattering signal was too weak. Even so, throughout this work the limiting factor for large wavevector measurements is rather the detector bandwidth, around 1 GHz, which forbids measurements when the spin noise linewidth exceeds $300-400$ MHz. This includes, for example, all measurements with $q \gtrsim 5$ µm^{-1} in the highest doped MX79 sample, including the backscattering.

We focused our experimental efforts on measuring linewidth dispersion curves for all listed samples at various temperatures, with the goal of obtaining data similar to the theoretical curves presented in Fig. 2.7. Although previous measurements on the M3460 sample were well-understood within a one-state spin jump model (see Ref. [22]), the data on samples MX77 and MX78 turn out to be in strong disagreement with it, both in terms of linewidth dispersion and lineshape. All the differences are accounted for by applying the two-state model with DP relaxation in the CB.

Table 2.1: CdTe parameters identical for all samples. Where several values are shown, the values in bold are those used in the calculations. m_0 is the free electron mass.

Parameter name	Symbol	Value
Effective mass	m_e^*	$0.11m_0$ [a]
Dielectric constant	ϵ	10.2 [b]
Donor Bohr radius	a_B	4.91 nm
Bandgap	E_g	1.606 eV [c]
Donor binding energy	E_b	14.2 ± 0.5 meV [d]
Activation energy	E_a	8 meV [e]
Spin-orbit constant	α_{so}	0.053 [f]
		0.073 [g]
		0.079 [h]
DP scattering parameter	Q	2.7 [i]
Precession frequency	δ_e	1.03×10^8 s^{-1} [h]
		$\mathbf{1.58 \times 10^8}$ s^{-1} [j]
Attempt-to-escape frequency	ν_{r0}	2.40×10^{11} s^{-1} [e]
HF scaling constant	ξ	0.8 [h,k]
		0.57 [e]

[a]Ref. [252]; [b]Ref. [253]; [c]Ref. [254]; [d]Ref. [255]; [e]This work; [f]Ref. [256]; [g]Ref. [257]; [h]Ref. [83]; [i]Ref. [258]; [j]Ref. [22]; [k]Ref. [68].

2.6 Results and discussion

2.6.1 Modeling details

The foundation of the model is formed by multiple parameters. However, most of them are either well-known or interdependent. The parameters common to the entire ensemble of data are given in Table 2.1. Regarding the donor activation energy E_a, we have to assume a value smaller than the binding energy in order to obtain satisfactory fits. This is consistent with the reduction of the gap between impurity states and the CB with increasing doping [105, 259]. A quantitative doping dependence of E_a is not available [260], hence we fixed its value to 8 meV, identical for all samples. For the local nuclear field precession frequency distribution, we take $\delta_e = 1.58 \times 10^8$ s^{-1}, as determined directly from the shift of the spin noise spectrum in zero field [22]. This value differs noticeably from an estimation based on the not very well-known hyperfine constants [83]. For the scattering parameter Q, which enters the DP formula, we take the value adapted to scattering by screened ionized impurities in the insulating regime. This means that the scattering is isotropic, the scattering factor $\gamma_3 = 1$ [105] and $\nu = -1/2$ [258] leading to $Q = 2.7$.

The parameters that are adjusted for each set of experimental conditions are shown in Table 2.2. We stress that in each set of experimental conditions, the wavevector dependence of the spin noise lineshape is reproduced by varying only the wavevector q and keeping all parameters constant. Several CB parameters, namely, the trapping rate ν_r and the mean square spin jump length l_s, are used as fitting parameters. The CB spin relaxation rate ν_{CB} is also treated as a fitting parameter. The results are found to be in remarkable agreement with DP relaxation. The escape rates are used to determine the activation energy and the temperature T_{fit} (see Table 2.2). We are then left with two sample-dependent parameters, the

Table 2.2: Studied samples and their parameters. The doping densities n_d are the nominal parameters. The acceptor densities n_a and the HF jump length coefficients β are fitting parameters that are kept constant for each sample. It was not possible to determine β for sample M3460 due to the negligible contribution of the mechanism.

Sample	$n_\mathrm{d}(\mathrm{cm}^{-3})$	$n_\mathrm{a}(\mathrm{cm}^{-3})$	β
M3460	2×10^{14}	3.3×10^{13}	—
MX77	4×10^{15}	7×10^{13}	0.61
MX78	2×10^{16}	3×10^{14}	0.78
MX79	1×10^{17}	3×10^{13}	0.69

Table 2.3: Parameters of the two-state model listed for all experiments presented throughout the work. The probe power P and heat exchanger temperature T_r were measured experimentally, while the rest are fitting parameters. Certain parameters were not possible to determine, namely: the CB scattering length l_s for three measurements on M3460, MX78, and MX79. The former was obtained at $T_\mathrm{e} = 4.4$ K, where the dispersion curve could not be measured with sufficient precision, and for the two latter experiments, the recorded wavevector range was insufficient.

Sample	P (mW)	T_e (K)	T_fit (K)	ν_CB ($\mu\mathrm{s}^{-1}$)	ν_t ($n\mathrm{s}^{-1}$)	l_s^{-2} ($\mu\mathrm{m}^{-2}$)
M3460	5.2	4.4	11.5 ± 0.2	115 ± 15	0.11 ± 0.03	—
		9	12.2 ± 0.1	145 ± 15	0.10 ± 0.03	1.6 ± 0.4
MX77	3	6.3	13.9 ± 0.2	130 ± 40	0.25 ± 0.1	8 ± 4
		10	13.5 ± 0.1	117 ± 30	0.17 ± 0.04	6.6 ± 1.4
		14	14.6 ± 0.1	130 ± 30	0.26 ± 0.06	8.7 ± 1.6
		17	17.2 ± 0.3	120 ± 20	0.82 ± 0.33	14.4 ± 3.2
MX78	1.8	5	12.4	25	0.17	—
	2	4.4	11.8 ± 0.1	23 ± 4	0.037 ± 0.004	12.4 ± 1.6
	2	12	12.1 ± 0.2	27 ± 5	0.043 ± 0.007	11.8 ± 1.8
	2	16.7	16.7 ± 0.4	76 ± 6	0.55 ± 0.1	19.4 ± 3.2
MX79	5.7	8	14 ± 1	65 ± 5	0.50 ± 0.2	9.1 ± 4.3
		10	14.8 ± 0.3	70 ± 10	0.65 ± 0.1	—
		15	17 ± 2	90	1.75	18 ± 8

acceptor density n_a, and β. The former defines the ionized impurity scattering rate (affects the CB diffusion coefficient D and DP relaxation rate ν_DP), while the latter determines the relationship between the characteristic HF interdonor electron jump distance and the neutral donor density n_d0. Additionally, in several measurements at higher temperatures on MX78 and MX79, where we must account for the MA mechanism, we use a parameter in analogy to β. This parameter is not shown in Table 2.2 due to its rarity, but it is around 0.4 across these measurements. All other parameters entering the model are obtained by using well-known equations.

Sample thermalization

The temperature T_e measured at the heat exchanger of the cold finger cryostat is meant to reflect the real temperature of the sample T. It is not *a priori* evident, however, that $T_\mathrm{e} = T$ exactly. The sample is cooled via thermal conductivity, which depends on the thermal coupling of the sample, the sample holder, and the cold finger. Competing effects include thermal radiation

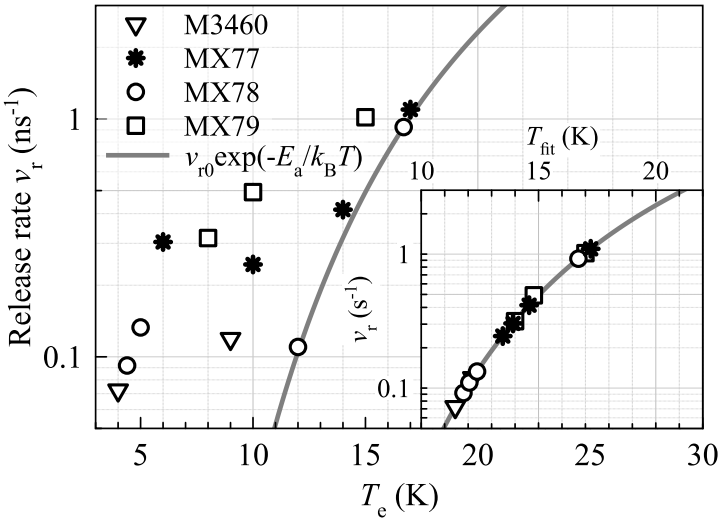

Figure 2.13: Release rate ν_r as a function of the heat exchanger temperature T_e. In the inset ν_r is plotted as a function of the fitting temperature T_{fit}. The gray line is the thermal activation function $\nu_{r0}\exp(-E_a/k_BT)$, with $\nu_{r0} = 240$ ns^{-1}.

and probe-induced heating of the sample. Indeed, analyzing the temperature dependence of the release rate ν_r as extracted from spin noise spectra fits (Fig. 2.13), we notice that ν_r is never below the activation curve $\nu_{r0}\exp[-E_a/k_BT]$ (gray curve), with an attempt-to-escape frequency $\nu_{r0} = 240$ ns^{-1}, close to the order-of-magnitude estimate of Ref. [96]. This can be viewed as a simplified version of the more rigorous expression $\nu_r = \sigma v N_c \exp[-E_a/k_BT] \approx \sigma v n_{CB}$, where σ is the donor trapping cross-section, v is the thermal velocity, N_c is the effective CB density of states, and n_{CB} is the CB electron density [73] [6]. At low power and low T_e the fitted ν_r and the activation curve never meet, indicating that the true temperatures significantly deviate from T_e. In experiments, this is observed as the spin noise spectra and the corresponding linewidth dispersions exhibiting no changes with decreasing temperature, even if we still have motional narrowing due to CB jumps. The poor thermalization is not surprising, however, as the samples were typically glued to the sample holder only on one side of the slit to avoid strain.

The higher the power, the later the fitted ν_r seem to join the activation curve, which leads one to suspect that the probe beam induces additional heating of the sample. Additional power-dependent measurements of the spin noise linewidth dispersion show that changes in probe power are well-described by increasing the model temperature. We do not discuss these results further here, as that would interrupt the flow of the presentation; the power-dependent measurements are fully discussed in Section 2.6.2.

The comparison of the release rate to the activation curve serves as an indicator of the sample temperature. In the inset of Fig. 2.13 it is plotted as a function of the fitting temperature T_{fit}. We use T_{fit} as an estimate of the true sample temperature T throughout this article.

Conduction band jumps

As we later show in Section 2.6.3, the only way to fully explain the lineshapes of the spin noise spectra and dispersion curves of samples M3460, MX77 and MX78 is to consider indirect

[6] The rigorous expression has a different temperature due to an additional $T^{3/2}$ factor in N_c, but it is unimportant when considering the small range of temperatures discussed in our experiments.

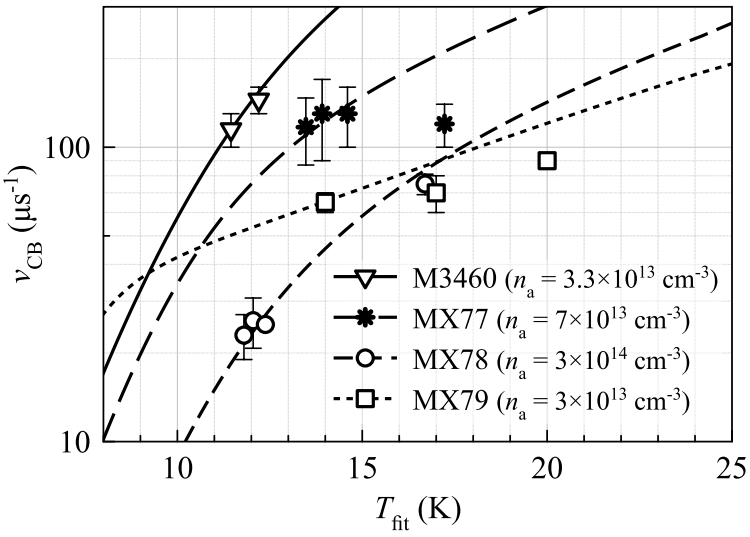

Figure 2.14: Fitted CB electron spin relaxation rates ν_{CB} plotted against the fitting temperature T_{fit} (symbols). Dyakonov-Perel spin relaxation via ionized impurities (curves) agrees well with the data, with the acceptor density n_a acting as a fitting parameter for each sample.

long-ranged spin jumps from neutral donors to ionized donors via the CB. The four parameters that characterize the CB jumps are: the conduction band spin relaxation time ν_{CB}, the release rate ν_r, the trapping rate ν_t and the scattering length l_s. The two latter parameters define the CB diffusion coefficient D. At small wavevectors $q \approx 0$, ν_{CB} and ν_t strongly influence the width and the shape of the spin noise line, as they determine the CB contribution to spin relaxation and motional narrowing. On the other hand, the linewidth dispersion curves permit the determination of l_s and ν_r: the former affects the shape of the linewidth dispersion curve, and the latter contributes to the backscattering linewidth [see Eq. (2.58) and the illustration in Fig. 2.7].

The CB spin relaxation rates ν_{CB} extracted from fitting the spin noise spectra are plotted against T_{fit} in Fig. 2.14. In order to compare these data to the theoretical ionized-impurity DP relaxation rate, we first determine the temperature-dependent ionized impurity density $n_{d+} = n_a + n_{CB}$, where the thermally activated density of carriers in the CB n_{CB} is given by the well-known relation [261]

$$\frac{n_{CB}(n_{CB}+n_a)}{n_d - n_a - n_{CB}} = \frac{N_c}{2}\exp\left[-E_a/k_BT\right], \tag{2.60}$$

where $N_c = 2(2\pi m_e^* k_B T)^{3/2}/h^3$ is the effective density of states in the CB, and E_a is the activation energy. In Fig. 2.14, we find excellent agreement with DP spin relaxation mediated by ionized impurity scattering, with the acceptor density n_a as the only adjustable parameter from sample to sample.

The obtained ionized impurity densities can also be cross-examined with both ν_t and l_s. In Fig. 2.15(a), we plot ν_t as a function of $v n_{d+}$, where $v = \sqrt{3k_BT/m_e^*}$ is the CB thermal velocity. The proportionality between ν_t and $v n_{d+}$ is indicative of a ballistic capture mechanism [103]; that is, the spin moves ballistically on the scale of a single trap. The scattering cross-section of about 1×10^{-13}cm^2 corresponds to a capture radius $r_c \approx 2$ nm, which is of the order of a_B. In panel (b) of Fig. 2.15, the trapping rate is plotted against $D_{\tau_p} n_{d+}$, where $D_{\tau_p} = \tau_p k_B T/m_e^*$ is the electron diffusion coefficient. This is consistent with the picture of diffusive trapping,

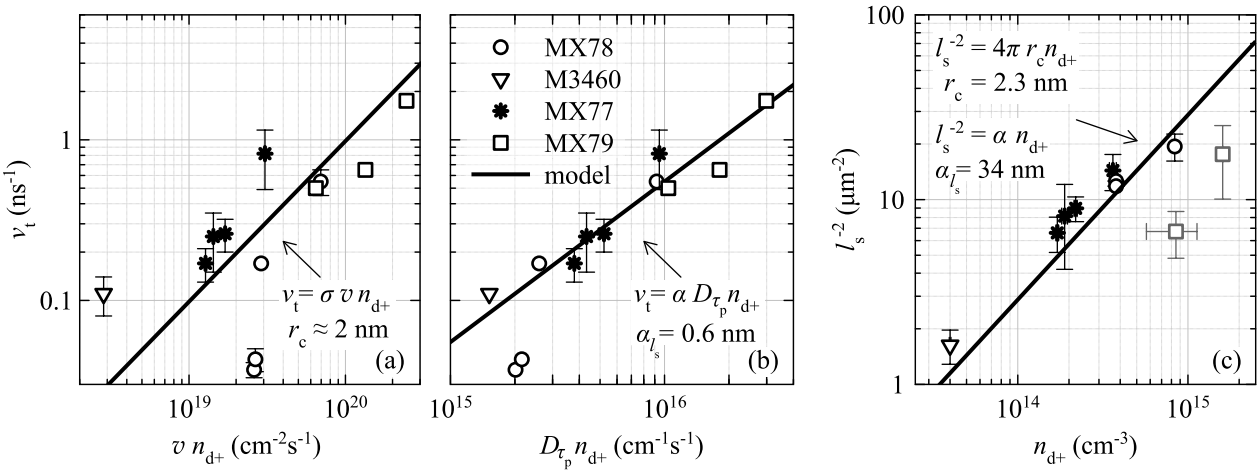

Figure 2.15: Fitted trapping rates ν_t plotted against the ionized donor density weighted by the CB thermal velocity v (a), and by the CB diffusion coefficient due to ionized impurity scattering D_{τ_p} (b). The solid curve in (a) is a fit using the ballistic trapping model, which yields a scattering cross-section $\sigma = \pi r_c^2$ that is linked to the correlation length r_c. The data in (b) is fitted by the diffusive trapping model, which uses the constant α as a fitting parameter. In panel (c), the inverse square of the CB scattering length l_s^{-2} is plotted as a function of ionized donor density n_{d+}. The data on the higher-doped MX79 are imprecise due to the weakness of the CB contribution to the spin noise signal. The remaining data can be fitted by a linear relationship which can be interpreted in terms of either ballistic or diffusive trapping [100].

when spin motion is diffusive on the scale of a single trap. We find a proportionality coefficient $\alpha_{l_s} = 0.6$ nm.

In Fig. 2.15(c), the quantity l_s^{-2} is plotted against the density of ionized impurities n_{d+}. A linear dependence is found for data measured on samples M3460, MX77 and MX78. In sample MX79, CB jumps contribute little to the dispersion curves, which leads to inaccurate determination of the scattering length. The linear dependence agrees well with the picture of electron spin diffusion and trapping by ionized impurities. In this case, the diffusing CB electron interacts with a density n_{d+} of impurities, each with linear size r_c [100]. A linear fit yields $r_c = (2.3 \pm 0.2)$ nm, which is in good agreement with the fit of Fig 2.15(b). Assuming diffusive trapping, one expects also a linear dependence, which notably includes the same coefficient α_{l_s} as in panel (b). However, we find that an optimal fit is reached with $\alpha_{l_s} = 34$ nm.

In principle, one expects ballistic capture to be the dominant mechanism in the regime $l_s \gg a_B$ observed in our experiments, as we have discussed in Section 1.2.4. Indeed, the cross-section σ we obtain is close to available data on Si [262, 263], especially acknowledging the higher binding energy of donors in Si. Somewhat surprisingly, the diffusive trapping model seems to describe the experiments equally well, though it must be considered that with diffusive trapping one expects to obtain the same parameter α in Figs. 2.15(b) and 2.15(c) due to $D = l_s^2 \nu_t$. Since this is not the case, it may be that the diffusive trapping mechanism is inapplicable, or that D_{τ_p} is not a good estimate of D, or both. We conclude that though ballistic trapping is more likely and finds better agreement with experimental data, the present measurements are not enough to exactly determine the trapping mechanism. In any case, the data shows that both ν_t and l_s^{-2} are strongly correlated to the density of ionized impurities n_{d+}, as one would expect.

Finally, it is worth looking into the relationship between ν_t and ν_r obtained across all our experiments. According to the ballistic trapping model as shown in Fig. 2.15, $\nu_t = \sigma v n_{d+} \approx$

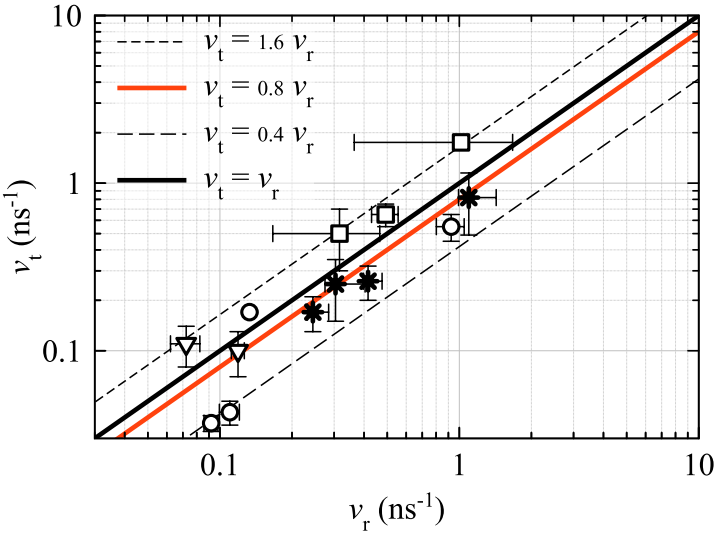

Figure 2.16: Fitted trapping rates ν_t plotted against the fitted release rates ν_r. The lines are linear fits $\nu_t = \alpha_\nu \nu_r$. From general considerations and ballistic trapping, one expects $\alpha_\nu \approx 1$ (see text), shown by the solid black line in (a), while a free fit yields $\alpha_\nu = (0.8 \pm 0.1)$ (red line), demonstrating good agreement.

$\sigma v n_{CB}$, where the approximation is valid for low electron densities. On the other hand, as we mentioned in the previous Section, $\nu_r \approx \sigma v n_{CB}$ [73]. Hence, one expects $\nu_t \approx \nu_r$, which seems to be observed in the data shown in Fig. 2.16. If we now use this result and go back to the main equation for the localized state (2.15), then neglecting relaxation we recover $\langle S_t \rangle \approx \langle S_c \rangle$. In the literature, this result is frequently attributed to efficient spin-exchange scattering between CB and localized electrons [83–88, 90–92]. However, in our experimental conditions, it seems that the release/trapping mechanism is efficient enough to establish equal average spin values in equilibrium, without the need to explicitly account for spin-exchange scattering. In the steady state, the effects of electron release/trapping and spin exchange on the average spins are indistinguishable.

Short-range hopping

The spin jumping rate W_{ij}^{HF} between two neutral donors separated by a distance $r_{ij} \gg a_B$ can be estimated by using the HF asymptotic formula for the exchange constant $J(r)$ for hydrogen-like centers

$$W_{ij}^{HF} = \xi \frac{J(r_{ij})}{\hbar} = 1.641\, \xi\, \frac{E_b}{\hbar} \left(\frac{r_{ij}}{a_B}\right)^{5/2} e^{-2r_{ij}/a_B}. \tag{2.61}$$

To take into account the random distribution of donors, usually r_{ij} is replaced by an average characteristic distance $r_c = \beta n_{d0}^{-1/3}$, with β expected to range between 0.54 and 0.8 [68]. These values of β correspond to the maxima of the Poisson distribution function of the distance to the first and third neighbor respectively. A value of 0.65, which interpolates the maxima in the distribution for nearest and next nearest-neighbors, has been used in bulk GaAs for a good fit to experimental data in the range from 4×10^{15} cm^{-3} to 2×10^{16} cm^{-3} [68, 71]. In a more recent study a value of 0.8 was used [83]. To account for the shape of the donor distribution, an additional numerical factor is generally used to reduce the hopping probability, i. e., the HF scaling constant ξ. For a sharply peaked distribution, $\xi = 1$. Throughout this work, we use the

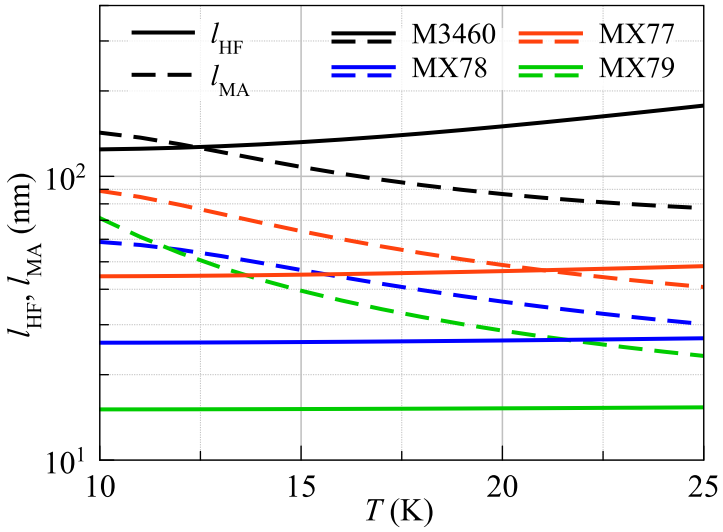

Figure 2.17: Characteristic jump lengths corresponding to mutual spin-flips of neutral donors (HF mechanism, $l_{\mathrm{HF}} = 0.7 n_{\mathrm{d0}}^{-1/3}$) and to jumps from neutral to ionized donors (MA mechanism, $l_{\mathrm{MA}} = 0.4 n_{\mathrm{d+}}^{-1/3}$) calculated via Eq. (2.60).

value $\xi = 0.57$. This was chosen so as to keep the value of β in sample MX77 constant in the studied temperature region.

In AR-SNS, the linewidth dispersion is sensitive to the spatial distribution of neutral donors through the angle-averaged structure factor $F_q = \int_0^\infty \frac{\sin(qr)}{qr} f(r)\mathrm{d}r$, where $f(r)$ is the scalar distribution of jump lengths. In the accessible wavevector range ($q \leq 48$ µs^{-1}), the linewidth dispersion due to neutral donor hopping is quadratic in samples MX78 and MX79. A very small deviation from a quadratic dispersion for this hopping mechanism would be expected in sample MX77. However, it cannot be observed for wavevectors ranging from 10 µm^{-1} to 48 µm^{-1} because of the "blind" range between AR-SNS and backscattering measurements. We are thus only sensitive to the second order Taylor expansion of the structure factor,

$$F_q \approx 1 - \bar{r^2} q^2/6, \tag{2.62}$$

$\bar{r^2} = \int r^2 f(r) dr$. We make use of the nearest neighbor distribution function of a Poisson process as the distribution of jump lengths,

$$f(r) = 3 \left[\frac{\Gamma\left(\frac{4}{3}\right)}{l_{\mathrm{HF}}} \right]^3 r^2 \exp\left(- \left[\Gamma\left(\frac{4}{3}\right) \frac{r}{l_{\mathrm{HF}}} \right]^3 \right), \tag{2.63}$$

$\Gamma(x)$ being the Gamma function and $l_{\mathrm{HF}} = \bar{r}$ the mean nearest neighbor distance. To calculate the hopping rate, we replace r_{ij} by $l_{\mathrm{HF}} = \beta n_{d0}^{-1/3}$ in the exchange constant. The broadening dispersion for Herring-Flicker mechanism, which is mainly quadratic in the wavevector and doping ranges studied, is given by

$$\Delta\Gamma_{\mathrm{HF}}(q) = \frac{\xi \Gamma\left(\frac{5}{3}\right)}{6\Gamma^2\left(\frac{4}{3}\right)} \frac{J(l_{\mathrm{HF}})}{\hbar} l_{\mathrm{HF}}^2 q^2 \approx \frac{\xi J(l_{\mathrm{HF}})}{\hbar} \frac{l_{\mathrm{HF}}^2}{6} q^2. \tag{2.64}$$

Since the maximum in the Poisson distribution is rather broad while it is narrow in the exchange constant, the simple substitution of the constant l_{HF} for r_{ij} in $J(r)$ may introduce considerable

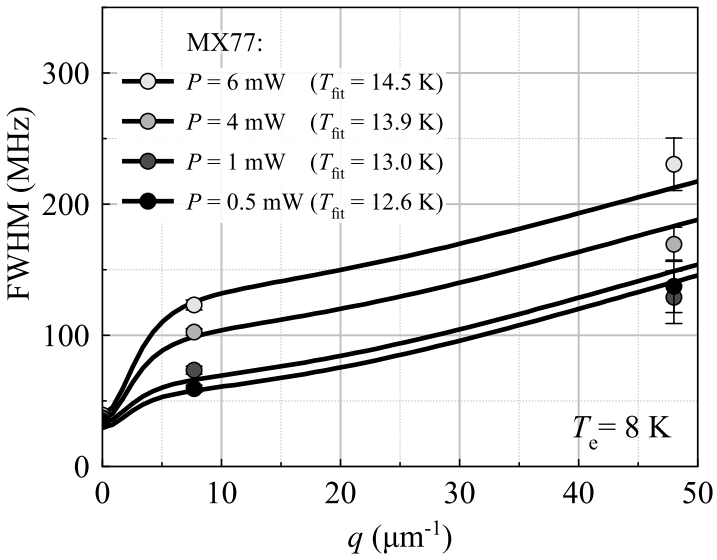

Figure 2.18: Linewidth dispersion power series measured on sample MX77 at $T_e = 8$ K for three different wavevectors $q = 0,\ 7.7,\ 48\ \mu m^{-1}$ (symbols). Only the fitting temperature T_{fit} is varied between measurements at different P. All other sample-specific parameters are the same as in Table 2.2, except for n_a, which must be taken as 4×10^{13} cm^{-3} here, perhaps due to slight inhomogeneity of compensation in the sample.

inaccuracy. However, this has the advantage of using the first moment l_{HF} of the distribution in Eq. (2.63) as the single fitting parameter in Eq. (2.64). l_{HF} is adjusted through β from one sample to another (see Table 2.2).

The same approach is used for jumps via the MA mechanism, which proceed only between ionized donors. Since $n_{d+} \ll n_{d0}$, this mechanism can typically be neglected, but becomes more important at higher doping densities and elevated temperatures. In our experiments, the mechanism appears in the $T_e = 16.7$ K series on MX78 and the $T_e = 15$ K series on MX79. In this case, the jump length $l_{MA} = \beta_{MA} n_{d+}^{-1/3}$, with $\beta_{MA} \approx 0.4$. The smaller value of the parameter may be due to the small density of ionized donors. The jump lengths calculated as $l_{HF} = 0.7 n_{d0}^{-1/3}$ and $l_{MA} = 0.4 n_{d+}^{-1/3}$ for doping and compensation corresponding to all the samples are plotted versus temperature in Fig. 2.17. The HF mechanism is relevant in every sample except M3460, and in the corresponding doping regime the inverse jump length is always greater than 20 μm^{-1}, meaning that the mechanism results in a quadratic linewidth dispersion in AR-SNS. The same is true for the MA mechanism in the regime where it becomes relevant, i. e., samples MX78 and MX79 at temperatures above 15 K.

2.6.2 Probe power and effective sample temperature

As we have mentioned in Section 2.6.1, to gauge the effects of a nonzero-power probe beam, we have performed a series of power-dependent measurements on sample MX77. This sample was chosen because at this level of doping, the interplay of direct vs. indirect hops is more sensitive to temperature changes in our experimental conditions, and as such the temperature dependence of spin noise spectra is more easily analyzed. The measurement results are shown in Fig. 2.18. Using the doping density n_d and the parameter β from Table 2.2, we model the power-dependent linewidth dispersion by a temperature-dependent evolution of parameters, which we find to be consistent with those presented in Table 2.2 for temperature-dependent

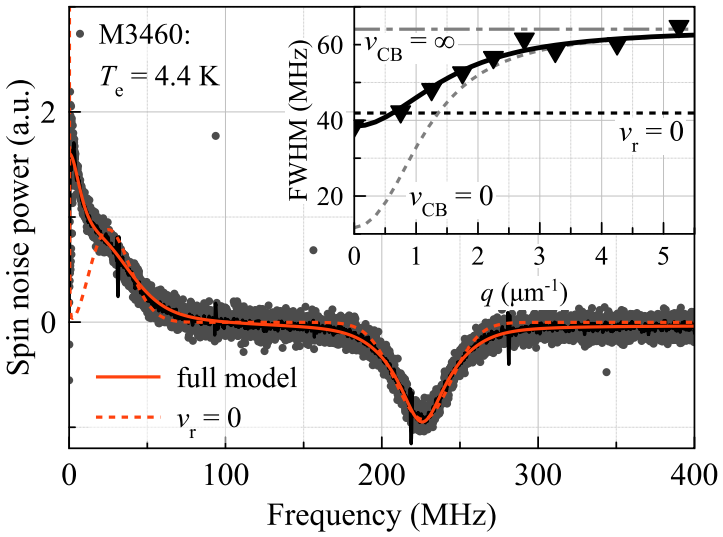

Figure 2.19: Differential normalized spin noise power spectrum (scattered dots) obtained from the difference between measurements at $B = 0$ mT and $B = 10$ mT at a temperature $T_e = 4.4$ K and $P = 5.2$ mW. The black curves are data smoothed by a Savitsky-Golay filter (second order, 10 side points over 16384), while the red lines are fits according to Eqs. (2.16-2.17) and Eq. (2.42). The smoothed data are almost totally hidden by the fit. The dashed red line is the differential spectrum calculated for $\nu_r = 0$ (note the discrepancy at low frequencies). The inset shows the wavevector dependence of the spin noise linewidth measured at $T_e = 9$ K, $P = 5.2$ mW and $B = 20$ mT, and its fit using Eq. (2.58).

series. We are obliged to choose a slightly different value for the acceptor density n_a. This could indicate that compensation is not homogeneous within the sample, which is entirely possible. We conclude that a nonzero-power probe beam affects measurements solely by introducing an additional source of heat to the sample lattice, an effect that is enhanced by the imperfect thermal contact of the sample and the cold finger.

2.6.3 Spin noise lineshapes and linewidth dispersion

We now discuss the results sample by sample, from the lowest to the highest doping. As the doping and temperature are increased, several spin relaxation mechanisms contribute successively. At the lowest doping $n_d = 2 \times 10^{14}$ cm^{-3} (sample M3460), the lineshape can be explained by considering only the interplay between the hyperfine interaction and the spin dynamics of CB electrons. At $n_d = 4 \times 10^{15}$ cm^{-3} (MX77), the hopping between neutral donors is more relevant, with a jump rate several times higher than the release rate, but both mechanisms are discriminated in the linewidth dispersion due to different characteristic lengths. At $n_d = 2 \times 10^{16}$ cm^{-3} (MX78), at the highest temperature $T_e = 16.7$ K studied in this sample, the thermally-activated MA process needs to be taken into account to properly fit the data. Finally, just below the Mott transition $n_d = 10^{17}$ cm^{-3} (MX79), we encounter a situation were mutual exchange spin flips between occupied sites dominate the dispersion, but become challenged by the thermally activated MA mechanism as the temperature is increased. In our temperature range, CB jumps affect the linewidth even in this regime.

As we discuss in the following, in all the situations studied, the linewidth of a classical spin noise measurement in forward geometry τ_s^{-1} is influenced by spin relaxation in the CB.

Interplay between the hyperfine interaction and conduction band jumps

Here, we discuss the results obtained on sample M3460 with a low doping of 2×10^{14} cm^{-3}, which was previously studied in Refs. [22, 181]. At such doping, the mean first nearest-neighbor distance $\sim 18\ a_B$ is so large that hops between donors are essentially forbidden. In this case, the correlation time of the localized spins should be long, at least if we neglect the stochastic thermal ionization of donors. In zero external magnetic field, one would expect the appearance of a well-resolved satellite line shifted with respect to the zero frequency, which corresponds to electron spin precession in the distribution of the nuclear field [62, 216, 250]. When an external magnetic field is applied in Voigt geometry, the spin noise line at Larmor frequency should be described by a Gaussian lineshape.

Figure 2.19 shows the difference between spin noise power spectra measured at $B = 0$ mT and at $B = 10$ mT. We observe that the satellite line is not well-resolved, appearing rather as a broad bump superimposed on the zero frequency peak. The line at Larmor frequency is best described by a predominantly Lorentzian Voigt profile. To explain the significantly broadened satellite line, one must assume a shorter correlation time. The weakness of the Gaussian component at Larmor frequency requires both a mechanism of motional narrowing, and a competing mechanism providing homogeneous spin relaxation. The only possible channel for the shortening of the correlation time is spin promotion to the CB. In principle, a spin can either accompany an electron as it is excited into the itinerant state, or spin promotion can occur via spin-exchange with an existing itinerant electron. In any case, followed by diffusion and capture on another donor, the process contributes both to the motional narrowing of the hyperfine contribution to the Larmor line, and to the eventual disappearance of the satellite line. To replicate the experimental linewidth and lineshape at Larmor frequency, we introduce spin relaxation in the CB via the rate ν_{CB}. This scenario, described by the two-state model defined in Eqs. (2.16-2.17) and solved in Eq. (2.42) of Section 2.4, perfectly reproduces the measured spectra, provided that the release and trapping rates are of the same order of magnitude (solid red line in Fig. 2.19).

If the trapping time ν_t^{-1} is assumed to be short, then according to Eq. (2.58), the spin relaxation of free electrons becomes inefficient, and a nonzero intrasite spin relaxation rate ν_s must be introduced to compensate. Fits with $\nu_s \neq 0$ and short ν_t^{-1} are not shown here, but in this case the satellite and Larmor lines cannot be fitted simultaneously: either the satellite line is too narrow, or the Larmor line is slightly too broad. In addition, in both situations, the wing of the satellite line drops too quickly.

In the inset of Fig. 2.19, an experimental dispersion curve (points) is compared to several calculations where some mechanisms are alternatively suppressed or amplified. Comparing the line widths at $q = 0$, one sees that the release/trapping mechanism in absence of CB spin relaxation induces an efficient narrowing of the spin noise line (dotted gray line), which can be strongly reduced by loss of spin coherence (solid black line). If spin coherence is totally lost during diffusion in the CB (dash-dotted gray line) the spin noise line is homogeneously broadened by the release rate. Finally, at $q = 0$ the spin noise linewidth is found smaller than what would be expected without CB jumps (dashed black line). These effects on the linewidth are well-described mathematically by Eqs. (2.58-2.59). At small $q \ll l_s^{-1}$, as it can be extracted from Eq. (2.58), the linewidth dispersion is approximately given by,

$$\Delta\Gamma_{CB}(q) \approx \frac{\nu_r}{1 + \nu_{CB}\nu_t^{-1}} l_s^2 q^2. \tag{2.65}$$

The coefficient before q^2 is directly related to the release rate ν_r, as well as the ratio $\nu_{CB}\nu_t^{-1}$, and thus to the spin noise linewidth at $q = 0$. l_s is determined from the shape of the dispersion

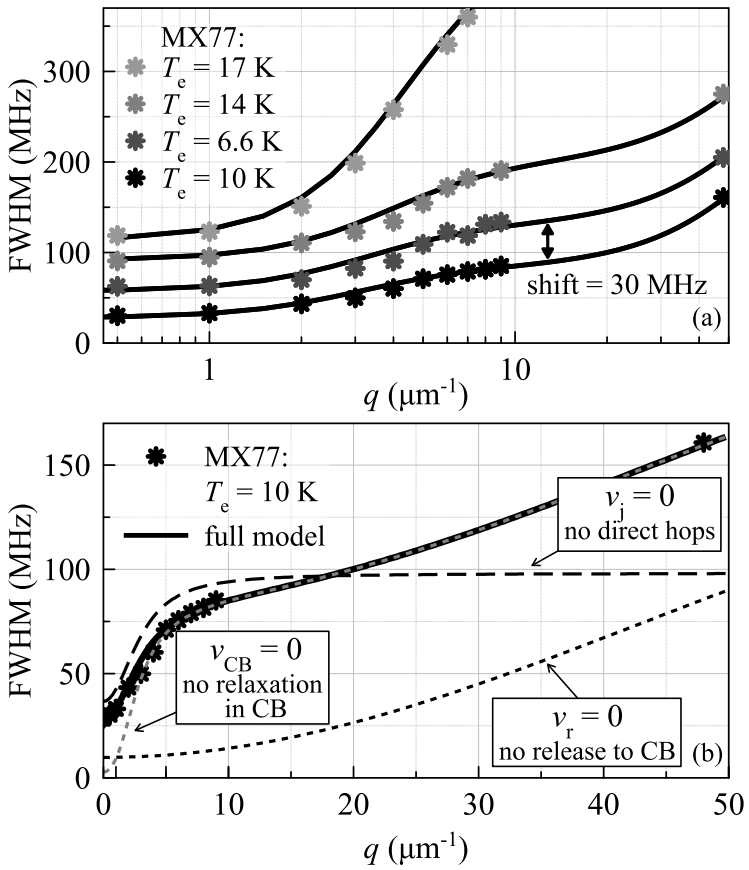

Figure 2.20: (a) measured (stars) and calculated (solid lines) spin noise linewidth dispersion in sample MX77 at various heat exchanger temperatures T_e. Data corresponding to different temperatures are vertically shifted for clarity. (b) breakdown of the different mechanisms contributing to the observed linewidth dispersion.

curve.

One could argue that it is straightforward to adjust the trapping rate in order to get the desired value of the linewidth at $q = 0$ using the theoretically expected DP spin relaxation rate $\nu_{CB} = \nu_{DP}$, since only the ratio $\nu_{CB}\nu_t^{-1}$ enters in Eq. (2.58). However, firstly, Eq. (2.58) is written in the short trapping time limit. The above reasoning does not hold when $\Omega_c\nu_t^{-1} \geq 1$, and for the solid red line fit of the peak in Fig. 2.19, $\Omega_c\nu_t^{-1} \approx 2$. Secondly, we must also reproduce the lineshape, which is determined by the interplay of hyperfine relaxation, spin jumps from donor sites and the amount of CB spin relaxation. At long trapping times, the lineshape is affected by ν_t even if $\nu_{CB}\nu_t^{-1}$ is kept constant, as we have shown in Section 2.4.

Hopping: long-range versus short-range

In sample MX77, $n_d = 4 \times 10^{15}$ cm^{-3}, the mean interdonor distance l_{HF} is of the order of $7a_B$. The HF mutual exchange spin flips start to become effective with a rate approaching 10^9 s^{-1}. In the temperature range between $T_e = 6$ and $T_e = 17$ K, the release rate ν_r increases from 2×10^8 s^{-1} to 10^9 s^{-1}. The experimental dispersion curves are shown in the upper panel of Fig. 2.20 (stars). At $T_e = 10$ K, interdonor hopping is almost one order of magnitude more efficient than CB jumps. Nevertheless, the hopping distance between donors is orders of magnitude smaller than the CB jumping distance l_s, which is of the order of half a micron. Consequently, both mechanisms are well-separated in reciprocal space, which is evident in the

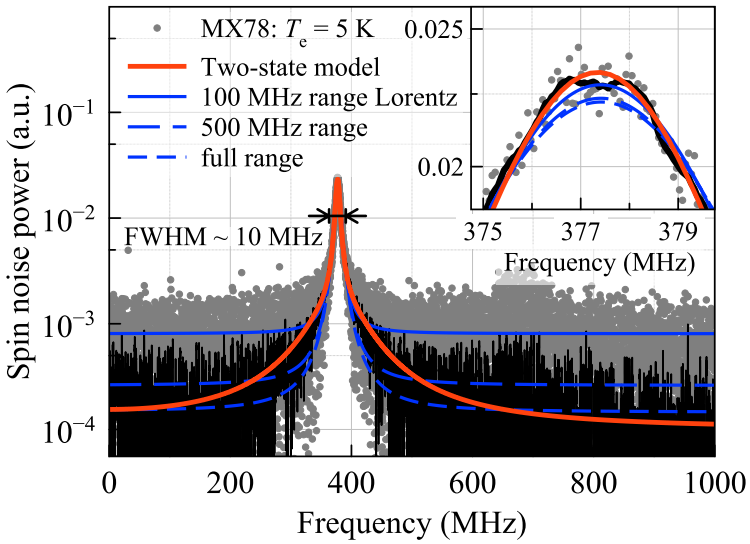

Figure 2.21: Typical measured (black line) and calculated (red line) spin noise spectrum common in the MX78 sample at $T_e = 5K$ (the behavior is similar in MX77). The black curve is the data (gray scattered dots) smoothed by a Savitsky-Golay filter (second order, 10 side points over 16384). Blue lines are fits using Lorentzian lines with different frequency ranges.

spin noise linewidth dispersion. At wavevectors above 8 µm^{-1}, the broadening due to CB jumps nearly reaches its asymptotic value, and all further broadening is then only due to direct interdonor hopping or localized-delocalized spin exchange. Already at $T_e = 17$ K, the CB release process becomes very efficient and overshadows the short-range hopping. As electron promotion to the CB becomes more efficient, l_s^2 decreases. This moves the CB dispersion plateau to higher wavevectors, and at $T_e = 17$ K it is unfortunately outside the range of AR-SNS. Theoretically, we estimate it to be near 20 µm^{-1}.

At low temperature and small wavevectors, where the linewidth dispersion is small compared to the linewidth at $q = 0$, the line profiles deviate from the Lorentzian lineshape. A typical spin noise spectrum is shown in Fig. 2.21. Depending on the frequency range of the fitting procedure, a Lorentzian function may miss the maximum, the wings and/or the background. The behavior is common to samples MX77 and MX78, but more pronounced in the latter due to narrower lines. The differences are not large, and Lorentzian fits still give good FWHM estimates. Nevertheless, this slight disagreement between experimental spin noise lineshapes and Lorentzian fits exists in multiple works [219, 231, 264], which indicates that the CB contribution to the spin noise spectra of localized spins is systematically underestimated or neglected altogether.

Frequency mismatch broadening

This section is dedicated to a peculiar behavior most clearly observed in sample MX78. While the spin noise line is symmetrical at normal incidence of the probe beam (see Fig. 2.21), it becomes asymmetrical when probed in oblique incidence by a TM-polarized probe (see Fig. 2.22). This effect disappears when increasing the temperature and, as it will be discussed below, can be attributed to a precession frequency mismatch between localized and free electron spins. It seems to be the signature of a small nuclear polarization induced by the probe. Different Overhauser fields experienced by localized and free electrons may then explain the frequency

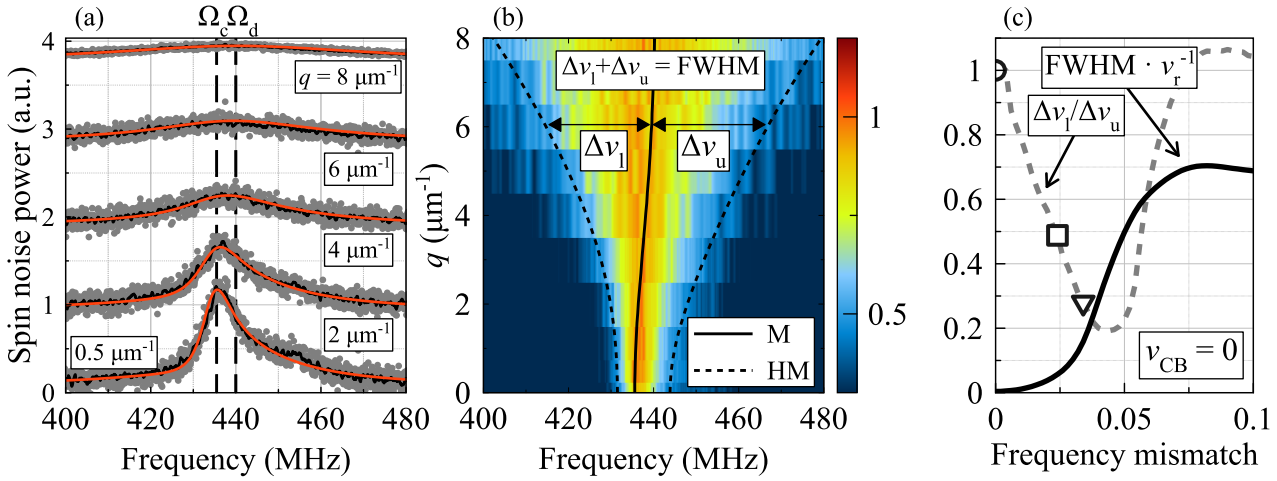

Figure 2.22: (a) MX78 spin noise power spectra (scattered gray dots) measured at $T_e = 12$ K, $P = 2$ mW at few wavevectors. The black curves are smoothed data by a Savitsky-Golay filter (second order, 10 side points over 16384), while the red lines are fits using Eq. (2.42). (b) Colormap based on normalized spin noise spectra measured on MX78 at $T_e = 12$ K, $P = 2$ mW. The superimposed lines are the calculated frequencies of the maximum (black line) and of the half maxima (dashed lines) of the spin noise line versus wavevector. (c) The line asymmetry (dashed gray line) and the line broadening normalized to ν_r (black line) as functions of the frequency mismatch $\Omega_d\Omega_c^{-1} - 1$, calculated using the parameters used to fit the spectra in the left panel, but with $\nu_{CB} = 0$. The open symbols mark the frequency mismatches used in calculations to account for the lineshapes at $T_e = 4.4$ K (triangle), 12 K (square), 16.7 K (circle).

mismatch [35].

Sample MX78 was studied at three different temperatures (see Table 2.2). The mean inter-neutral donor distance is of the order of $5-6\ a_B$ and the HF hopping rate ranges from 15 ns^{-1} to 17 ns^{-1}. Motional narrowing due to frequent interdonor hopping should lead to a very narrow spin noise line, < 1 MHz wide. This is in contrast to the observed linewidths at $q = 0$, which are an order of magnitude larger (Fig. 2.23). We attribute this broadening to the electron spin dynamics in the CB, where the spin undergoes DP relaxation.

One may reproduce the linewidth, the asymmetric lineshape, and the recovery of symmetric lines as the wavevector increases by setting $\Omega_c < \Omega_d$ in Eqs. (2.16-2.17) [see also Eq. (2.42)]. We obtain a precession frequency mismatch of $\Omega_d\Omega_c^{-1} - 1 = 3.5\%$ and 2.5% at $T_e = 4.4$ K and 12 K, respectively. At $T_e = 16.7$ K, the spin noise line demonstrates no visible asymmetry, and good fits are accomplished without a frequency mismatch. Indeed, introducing a mismatch smaller than 3.5% has no observable effect on the theoretical lineshape, which is due to faster trapping and spin relaxation at this temperature. Qualitatively, the temperature dependence is to be expected, since: i) the trapping rate ν_t increases with temperature, reducing the time spins spend in the CB; ii) the efficiency of nuclear spin pumping diminishes with temperature, leading to smaller nuclear fields [10], hence to a smaller frequency mismatch.

The measured spin noise spectra are shown in the left panel of Fig. 2.22 for $T_e = 12$ K. The maximum and the half-maxima of the spin noise line calculated as functions of q are shown in the middle panel, superimposed on a color map of the experimental spin noise spectra. As the wavevector increases, the line shifts towards the precession frequency of localized spins and the half-maxima become symmetrical with respect to the maximum. The q-dependent asymmetry

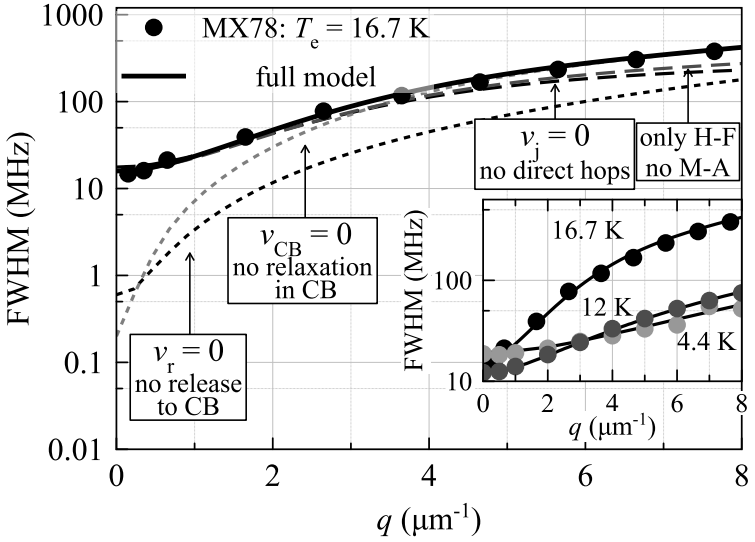

Figure 2.23: Continuous dispersion curve calculated at $T_e = T_{fit} = 16.7$ K (black line) along with the FWHM of the spin noise line at the wavevectors of the measurements (symbols). The gray dotted line is the dispersion curve calculated with $\nu_{CB} = 0$, while the black dotted line is calculated without accounting for the CB at all, $\nu_r = 0$. The black dashed line is obtained when suppressing all direct jumps. The gray dashed line is the same, only with the Herring-Flicker process included. The inset shows the dispersion curves at the three different temperatures studied with this sample.

and lineshift are clearly signatures of CB spin dynamics, and follow the reduction of the CB spin lifetime $T_{q,\omega}$ [see Eq. (2.54)] as the wavevector increases. At large wavevectors $T_{q,\omega} \to 0$, and the spin noise line becomes symmetrical, but broadened by the release rate.

The right panel of Fig. 2.22 shows the asymmetry (dashed gray line) and the spin noise line broadening (FWHM $\cdot\, \nu_r^{-1}$, black line) at $q = 0$ caused by the mismatch. These calculations are based on the same parameters that were used to fit the spin noise line at $T_e = 12$ K, except for the CB spin relaxation which has been suppressed in order to clearly demonstrate the broadening resulting only from the frequency mismatch.

The frequency mismatch broadening can be explained as follows. Due to the different precession frequencies, the spins undergo a rotation that is proportional to ν_t^{-1} while jumping through the CB. As the time spent in the CB by any one spin is ultimately random, this induces a loss of coherence. As a result, the spin noise line is broadened more or less depending on the ratio $\nu_t^{-1}(\Omega_d - \Omega_c)$. The overall magnitude of this broadening is also proportional to ν_r as it defines the CB contribution to the spin noise linewidth. Concerning the asymmetry, it behaves non-monotonously, first increasing strongly with the mismatch, then decreasing. The eventual decrease at large mismatch is due to the same reason as the increasing broadening, i.e., the accumulation of the phase difference due to different precession frequencies. Both of these effects are entirely due to the CB electron contribution to the spin noise spectra, and thus disappear when $\nu_r \to 0$. The effect disappears also when $\nu_t \to \infty$, as in this case no phase difference is accumulated during the instantaneous CB jump.

The linewidth dispersion for all MX78 measurements at oblique incidence is shown in Fig. 2.23. At this temperature, attempting to fit the spectra at $q > 4$ μm^{-1} with $\beta = 0.76 - 0.8$ used for the two lower temperatures 12 K and 4.4 K, respectively, results in slightly narrower lines. Therefore, the thermally activated Miller-Abrahams jump process is explicitly

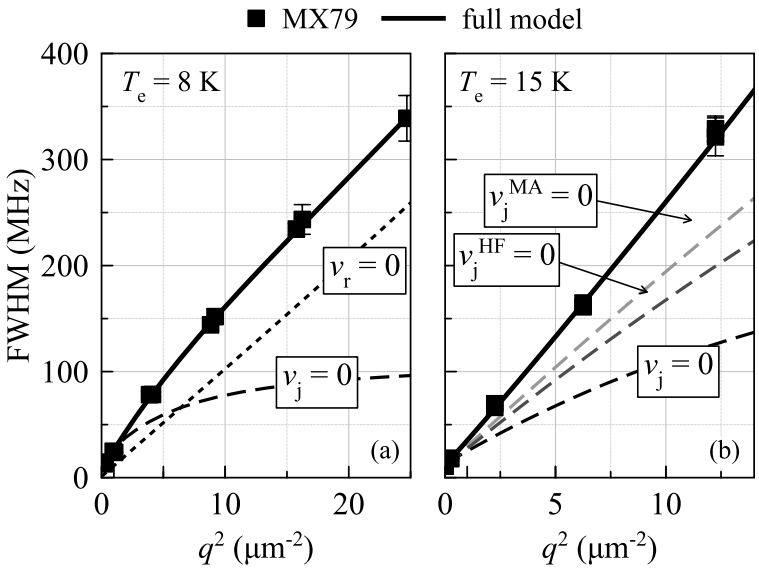

Figure 2.24: Measured (symbols) and calculated (solid black lines) wavevector dependence of the FWHM in sample MX79 at (a) $T_e = 8$ K and (b) $T_e = 15$ K. The dotted line in the left panel demonstrates that CB jumps still have an effect in MX79, despite high doping just below the Mott transition. The dashed lines are the dispersion curves when direct jumps [MA (light gray), HF (dark gray) or both (black)] are excluded from the simulation.

taken into account. To reproduce the linewidth dispersion curve, we use an MA jump length $l_{\mathrm{MA}} \approx 42.7$ nm $\approx 0.42\, n_{\mathrm{d+}}^{-1/3}$.

Manifestations of this frequency mismatch exist in other samples we have studied, namely MX77 and MX79. Due to unfavorable parameters, it has a weaker effect on the lineshape, which is clearly visible only in theoretical curves. In sample MX77, it results in a slight shift of the spin noise line. Indeed, a shift of about 1.5MHz is observed in sample MX77 between the spin noise lines measured at 10 K and 17 K. A slight asymmetry has been observed also in sample MX79, where we have verified that the lineshape is flipped when the direction of the applied field is reversed. Asymmetric spin noise lines have been observed in SNS in n-type GaAs previously, e. g., in Ref. [264] [Fig. 2 and Figs. 15(a)-(d)]. The small asymmetry is partly hidden by the Lorentzian fits, which fail to reproduce also the peak of the experimental line, similarly to what we show in Fig. 2.21. The asymmetry lessens when the excitation is shifted to a higher wavelength [Fig. 15 (e)-(f)]. A similarly unnoticed small asymmetry can also be seen in Fig. 4(a) of Ref. [219], where InGaAs with small In content was studied.

Short-range jumps

In MX79, short-range jumps always dominate. This is to be expected, since the donor density $n_{\mathrm{d}} = 1 \times 10^{17}$ cm^{-3} is close to the Mott transition. At the lowest temperature studied, $T_{\mathrm{e}} = 8$ K (see Fig. 2.24, left panel), the jump rate via the HF mechanism $\nu_{\mathrm{j}}^{\mathrm{HF}} = 0.78 - 1.23$ ps^{-1} is quite high compared to the release rate $\nu_{\mathrm{r}} = 0.2{-}0.5$ ns^{-1}. Nevertheless, CB spin diffusion contributes to the linewidth dispersion, leading to a slightly subquadratic dispersion curve. This is visible when the dispersion is plotted against q^2 as in Fig. 2.24. At $q = 0$, frequent hops between neutral donors strongly reduce the spin noise linewidth via motional narrowing. Spin rotation during hops due to SOC contributes to the linewidth by less than 1 MHz and cannot explain the observed linewidth ($\approx$ 9MHz). This large width can be explained by incorporating CB

relaxation with a long trapping time.

At $T_e = 15$ K (see Fig. 2.24, right panel) the spin noise line broadens very rapidly as the wavevector increases, which limits the measurements to $q < 4$ µm^{-1} due to the 1 GHz bandwidth of the detector. The dispersion is completely quadratic, and it is not straightforward to discriminate between the different jump mechanisms. Assuming that the HF mechanism is well-characterized by the parameter $\beta = 0.69$ in the measurement at $T_e = 8$ K, one must account for the MA process to describe the fast quadratic dispersion at $T_e = 15$ K. The l_{MA} length used was such that $l_{MA} \approx 36.6$ nm $\approx 0.43\, n_{d+}^{-1/3}$, with a coefficient almost identical to what was used in sample MX78 at $T_e = 16.7$ K. In MX79, the spin noise lines are Lorentzian. We can thus only give a lower bound estimate of the trapping rate and the CB spin relaxation rate (see discussion about the short trapping time regime at the end of Section 2.4). At $T_e = 15$ K even the lower estimate has a large uncertainty, and we have taken a value of the CB spin relaxation rate in agreement with measurements at the lowest temperature. The measurements show that spin diffusion is dominated by short range hopping, but do not afford an in-depth look into the interplay of localized and free electron spin dynamics.

2.6.4 Electron spin relaxation time as a function of doping density and temperature

The electron spin relaxation time τ_s is often discussed using relaxation time composition laws [68, 83], such as

$$\tau_s = \left(\frac{1}{\tau_{sn} + \sqrt{\pi}\delta_e^{-1}} + \frac{1}{\tau_{sa}} \right)^{-1}. \tag{2.66}$$

In the above, $\tau_{sn} = \frac{2\pi}{3}\delta_e^{-2}\nu_j$ is the spin relaxation time in the motional narrowing regime, $1/\tau_{sa} \approx \frac{1}{3}\frac{l_{HF}^2}{L_{SO}^2}\nu_j$ is the spin relaxation rate due to random spin rotation at hopping events due to SOC, and $\sqrt{\pi}/\delta_e$ is the spin dephasing time due to fluctuating local nuclear fields. The doping dependence of the spin relaxation time has already been calculated for CdTe using Eq. (2.66) in Ref. [83]. Similarly to GaAs, at low doping, spin relaxation is induced by fluctuating nuclear fields, and the rate is independent of donor density. With increasing doping, τ_{sn} becomes larger as motional narrowing comes into play. The spin relaxation time increases significantly, after which it finally decreases due to spin coherence losses in the effective spin orbit field, quantified by τ_{sa}.

Strictly speaking, Eq. (2.66) is correct only in the regimes $\tau_{sn} \ll \sqrt{\pi}\delta_e^{-1}$ and $\tau_{sn} \gg \sqrt{\pi}\delta_e^{-1}$, where, neglecting intrasite spin relaxation and CB jumps, Eq. (2.66) and the more rigorous expression of the spin relaxation time given by Eq. (2.59) meet perfectly. As τ_{sn} approaches $\sqrt{\pi}\delta_e^{-1}$ the composition formula deviates from Eq. (2.59) due to an overestimation of the motional narrowing effect, which results in the composition formula giving longer spin relaxation times. Still, the deviation never exceeds 25%.

When considering CB jumps accompanied by relaxation, and accounting for a nonzero intrasite spin relaxation rate, Eq. (2.66) has to be completed as follows:

$$\tau_s = \left(\frac{1}{\tau_{sn} + \sqrt{\pi}\delta_e^{-1}} + \frac{1}{\tau_{sa}} + \nu_s + \frac{\nu_r}{1 + \nu_t \nu_{CB}^{-1}} \right)^{-1}, \tag{2.67}$$

where $\tau_{sn} = \frac{2\pi}{3}\delta_e^{-2}(\nu_j + \nu_r)$. In this case, apart from the previously mentioned overestimation of the motional narrowing effect, the composition formula underestimates the spin relaxation time at very low doping densities as compared to Eq. (2.59) if ν_s is significant. This is basically

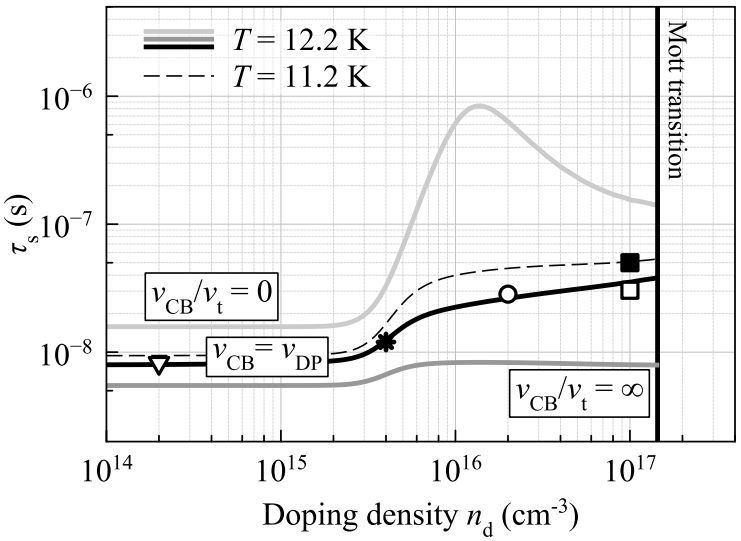

Figure 2.25: Spin relaxation time versus doping density calculated via Eq. (2.59) with $\beta = 0.63$, $n_a = 10^{14}$ cm^{-3}. The symbols are experimental spin relaxation times τ_s extracted from the FWHMs at $q = 0$. The experimental points are chosen to have similar fitting temperatures $T_{fit} \approx 12 - 14$ K, which correspond to different heat exchanger temperatures T_e due to varying quality of thermalization: $T_e = 9$ K (M3460, triangle), $T_e = 10$ K (MX77, star), $T_e = 12$ K (MX78, circle), $T_e = 8$ K (MX79, empty square). The filled black square was measured on MX79 at $T_e = 4.4$ K and $P = 0.5$ mW and corresponds to the longest spin relaxation time measured in this work.

due to the lineshape continuously changing from Gaussian to Lorentzian as the homogeneous contribution due to ν_s is increased, and leads to a maximum deviation of no more than 20% as ν_s approaches δ_e.

In theory, spin relaxation in n-doped CdTe and GaAs should behave largely the same way, with the longest spin relaxation times expected to be about twice as long in GaAs due to favorable material parameters. In GaAs, data on spin relaxation times measured as a function of doping density are scattered, but they are overall in good agreement with theoretical predictions [83]. Conversely, in bulk n-CdTe, the only study of electron spin relaxation as a function of doping shows relaxation times orders of magnitude shorter [249]. Despite the fact that the short spin relaxation times measured in Ref. [249] have been interpreted in terms of Dresselhaus spin orbit coupling near the MIT [265], it seems that the measurements in Ref. [249] have simply been carried out under very high densities of photo-excited carriers. With AR-SNS, we do not excite the samples as strongly, and therefore the low-temperature spin relaxation times measured in our experiments are closer to theoretical predictions.

Figure 2.25 shows the spin relaxation times extracted from the linewidths of the spin noise lines for the four samples. The heat exchanger temperatures T_e of the points shown are somewhat scattered. However, the fitting temperatures T_{fit}, which we are more accurate estimates of the true sample temperature T, are all very close, around $12 - 13.5$ K. The measured doping dependence follows the one calculated using Eq. (2.59) at $T = 12.2$ K (solid black line) quite well, assuming DP spin relaxation in the CB. In fact, spin relaxation in the CB significantly affects the spin relaxation rate in the intermediate doping range. The effect of motional narrowing can be stronger or weaker, depending on how much spin coherence is lost during CB jumps (solid light and dark gray lines). These measurements suggest that, contrary to what was measured

in Ref. [249], CdTe behaves as expected, and similarly to GaAs, with the differences coming solely from different material parameters.

In the highest-doped sample MX79, after lowering the power to 0.5 mW and maintaining the heat exchanger at $T_e = 4.4$ K, we obtain the narrowest spin noise line of our experiments. The 6 MHz linewidth corresponds to a long spin relaxation time of about 50 ns (filled black square in Fig. 2.25). This experimental value matches the spin relaxation we calculate at $T = 11.2$ K, which seems to be the lowest temperature we could reach in this work. We note that this value of 50 ns at a doping of 1×10^{17} cm^{-3} is longer than the theoretical prediction of Ref. [83] for this doping. This places the near-Mott-transition spin relaxation time in CdTe on the short side of those measured in GaAs. Spin relaxation times of the order of a hundred nanoseconds at $n_d \approx 10^{17}$ cm^{-3} and approaching microseconds around $n_d \approx 1 - 2 \times 10^{16}$ cm^{-3} can be expected in samples where DP relaxation is weakened and/or spin trapping from the CB is enhanced.

2.7 Conclusions

Standard SNS gives only a spatially averaged view of spin dynamics, while spatiotemporal SNS detected with a fixed objective is intrinsically limited by the wavevector cutoff effect due to the finite numerical aperture. The AR-SNS technique introduced here removes these limitations by introducing a goniometric detection scheme, which gives access to spatial spin correlations at the submicron scale. The enhanced wavevector bandwidth turns out to be invaluable to fully characterize the spin decoherence of electrons bound to donors in insulating n-CdTe at low temperatures, that is $k_B T \ll E_b$.

Our work demonstrates that the spin relaxation of localized electrons cannot be understood without invoking spin relaxation in the conduction band, even when $k_B T$ is much smaller than the activation energy. We are able to qualitatively explain and quantitatively reproduce all the lineshapes observed in the spatiotemporal spin noise spectra in a satisfying and consistent way, for the entire gamut of doping densities studied. Indeed, though the admixture of CB spin relaxation to the localized spin dynamics has been suggested and observed before [84, 90], our results suggest that its impact on spin noise spectra at low temperatures in weakly doped samples may have been underestimated in the literature. We also measure the spin relaxation time as a function of doping density and analyze the doping dependence in light of the two-state model, finding good agreement with our data. The longest spin relaxation time that has been measured in our work is about 50 ns (MX79 sample, $T_e = 4.4$ K, $T_{fit} \approx 11$ K), which is longer than the theoretical prediction of Ref. [83] and is the longest spin relaxation time to have been measured in n-CdTe, to our knowledge. Finally, this work offers a unified vision of electron spin relaxation in semiconductors, which resolves the somewhat conflicting results between CdTe and GaAs observed in previous works [83, 249].

The theoretical model introduced above explicitly includes cross-correlations between two systems of moving spins. Here, it is specifically established for the case of continuous diffusion in one system, and hopping diffusion in the other, but it can be easily generalized to other cases of interest, e. g., intra- and intermolecular spin transfer. The AR-SNS technique as well can be used for studying two-component interacting spin systems, even if only one component is detectable or effectively measured. Systems of this kind can be found in solid state physics, e. g., artifical semiconductor nanostructures, and also in heterogeneous interacting atomic spin systems [266]. Together, the theoretical and experimental tools introduced in this work are key for an in-depth understanding of the spatiotemporal spin dynamics at the submicron scale in these systems, from which optimization of spintronic devices can benefit.

Chapter 3

Interplay of nuclear spin relaxation and diffusion in wide n-CdTe QWs

In contrast to the previous Chapter, where have dealt mainly with electron spins in CdTe, here we concern ourselves with nuclear spin dynamics. In this Chapter, we report on a series of experiments performed on two distinct samples with wide CdTe quantum wells (QWs), accompanied by theoretical modeling. The experiments were conducted by colleagues at the Technische Universität Dortmund and at Saint Petersburg State University. The interpretation of experimental results and quantitative theoretical modeling was performed by the author under the supervision of K. V. Kavokin and with the aid of M. Vladimirova.

We find that the nuclear spin dynamics are drastically different in the two samples, both in terms of overall relaxation rate and magnetic field dependence. The differences are thoroughly explained by different electron localization in the two samples, as one of the samples features a low-density of shallow donors, while the other hosts puddles of two-dimensional electron gas (2DEG). The difference in the strength of the hyperfine coupling leads to qualitatively different results. In particular, we show that the peculiar field dependence observed for shallow donors is a signature of nuclear spin diffusion barrier formation, and cannot be simply explained by a decrease of the diffusion coefficient due to the decoupling of unlike spins with increasing field. The other sample demonstrates no field dependence of the nuclear spin relaxation rate, with the relaxation rate being in good agreement with Korringa-like nuclear spin relaxation. The latter is calculated for a quasi-2DEG of arbitrary areal density embedded in a QW.

The main findings presented in this Chapter are published as a regular article in Physical Review B [27].

3.1 Introduction

The nuclear spin physics of solids has enjoyed renewed interest from the scientific community in recent years, with modern research being largely stimulated by the possible spintronics and quantum computing applications. Frequently, nuclear spins are seen as an obstacle to reaching long electron coherence times, especially in quantum dots, where the hyperfine interaction is particularly important due to the strong localization of spins [6, 108]. However, they can also be used to the opposite effect. For example, the feedback from the nuclei can be used for frequency focusing of electron spin precession in quantum dots [7], and there is a growing body of encouraging research on the topic of hybrid quantum registers employing nuclear spins as long-lived quantum bits [109–113]. As the nuclear spins do not interact directly with light, they are controlled via hyperfine interaction with electrons, which is typically achieved through

resonant or nonresonant optical pumping, with protocols of increasing complexity [111, 114–116].

In GaAs, the model semiconductor, every nucleus has spin $I = 3/2$, and therefore possesses a nonzero quadrupolar magnetic moment. Once the cubic symmetry is lifted by, e. g., strain or defects, the uncontrollable quadrupolar interactions shorten the nuclear spin lifetime and fundamentally limit nuclear spin temperatures achievable via adiabatic demagnetization. Furthermore, a strong field dependence of nuclear spin relaxation is introduced [119, 138]. Although there is ongoing research on comparatively strain-free GaAs/(Al,Ga)As quantum dots (see, e. g., Ref. [111]), the quadrupolar effects can hardly be eliminated completely and become particularly important in small magnetic fields.

Consequently, materials with $I = 1/2$ are intriguing, as the nuclei do possess spin, but completely lack quadrupolar moments, and thus the aforementioned properties of their nuclear spin systems are robust with respect to stress, defects and electric fields. As discussed in Section 1.3, conventional semiconductors with nuclear spin systems largely composed of $I = 1/2$ are Si, CdSe, and CdTe. In this work, we focus on CdTe. The local field describing nuclear spin-spin interactions in CdTe $B_L \approx 0.03$ mT, as calculated in Appendix A.1, is significantly smaller than that in GaAs (≈ 0.1 mT [136]). One would expect the difference to be greater based on the magnetic dipole-dipole interaction alone due to the low abundance of magnetic isotopes of Cd and Te. However, as we mention in Section 1.3.3, the indirect interactions have different signs in GaAs and CdTe: in GaAs, they reduce the effective local field, whereas in CdTe they contribute to it [130, 136]. Nevertheless, the smaller local field is expected to reduce the lowest achievable nuclear spin temperature [147, 149] and to influence nuclear spin diffusion [165]. Additionally, CdTe is very similar to GaAs in electronic properties, the primary difference being the higher exciton/donor binding energy and, consequently, the smaller Bohr radius $a_B \approx 5$ nm [52, 83].

To use the nuclear spin system in a device, one should find a way of controlling it. A seldom explored possibility consists in using an external magnetic field to manipulate the diffusion barrier [165] (see also Section 1.4.7). Upon applying a threshold magnetic field, the bulk polarized nuclei would be separated from the donor site, preventing rapid diffusion and relaxation on the donor after pumping is stopped [159]. In semiconductors, there is no consensus on the subject of diffusion barriers due to the complex interplay of effects that arise when an inhomogeneous magnetic field is applied to the disordered nuclear spin system. As we have discussed in Section 1.4.7, as the amplitude of the inhomogeneous field increases, some nuclear spin-flip transitions become forbidden, while others may become allowed. The resulting permeability of the prospective diffusion barrier must be hardest to overcome in samples with large zero-field energy splitting in the nuclear spin system, for example GaAs-based quantum dots. Therefore, it is tempting to search for diffusion barrier formation in lightly or even unintentionally n-doped CdTe, as the relatively strong localization on donors together with the small local field should make the effect quite observable as far as the electrons remain localized. Additionally, the absence of random spatially inhomogeneous quadrupolar shifts should suppress the permeability of the barrier. In the opposite case of weak electron localization provided, one would not expect to see a response to the magnetic field apart from the weak field dependence of the nuclear spin warm-up rate, which is virtually absent in CdTe altogether due to the fortuitous parameters of the indirect coupling (see Section 1.4.4).

In this work, two CdTe-based nanostructures are studied, which will be referred to as Sample A and Sample B. This allows us to probe the CdTe nuclear spin system in two very different regimes of electron-nuclear coupling. Both samples are studied in similar conditions via optical pumping followed by adiabatic demagnetization, with Hanle photoluminescence (PL)

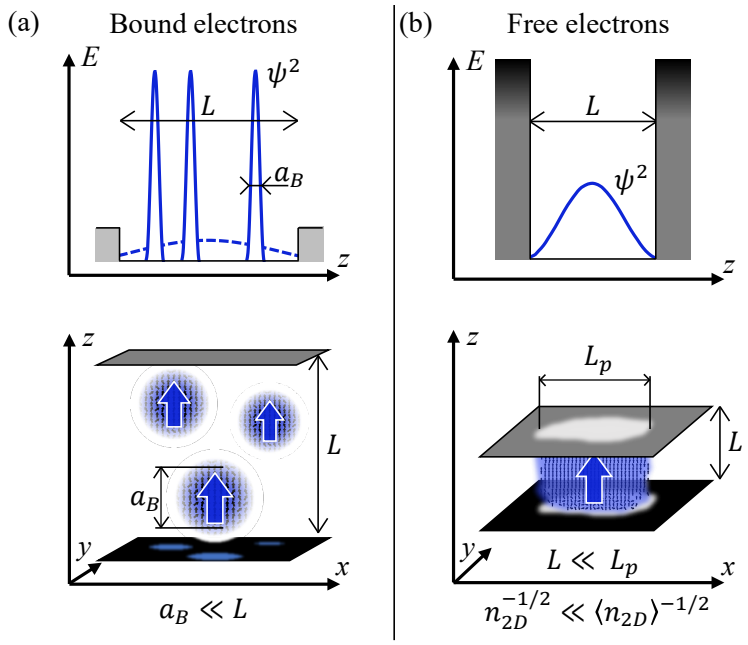

Figure 3.1: Schematic diagrams of the spin-lattice interactions studied in this work. (a) Donor-bound electrons in a wide insulating CdTe QW with low barriers; nuclear spins interact with the strongly localized individual electron spins. (b) Resident electron gas forming on QW potential fluctuations (shown by barrier color) in a deep CdTe QW with unintentional barrier doping; nuclear spins interact with the weakly localized 2D electron gas. The electron gas puddles are large compared to the QW width, but constitute only a small portion of the entire QW area ($\langle n_{2D} \rangle$ is the electron gas density averaged over the entire QW).

polarization measurements serving as a probe of the nuclear spin state. Sample A is a very wide high-quality CdTe quantum well (QW) sandwiched between low (Cd,Zn)Te barriers. The QW is contaminated with a low density of donors due to unintentional doping. According to the interpretation of the author, the nuclear spin dynamics develops around these donors, as illustrated in Fig. 3.1 (a). The inhomogeneous Knight field of the donor-bound electrons creates a diffusion barrier, which results in a magnetic field dependence of the nuclear spin relaxation. Sample B is a thinner CdTe QW surrounded by very high (Cd,Mg)Te barriers, and hosting a dilute two-dimensional (2D) electron gas. Such nanostructures are prone to both well-width fluctuations and barrier alloy fluctuations [187], and hence a localization potential is formed along the QW plane. As a result, the electrons are not distributed homogeneously in the QW plane, being collected in shallow puddles instead. The electron gas density inside the puddles n_{2D} is around $5{\times}10^{10}\text{cm}^{-2}$, while the rest of the QW remains basically electron-free. The density of electrons in these puddles is expected to be greater than the electron density averaged across the entire QW, $n_{2D} \gg \langle n_{2D} \rangle$, see Fig. 3.1 (a). This leads to temperature-dependent nuclear spin relaxation induced by fluctuations of the electron spin near the Fermi level in the areas covered by 2D electron gas, with a large contribution due to nuclear spin diffusion from electron-free areas, but with no notable dependence on the applied magnetic field. The overall nuclear spin relaxation rate is much slower than in Sample A. Phenomenological modeling of nuclear spin relaxation in these two different regimes supports the proposed interpretations.

This Chapter is organized as follows. Section 3.2.1 describes the studied samples in more detail. It is followed by Section 3.2.2, which describes the setup and experiments, and Section 3.2.3, which demonstrates the obtained measurements. In Section 3.3, we examine the

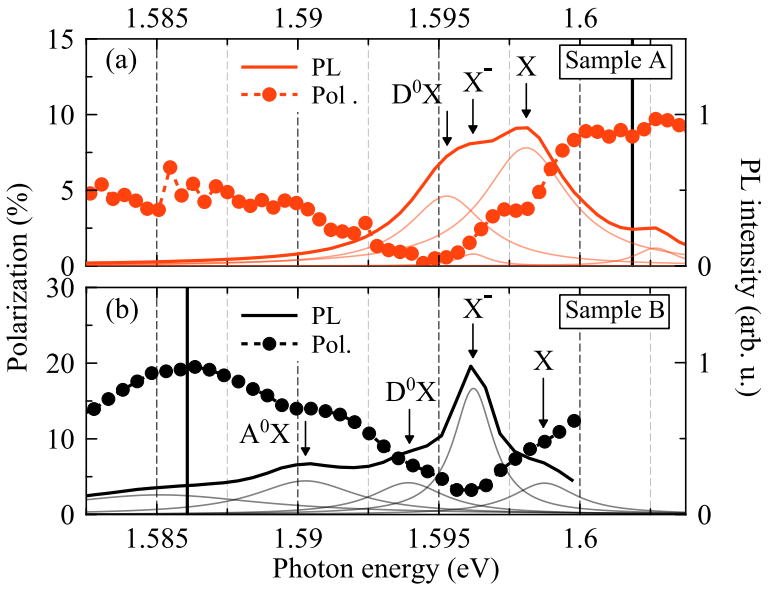

Figure 3.2: Low-temperature PL and PL polarization spectra of the two samples studied: (a) Sample A, (b) Sample B. Black vertical lines show the energies used for nuclear spin polarization measurements.

experimental results and present their theoretical modeling, summarizing our findings in Section 3.4.

3.2 Experimental

3.2.1 Samples and characterization

The two samples were grown by molecular beam epitaxy. Sample A, made at Institut Néel, CNRS, Grenoble by R. André, is a 30-nm-wide CdTe QW sandwiched between $Cd_{0.95}Zn_{0.05}Te$ barriers, grown on a $Cd_{0.96}Zn_{0.04}Te$ substrate. The top barrier also functions as the capping layer and is 93 nm thick. Sample B, grown at the Institute of Physics, Polish Academy of Sciences under G. Karczewski, is a 20-nm CdTe QW surrounded by high $Cd_{0.77}Mg_{0.23}Te$ barriers on top of a (100)-GaAs substrate. The top barrier (= cap layer) has a thickness of 17.5 nm.

Both samples are nominally undoped, however, the PL spectra recorded at liquid helium temperatures shown in Fig. 3.2 indicate some unintentional doping. In Sample A, we interpret the main PL features as the free exciton ground state X (1.5981 eV), the negative trion X^- (1.5962 eV), and the exciton bound to neutral donor D^0X (1.5953 eV), as the binding energies are consistent with literature data [41, 48, 49]. The structure of the free exciton resonance series is also reproduced by calculations similar to that of Ref. [21], where a sample grown under the same conditions as Sample A was studied. The calculation was performed by E. Khramtsov at the Spin Optics Laboratory.

In Sample B, the overall blueshift due to additional quantum confinement energy is partly compensated by the enhanced exciton binding energy [83]. We interpret the spectrum similarly to Sample A. Evidently, there are some donors inside the QW as well as acceptors (the D^0X, A^0X peaks at 1.5939 and 1.5903 eV, respectively) [49]. However, the relative intensity of the trion line (1.5962 eV) as compared with the free exciton (1.5988 eV) suggests that a dilute carrier gas is present. Although a structure similar to Sample B was shown to contain a hole gas, with the carrier type changing under above-barrier excitation [40], supplementary pump-probe

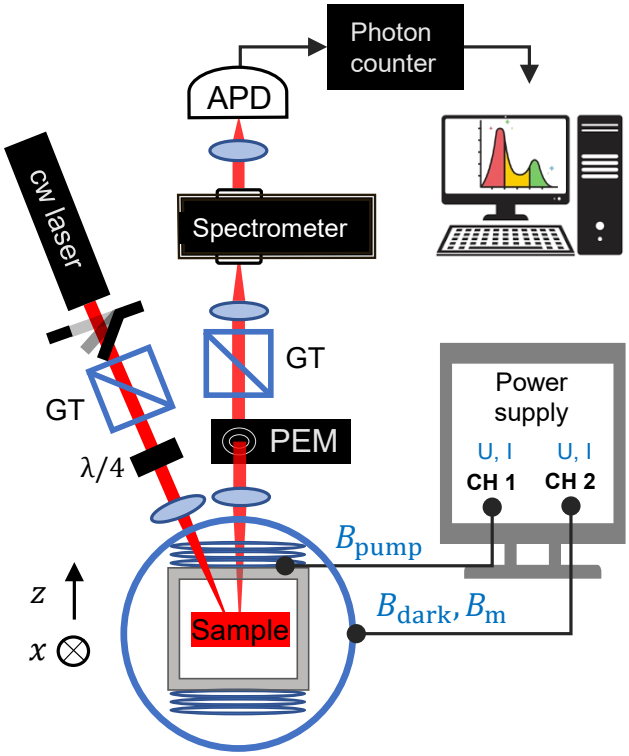

Figure 3.3: A schematic diagram of the experimental setup. GT are Glan-Taylor prisms, PEM is a photoelastic modulator, APD is an avalanche photodiode. The sample is pumped with circularly polarized light in Faraday geometry $B_{\text{pump}} \parallel z$, and the nuclear spin polarization is detected via PL polarization degree in Voigt geometry $B_{\text{m}} \parallel x$.

measurements performed by E. Zhukov at Technische Universität Dortmund (data not shown) confirm the presence of a resident electron gas in Sample B. To explain the experimental results presented in Section 3.2.3, we hypothesize that the resident electron gas is inhomogeneous, i. e., there are areas hosting electron gas puddles, and there are areas that are electron-free. This electron landscape results from a fluctuating QW potential, which traps electrons coming from the barriers. The roughness of the QW potential could be a consequence of QW width fluctuations and, more probably, barrier height fluctuations, as due to the height of the Mg barriers, small variations of Mg content lead to rather large QW potential fluctuations. That is to say, a Mg density variation of just 1% would lead to more than a 10 meV change in total barrier height [29, 267]. Overall, the scale of QW potential fluctuations in Sample B seems to be around several meV, as evidenced by the PL spectrum, and this should be enough to confine the dilute electron gas into puddles at the low temperatures studied, assuming it follows the Fermi-Dirac distribution. As we will show in Section 3.3, the electron gas density in these puddles does not exceed 10^{10} cm^{-2}.

Both samples are homogeneous on the scale of laser spot size (around 50 µm) and show very similar behavior for different pieces taken from the same substrate. This has been verified by supplementary measurements of carrier dynamics using photoluminescence on both samples, and pump-probe Kerr rotation experiments performed on Sample B by E. Zhukov.

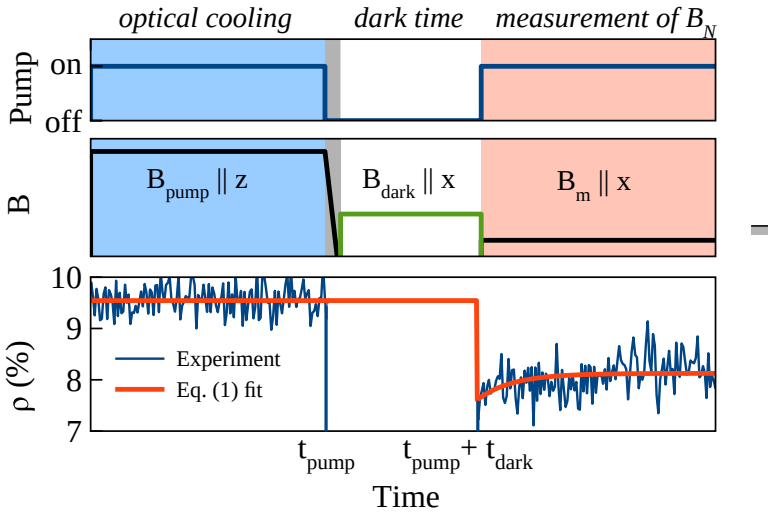

Figure 3.4: An illustration of the experimental protocol used to measure nuclear spin relaxation as a function of the magnetic field $B_{\rm dark}$. The demagnetization stage (shown by gray area) is very short and takes place between the cooling and relaxation stages. The times $t_{\rm pump}$, $t_{\rm dark}$ are not to scale. The data shown in the lower panel have been measured on Sample A at $B_{\rm dark} = 2.5$ mT at $t_{\rm dark} = 25$ s.

3.2.2 Setup and experiments

Nuclear spin polarization experiments were performed following the standard optical orientation technique [10]. Overall, the setups and experimental protocols are quite similar to Refs. [119, 120, 138, 150], and have been extensively used in studies of nuclear spin relaxation in GaAs. Experiments on Sample A were carried out at the Spin Optics Laboratory (Saint Petersburg State University) by V. Litvyak. Sample B was studied at the Technische Universität Dortmund by M. Kotur.

A schematic diagram of the experimental setup is shown in Fig. 3.3, while Fig. 3.4 illustrates the experimental protocol. During the optical cooling stage, the nuclear spins are dynamically polarized in a longitudinal magnetic field $B_{\rm pump}$ under optical pumping with circularly polarized light (Faraday geometry). Once the pumping is stopped, one proceeds with adiabatic demagnetization to zero field. During this process, the nuclear spin system reaches internal equilibrium and its lowest spin temperature $\theta_N^{(0)}$. In the next stage, the transverse field $B_{\rm dark} \parallel x$ is applied, and nuclear spin relaxation proceeds for a time $t_{\rm dark}$, after which the measurement is conducted.

The measurement procedure yields the effective nuclear field B_N (the Overhauser field [268] that the nuclei exert on the electrons via hyperfine interaction, see Section 1.3.2). The procedure consists in switching on simultaneously the transverse measuring field $B_{\rm m}$ and the pumping beam (Voigt geometry), and then recording the PL depolarization. The PL polarization degree $\rho(t)$ is then determined by the total field $B_{\rm m} + B_N$ experienced by the electrons (the Hanle effect, see Sections 1.5.2 and 1.6.1), and can be described with

$$\rho(t) = \frac{\rho_0 B_{1/2}^2}{B_{1/2}^2 + \left[B_{\rm m} + b + (B_N(t_{\rm dark}) - b)\exp\left(-\frac{t-t_{\rm dark}}{T_1}\right)\right]^2}, \tag{3.1}$$

where ρ_0 is the PL polarization degree in zero transverse field, $B_{1/2}$ is the half-width of the Hanle curve that has been measured independently in absence of nuclear effects, T_1 is longitudinal nuclear spin relaxation time, and b is a small nuclear field brought about by additional nuclear spin cooling in the Knight field of photocreated electrons during measurement [119].

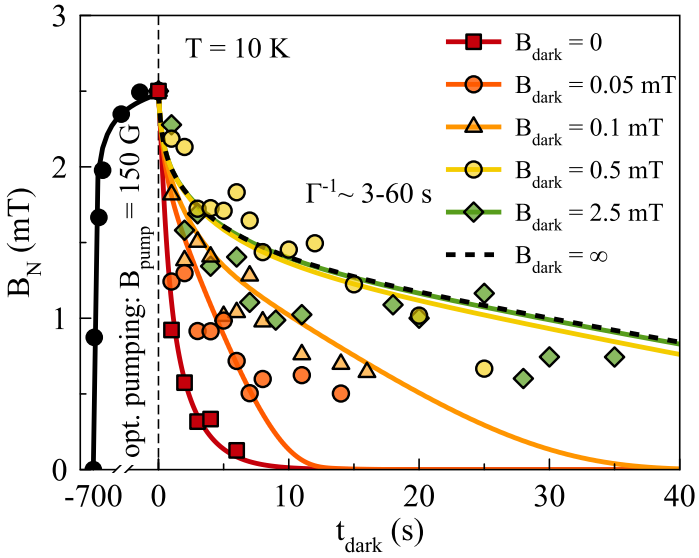

Figure 3.5: Nuclear spin dynamics in Sample A. Symbols: experimental data. Solid lines: self-consistent theoretical modeling via diffusion equation. The strong dependence on magnetic field is well-described by the onset of a diffusion barrier due to the inhomogeneous Knight field. The curve at $B_{\text{dark}} = 0$ corresponds to spatially homogeneous diffusion with $D = 3 \times 10^{-13}$ cm^{2}s^{-1} with relaxation via bound electrons. The diffusion barrier becomes more significant as B_{dark} grows, slowing nuclear spin diffusion and impeding relaxation.

In experiments on Sample A, the nuclear spins were pumped for $t_{\text{pump}} = 610$ s in an external field of $B_{\text{pump}} = 15$ mT by a laser tuned to $E = 1.822$ eV (above-barrier excitation), with $B_{\text{m}} = 0.12$ mT. Sample B was subjected to a shorter pumping time of $t_{\text{pump}} = 100$ s, and the applied field was also somewhat weaker, $B_{\text{pump}} = 11.5$ mT. The pumping energy was $E = 1.631$ eV (below-barrier excitation), and the measuring field was chosen equal to the pumping field, $B_{\text{m}} = 11.5$ mT. We note that in experiments on both samples the pumping energy was dictated by laser availability, not pumping efficiency.

The average spin of electrons occupying different states (e. g., neutral donors and free electrons) equalizes on a very short timescale which is orders of magnitude faster than the nuclear spin dynamics [85] (see also Section 1.2.3). Indeed, this result has also been recovered in AR-SNS experiments in Chapter 2. Therefore, all the electron states are equally valid sensors of the nuclear spin state. As such, the detection energies were chosen to maximize the PL polarization degree $\rho(t)$. The PL intensity and polarization spectra are shown in Fig. 3.2. Solid black lines indicate the detection energies, 1.6019 eV and 1.5861 eV for Samples A and B respectively. Additional modeling performed by E. Khramtsov shows that in Sample A, this roughly corresponds to the free exciton state formed by the $e1$-$hh3$ quantum-confined states. In Sample B we are likely probing states that are localized on QW potential fluctuations.

3.2.3 Main experimental results

The results of measurements on Samples A and B are presented in Figs. 3.5 and 3.6, respectively. The two samples exhibit drastically different nuclear spin dynamics. In Sample A, we observe a dramatic increase of the nuclear spin lifetime in very weak transverse magnetic fields $B_{\text{dark}} < 3$ mT, though it reaches tens of seconds at best. Sample B demonstrates a much longer nuclear spin lifetime of the order of hundreds of seconds, which is independent of B_{dark} at

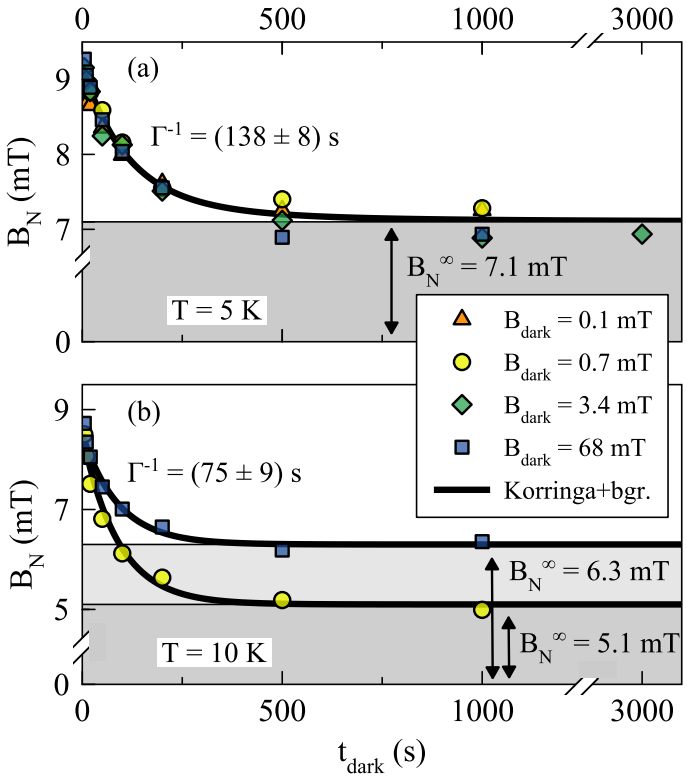

Figure 3.6: Nuclear spin dynamics in Sample B at $T = 5$ K (a) and 10 K (b). Symbols: experimental data. Solid lines: modeling via Eq. (3.29). The dynamics is governed by free electron-induced relaxation and spin diffusion. It is independent of the magnetic field, as the electron localization is insufficient for the diffusion barrier effect. At 5 K essentially nothing changes with the magnetic field. At 10 K the relaxation rate is independent of $B_{\rm dark}$, only the backgrounds are different.

5 K. Additionally, there is a background — an extremely long-lived component of the nuclear spin polarization that persists for thousands of seconds. The nuclear spin relaxation shows a pronounced temperature dependence. Measurements at $B_{\rm dark} = 0.68$ mT and $T = 10$ K, see Fig. 3.6 (b), indicate the reduction of the rate at 10 K by almost a factor of 2 with respect to the rate measured at 5 K. Increasing $B_{\rm dark}$ up to 6.8 mT does not affect the relaxation rate. By contrast, the long-lived component of the nuclear spin polarization appears to be sensitive to both temperature and magnetic field.

Estimates of nuclear spin temperature

It is instructive to estimate the lowest nuclear spin temperature reached in these experiments on CdTe, and to compare them to existing measurements on GaAs samples. For this, we need to calculate the spin temperature right after demagnetization to the measurement field $\theta_N(B_{\rm m})$ via the Curie law, and then rescale it to zero field to obtain $\theta_N^{(0)}$. Recalling Eqs. (1.30) and

(1.31), we write

$$\theta_N^{(0)} = \frac{B_L \theta_N(B_\mathrm{m})}{\sqrt{B_\mathrm{m}^2 + B_L^2}} = \frac{\hbar\langle\gamma\rangle I(I+1)}{3k_\mathrm{B}} \frac{B_L B_\mathrm{m}}{\sqrt{B_\mathrm{m}^2 + B_L^2}} \frac{b_N}{B_N(t_\mathrm{dark})}\bigg|_{t_\mathrm{dark}=0}$$
$$\approx \frac{\hbar\langle\gamma\rangle I(I+1)}{3k_\mathrm{B}} \frac{B_L b_N}{B_N(t_\mathrm{dark})}\bigg|_{t_\mathrm{dark}=0}, \tag{3.2}$$

where k_B is the Boltzmann constant, $\langle\gamma\rangle = -6.47 \times 10^7$ rad s^{-1} T^{-1} is the average gyromagnetic ratio of magnetic isotopes (see Table 1.1). The local field is around $B_L = 0.03$ mT, see Section 1.3.3 and Appendix A.1. The nuclear field at saturation $b_N \approx 700$ mT (see Section 1.3.2).

Applying Eq. (3.2), we find that the nuclear spins of Sample A are cooled down to around 0.3 µK. In Sample B the temperature is even lower, possibly reaching as low as 0.08 µK, although it is difficult to make a precise measurement due to the electronic structure of the sample being composed of 2D electron gas puddles on the µm scale. Nevertheless, even after subtracting the background completely, we arrive at around the same nuclear spin temperature as for Sample A, $\theta_N^{(0)} \approx 0.3$ µK. For comparison, in GaAs, which is a common platform for dynamic nuclear polarization experiments, the lowest spin temperatures obtained are 0.5 µK ([120], rotating frame) and 2 µK ([149], laboratory frame).

It is not trivial to compare these results to other materials with $I = 1/2$, due to the lack of available low-field data, and significant differences between implemented experimental approaches. In principle, nuclei in silicon are quite interesting because the only magnetic isotope, ^{29}Si, has only 4.6% natural abundance, and paramagnetic centers allow for efficient dynamic nuclear polarization. In particular, in Ref. [269] a ^{29}Si spin temperature as low as 5 µK is achieved at 30 mT (a resonant magnetic field that ensures anti-crossing of electron and nuclear spin levels) near paramagnetic color centers in SiC. In Ref. [270], a spin temperature of 5 mK for a phosphorus nuclei spin subsystem in Si:P is reported at 8.6 T. This result relies on electrically detected magnetic resonance, and it requires high fields and an electric current. In both cases, however, direct comparison with the zero-field temperature determined is this work is difficult.

Considering that in the experiments performed in this work, such low temperatures are obtained under pumping conditions which were not purposely optimized for the most efficient nuclear spin cooling, these results suggest that CdTe is a potential candidate for reaching record low temperatures in the semiconductor nuclear spin system.

3.3 Modeling and discussion

In this Section, we construct theoretical models to qualitatively and quantitatively explain the experimental results.

3.3.1 Donor-bound electrons (Sample A)

The nuclear spin relaxation in Sample A shown in Fig. 3.5 is rather fast, with nuclear spin lifetimes of the order of seconds. We assume that the relaxation is due to hyperfine interaction with donor-bound electrons, as these are essentially the only resident electrons in the sample. Dynamic nuclear polarization during pumping also occurs via localized electrons due to an efficient hyperfine coupling.

The nuclear spin system can be described by the average nuclear spin $\langle I_z(\mathbf{r}, t)\rangle$ as experienced by the electrons, that is, the angled brackets imply a spatial average over an area that is

small in comparison to a_B, but large enough to include thousands of nuclei. A largely equivalent approach relies on tracking the inverse spin temperature $\beta_N = 1/(k_\mathrm{B}\theta_N)$, which can also be time-dependent and spatially inhomogeneous. This approach is more versatile, since it gives nontrivial solutions at $B_\mathrm{dark} = 0$.

To model the behavior of the nuclear spin polarization, following the seminal work of D. Paget [159] and many others, we write a spin diffusion equation with relaxation and pumping terms. In the spirit of Eq. (1.40), we write the equation as

$$\frac{\partial \beta_N}{\partial t} = \nabla \left[D(\mathbf{r}, t|B_\mathrm{dark}) \nabla \beta_N \right] - \Gamma(\mathbf{r}, t)\beta_N + P(\mathbf{r}, t). \tag{3.3}$$

Here $\Gamma(\mathbf{r}, t)$ and $P(\mathbf{r}, t)$ are the electron-mediated nuclear spin relaxation and polarization rates, and $D(\mathbf{r}, t|B)$ is diffusion coefficient which is generally time- and coordinate-dependent, and also depends on the external magnetic field.

We consider a perfect crystal that is weakly doped with donors. That is to say, at low temperatures the only electrons in the system are the electrons localized on donors, which are separated by distances much greater than the Bohr radius ($a_B \approx 5$ nm in CdTe). Since all electrons contribute to the signal independently, it is sufficient to describe what happens under one donor orbit, and in what follows, we neglect the possibility of nuclear spin diffusion from one site reaching another. The spherical symmetry of the problem reduces Eq. (3.3) to its radial part. The experimentally measured Overhauser field acting on the donor-bound electron is recovered by performing the integration

$$B_N(t) = \frac{b_N}{I} \int \langle I_z(\mathbf{r}, t) \rangle |\psi_{e,\mathrm{loc}}(\mathbf{r})|^2 \mathrm{d}\mathbf{r}, \tag{3.4}$$

where $\psi_{e,\mathrm{loc}}(r) = (\pi a_B^3)^{-1/2} \exp(-r/a_B)$ is the wave function of the donor-bound electrons, and the average nuclear spin is recovered via

$$\langle I_z(\mathbf{r}, t) \rangle = \frac{1}{3} \hbar \langle \gamma \rangle I(I+1) B_\mathrm{m} \beta_N. \tag{3.5}$$

In the following, we elaborate on the polarization and relaxation terms, as well as the diffusion term.

Nuclear spin polarization and relaxation

Because of the above-barrier pumping and the strong localization of a donor-bound electron, we assume that both the pumping and the relaxation occur only via the donor-bound electrons. In principle, it is feasible to directly calculate the nuclear spin pumping and relaxation rates due to spin-flips with a donor-bound electron described by the wave function $\psi_{e,\mathrm{loc}}(r)$. Here, we limit ourselves to a simpler approach. The nature of the contact hyperfine interaction requires the rates to be proportional to $|\psi_{e,\mathrm{loc}}(r)|^4$. We may therefore simply write

$$\Gamma(r, t) = \Gamma_0 \exp(-4r/a_B), \tag{3.6}$$
$$P(r, t) = P_0 \exp(-4r/a_B), \tag{3.7}$$

with Γ_0 and P_0 being the relaxation and pumping rates at the center of the donor. In the steady-state, these rates are related through [118, 144]

$$P(r, t) = \frac{I+1}{S+1} \Gamma(r, t) p_e, \tag{3.8}$$

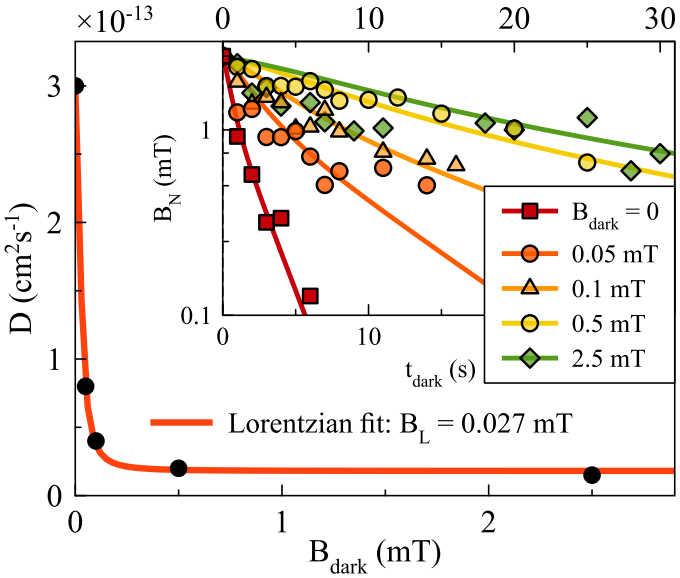

Figure 3.7: Results of modeling the Sample A nuclear spin dynamics with a field-dependent diffusion coefficient $D(B_{\text{dark}})$. Sharp changes in diffusion occur in fields close to the local field $B_L \approx 0.03$ mT. Inset: experimental data (points) and fits via Eq. 3.9 (lines).

where $S = 1/2$ is the electron spin, $I = 1/2$ is the spin of magnetic isotopes in CdTe, and $p_e = \langle S_z \rangle / S$ is the electron spin polarization [see also Eq. (1.42)]. The fitted curves in Fig. 3.5 correspond to $P_0 = 0.54$ s^{-1} and $\Gamma_0 = 13.2$ s^{-1} during pumping ($p_e = 0.04$), and $\Gamma_0 = 0.08$ s^{-1} during relaxation.

An expression for Γ_0 based on hyperfine spin flips with a localized electron spin can be found in Eq. (21) of Ref. [136], which we may use to extract the correlation time τ_c. This yields $\tau_c = 0.05$ ns, which is much shorter than what one would expect from our estimate using the results of Chapter 2. On the other hand, this result is consistent with the correlation time fitted in Ref. [219], and seems to be indicative of the very efficient spin exchange between localized and free electrons [85].

Field-dependent diffusion coefficient

For the sake of simplicity, let us first assume that the nuclear spin diffusion coefficient D is constant, but depends on B_{dark}:

$$\frac{\partial \beta_N}{\partial t} = D(B_{\text{dark}}) \Delta \beta_N - \Gamma(\mathbf{r}, t) \beta_N + P(\mathbf{r}, t). \tag{3.9}$$

Once the equation is solved for β_N, the nuclear field B_N in the measurement field $B_{\text{m}} = 0.12$ mT is obtained via the Curie law; the results are presented in Fig. 3.7.

To account for the experimental results, the diffusion coefficient must experience a sharp change in fields of the order of 0.03 mT, in excellent agreement with the value of the local field B_L obtained in Appendix A.1 considering both the magnetic dipole-dipole interaction and indirect interactions. The field dependence of the diffusion coefficient $D(B_{\text{dark}})$ can in principle be due to two separate reasons: (i) enhancement of the nuclear spin warm up rate in weak fields, (ii) the decoupling of unlike spins in sufficiently strong magnetic fields, and (iii) the formation of a nuclear spin diffusion barrier. Concerning (i), as discussed in Section 1.4.4, one does not expect a significant enhancement of the warm-up rate in CdTe in fields below

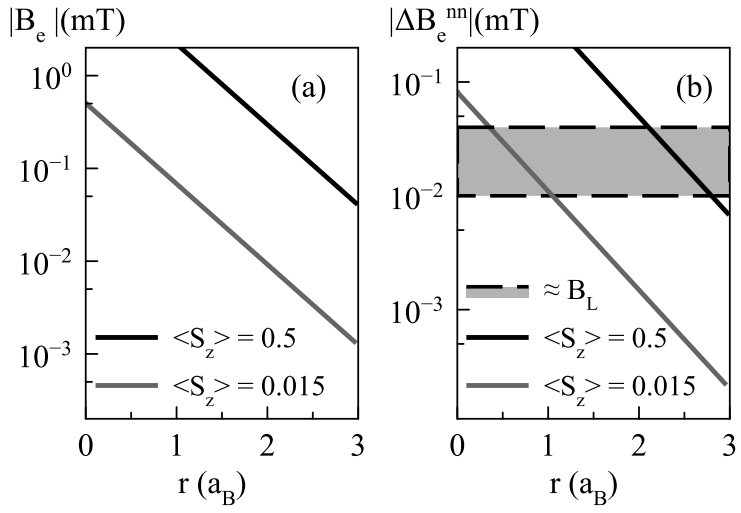

Figure 3.8: (a) Magnitude of the Knight field produced by a donor-bound electron vs. distance from donor r, measured in units of $a_B = 5$ nm; (b) difference of Knight fields experienced by two nuclei separated by the most probable nearest-neighbor distance $r_{\rm nn} = 0.41$ nm. Colors denote values of electron polarization: $\langle S_z \rangle = 0.5$ (maximum value [10]) and $\langle S_z \rangle = 0.015$ (estimated from experimental nuclear polarization right after pumping, $B = 0.1$ mT). Gray area in (b): approximate value of local field B_L.

B_L due to the mostly scalar nature of the indirect interactions which work to increase B_L, but not the kinetic local field B_{LK}, offsetting the effect of the non-secular part of the dipole-dipole interaction. Therefore, enhancement of the nuclear spin warm up rate can be safely neglected. Let us now address the field-dependent decoupling (ii). In Section 1.4.5, we estimate that Cd and Te nuclear spins are completely decoupled already in a field of around 0.1 mT. Translating to the obtained measurements, this means that Cd-Te spin flips would contribute to the $B_{\rm dark} = 0, 0.05$ mT points, and otherwise nuclear spin diffusion is always forbidden between these isotopes, proceeding only via the ^{111}Cd and ^{113}Cd. However, ^{125}Te makes up only a quarter of all magnetic nuclei (see Table 1.1), hence the Cd-Te decoupling should not have a strong effect on the diffusion coefficient, despite occurring in the relevant field range. Spin flips between the two Cd isotopes, ^{111}Cd and ^{113}Cd, become forbidden in an external field of around 10 mT, which should then lead to an approximately two-fold decrease of the diffusion coefficient, judging from the near-equal abundances of the two isotopes. Meanwhile, the data in Fig. 3.7 shows that the characteristic field when diffusion becomes strongly suppressed is around 0.03 mT, i. e., the Cd-Cd decoupling occurs outside the relevant range of magnetic fields and is also unimportant. We conclude that the partial suppression of diffusion between unlike spins cannot explain the observed experimental data, and we must invoke the nuclear spin diffusion barrier concept.

Nuclear spin diffusion barrier formation around neutral donors

The main principles of nuclear spin diffusion barrier formation are given in Section 1.4.7. In weak magnetic fields $B_{\rm dark} \gtrsim B_L$, the cold nuclear spins are easily polarized, resulting in an Overhauser field $B_N \gg B_{\rm dark}$. The polarized nuclei interact with electrons. Since the resident electrons are localized on donors and their density is low, the hyperfine relaxation mechanism is dominant over the spin-orbit one. In this regime, dynamic electron polarization by nuclei takes place [169], which means that the average electron spin $\langle S_z \rangle$ is determined by the mean

nuclear spin $\langle I_z \rangle$, and is therefore proportional to the Overhauser field B_N. In turn, the polarized electrons exert a weak but highly inhomogeneous Knight field back upon the nuclei, $B_e(\mathbf{r}_j) \propto |\psi(\mathbf{r}_j)|^2 \langle S \rangle$, where $\psi(\mathbf{r}_j)$ is the electron wave function at the nucleus located at $\mathbf{r}_j$. Indeed, the Knight fields experienced by two nearby nuclei situated at a distance r away from the donor and separated by $r_{ij} \ll a_B$ differ by:

$$\Delta B_e(r, B_N) = r_{ij} \left| \frac{\partial B_e(r)}{\partial r} \right|. \tag{3.10}$$

If at any distance r from the donor $\Delta B_e(r, B_N) > B_L$, then the corresponding nuclear spin flips are suppressed due to energy conservation. Equation (3.10) allows us to estimate that in B_{dark} as small as 0.1 mT in the immediate vicinity of the donor site, $\Delta B_e(r, B_N) > B_L$ even for a pair of nearest-neighbor nuclei with nonzero spin separated by r_{nn}, so nuclear spin diffusion is expected to be strongly suppressed.

The rigorous calculation of the spatial and field-dependent behavior of the diffusion coefficient is outside the scope of this work; a detailed study can be found in Ref. [166]. Instead, we incorporate the effect by introducing a phenomenological dependence of the diffusion coefficient D on the Overhauser field B_N through the Knight field gradient $\Delta B_e(r_{\text{nn}}, B_N)$ (hereafter referred to as ΔB_e^{nn}) as defined by Eq. (3.10). This dependence must ensure that

$$D(\Delta B_e^{\text{nn}}) \approx 0, \qquad \text{if} \qquad \Delta B_e^{\text{nn}} \gg B_L; \tag{3.11}$$

$$D(\Delta B_e^{\text{nn}}) \approx D_0, \qquad \text{if} \qquad \Delta B_e^{\text{nn}} \ll B_L. \tag{3.12}$$

In the above, D_0 is the nuclear spin diffusion coefficient in the absence of Knight field feedback, i. e., in zero external field. Thus, the nuclear spin diffusion barrier builds up wherever the Overhauser field induces a sufficiently inhomogeneous Knight field. In the theoretical curves of Fig. 3.5, a step-like $D(\Delta B_e^{\text{nn}})$ was used, accurately describing the data with $B_L = 0.04$ mT, not far from our estimate of 0.03 mT (see Appendix A.1). We will now incorporate the diffusion barrier into the phenomenological diffusion equation.

The distance r_{nn} between two nearest-neighbor magnetic nuclei may be estimated assuming a continuous Poisson distribution with an average density of magnetic isotopes per unit volume σ:

$$r_{\text{nn}} = \int_0^\infty r e^{-\frac{4}{3}\pi\sigma r^3} 4\pi r^2 \mathrm{d}r \approx 0.55\, \sigma^{-1/3}. \tag{3.13}$$

Taking into account the isotopic abundances from Table 1.1 along with the CdTe lattice constant $a_0 = 0.648$ nm, we obtain $r_{\text{nn}} = 0.41$ nm. The Knight field experienced by an average magnetic nucleus may be written as:

$$B_e(\mathbf{r}) = -\nu_0 \frac{\sum_\alpha x_\alpha A_\alpha / \gamma_\alpha}{\sum_\alpha x_\alpha} |\psi_{e,\text{loc}}(r)|^2 \langle S_z \rangle, \tag{3.14}$$

where A_α, γ_α and x_α are the hyperfine constants, gyromagnetic ratios and abundances of magnetic isotopes in CdTe (see Table 1.1), and $\nu_0 = a_0^3/4$ is the elementary cell volume. The average electron spin is tied to the Overhauser field via

$$\langle I_z \rangle = \langle S_z \rangle \frac{I(I+1)}{S(S+1)}, \tag{3.15}$$

which is another form of Eq. (3.8). The difference of Knight fields experienced by two nuclei is given by Eq. (3.10). A simple calculation of ΔB_e^{nn} is displayed in Fig. 3.8, showing that a diffusion barrier should indeed arise at distances of the order of a_B, depending on the electron spin polarization.

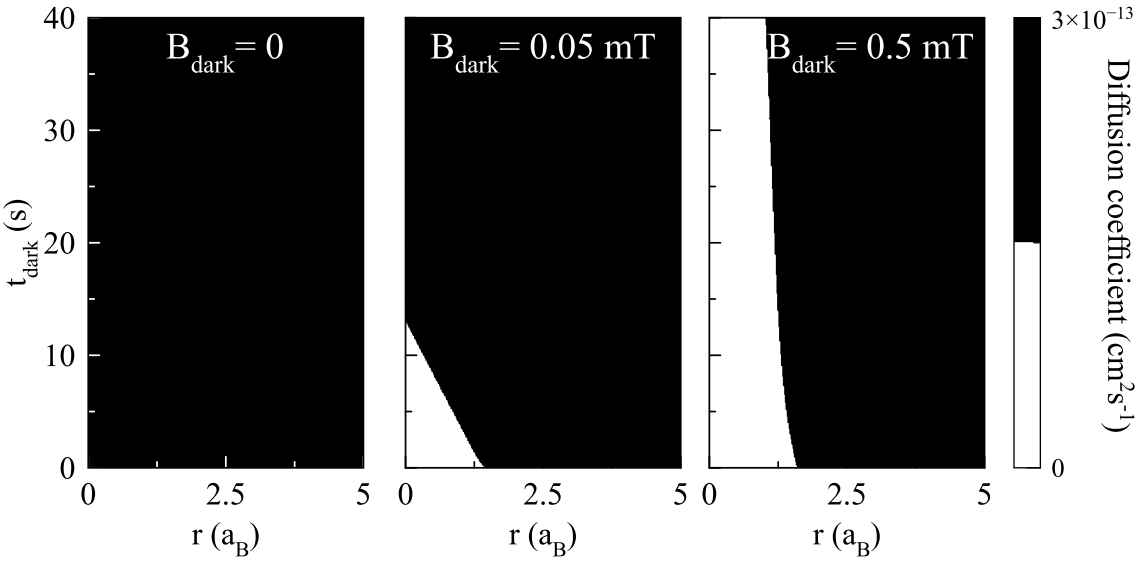

Figure 3.9: Colormaps of the temporal evolution of the spatially inhomogeneous diffusion coefficient for various values of $B_{\rm dark}$, calculated assuming that the diffusion barrier is abrupt, see Eq. (3.16). The initial ($t_{\rm dark} = 0$) distribution of nuclear spin temperature and diffusion coefficient is determined by fitting the pumping curve.

Nuclear spin relaxation and diffusion in the vicinity of donor-bound electrons

We now suggest a phenomenological expression to model $D(\mathbf{r}, t|B)$. The asymptotic conditions of Eqs. (3.11) and (3.12) can be fulfilled most easily by a step function

$$D(\mathbf{r}, t|B) = D_0 \; H(B_L^{(\rm fit)} - \Delta B_e^{\rm nn}), \tag{3.16}$$

where $H(x)$ is the Heaviside function, and $B_L^{(\rm fit)}$ is a fitting parameter close to the value of B_L. Of course, the choice of fitting function is not unique. We have also tested Lorentzian, Gaussian and Fermi functions, as well as a smoothed Heaviside function with similar results, so Eq. (3.16) was chosen for simplicity. A general problem that is inherent in this approach has to do with the Knight field following the evolution of the nuclear spin polarization. Because of this, when solving the diffusion equation (3.3), in principle one must recalculate $B_N \sim \int \langle I_z(r,t)\rangle |\psi_{e,\rm loc}(r)|^2 r^2 {\rm d}r$ at every time-step of the calculation. We evade this by first modeling the experimental data using a set of constant diffusion coefficients $D(B_{\rm dark})$, as shown in Fig. 3.7. The resulting theoretical curves are used as estimates of the Overhauser field for the purposes of calculating the diffusion coefficient according to Eq. (3.16). Colormaps of $D(r, t|B)$ are presented in Fig. 3.9. Evidently, the diffusion barrier produces a more lasting effect with increasing $B_{\rm dark}$. Injecting these into the diffusion equation, we obtain the spatiotemporal evolution of the nuclear spin polarization shown in Fig. 3.10. Performing a spatial integration weighted by the localized electron probability density [Eq. (3.4)] produces the theoretical curves demonstrated in Fig. 3.5. A quantitative agreement with the experimental observations is evident.

Note that the optical cooling stage, where the strong field $B_{\rm pump}$ is applied, is modeled with the diffusion coefficient $D = 0$, while the curve at $B_{\rm dark} = 0$ corresponds to the maximum diffusion coefficient $D_0 = 3 \times 10^{-13}$ cm^{2}s^{-1}, which is within expectations as it similar to what is typically seen in GaAs [153, 159].

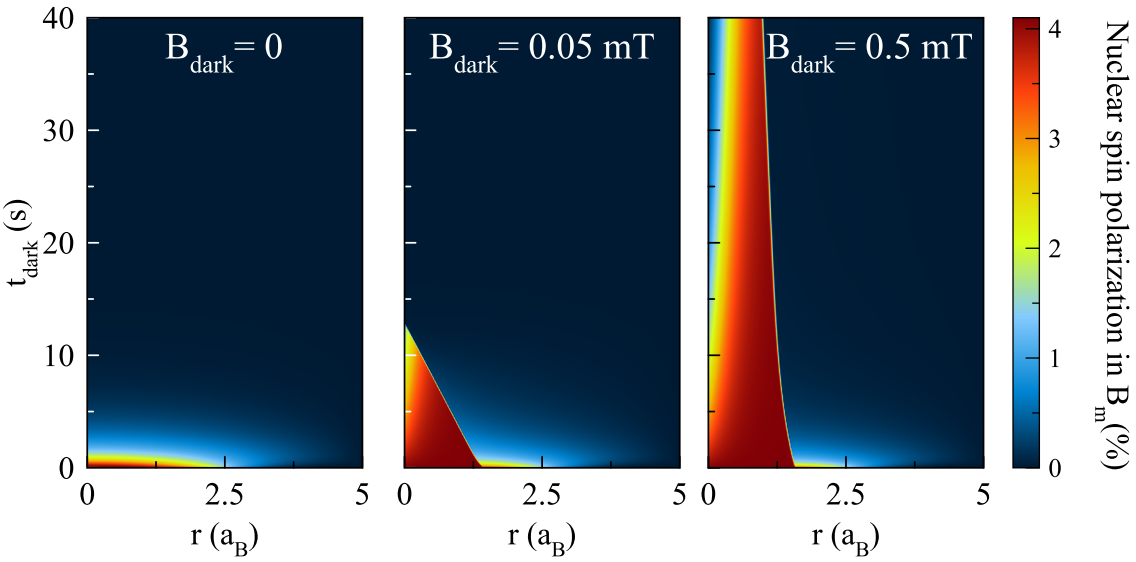

Figure 3.10: Colormaps of the temporal evolution of $\langle I_z \rangle$ accounting for the formation of a nuclear spin diffusion barrier. Diffusion is forbidden inside the barrier (see Fig. 3.9), and the decay of nuclear spin polarization follows the relaxation rate $\Gamma(r,t)$. The inhibition of nuclear spin diffusion towards the center of the neutral donor leads to the increase of nuclear spin relaxation times.

3.3.2 Free electrons (Sample B)

As discussed in the previous Section, the seconds-long nuclear spin relaxation and its magnetic field dependence in Sample A are direct consequences of strong electron localization. Since in Sample B we observe nuclear spin relaxation times of the order of a hundred seconds, the electrons responsible for this relaxation must be much less localized. Indeed, as discussed in Section 3.2.1, there is a resident electron gas in Sample B, so we turn our attention to free 2D electrons.

In structures hosting an electron gas, nuclear spin relaxation via interaction with free electrons is known to be relevant [141, 153, 155, 157, 219]. In the extreme case of a degenerate electron gas, one expects the Korringa relaxation mechanism to dominate. Its defining feature is the simple relationship $\gamma_\mathrm{K} \propto k_\mathrm{B}T$ between the Korringa relaxation rate γ_K and the temperature of the electron gas [154]. This is consistent with our measurements, which yield $\Gamma^{-1} = (138 \pm 8)\,\mathrm{s}$ at $T = 5$ K and $\Gamma^{-1} = (75 \pm 9)\,\mathrm{s}$ at $T = 10$ K, as determined from single-exponential fits of the data shown in Fig. 3.6. Moreover, this excludes localized electrons as the source of nuclear spin relaxation, as one would expect the opposite trend with increasing temperature. Indeed, delocalization of electrons with increasing temperature would more likely lead to dynamical averaging of the hyperfine interaction, which would slow down nuclear spin relaxation, in contrast to our observations. Nevertheless, since Sample B was not intentionally doped, it is doubtful that the electron gas can be considered degenerate, which raises questions regarding the observed temperature dependence. Furthermore, it would be preferable to quantitatively reproduce the experimental nuclear spin relaxation rates, using as few free parameters as possible. Thus, we perform a quantum-mechanical calculation of nuclear spin relaxation mediated by a 2D electron gas of arbitrary density.

Nuclear spin relaxation induced by hyperfine interaction with a 2D electron gas

Let us consider a perfect infinite QW of width L hosting a 2D electron gas described by Fermi statistics covering an in-plane area S. Applying the same approach as in Ref. [158], we calculate the matrix elements of the electron-nucleus spin-flip transitions due to hyperfine interaction.

Let S_z be the electron spin projection on the QW growth axis, and let $I_{z,j}$ be that for the j-th nucleus. The free electron's wave function in the QW $\psi_{e,\mathrm{free}}(\mathbf{r})$ is given by:

$$\psi_{e,\mathrm{free}}(\mathbf{r}) = \sqrt{\frac{2}{LS}} \cos\left(\frac{\pi}{L} z\right). \tag{3.17}$$

Denoting the hyperfine interaction operator as $\hat{V}_j(\mathbf{r}) = A_j\, \nu_0\, \hat{\mathbf{I}}_j \cdot \hat{\mathbf{S}}\, \delta(\mathbf{r} - \mathbf{r}_j)$, where $\hat{\mathbf{S}}$ and $\hat{\mathbf{I}}_j$ are the spin operators for electron and j-th nucleus, respectively, we may write the matrix elements for the mutual spin-flips of the electron and a nucleus as

$$M_{\pm,j} = \langle S_z \mp 1, I_{z,j} \pm 1, \psi_{e,\mathrm{free}} |\, \hat{V}_j \,| S_z, I_{z,j} \psi_{e,\mathrm{free}} \rangle\,. \tag{3.18}$$

A straightforward calculation gives

$$|M_{\pm,j}|^2 = \frac{1}{4} \left(A_j\, \nu_0\right)^2 |\psi_{e,\mathrm{free}}(z_j)|^4 \left[I(I+1) - I_{z,j}^2 \mp I_{z,j}\right]. \tag{3.19}$$

To deal with the average nuclear spin $\langle I_z(\mathbf{r}, t)\rangle$ interacting with the electron at a given position, we average the matrix elements as

$$|M_{\pm}(z)|^2 = \frac{1}{4} \langle A^2 \rangle\, \nu_0^2\, |\psi_{e,\mathrm{free}}(z)|^4 \left[I(I+1) - \langle I_z^2 \rangle \mp \langle I_z \rangle\right]. \tag{3.20}$$

The average square of the hyperfine constant $\langle A^2 \rangle$ is given by

$$\langle A^2 \rangle = \frac{\sum_\alpha A_\alpha^2 x_\alpha}{\sum_\alpha x_\alpha}, \tag{3.21}$$

where the sum goes over all magnetic isotopes in CdTe, see Table 1.1.

To obtain the nuclear spin flip rate we average the matrix elements over the statistics of the electron gas, i. e., the Fermi-Dirac distribution $f(E, E_\mathrm{F}) = \left(1 + \exp\left[(E - E_\mathrm{F})/k_\mathrm{B}T\right]\right)^{-1}$. According to the Fermi's golden rule

$$W_\pm = \frac{2\pi}{\hbar} |M_\pm|^2 g_{2\mathrm{D}}^2 \int_0^\infty f(E, E_{\mathrm{F},\pm}) \left[1 - f(E, E_{\mathrm{F},\mp})\right] \mathrm{d}E, \tag{3.22}$$

where $g_{2\mathrm{D}} = m_e S/\pi\hbar^2$ is the 2D density of states, $E_{\mathrm{F},\pm} = E_\mathrm{F} \pm \Delta/2$ is the quasi-Fermi level of the $S_z = \pm 1/2$ electrons, Δ is the splitting of the quasi-Fermi levels, and $E = 0$ corresponds to the bottom of the conduction band. Neglecting nuclear spin diffusion, we write the rate of change of the nuclear spin as

$$\frac{\mathrm{d}\langle I_z \rangle}{\mathrm{d}t} = W_+ - W_-. \tag{3.23}$$

Performing the integration in Eq. (3.22) we find

$$\begin{aligned} W_+ - W_- = {} & \frac{\pi}{\hbar} k_\mathrm{B} T \langle A^2 \rangle\, \nu_0^2 g_{2\mathrm{D}}^2 |\psi_{e,\mathrm{free}}(z)|^4 \\ & \times \left[\tanh \tfrac{\Delta}{2k_\mathrm{B}T} \left[I(I+1) - \langle I_z^2 \rangle\right] - \langle I_z \rangle\right] \\ & \times f(\Delta, E_\mathrm{F}, T), \end{aligned} \tag{3.24}$$

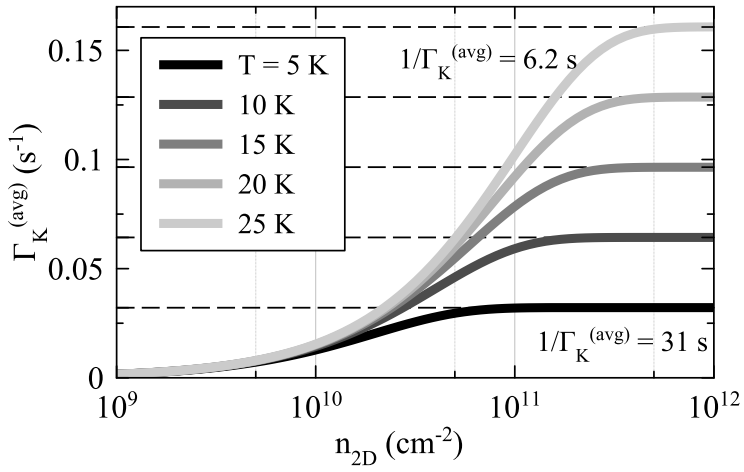

Figure 3.11: Average Korringa-like relaxation rate $\langle\Gamma_K\rangle$ as a function of 2D electron gas density at various temperatures in a 20-nm CdTe QW, calculated according to Eqs. (3.26) and (3.28). The relaxation time of a degenerate electron gas τ_K^d is marked for $T = 5$ K and 25 K, highlighting the distinct $\tau_K^d T = \text{const}$ behavior.

where

$$f(\Delta, E_F, T) = \frac{1}{2} \ln \left| \frac{e^{-E_F/k_B T} + e^{\Delta/2k_B T}}{e^{-E_F/k_B T} + e^{-\Delta/2k_B T}} \right| \coth \frac{\Delta}{2k_B T} \tag{3.25}$$

is a dimensionless factor that depends on the 2D electron gas density and temperature. For a degenerate unpolarized gas $f(\Delta, E_F, T) = 1$, and we recover the classic Korringa relaxation [154].

In Eq. (3.24), the term proportional to $[I(I+1) - \langle I_z^2\rangle]$ can be identified as the pumping term, while the coefficient before $\langle I_z\rangle$ is the relaxation rate. When the pumping beam is turned off after the optical cooling stage, the few resident electrons in Sample B rapidly lose the light-induced polarization, and the pumping term disappears as $\Delta \to 0$. We are then left with the Korringa-like nuclear spin relaxation rate

$$\Gamma_K(z) = \frac{\pi}{\hbar} \frac{k_B T}{1 + e^{-E_F/k_B T}} \langle A^2\rangle \, \nu_0^2 \, g_{2D}^2 |\psi_{e,\text{free}}(z)|^4, \tag{3.26}$$

which recovers the Korringa behavior $\Gamma_K(z) \propto k_B T$ at high electron densities, where $E_F \gg k_B T$, but is always spatially inhomogeneous due to the $|\psi_{e,\text{free}}(z)|^4$ factor. The result is similar to the usual bulk Korringa relaxation [154] and the results of Ref. [158], though the low-density correction has not been discussed previously in the literature.

A spatially averaged relaxation rate $\Gamma_K^{(avg)}$ can be used as an estimate of the observed nuclear spin relaxation rate:

$$\Gamma_K^{(avg)} = \frac{1}{L} \int_{QW} \Gamma_K(z) dz \tag{3.27}$$

Considering that the Fermi energy and the electron density are linked by

$$n_{2D} = \int_0^\infty g_{2D} f(E, E_F) dE, \tag{3.28}$$

we may directly plot $\Gamma_K^{(avg)}$ as a function of electron density using the parameters from Table 1.1, see Fig. 3.11.

Korringa-like relaxation and nuclear spin diffusion

As shown above, a prominent feature of nuclear spin relaxation via QW electrons is the dependence of their relaxation rate Γ_K on the position of the nucleus along the QW growth axis: $\Gamma_\mathrm{K} \propto |\psi_{e,\mathrm{free}}(z)|^4$. Performing a calculation of ΔB_e^nn similar to that made for Sample A via Eq. (3.10), we find that during pumping, when the Knight field is at its maximum due to the high density and average spin of photocreated electrons, a soft diffusion barrier may arise along the growth axis. During relaxation, however, confinement-induced localization of resident electrons in the QW is certainly insufficient to significantly affect spin diffusion along z, and the diffusion barrier does not need to be considered.

Until now, we have not discussed the large long-lived backgrounds seen in Fig. 3.6. Their presence is quite surprising, especially in comparison with Sample A, where no long-lived signals are observed. We believe they can only be explained by assuming that the entirety of the QW is polarized during pumping, while the resident electron gas is only present in some areas of the QW, forming puddles. The former is consistent with Ref. [271], where homogeneous polarization occurs under resonant pumping. Although in our case the optical pumping is nonresonant, Sample B is pumped below the barrier, which ensures efficient polarization of the QW nuclei. It is possible that the bulk nuclei are also polarized indirectly, via spin diffusion. Once pumping is stopped, a slow relaxation process is observed. This could be caused by two factors: (i) The unpolarized resident electron gas siphons the nuclear spin polarization via Korringa-like relaxation as discussed above; (ii) Simultaneously, a portion of the polarization escapes into the electron-free parts of the QW via spin diffusion. However, the resident electron gas induces relaxation also during pumping. Hence, the nuclei situated within electron puddles should not be more polarized than the rest of the QW, and the second mechanism is unlikely to be significant. Additionally, as we have shown in Section 1.4.5, mutual spin flips between ^{111}Cd and ^{113}Cd isotopes become forbidden in magnetic fields of around 1 mT, and this should lead to around a two-fold decrease of the spin diffusion coefficient. The fact that the observed relaxation rate is quite insensitive to changes in magnetic field is another argument against (ii). Therefore, it seems that the relaxation is mostly due to the electron gas, and not spin diffusion. However weak the spin diffusion, eventually a quasi-stationary regime is reached, where the flow of nuclear spin into the puddles becomes completely compensated by the slow Korringa-like relaxation, leading to the long-lived signal.

Unfortunately, it is not feasible to meaningfully model the spatiotemporal nuclear spin dynamics of Sample B with a diffusion equation similarly to Section 3.3.1, as that requires knowledge of the in-plane electron gas localization area (i. e., the puddle size) in addition to other parameters such as the Fermi energy and the diffusion coefficient. A simpler but nevertheless insightful model can be derived by performing a spatial integration of the diffusion equation over the area occupied by the resident electron gas. This yields a rate equation for the Overhauser field, or, equivalently, for the spatially averaged nuclear spin $\langle I_z \rangle = IB_N/b_N$ with the average Korringa-like relaxation rate $\Gamma_\mathrm{K}^{(\mathrm{avg})}$ [see Eq. (3.27)]. An additional term $P_D(t)$ describes the nuclear spin diffusion flow into or out of the area:

$$\frac{\partial \langle I_z \rangle(t)}{\partial t} = P_D(t) - \Gamma_\mathrm{K}^{(\mathrm{avg})} I_z(t). \tag{3.29}$$

Since one cannot easily calculate $P_D(t)$, we shall use a simplified phenomenological expression:

$$P_D(t) = \Gamma_D \left[J_z - \langle I_z \rangle(z) \right], \tag{3.30}$$

where J_z is the average nuclear spin in electron-free areas which are unaffected by Korringa-like relaxation, and Γ_D is the diffusion rate. The diffusion coefficient cannot be extracted

with this approach, unfortunately. Furthermore, only the sum $\Gamma_{\mathrm{K}}^{(\mathrm{avg})} + \Gamma_D$ is determined from experiments, although we would expect $\Gamma_D \ll \Gamma_{\mathrm{K}}^{(\mathrm{avg})}$, as discussed above.

Fitting the model defined by Eqs. (3.29) and (3.30) to the data shown in Fig. 3.6 enables us to derive the lower limit of the nuclear spin polarization of the entire QW in Sample B, which is around 15% at $T = 5$ K and $6.5 - 8\%$ at 10 K. These estimates are obtained under the assumption that the observed relaxation is entirely due to diffusion, so $\Gamma_D \gg \Gamma_{\mathrm{K}}^{(\mathrm{avg})}$. This is very unlikely as we have discussed above, hence we expect that the nuclear spin polarization in electron-free areas is much higher than these lower bound estimates. On the other hand, if the relaxation was entirely due to the resident electron gas, that would require small 2D densities of approximately 5×10^9 cm^{-2} and 8×10^9 cm^{-2} for $T = 5$ K and 10 K, respectively (see Fig. 3.11), which are reasonable carrier densities considering the PL spectrum in Fig. 3.2 (b) [40, 42]. The difference between the two densities is also unsurprising, as it is possible that at higher temperatures more electrons from the barriers are collected into the QW, and more donor-acceptor pairs inside the QW are ionized. The noticeable difference between the backgrounds in $B_{\mathrm{dark}} = 0.68$ mT and 6.8 mT data at $T = 10$ K is not clear as the nature of the background signal is not identified in sufficient detail.

3.4 Conclusions

The nuclear spin dynamics in CdTe QWs is shown to depend strongly on the nature of the electrons present in the sample. In the presence of donor-bound electrons, like in the CdTe/(Cd,Zn)Te QW studied here, the enhanced role of the hyperfine interaction is a direct consequence of features specific to CdTe: the low density of magnetic nuclei and absence of quadrupole nuclear moments lead to very efficient nuclear spin cooling, while the large binding energy of electrons produces a strong hyperfine interaction. Thus, the normally weak effect of dynamic polarization of electron spins by the nuclei is enhanced, and leads to the formation of nuclear spin diffusion barrier around neutral donors. The nuclear spin relaxation is then easily tunable. In zero field nuclear spin diffusion is efficient and the relaxation time is of the order of seconds. In fields larger than B_L, diffusion is strongly suppressed, increasing the nuclear spin lifetime by more than an order of magnitude in a field of 2.5 mT. A model that accounts for the spatial inhomogeneity of the Knight field and the resulting field-dependent diffusion barrier allows us to satisfyingly describe the experimental results both qualitatively and quantitatively.

On the other hand, if resident electrons form a nondegenerate 2D electron gas, as it is in the CdTe/(Cd,Mg)Te QW studied in this work, nuclear spin relaxation is much slower, and is field-independent at least up to fields of the order of 7 mT. At $T = 10$ K, the relaxation time is of the order of 70 s, and twice as slow at $T = 5$ K, much longer than what was measured near neutral donors in the CdTe/(Cd,Zn)Te QW. The observed nuclear spin relaxation is consistent with the Korringa-like mechanism, which is supported by the quantitative agreement of relaxation rate calculations with the experiments at two temperatures. Notably, not only the nuclei in the areas covered by electron gas puddles, but the nuclear spin system across the entire QW plane is polarized due to efficient below-barrier pumping. This introduces a spin diffusion flow into the areas occupied by the resident electrons. Eventually a steady state is reached, where we observe a stable nuclear spin polarization that persists for thousands of seconds, dynamically supported by spin diffusion. Modeling shows that at least a $\sim 15\%$ polarization of the bulk nuclei is achieved at $T = 5$ K in fields as small as 0.1 mT, although further study is required to completely unveil the nature of the long-lived signal and its temperature dependence. The theoretical description of free electron-mediated relaxation includes a low-density correction, which generalizes the Korringa relaxation mechanism for arbitrary QW electron densities. This

may become useful if the electron gas is purposely injected, either electrically or by modulation doping, at densities below the Mott transition.

Finally, the sub-microkelvin temperatures that have been reached by unoptimized optical pumping indicate that CdTe is a potential candidate for reaching record low nuclear spin temperatures, presumably due to the low abundance of magnetic isotopes and their zero quadrupole moment. The very long nuclear spin relaxation times achieved in Sample B under non-optimized conditions serve as a great motivator for further studies.

Chapter 4

Conclusions and perspectives

In this work, we have performed a detailed study of electron and nuclear spatiotemporal spin dynamics of various nanostructures based on n-CdTe.

The angle-resolved implementation of spin noise spectroscopy reported in this work significantly expands the experimental power of the original technique, permitting the direct observation of distinct spin jump mechanisms in epitaxial n-CdTe in reciprocal space within an all-optical technique. The two-state model provides deep insight into the spatiotemporal spin dynamics of donor-bound electrons in n-CdTe and enables us to explain all the experimental data, highlighting the previously underestimated effect of conduction band electrons one the spin noise lineshape. The technique can be applied to other semiconductors. A particularly interesting and straightforward subject could be n-GaAs, as the wavevector region of interest is more compact due to the larger Bohr radius; AR-SNS studies on n-GaAs could yield interesting information on the spatiotemporal spin dynamics that could be directly compared to existing works combining Hanle and electrical transport measurements, e. g., Ref. [105]. The technique could also be applied to emerging and cosequently less-understood materials such as TMDs, as it presents a very detailed but straightforward picture of spin dynamics, and to systems with larger bandgaps, for example GaN, as that would facilitate access to larger wavevectors, up to $\sim$100 µm^{-1} in backscattering geometry, corresponding to a spatial resolution of around 10 nm. GaN could be a particularly interesting platform for AR-SNS studies of conduction band dynamics via donor-bound spins, as the greater binding energy should result in a generally much weaker contribution of mutual spin flips between donors.

The physics of the nuclear spin system of n-CdTe is significantly affected by the electronic structure of the sample, which results in qualitatively different nuclear spin dynamics in cases where electrons are strongly or weakly localized. In particular, we present strong evidence to the formation of a nuclear spin diffusion barrier around neutral donors in fields exceeding the local field. We show that the onset of the diffusion barrier is made possible due to the intrinsic properties of n-CdTe: large neutral donor binding energy, small local nuclear field, and absence of quadrupolar effects. Conversely, in the presence of low-density puddles of two-dimensional electron gas, no diffusion barrier is formed due to weak localization, and consequently no field-dependence of nuclear spin dynamics is observed. The interplay of slow Korringa-like relaxation and a spin diffusion flow into areas hosting the electron gas results in complex nuclear spin dynamics that are governed by the Korringa-like relaxation rate ($\sim$ 100 s) and a very long-lived ($\sim$ 1000 s) contribution, the exact nature of which is not completely understood. These findings are one of the stepping stones to more profound studies of the CdTe nuclear spin system.

Appendix A

Calculation of the local and kinetic local fields

As mentioned in a footnote in Section 1.3.3, we are following the convention of Ref. [137], where the trace operation includes a normalizing coefficient for the density matrix. Although the density matrix is not directly encountered in Eq. (1.29), it is used to obtain the formula for B_L, which has historically been used to describe adiabatic changes of the nuclear spin system, particularly in weak fields. Assuming high temperatures, the spin density matrix is written as $\sigma = 1 - \beta_N \hat{\mathcal{H}}_{\mathrm{SS}}$, where β_N is the inverse spin temperature. Evidently, at infinite temperature, the trace of this matrix is equal to the dimension of $\hat{\mathcal{H}}_{\mathrm{SS}}$, which is $(2I+1)$ for a single spin I.

A.1 Local field

We proceed to calculating the local field B_L given by Eq. (1.29) within the aforementioned convention, assuming identical nuclei; an alternative derivation can be found, e. g., in Ref. [144]. Let us assume that the spin Hamiltonian of a pair of interacting spins $\mathcal{H}_{\mathrm{SS},ij}$ is given by an interaction with the symmetry of the magnetic dipole-dipole coupling, i. e.,

$$\hat{\mathcal{H}}_{\mathrm{SS},ij} = \mathcal{A}_{ij} \hat{\mathbf{I}}_i \cdot \hat{\mathbf{I}}_j + \mathcal{B}_{ij} \left(\hat{\mathbf{I}}_i \cdot \hat{\mathbf{r}}_{ij} \right) \left(\hat{\mathbf{I}}_j \cdot \hat{\mathbf{r}}_{ij} \right), \tag{A.1}$$

where $\mathcal{A}_{ij}$ and $\mathcal{B}_{ij}$ are the interaction constants, and $\hat{\mathbf{r}}_{ij} = (r_x \; r_y \; r_z)$ is a unit vector connecting the two spins. Writing out all terms of the Hamiltonian, we get

$$\hat{\mathcal{H}}_{\mathrm{SS},ij} = \sum_{\alpha=x,y,z} (\mathcal{A}_{ij} + \mathcal{B}_{ij} r_\alpha^2) \hat{I}_{i,\alpha} \hat{I}_{j,\alpha} + \mathcal{B}_{ij} \sum_{\alpha \neq \beta} r_\alpha r_\beta \left(\hat{I}_{i,\alpha} \hat{I}_{j,\beta} \right). \tag{A.2}$$

$\hat{\mathcal{H}}^2_{\mathrm{SS},ij}$ contains all the listed terms squared, and also various cross terms. The latter contain odd powers of the angular momentum operators, and do not contribute to the trace due to the following property of angular momentum operators [272]:

$$\mathrm{Tr}\left\{ I_{i,\alpha} I_{j,\beta} \right\} = \frac{I(I+1)}{3} \delta_{\alpha\beta}, \tag{A.3}$$

We end up with

$$\mathrm{Tr}\left\{ \hat{\mathcal{H}}^2_{\mathrm{SS},ij} \right\} = \left[\frac{I(I+1)}{3} \right]^2 \left(3\mathcal{A}_{ij}^2 + \mathcal{B}_{ij}^2 + 2\mathcal{A}_{ij}\mathcal{B}_{ij} \right). \tag{A.4}$$

For the dipole-dipole coupling, we introduce the constant $\mathcal{D}_{ij} = \hbar^2 \gamma_N^2 r_{ij}^{-3}$. Then, $\mathcal{A}_{ij} = \mathcal{D}_{ij}$, $\mathcal{B}_{ij} = -3\mathcal{D}_{ij}$, and

$$\mathrm{Tr}\left\{ \hat{\mathcal{H}}^2_{\mathrm{dd},ij} \right\} = \left[\frac{I(I+1)}{3} \right]^2 6\mathcal{D}_{ij}^2. \tag{A.5}$$

The two equations above must be summed over all sites j and divided by 2 to obtain the trace per single spin. Using Eq. (1.29), we complete the calculation with

$$B_{L,\mathrm{SS}}^2 = \frac{1}{N}\frac{I(I+1)}{3\hbar^2\gamma_N^2}\sum_{ij}\frac{1}{2}\left(3\mathcal{A}_{ij}^2 + \mathcal{B}_{ij}^2 + 2\mathcal{A}_{ij}\mathcal{B}_{ij}\right) \tag{A.6}$$

for an arbitrary spin Hamiltonian containing pseudodipolar and exchange terms, and

$$B_{L,\mathrm{dd}}^2 = \frac{1}{N}\frac{I(I+1)}{3\hbar^2\gamma_N^2}\sum_{ij}3\mathcal{D}_{ij}^2 = I(I+1)\hbar^2\gamma_N^2\sum_j\frac{1}{r_{ij}^6} \tag{A.7}$$

for a strictly dipole-dipole coupling. In Ref. [136], a rigorous calculation over the entire GaAs lattice is presented, accounting for the different nuclei, yielding $B_{L,\mathrm{dd}} = 0.16$ mT. Equation (11) of Ref. [136] is equally applicable to the nuclear spin system of CdTe. A rigorous calculation shows that the result is unaffected by the diluted nature of the CdTe nuclear spin system, as long as one averages the gyromagnetic ratios over all isotopes, including those that do not possess nonzero spin. The equation is as follows:

$$\begin{aligned} B_{L,\mathrm{dd}}^2 = \frac{\mathrm{Tr}\left\{\hat{\mathcal{H}}_{\mathrm{dd}}^2\right\}}{\mathrm{Tr}\left\{M_z^2\right\}} = &\frac{\hbar^2 I(I+1)}{2\langle\gamma^2\rangle a_0^6}\left\{\left[\langle\gamma_{\mathrm{Cd}}^2\rangle^2 + \langle\gamma_{\mathrm{Te}}^2\rangle^2\right]F_1\right. \\ &\left. + 2\langle\gamma_{\mathrm{Cd}}^2\rangle\langle\gamma_{\mathrm{Te}}^2\rangle\left[F_2 + (2B_{\mathrm{nn}} + B_{\mathrm{nn}}^2 + \frac{A_{\mathrm{nn}}^2}{2})F_3\right]\right\} \end{aligned} \tag{A.8}$$

where $\gamma_{(\mathrm{Cd,Te})}$ stands for the gyromagnetic ratios of CdTe (Cd, Te) nuclei, the $\langle ...\rangle$ operation averages over all isotopes α described by the abundances x_α, and the quantities $F_1 = 115.6$, $F_2 = 660.6$, and $F_3 = 606.8$ are lattice sums that can be consulted in Ref. [136]. In particular,

$$\langle\gamma^2\rangle = \frac{1}{2}\sum_\alpha\gamma_\alpha^2 x_\alpha \tag{A.9}$$

for all nuclei in CdTe, where the 1/2 factor accounts for the presence of two types of nuclei. The constants A_{nn}, B_{nn} can be converted to $\mathcal{A}_{ij}$ and $\mathcal{B}_{ij}$ in a straightforward way. This calculation results in $B_{L,\mathrm{dd}} = 0.019$ mT and $B_{L,\mathrm{SS}} = 0.030$ mT. The latter value is in excellent agreement with the half-width of the Lorentz curve modeling the $D(B)$ dependence in Fig. 3.7 of Chapter 3.

A.2 Kinetic local field

We now turn our attention to the kinetic local field B_{LK} which becomes important for the nuclear spin warm-up rate in fields of the order of B_L. The basic formula is shown in Eq. (1.34). For the following calculation, we can start from the Hamiltonian (A.1) without its secular part, i. e.,

$$\hat{\mathcal{H}}'_{\mathrm{SS},ij} = \mathcal{B}_{ij}\sum_{\alpha\neq\beta}r_\alpha r_\beta\left(\hat{I}_{i,\alpha}\hat{I}_{j,\beta}\right), \tag{A.10}$$

as the secular part conserves total spin and does not contribute to B_{LK}. Similarly to A.1, we obtain

$$\mathrm{Tr}\left\{\left[\hat{\mathcal{H}}_{\mathrm{SS},ij}^2, \hat{I}_{i,x} + \hat{I}_{j,x}\right]\right\} = -\left[\frac{I(I+1)}{3}\right]^2 2B^2\left(1 - r_x^2\right). \tag{A.11}$$

Dividing by 2 and averaging over all possible orientations, $\langle r_x^2\rangle = \langle \hat{r_{ij}}\rangle/3 = 1/3$, we arrive at

$$B^2_{LK,\mathrm{SS}} = \frac{1}{N}\frac{I(I+1)}{3\hbar^2\gamma_N^2}\sum_{ij}\frac{2}{3}\mathcal{B}^2_{ij}. \tag{A.12}$$

This result can be used to express $B^2_{LK,\mathrm{SS}}$ through $B^2_{L,\mathrm{SS}}$:

$$B^2_{LK,\mathrm{SS}} = \frac{4}{3}\, B^2_{L,\mathrm{SS}}\Big|_{\mathcal{A}_{ij}=0}. \tag{A.13}$$

Alternatively, if using the convention of Ref. [136],

$$B^2_{LK,\mathrm{SS}} = \frac{1}{N}\frac{I(I+1)}{3\hbar^2\gamma_N^2}\sum_{ij}12\mathcal{D}^2_{ij}(1+B_{\mathrm{nn}})^2 = 2\, B^2_{L,\mathrm{SS}}\Big|_{A_{\mathrm{nn}}=0}. \tag{A.14}$$

For the particular case of a strictly dipolar Hamiltonian,

$$B^2_{LK,\mathrm{dd}} = 2B^2_{L,\mathrm{dd}}. \tag{A.15}$$

Equation (A.8) can then be easily adapted to the calculation of $B_{LK,\mathrm{SS}}$ using Eq. (A.14):

$$B^2_{LK,\mathrm{SS}} = \frac{\hbar^2 I(I+1)}{\langle\gamma^2\rangle a_0^6}\left\{\left[\langle\gamma^2_{\mathrm{Cd}}\rangle^2 + \langle\gamma^2_{\mathrm{Te}}\rangle^2\right]F_1 2\langle\gamma^2_{\mathrm{Cd}}\rangle\langle\gamma^2_{\mathrm{Te}}\rangle\left[F_2 + (2B_{\mathrm{nn}} + B^2_{\mathrm{nn}})F_3\right]\right\}, \tag{A.16}$$

which yields $B_{LK,\mathrm{dd}} = 0.038$ mT and $B_{LK,\mathrm{SS}} = 0.031$ mT. Though indirect interactions in CdTe are stronger than the dipole-dipole interaction, they are mostly scalar, hence they barely contribute to the kinetic local field. Indeed, the CdTe kinetic local field is actually decreased when accounting for indirect interactions using the parameters of Refs. [129, 130]. The resulting values of $B_{L,\mathrm{SS}}$ and $B_{LK,\mathrm{SS}}$ are practically identical, hence the intrinsic warm-up rate of CdTe is essentially field-independent even in very weak fields [see Eq. (1.33)].

Appendix B

Faddeeva function

Here, we provide a simple description of the Faddeeva function $w(z)$. The Faddeeva function, also known as the Kramp function, is a scaled complementary error function of a complex argument defined as

$$w(z) = e^{-z^2}\mathrm{erfc}(-iz) = e^{-z^2}\left(1 + \frac{2i}{\sqrt{\pi}}\int_0^z e^{t^2}\mathrm{d}t\right). \tag{B.1}$$

It was first tabulated by Faddeeva [273]. The function is useful in the description of localized electron spin noise affected by hyperfine interactions. For example, it appears when describing the effects of hops and hyperfine interactions on the spin noise spectrum of localized electron spins [22, 62] [see Eqs. (2.51, 2.55-2.57)]. In this context, it appears as

$$f(\omega) = w(i/\tau_\omega\delta_e) + \mathrm{c.\,c.}, \tag{B.2}$$

where $\tau_\omega = (-i\omega + \nu)$; ω is the frequency, ν combines the escape and relaxation rates, and δ_e describes the distribution of precession frequencies in the nuclear field. This function is plotted in Fig. B.1 for different regimes. Essentially, its behavior spans various lineshapes between Gaussian and Lorentzian, depending on the relative magnitude of δ_e and ν. The spin noise spectra in a magnetic field $\Omega \gg \delta_e$ can also be modeled by the Faddeeva function using the approximate Eq. (2.57). Indeed, Eq. (2.57) is the same lineshape as Eq. (B.2), but shifted by the value of the precession frequency Ω.

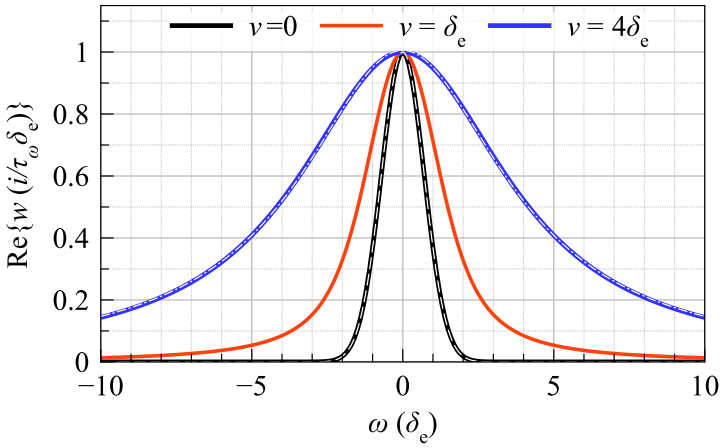

Figure B.1: Normalized function defined in Eq. (B.2), based on the Faddeeva function. In the absence of hops and relaxation ($\nu \ll \delta_e$), the function is essentially a Gaussian curve with width δ_e (dashed white line superimposed on the $\nu = 0$ curve). In the opposite case ($\nu \gg \delta_e$) the curve is well-fitted by a Lorentzian lineshape (dash-dotted white line over the $\nu = 4\delta_e$ curve).

Bibliography

[1] T. Na, S. H. Kang, and S.-O. Jung, "STT-MRAM sensing: a review", IEEE Transactions on Circuits and Systems II: Express Briefs **68**, 12–18 (2021).

[2] S. S. P. Parkin, M. Hayashi, and L. Thomas, "Magnetic domain-wall racetrack memory", Science **320**, 190–194 (2008).

[3] D. Kumar, T. Jin, R. Sbiaa, M. Kläui, S. Bedanta, S. Fukami, D. Ravelosona, S.-H. Yang, X. Liu, and S. Piramanayagam, "Domain wall memory: physics, materials, and devices", Physics Reports **958**, Domain Wall Memory: Physics, Materials, and Devices, 1–35 (2022).

[4] A. Sommerfeld, "Zur elektronentheorie der metalle auf grund der fermischen statistik", Zeitschrift für Physik **47**, 1–32 (1928).

[5] M. I. Dyakonov, *Spintronics?*, arXiv:cond-mat/0401369, 2004.

[6] I. A. Merkulov, A. L. Efros, and M. Rosen, "Electron spin relaxation by nuclei in semiconductor quantum dots", Phys. Rev. B **65**, 205309 (2002).

[7] A. Greilich, A. Shabaev, D. R. Yakovlev, A. L. Efros, I. A. Yugova, D. Reuter, A. D. Wieck, and M. Bayer, "Nuclei-induced frequency focusing of electron spin coherence", Science **317**, 1896–1899 (2007).

[8] J. Brossel and A. Kastler, "Detection of magnetic resonance in excited levels - an effect of resonance radiation depolarization", C. r. hebd. séances Acad. sci **229**, 1213–1215 (1949).

[9] G. Lampel, "Nuclear dynamic polarization by optical electronic saturation and optical pumping in semiconductors", Phys. Rev. Lett. **20**, 491–493 (1968).

[10] F. Meier and B. P. Zakharchenya, *Optical orientation* (North-Holland, Amsterdam, 1984).

[11] J. Shah, *Ultrafast spectroscopy of semiconductors and semiconductor nanostructures* (Springer Berlin, Heidelberg, 1996).

[12] M. M. Glazov, "Coherent spin dynamics of electrons and excitons in nanostructures (a review)", Physics of the Solid State **54**, 1–27 (2012).

[13] B. Náfrádi, M. Choucair, and L. Forró, "Electron spin dynamics of two-dimensional layered materials", Advanced Functional Materials **27**, 1604040 (2017).

[14] J. Zerhoch, S. Bodnar, J. E. Lerpinière, S. Liu, T. Neumann, B. Sergl, M. W. Heindl, A. Shcherbakov, A. Elghandour, R. Klingeler, A. B. Walker, and F. Deschler, "Motional narrowing effects in the excited state spin populations of Mn-doped hybrid perovskites", The Journal of Physical Chemistry Letters **15**, 2851–2858 (2024).

[15] D. Kudlacik, N. E. Kopteva, M. Kotur, D. R. Yakovlev, K. V. Kavokin, C. Harkort, M. Karzel, E. A. Zhukov, E. Evers, V. V. Belykh, and M. Bayer, "Optical spin orientation of localized electrons and holes interacting with nuclei in a $FA_{0.9}Cs_{0.1}PbI_{2.8}Br_{0.2}$ perovskite crystal", ACS Photonics **11**, 2757–2769 (2024).

[16] S. Philipps and W. Warmuth, *Photovoltaics Report*, https://www.ise.fraunhofer.de/en/publications/studies/photovoltaics-report.html, Accessed: 2024-08-16.

[17] M. (Mariska) de Wild-Scholten, "Energy payback time and carbon footprint of commercial photovoltaic systems", Solar Energy Materials and Solar Cells **119**, Thin-film Photovoltaic Solar Cells, 296–305 (2013).

[18] K. Kheng, R. T. Cox, M. Y. d'Aubigné, F. Bassani, K. Saminadayar, and S. Tatarenko, "Observation of negatively charged excitons X^- in semiconductor quantum wells", Phys. Rev. Lett. **71**, 1752–1755 (1993).

[19] L. S. Dang, D. Heger, R. André, F. Bœuf, and R. Romestain, "Stimulation of polariton photoluminescence in semiconductor microcavity", Phys. Rev. Lett. **81**, 3920–3923 (1998).

[20] J. Kasprzak, M. Richard, S. Kundermann, A. Baas, P. Jeambrun, J. M. J. Keeling, F. M. Marchetti, M. H. Szymańska, R. André, J. L. Staehli, V. Savona, P. B. Littlewood, B. Deveaud, and L. S. Dang, "Bose–einstein condensation of exciton polaritons", Nature **443**, 409–414 (2006).

[21] A. V. Mikhailov, A. S. Kurdyubov, E. S. Khramtsov, I. V. Ignatiev, B. F. Gribakin, S. Cronenberger, D. Scalbert, M. R. Vladimirova, and R. André, "Exciton dynamics in CdTe/CdZnTe quantum well", Semiconductors **57**, [Fiz. i tech. pol., **7**, 603 (2023)] (2023).

[22] S. Cronenberger, H. Boukari, D. Ferrand, J. Cibert, and D. Scalbert, "Long-range spin jump diffusion revealed by dynamic light scattering", Phys. Rev. B **103**, 205208 (2021).

[23] K. Wichrowska, T. Wosinski, J. Z. Domagala, S. Kret, S. Chusnutdinow, and G. Karczewski, "Structural defects in MBE-grown CdTe-basing heterojunctions designed for photovoltaic applications", Semiconductor Science and Technology **36**, 045022 (2021).

[24] V. Kochereshko, D. Yakovlev, R. Suris, W. Ossau, G. Landwehr, T. Wojtowicz, M. Kutrowski, G. Karczewski, and J. Kossut, "Exciton—electron interactions in CdTe/CdMgTe modulation-doped QW structures", Journal of Crystal Growth **184-185**, 826–830 (1998).

[25] V. L. Korenev, M. Salewski, I. A. Akimov, V. F. Sapega, L. Langer, I. V. Kalitukha, J. Debus, R. I. Dzhioev, D. R. Yakovlev, D. Müller, C. Schröder, H. Hövel, G. Karczewski, M. Wiater, T. Wojtowicz, Y. G. Kusrayev, and M. Bayer, "Long-range p–d exchange interaction in a ferromagnet–semiconductor hybrid structure", Nature Physics **12**, 85–91 (2016).

[26] B. F. Gribakin, S. Cronenberger, H. Boukari, and D. Scalbert, "Angle-resolved spin noise spectroscopy in semiconductors: two-state theory and experiments", Phys. Rev. Res. **7**, 013222 (2025).

[27] B. F. Gribakin, V. M. Litvyak, M. Kotur, R. André, M. Vladimirova, D. R. Yakovlev, and K. V. Kavokin, "Nuclear spin relaxation mediated by donor-bound and free electrons in wide CdTe quantum wells", Phys. Rev. B **109**, 195302 (2024).

[28] C. Kittel, *Quantum theory of solids* (Wiley, New York, 1963).

[29] S. Adachi, "Energy-band structure: energy-band gaps", in *Properties of group-IV, III-V and II-VI semiconductors* (John Wiley & Sons, Ltd, 2005) Chap. 6, pp. 103–145.

[30] A. Kiselev, E. Ivchenko, A. Sirenko, T. Ruf, M. Cardona, D. Yakovlev, W. Ossau, A. Waag, and G. Landwehr, "Electron and hole g factor anisotropy in CdTe/CdMgTe quantum wells", Journal of Crystal Growth **184-185**, 831–834 (1998).

[31] R. Braunstein and E. Kane, "The valence band structure of the III–V compounds", Journal of Physics and Chemistry of Solids **23**, 1423–1431 (1962).

[32] V. Čápek, K. Zimmerman, Č. Koňák, M. Popova, and P. Polivka, "Valence band structure of CdTe", physica status solidi (b) **56**, 739–747 (1973).

[33] P. Lefebvre, T. Richard, H. Mathieu, and J. Allègre, "Influence of spin-orbit split-off band on optical properties of spherical semiconductor nanocrystals. the case of CdTe", Solid State Communications **98**, 303–306 (1996).

[34] D. T. F. Marple, "Effective electron mass in CdTe", Phys. Rev. **129**, 2466–2470 (1963).

[35] M. Dyakonov, *Spin physics in semiconductors*, Springer Series in Solid-State Sciences (Springer Berlin, Heidelberg, 2008).

[36] R. D. L. Kronig, W. G. Penney, and R. H. Fowler, "Quantum mechanics of electrons in crystal lattices", Proceedings of the Royal Society of London. Series A, Containing Papers of a Mathematical and Physical Character **130**, 499–513 (1931).

[37] G. Garcia-Arellano, F. Bernardot, C. Testelin, and M. Chamarro, "Electron exchange energy of neutral donors inside a quantum well", Phys. Rev. B **98**, 195308 (2018).

[38] P. Y. Yu and M. Cardona, *Fundamentals of semiconductors: physics and materials properties* (Springer Berlin, 2010).

[39] J. Hubbard and B. H. Flowers, "Electron correlations in narrow energy bands", Proceedings of the Royal Society of London. Series A. Mathematical and Physical Sciences **276**, 238–257 (1963).

[40] G. Bartsch, M. Gerbracht, D. R. Yakovlev, J. H. Blokland, P. C. M. Christianen, E. A. Zhukov, A. B. Dzyubenko, G. Karczewski, T. Wojtowicz, J. Kossut, J. C. Maan, and M. Bayer, "Positively versus negatively charged excitons: a high magnetic field study of CdTe/$Cd_{1-x}Mg_xTe$ quantum wells", Phys. Rev. B **83**, 235317 (2011).

[41] G. V. Astakhov, M. M. Glazov, D. R. Yakovlev, E. A. Zhukov, W. Ossau, L. W. Molenkamp, and M. Bayer, "Time-resolved and continuous-wave optical spin pumping of semiconductor quantum wells", Semiconductor Science and Technology **23**, 114001 (2008).

[42] E. A. Zhukov, A. Greilich, D. R. Yakovlev, K. V. Kavokin, I. A. Yugova, O. A. Yugov, D. Suter, G. Karczewski, T. Wojtowicz, J. Kossut, V. V. Petrov, Y. K. Dolgikh, A. Pawlis, and M. Bayer, "All-optical NMR in semiconductors provided by resonant cooling of nuclear spins interacting with electrons in the resonant spin amplification regime", Phys. Rev. B **90**, 085311 (2014).

[43] E. Ivchenko, *Optical spectroscopy of semiconductor nanostructures* (Alpha Science, Harrow, 2005).

[44] M. Z. Maialle, E. A. de Andrada e Silva, and L. J. Sham, "Exciton spin dynamics in quantum wells", Phys. Rev. B **47**, 15776–15788 (1993).

[45] A. V. Trifonov, E. S. Khramtsov, K. V. Kavokin, I. V. Ignatiev, A. V. Kavokin, Y. P. Efimov, S. A. Eliseev, P. Y. Shapochkin, and M. Bayer, "Nanosecond spin coherence time of nonradiative excitons in GaAs/AlGaAs quantum wells", Phys. Rev. Lett. **122**, 147401 (2019).

[46] A. S. Kurdyubov, A. V. Trifonov, I. Y. Gerlovin, B. F. Gribakin, P. S. Grigoryev, A. V. Mikhailov, I. V. Ignatiev, Y. P. Efimov, S. A. Eliseev, V. A. Lovtcius, M. Aßmann, M. Bayer, and A. V. Kavokin, "Optical control of a dark exciton reservoir", Phys. Rev. B **104**, 035414 (2021).

[47] I. Filikhin, R. Y. Kezerashvili, S. M. Tsiklauri, and B. Vlahovic, "Trions in bulk and monolayer materials: Faddeev equations and hyperspherical harmonics", Nanotechnology **29**, 124002 (2018).

[48] J. M. Francou, K. Saminadayar, and J. L. Pautrat, "Shallow donors in CdTe", Phys. Rev. B **41**, 12035–12046 (1990).

[49] T. Schmidt, K. Lischka, and W. Zulehner, "Excitation-power dependence of the near-band-edge photoluminescence of semiconductors", Phys. Rev. B **45**, 8989–8994 (1992).

[50] A. Esser, E. Runge, R. Zimmermann, and W. Langbein, "Trions in GaAs quantum wells: photoluminescence lineshape analysis", physica status solidi (a) **178**, 489–494 (2000).

[51] F. J. Teran, L. Eaves, L. Mansouri, H. Buhmann, D. K. Maude, M. Potemski, M. Henini, and G. Hill, "Trion formation in narrow GaAs quantum well structures", Phys. Rev. B **71**, 161309 (2005).

[52] K. Kheng, R. T. Cox, M. Mamor, K. Saminadayar, and S. Tatarenko, "Negatively charged exciton X and donor bound exciton D^0X in planar doped CdTe/$Cd_{1-x}Zn_xTe$ quantum well heterostructures", Le Journal de Physique IV **03**, Publisher: EDP Sciences, C5–98 (1993).

[53] E. A. Chekhovich, M. N. Makhonin, A. I. Tartakovskii, A. Yacoby, H. Bluhm, K. C. Nowack, and L. M. K. Vandersypen, "Nuclear spin effects in semiconductor quantum dots", Nature Materials **12**, 494–504 (2013).

[54] M. M. Glazov, *Electron & Nuclear Spin Dynamics in Semiconductor Nanostructures* (Oxford University Press, Oxford, Sept. 2018).

[55] F. Bloch, "Nuclear induction", Phys. Rev. **70**, 460–474 (1946).

[56] F. H. L. Koppens, K. C. Nowack, and L. M. K. Vandersypen, "Spin echo of a single electron spin in a quantum dot", Phys. Rev. Lett. **100**, 236802 (2008).

[57] H. Bluhm, S. Foletti, I. Neder, M. Rudner, D. Mahalu, V. Umansky, and A. Yacoby, "Dephasing time of gaas electron-spin qubits coupled to a nuclear bath exceeding 200 µs", Nature Physics **7**, 109–113 (2011).

[58] A. Greilich, R. Oulton, E. A. Zhukov, I. A. Yugova, D. R. Yakovlev, M. Bayer, A. Shabaev, A. L. Efros, I. A. Merkulov, V. Stavarache, D. Reuter, and A. Wieck, "Optical control of spin coherence in singly charged (In, Ga)As/GaAs quantum dots", Phys. Rev. Lett. **96**, 227401 (2006).

[59] A. N. Kosarev, S. V. Poltavtsev, L. E. Golub, M. M. Glazov, M. Salewski, N. V. Kozyrev, E. A. Zhukov, D. R. Yakovlev, G. Karczewski, S. Chusnutdinow, T. Wojtowicz, I. A. Akimov, and M. Bayer, "Microscopic dynamics of electron hopping in a semiconductor quantum well probed by spin-dependent photon echoes", Phys. Rev. B **100**, 121401 (2019).

[60] B. Eble, O. Krebs, A. Lemaître, K. Kowalik, A. Kudelski, P. Voisin, B. Urbaszek, X. Marie, and T. Amand, "Dynamic nuclear polarization of a single charge-tunable InAs/GaAs quantum dot", Phys. Rev. B **74**, 081306 (2006).

[61] H. C. Torrey, "Bloch equations with diffusion terms", Phys. Rev. **104**, 563–565 (1956).

[62] M. M. Glazov, "Spin noise of localized electrons: interplay of hopping and hyperfine interaction", Phys. Rev. B **91**, 195301 (2015).

[63] N. Bloembergen, E. M. Purcell, and R. V. Pound, "Relaxation effects in nuclear magnetic resonance absorption", Phys. Rev. **73**, 679–712 (1948).

[64] M. Wurdack, E. Estrecho, S. Todd, T. Yun, M. Pieczarka, S. K. Earl, J. A. Davis, C. Schneider, A. G. Truscott, and E. A. Ostrovskaya, "Motional narrowing, ballistic transport, and trapping of room-temperature exciton polaritons in an atomically-thin semiconductor", Nature Communications **12**, 5366 (2021).

[65] G. Dresselhaus, "Spin-orbit coupling effects in zinc blende structures", Phys. Rev. **100**, 580–586 (1955).

[66] M. I. Dyakonov and V. Y. Kachorovskii, "Spin relaxation of two dimensional electrons in noncentrosymetric semiconductors", Soviet Physics: Semiconductors **20**, 110–116 (1986).

[67] M. Dyakonov and V. Perel, "Spin relaxation of conduction electrons in noncentrosymetric semiconductors", Solid State Physics **13**, 3023 (1972).

[68] R. I. Dzhioev, K. V. Kavokin, V. L. Korenev, M. V. Lazarev, B. Y. Meltser, M. N. Stepanova, B. P. Zakharchenya, D. Gammon, and D. S. Katzer, "Low-temperature spin relaxation in n-type GaAs", Phys. Rev. B **66**, 245204 (2002).

[69] P. H. Song and K. W. Kim, "Spin relaxation of conduction electrons in bulk III-V semiconductors", Phys. Rev. B **66**, 035207 (2002).

[70] K. V. Kavokin, "Anisotropic exchange interaction of localized conduction-band electrons in semiconductors", Phys. Rev. B **64**, 075305 (2001).

[71] L. P. Gor'kov and P. L. Krotkov, "Spin relaxation and antisymmetric exchange in n-doped III-V semiconductors", Phys. Rev. B **67**, 033203 (2003).

[72] C. M. Bender and S. A. Orszag, *Advanced mathematical methods for scientists and engineers i: asymptotic methods and perturbation theory* (Springer New York, New York, 2013).

[73] K. V. Kavokin, "Spin relaxation of localized electrons in n-type semiconductors", Semiconductor Science and Technology **23**, 114009 (2008).

[74] H. Goldstein, C. Poole, and J. Safko, *Classical mechanics* (Addison Wesley, Reading, MA, 2002).

[75] L. Fraiture, "A history of the description of the three-dimensional finite rotation", The Journal of the Astronautical Sciences **57**, 207–232 (2009).

[76] W. M. Witzel and S. Das Sarma, "Quantum theory for electron spin decoherence induced by nuclear spin dynamics in semiconductor quantum computer architectures: spectral diffusion of localized electron spins in the nuclear solid-state environment", Phys. Rev. B **74**, 035322 (2006).

[77] W. Yao, R.-B. Liu, and L. J. Sham, "Theory of electron spin decoherence by interacting nuclear spins in a quantum dot", Phys. Rev. B **74**, 195301 (2006).

[78] L. Zaporski, N. Shofer, J. H. Bodey, S. Manna, G. Gillard, M. H. Appel, C. Schimpf, S. F. Covre da Silva, J. Jarman, G. Delamare, G. Park, U. Haeusler, E. A. Chekhovich, A. Rastelli, D. A. Gangloff, M. Atatüre, and C. Le Gall, "Ideal refocusing of an optically active spin qubit under strong hyperfine interactions", Nature Nanotechnology **18**, 257–263 (2023).

[79] P.-F. Braun, X. Marie, L. Lombez, B. Urbaszek, T. Amand, P. Renucci, V. K. Kalevich, K. V. Kavokin, O. Krebs, P. Voisin, and Y. Masumoto, "Direct observation of the electron spin relaxation induced by nuclei in quantum dots", Phys. Rev. Lett. **94**, 116601 (2005).

[80] V. V. Belykh, K. V. Kavokin, D. R. Yakovlev, and M. Bayer, "Electron charge and spin delocalization revealed in the optically probed longitudinal and transverse spin dynamics in n-GaAs", Phys. Rev. B **96**, 241201(R) (2017).

[81] M. M. Glazov, "Magnetic field effects on spin relaxation in heterostructures", Phys. Rev. B **70**, 195314 (2004).

[82] X. Linpeng, T. Karin, M. V. Durnev, R. Barbour, M. M. Glazov, E. Y. Sherman, S. P. Watkins, S. Seto, and K.-M. C. Fu, "Longitudinal spin relaxation of donor-bound electrons in direct band-gap semiconductors", Phys. Rev. B **94**, 125401 (2016).

[83] G. Garcia-Arellano, F. Bernardot, G. Karczewski, C. Testelin, and M. Chamarro, "Spin relaxation time of donor-bound electrons in a CdTe quantum well", Phys. Rev. B **99**, 235301 (2019).

[84] P. Sterin, L. Abaspour, J. G. Lonnemann, E. P. Rugeramigabo, J. Hübner, and M. Oestreich, "Temperature-dependent electron spin relaxation at the metal-to-insulator transition in n-type GaAs", Phys. Rev. B **106**, 125202 (2022).

[85] D. Paget, "Optical detection of NMR in high-purity GaAs under optical pumping: efficient spin-exchange averaging between electronic states", Phys. Rev. B **24**, 3776–3793 (1981).

[86] R. I. Dzhioev, V. L. Korenev, I. A. Merkulov, B. P. Zakharchenya, D. Gammon, A. L. Efros, and D. S. Katzer, "Manipulation of the spin memory of electrons in n-GaAs", Phys. Rev. Lett. **88**, 256801 (2002).

[87] W. O. Putikka and R. Joynt, "Theory of optical orientation in n-type semiconductors", Phys. Rev. B **70**, 113201 (2004).

[88] G. D. Mahan and R. Woodworth, "Spin-exchange scattering in semiconductors", Phys. Rev. B **78**, 075205 (2008).

[89] N. J. Harmon, W. O. Putikka, and R. Joynt, "Theory of electron spin relaxation in ZnO", Phys. Rev. B **79**, 115204 (2009).

[90] N. J. Harmon, W. O. Putikka, and R. Joynt, "Theory of electron spin relaxation in n-doped quantum wells", Phys. Rev. B **81**, 085320 (2010).

[91] R. Giri, S. Cronenberger, M. M. Glazov, K. V. Kavokin, A. Lemaître, J. Bloch, M. Vladimirova, and D. Scalbert, "Nondestructive measurement of nuclear magnetization by off-resonant Faraday rotation", Phys. Rev. Lett. **111**, 087603 (2013).

[92] V. V. Belykh, E. Evers, D. R. Yakovlev, F. Fobbe, A. Greilich, and M. Bayer, "Extended pump-probe Faraday rotation spectroscopy of the submicrosecond electron spin dynamics in n-type GaAs", Phys. Rev. B **94**, 241202 (2016).

[93] N. J. Harmon, "Topics on the theory of electron spins in semiconductors", PhD thesis (Ohio State University, 2010).

[94] A. Halperin and A. A. Braner, "Evaluation of thermal activation energies from glow curves", Phys. Rev. **117**, 408–415 (1960).

[95] H. L. Cotal, A. C. Lewandowski, B. G. Markey, S. W. S. McKeever, E. Cantwell, and J. Aldridge, "1.4-eV photoluminescence and thermally stimulated conductivity in cadmium telluride", Journal of Applied Physics **67**, 975–982 (1990).

[96] J. Krustok, H. Collan, and K. Hjelt, "Does the low-temperature Arrhenius plot of the photoluminescence intensity in CdTe point towards an erroneous activation energy?", Journal of Applied Physics **81**, 1442–1445 (1997).

[97] D. Long and J. Myers, "Ionized-impurity scattering mobility of electrons in silicon", Phys. Rev. **115**, 1107–1118 (1959).

[98] S. Mandal, R. Dasgupta, T. K. Ballabh, T. R. Middya, and S. Tarafdar, "Diffusion with rearranging traps", Phys. Rev. E **63**, 026205 (2001).

[99] G. T. Barkema, P. Biswas, and H. van Beijeren, "Diffusion with random distribution of static traps", Phys. Rev. Lett. **87**, 170601 (2001).

[100] D. L. Huber, "Trapping of excitation in the average T-matrix approximation", Journal of Statistical Physics **30**, 345–354 (1983).

[101] S. Mora and Y. Pomeau, "Brownian diffusion in a dilute field of traps is Fickean but non-Gaussian", Phys. Rev. E **98**, 040101 (2018).

[102] D. L. Huber and K. K. Ghosh, "Trapping of excitation in the diffusion limit. Response at finite wave vector", Phys. Rev. B **26**, 3453–3455 (1982).

[103] J. C. Maxwel, "Illustrations of the dynamical theory of gases. Part I. On the motions and collisions of perfectly elastic spheres", Philosophical Magazine Series **19**, 19–32 (1860).

[104] P.-G. de Gennes, "Sur la relaxation nucleaire dans les cristaux ioniques", Journal of Physics and Chemistry of Solids **7**, 345–350 (1958).

[105] J. G. Lonnemann, E. P. Rugeramigabo, M. Oestreich, and J. Hübner, "Closing the gap between spatial and spin dynamics of electrons at the metal-to-insulator transition", Phys. Rev. B **96**, 045201 (2017).

[106] R. K. Harris, E. D. Becker, S. M. Cabral De Menezes, R. Goodfellow, and P. Granger, "NMR nomenclature: Nuclear spin properties and conventions for chemical shifts (IUPAC recommendations 2001)", Concepts in Magnetic Resonance **14**, 326–346 (2002).

[107] M. Syperek, D. R. Yakovlev, I. A. Yugova, J. Misiewicz, I. V. Sedova, S. V. Sorokin, A. A. Toropov, S. V. Ivanov, and M. Bayer, "Long-lived electron spin coherence in CdSe/Zn(S,Se) self-assembled quantum dots", Physical Review B **84**, Publisher: American Physical Society, 085304 (2011).

[108] A. V. Khaetskii, D. Loss, and L. Glazman, "Electron spin decoherence in quantum dots due to interaction with nuclei", Phys. Rev. Lett. **88**, 186802 (2002).

[109] G. Waldherr, Y. Wang, S. Zaiser, M. Jamali, T. Schulte-Herbrüggen, H. Abe, T. Ohshima, J. Isoya, J. F. Du, P. Neumann, and J. Wrachtrup, "Quantum error correction in a solid-state hybrid spin register", Nature **506**, 204–207 (2014).

[110] T. H. Taminiau, J. Cramer, T. van der Sar, V. V. Dobrovitski, and R. Hanson, "Universal control and error correction in multi-qubit spin registers in diamond", Nature Nanotechnology **9**, 171–176 (2014).

[111] E. A. Chekhovich, S. F. C. da Silva, and A. Rastelli, "Nuclear spin quantum register in an optically active semiconductor quantum dot", Nature Nanotechnology **15**, 999–1004 (2020).

[112] E. V. Denning, D. A. Gangloff, M. Atatüre, J. Mørk, and C. Le Gall, "Collective quantum memory activated by a driven central spin", Phys. Rev. Lett. **123**, 140502 (2019).

[113] D. A. Gangloff, G. Éthier-Majcher, C. Lang, E. V. Denning, J. H. Bodey, D. M. Jackson, E. Clarke, M. Hugues, C. Le Gall, and M. Atatüre, "Quantum interface of an electron and a nuclear ensemble", Science **364**, 62–66 (2019).

[114] M. V. G. Dutt, L. Childress, L. Jiang, E. Togan, J. Maze, F. Jelezko, A. S. Zibrov, P. R. Hemmer, and M. D. Lukin, "Quantum register based on individual electronic and nuclear spin qubits in diamond", Science **316**, 1312–1316 (2007).

[115] J. Reiner, Y. Chung, S. H. Misha, C. Lehner, C. Moehle, D. Poulos, S. Monir, K. J. Charde, P. Macha, L. Kranz, I. Thorvaldson, B. Thorgrimsson, D. Keith, Y. L. Hsueh, R. Rahman, S. K. Gorman, J. G. Keizer, and M. Y. Simmons, "High-fidelity initialization and control of electron and nuclear spins in a four-qubit register", Nature Nanotechnology (2024).

[116] C. E. Bradley, J. Randall, M. H. Abobeih, R. C. Berrevoets, M. J. Degen, M. A. Bakker, M. Markham, D. J. Twitchen, and T. H. Taminiau, "A ten-qubit solid-state spin register with quantum memory up to one minute", Phys. Rev. X **9**, 031045 (2019).

[117] E. A. Chekhovich, I. M. Griffiths, M. S. Skolnick, H. Huang, S. F. C. da Silva, X. Yuan, and A. Rastelli, "Cross calibration of deformation potentials and gradient-elastic tensors of gaas using photoluminescence and nuclear magnetic resonance spectroscopy in GaAs/AlGaAs quantum dot structures", Phys. Rev. B **97**, 235311 (2018).

[118] A. Abragam, *The principles of nuclear magnetism* (Oxford University Press, Oxford, 1961).

[119] V. M. Litvyak, R. V. Cherbunin, V. K. Kalevich, A. I. Lihachev, A. V. Nashchekin, M. Vladimirova, and K. V. Kavokin, "Warm-up spectroscopy of quadrupole-split nuclear spins in n-GaAs epitaxial layers", Phys. Rev. B **104**, 235201 (2021).

[120] M. Kotur, D. O. Tolmachev, V. M. Litvyak, K. V. Kavokin, D. Suter, D. R. Yakovlev, and M. Bayer, "Ultra-deep optical cooling of coupled nuclear spin-spin and quadrupole reservoirs in a GaAs/(Al,Ga)As quantum well", Communications Physics **4**, 193 (2021).

[121] J. Fischer, W. A. Coish, D. V. Bulaev, and D. Loss, "Spin decoherence of a heavy hole coupled to nuclear spins in a quantum dot", Phys. Rev. B **78**, 155329 (2008).

[122] B. Eble, C. Testelin, P. Desfonds, F. Bernardot, A. Balocchi, T. Amand, A. Miard, A. Lemaître, X. Marie, and M. Chamarro, "Hole–nuclear spin interaction in quantum dots", Phys. Rev. Lett. **102**, 146601 (2009).

[123] M. Syperek, D. R. Yakovlev, A. Greilich, J. Misiewicz, M. Bayer, D. Reuter, and A. D. Wieck, "Spin coherence of holes in GaAs/(Al, Ga)As quantum wells", Phys. Rev. Lett. **99**, 187401 (2007).

[124] D. Gammon, A. L. Efros, T. A. Kennedy, M. Rosen, D. S. Katzer, D. Park, S. W. Brown, V. L. Korenev, and I. A. Merkulov, "Electron and nuclear spin interactions in the optical spectra of single GaAs quantum dots", Phys. Rev. Lett. **86**, 5176–5179 (2001).

[125] C. W. Lai, P. Maletinsky, A. Badolato, and A. Imamoglu, "Knight-field-enabled nuclear spin polarization in single quantum dots", Phys. Rev. Lett. **96**, 167403 (2006).

[126] G. Sallen, S. Kunz, T. Amand, L. Bouet, T. Kuroda, T. Mano, D. Paget, O. Krebs, X. Marie, K. Sakoda, and B. Urbaszek, "Nuclear magnetization in gallium arsenide quantum dots at zero magnetic field", Nature Communications **5**, 3268 (2014).

[127] K. J. Dwyer, J. M. Pomeroy, D. S. Simons, K. L. Steffens, and J. W. Lau, "Enriching 28Si beyond 99.9998 % for semiconductor quantum computing", Journal of Physics D: Applied Physics **47**, 345105 (2014).

[128] E. A. Chekhovich, M. Hopkinson, M. S. Skolnick, and A. I. Tartakovskii, "Suppression of nuclear spin bath fluctuations in self-assembled quantum dots induced by inhomogeneous strain", Nature Communications **6**, 6348 (2015).

[129] A. Nolle, "Direct and indirect dipole-dipole coupling between ^{111}Cd,^{113}Cd and ^{125}Te in solid CdTe", Zeitschrift für Physik B Condensed Matter **34**, 175–182 (1979).

[130] V. M. Litvyak, P. Bazhin, R. André, M. Vladimirova, and K. V. Kavokin, *Nuclear spin-spin interactions in CdTe probed by zero and ultra-low-field optically detected NMR*, arXiv:2403.17593, 2024.

[131] M. A. Ruderman and C. Kittel, "Indirect exchange coupling of nuclear magnetic moments by conduction electrons", Phys. Rev. **96**, 99–102 (1954).

[132] N. Bloembergen and T. J. Rowland, "Nuclear spin exchange in solids: Tl^{203} and Tl^{205} magnetic resonance in thallium and thallic oxide", Phys. Rev. **97**, 1679–1698 (1955).

[133] N. F. Ramsey and E. M. Purcell, "Interactions between nuclear spins in molecules", Phys. Rev. **85**, 143–144 (1952).

[134] N. Bloembergen, "On the interaction of nuclear spins in a crystalline lattice", Physica **15**, 386–426 (1949).

[135] R. K. Hester, A. Sher, J. F. Soest, and G. Weisz, "Nuclear-magnetic-resonance detection of charge defects in gallium arsenide", Phys. Rev. B **10**, 4262–4273 (1974).

[136] V. M. Litvyak, R. V. Cherbunin, V. K. Kalevich, and K. V. Kavokin, "Local field of spin-spin interactions in the nuclear spin system of *n*-GaAs", Phys. Rev. B **108**, 235204 (2023).

[137] M. Goldman, *Spin temperature and nuclear magnetic resonance in solids* (Clarendon Press, Oxford, 1970).

[138] M. Vladimirova, S. Cronenberger, A. Colombier, D. Scalbert, V. M. Litvyak, K. V. Kavokin, and A. Lemaître, "Simultaneous measurements of nuclear-spin heat capacity, temperature, and relaxation in GaAs microstructures", Phys. Rev. B **105**, 155305 (2022).

[139] P. Maletinsky, M. Kroner, and A. Imamoglu, "Breakdown of the nuclear-spin-temperature approach in quantum-dot demagnetization experiments", Nature Physics **5**, 407–411 (2009).

[140] A. S. Oja and O. V. Lounasmaa, "Nuclear magnetic ordering in simple metals at positive and negative nanokelvin temperatures", Rev. Mod. Phys. **69**, 1–136 (1997).

[141] M. Kotur, R. Dzhioev, K. Kavokin, V. L. Korenev, B. Namozov, P. Pak, and Y. G. Kusrayev, "Nuclear spin relaxation mediated by Fermi-edge electrons in *n*-type GaAs", JETP letters **99**, 37–41 (2014).

[142] A. Ruskuc, C.-J. Wu, J. Rochman, J. Choi, and A. Faraon, "Nuclear spin-wave quantum register for a solid-state qubit", Nature **602**, 408–413 (2022).

[143] R. I. Dzhioev and V. L. Korenev, "Stabilization of the electron-nuclear spin orientation in quantum dots by the nuclear quadrupole interaction", Phys. Rev. Lett. **99**, 037401 (2007).

[144] D. Paget, G. Lampel, B. Sapoval, and V. I. Safarov, "Low field electron-nuclear spin coupling in gallium arsenide under optical pumping conditions", Phys. Rev. B **15**, 5780–5796 (1977).

[145] C. P. Slichter and W. C. Holton, "Adiabatic demagnetization in a rotating reference system", Phys. Rev. **122**, 1701–1708 (1961).

[146] V. D. K. V. K. Kalevich and V. G. Fleisher, JETP Lett. **35** (1982).

[147] A. Abragam and W. G. Proctor, "Spin temperature", Phys. Rev. **109**, 1441 (1958).

[148] R. Mountain, "Statistical mechanics of adiabatic processes", Physica **30**, 808–817 (1964).

[149] M. Vladimirova, S. Cronenberger, D. Scalbert, I. I. Ryzhov, V. S. Zapasskii, G. G. Kozlov, A. Lemaître, and K. V. Kavokin, "Spin temperature concept verified by optical magnetometry of nuclear spins", Phys. Rev. B **97**, 041301(R) (2018).

[150] M. Kotur, R. I. Dzhioev, M. Vladimirova, B. Jouault, V. L. Korenev, and K. V. Kavokin, "Nuclear spin warm up in bulk n-GaAs", Phys. Rev. B **94**, 081201(R) (2016).

[151] E. A. Chekhovich, A. Ulhaq, E. Zallo, F. Ding, O. G. Schmidt, and M. S. Skolnick, "Measurement of the spin temperature of optically cooled nuclei and gaas hyperfine constants in GaAs/AlGaAs quantum dots", Nature Materials **16**, 982–986 (2017).

[152] V. Kalevich, V. Kulkov, and V. Fleisher, "Optical cooling of the nuclear spin system of a semiconductor in a conjunction with the adiabatic demagnetization", Bulletin of Academy of Science of the USSR, Physical Series **46**, 492–494 (1982).

[153] M. Vladimirova, S. Cronenberger, D. Scalbert, M. Kotur, R. I. Dzhioev, I. I. Ryzhov, G. G. Kozlov, V. S. Zapasskii, A. Lemaître, and K. V. Kavokin, "Nuclear spin relaxation in n-GaAs: from insulating to metallic regime", Phys. Rev. B **95**, 125312 (2017).

[154] J. Korringa, "Nuclear magnetic relaxation and resonnance line shift in metals", Physica **16**, 601–610 (1950).

[155] L. Tracy, I. Spielman, J. Eisenstein, L. Pfeiffer, and K. West, "Korringa-like nuclear spin–lattice relaxation in a 2DES at ν=1/2", Physica E: Low-dimensional Systems and Nanostructures **34**, 220–223 (2006).

[156] L. Abaspour, P. Sterin, E. P. Rugeramigabo, J. Hübner, and M. Oestreich, "Doping and temperature dependence of nuclear spin relaxation in n-type GaAs", Phys. Rev. B **102**, 235205 (2020).

[157] E. Evers, T. Kazimierczuk, F. Mertens, D. R. Yakovlev, G. Karczewski, T. Wojtowicz, J. Kossut, M. Bayer, and A. Greilich, "Nuclear spin dynamics influenced and detected by electron spin polarization in CdTe/(Cd,Mg)Te quantum wells", Phys. Rev. B **99**, 045303 (2019).

[158] A. Berg, M. Dobers, R. R. Gerhardts, and K. v. Klitzing, "Magnetoquantum oscillations of the nuclear-spin-lattice relaxation near a two-dimensional electron gas", Phys. Rev. Lett. **64**, 2563–2566 (1990).

[159] D. Paget, "Optical detection of NMR in high-purity GaAs: direct study of the relaxation of nuclei close to shallow donors", Phys. Rev. B **25**, 4444–4451 (1982).

[160] J. Lu, M. J. R. Hoch, P. L. Kuhns, W. G. Moulton, Z. Gan, and A. P. Reyes, "Nuclear spin-lattice relaxation in n-type insulating and metallic GaAs single crystals", Phys. Rev. B **74**, 125208 (2006).

[161] P. Millington-Hotze, S. Manna, S. F. Covre da Silva, A. Rastelli, and E. A. Chekhovich, "Nuclear spin diffusion in the central spin system of a GaAs/AlGaAs quantum dot", Nature Communications **14**, 2677 (2023).

[162] F. Heisterkamp, A. Greilich, E. A. Zhukov, E. Kirstein, T. Kazimierczuk, V. L. Korenev, I. A. Yugova, D. R. Yakovlev, A. Pawlis, and M. Bayer, "Inhomogeneous nuclear spin polarization induced by helicity-modulated optical excitation of fluorine-bound electron spins in ZnSe", Phys. Rev. B **92**, 245441 (2015).

[163] W. Zhang and D. G. Cory, "First direct measurement of the spin diffusion rate in a homogenous solid", Phys. Rev. Lett. **80**, 1324–1327 (1998).

[164] K. W. Eberhardt, S. Mouaziz, G. Boero, J. Brugger, and B. H. Meier, "Direct observation of nuclear spin diffusion in real space", Phys. Rev. Lett. **99**, 227603 (2007).

[165] G. R. Khutsishvili, "Spin diffusion", Soviet Physics Uspekhi **8**, 743 (1966).

[166] Z.-X. Gong, Z.-q. Yin, and L.-M. Duan, "Dynamics of the overhauser field under nuclear spin diffusion in a quantum dot", New Journal of Physics **13**, 033036 (2011).

[167] J. A. Gaj and J. Kossut, *Introduction to the physics of diluted magnetic semiconductors*, Vol. 144 (Springer Berlin, Heidelberg, 2011).

[168] I. A. Merkulov, "Formation of a nuclear spin polaron under optical orientation in GaAs-type semiconductors", Physics of the Solid State **40**, 930–933 (1998).

[169] M. Vladimirova, D. Scalbert, M. S. Kuznetsova, and K. V. Kavokin, "Electron-induced nuclear magnetic ordering in n-type semiconductors", Phys. Rev. B **103**, 205207 (2021).

[170] M. D'yakonov and V. Perel, "Optical orientation in a system of electrons and lattice nuclei in semiconductors. theory", Zh. Eksp. Teor. Fiz **65**, 362–375 (1973).

[171] J. P. Wolfe, "Direct observation of a nuclear spin diffusion barrier", Phys. Rev. Lett. **31**, 907–910 (1973).

[172] P. Maletinsky, A. Badolato, and A. Imamoglu, "Dynamics of quantum dot nuclear spin polarization controlled by a single electron", Phys. Rev. Lett. **99**, 056804 (2007).

[173] T. Auer, R. Oulton, A. Bauschulte, D. R. Yakovlev, M. Bayer, S. Y. Verbin, R. V. Cherbunin, D. Reuter, and A. D. Wieck, "Measurement of the knight field and local nuclear dipole-dipole field in an InGaAs/GaAs quantum dot ensemble", Phys. Rev. B **80**, 205303 (2009).

[174] L. Langer, S. V. Poltavtsev, I. A. Yugova, M. Salewski, D. R. Yakovlev, G. Karczewski, T. Wojtowicz, I. A. Akimov, and M. Bayer, "Access to long-term optical memories using photon echoes retrieved from semiconductor spins", Nature Photonics **8**, 851–857 (2014).

[175] F. Saeed, M. Kuhnert, I. A. Akimov, V. L. Korenev, G. Karczewski, M. Wiater, T. Wojtowicz, A. Ali, A. S. Bhatti, D. R. Yakovlev, and M. Bayer, "Single-beam optical measurement of spin dynamics in CdTe/(Cd,Mg)Te quantum wells", Phys. Rev. B **98**, 075308 (2018).

[176] M. M. Rahman, M. R. Karim, H. F. Alharbi, B. Aldokhayel, T. Uzzaman, and H. Zahir, "Cadmium selenide quantum dots for solar cell applications: a review", Chemistry – An Asian Journal **16**, 902–921 (2021).

[177] J. Kim, C. Y. Wong, and G. D. Scholes, "Exciton fine structure and spin relaxation in semiconductor colloidal quantum dots", Accounts of Chemical Research **42**, 1037–1046 (2009).

[178] S. T. Cundiff, A. Knorr, J. Feldmann, S. W. Koch, E. O. Göbel, and H. Nickel, "Rabi flopping in semiconductors", Phys. Rev. Lett. **73**, 1178–1181 (1994).

[179] N. A. Sinitsyn and Y. V. Pershin, "The theory of spin noise spectroscopy: a review", Reports on Progress in Physics **79**, 106501 (2016).

[180] G. G. Kozlov, I. I. Ryzhov, and V. S. Zapasskii, "Light scattering in a medium with fluctuating gyrotropy: application to spin-noise spectroscopy", Phys. Rev. A **95**, 043810 (2017).

[181] S. Cronenberger, C. Abbas, D. Scalbert, and H. Boukari, "Spatiotemporal spin noise spectroscopy", Phys. Rev. Lett. **123**, 017401 (2019).

[182] T. C. Damen, K. Leo, J. Shah, and J. E. Cunningham, "Spin relaxation and thermalization of excitons in GaAs quantum wells", Applied Physics Letters **58**, 1902–1904 (1991).

[183] M. Oestreich, S. Hallstein, and W. Ruhle, "Spin quantum beats in semiconductors", IEEE Journal of Selected Topics in Quantum Electronics **2**, 747–755 (1996).

[184] L. V. Fokina, I. A. Yugova, D. R. Yakovlev, M. M. Glazov, I. A. Akimov, A. Greilich, D. Reuter, A. D. Wieck, and M. Bayer, "Spin dynamics of electrons and holes in InGaAs/GaAs quantum wells at millikelvin temperatures", Phys. Rev. B **81**, 195304 (2010).

[185] P. S. Pershan, "Magneto-Optical Effects", Journal of Applied Physics **38**, 1482–1490 (1967).

[186] D. D. Awschalom, D. Loss, and N. Samarth, *Semiconductor spintronics and quantum computation* (Springer Berlin, Heidelberg, 2002).

[187] E. A. Zhukov, D. R. Yakovlev, M. Bayer, M. M. Glazov, E. L. Ivchenko, G. Karczewski, T. Wojtowicz, and J. Kossut, "Spin coherence of a two-dimensional electron gas induced by resonant excitation of trions and excitons in CdTe/(Cd, Mg)Te quantum wells", Phys. Rev. B **76**, 205310 (2007).

[188] J. M. Kikkawa and D. D. Awschalom, "Resonant spin amplification in n-type GaAs", Phys. Rev. Lett. **80**, 4313–4316 (1998).

[189] V. V. Belykh, K. V. Kavokin, D. R. Yakovlev, and M. Bayer, "Electron charge and spin delocalization revealed in the optically probed longitudinal and transverse spin dynamics in n-GaAs", Phys. Rev. B **96**, 241201 (2017).

[190] L. Langer, S. V. Poltavtsev, I. A. Yugova, D. R. Yakovlev, G. Karczewski, T. Wojtowicz, J. Kossut, I. A. Akimov, and M. Bayer, "Magnetic-field control of photon echo from the electron-trion system in a CdTe quantum well: Shuffling coherence between optically accessible and inaccessible states", Phys. Rev. Lett. **109**, 157403 (2012).

[191] A. R. Cameron, P. Riblet, and A. Miller, "Spin gratings and the measurement of electron drift mobility in multiple quantum well semiconductors", Phys. Rev. Lett. **76**, 4793–4796 (1996).

[192] M. Q. Weng, M. W. Wu, and H. L. Cui, "Spin relaxation in n-type GaAs quantum wells with transient spin grating", Journal of Applied Physics **103**, 063714 (2008).

[193] M. Salewski, S. V. Poltavtsev, I. A. Yugova, G. Karczewski, M. Wiater, T. Wojtowicz, D. R. Yakovlev, I. A. Akimov, T. Meier, and M. Bayer, "High-resolution two-dimensional optical spectroscopy of electron spins", Phys. Rev. X **7**, 031030 (2017).

[194] W. Hanle, "Über magnetische beeinflussung der polarisation der resonanzfluoreszenz", Zeitschrift für Physik **30**, 93–105 (1924).

[195] H. Hoffmann, G. V. Astakhov, T. Kiessling, W. Ossau, G. Karczewski, T. Wojtowicz, J. Kossut, and L. W. Molenkamp, "Optical spin pumping of modulation-doped electrons probed by a two-color Kerr rotation technique", Phys. Rev. B **74**, 073407 (2006).

[196] M. Furis, D. L. Smith, S. Kos, E. S. Garlid, K. S. M. Reddy, C. J. Palmstrøm, P. A. Crowell, and S. A. Crooker, "Local Hanle-effect studies of spin drift and diffusion in n:gaas epilayers and spin-transport devices", New Journal of Physics **9**, 347 (2007).

[197] M. S. Kuznetsova, J. Rautert, K. V. Kavokin, D. S. Smirnov, D. R. Yakovlev, A. K. Bakarov, A. K. Gutakovskii, T. S. Shamirzaev, and M. Bayer, "Electron-nuclei interaction in the X valley of (In,Al)As/AlAs quantum dots", Phys. Rev. B **101**, 075412 (2020).

[198] D. S. Smirnov, E. A. Zhukov, D. R. Yakovlev, E. Kirstein, M. Bayer, and A. Greilich, "Spin polarization recovery and Hanle effect for charge carriers interacting with nuclear spins in semiconductors", Phys. Rev. B **102**, 235413 (2020).

[199] E. B. Aleksandrov and V. S. Zapasskii, "Magnetic resonance in the Faraday-rotation noise spectrum", Zh. Eksp. Teor. Fiz **81**, 132–138 (1981).

[200] M. Oestreich, M. Römer, R. J. Haug, and D. Hägele, "Spin noise spectroscopy in GaAs", Phys. Rev. Lett. **95**, 216603 (2005).

[201] R. Dahbashi, J. Hübner, F. Berski, K. Pierz, and M. Oestreich, "Optical spin noise of a single hole spin localized in an (InGa)As quantum dot", Phys. Rev. Lett. **112**, 156601 (2014).

[202] M. Römer, J. Hübner, and M. Oestreich, "Spatially resolved doping concentration measurement in semiconductors via spin noise spectroscopy", Applied Physics Letters **94**, 112105 (2009).

[203] L. Yang, P. Glasenapp, A. Greilich, D. Reuter, A. D. Wieck, D. R. Yakovlev, M. Bayer, and S. A. Crooker, "Two-colour spin noise spectroscopy and fluctuation correlations reveal homogeneous linewidths within quantum-dot ensembles", Nature Communications **5**, 4949 (2014).

[204] Y. V. Pershin, V. A. Slipko, D. Roy, and N. A. Sinitsyn, "Two-beam spin noise spectroscopy", Applied Physics Letters **102**, 202405 (2013).

[205] D. Roy, L. Yang, S. A. Crooker, and N. A. Sinitsyn, "Cross-correlation spin noise spectroscopy of heterogeneous interacting spin systems", Scientific Reports **5**, 9573 (2015).

[206] J. Hübner, F. Berski, R. Dahbashi, and M. Oestreich, "The rise of spin noise spectroscopy in semiconductors: From acoustic to GHz frequencies", physica status solidi (b) **251**, 1824–1838 (2014).

[207] R. Paschotta, *Balanced photodetection*, RP Photonics Encyclopedia, Available online at `https://www.rp-photonics.com/balanced_photodetection.html`, May 2019.

[208] S. Cronenberger and D. Scalbert, "Quantum limited heterodyne detection of spin noise", Review of Scientific Instruments **87**, 093111 (2016).

[209] M. Römer, J. Hübner, and M. Oestreich, "Spin noise spectroscopy in semiconductors", Review of Scientific Instruments **78**, 103903 (2007).

[210] B. M. Gorbovitsky and V. I. Perel, "Aleksandrov and Zapasskii experiment and the Raman effect", Opt. and Spectrosc. (1983).

[211] M. M. Glazov and V. S. Zapasskii, "Linear optics, Raman scattering, and spin noise spectroscopy", Opt. Express **23**, 11713–11723 (2015).

[212] L. Van Hove, "Correlations in space and time and born approximation scattering in systems of interacting particles", Phys. Rev. **95**, 249–262 (1954).

[213] A. N. Kamenskii, M. Y. Petrov, G. G. Kozlov, V. S. Zapasskii, S. E. Scholz, C. Sgroi, A. Ludwig, A. D. Wieck, M. Bayer, and A. Greilich, "Detection and amplification of spin noise using scattered laser light in a quantum-dot microcavity", Phys. Rev. B **101**, 041401(R) (2020).

[214] G. Lampel, "Nuclear dynamic polarization by optical electronic saturation and optical pumping in semiconductors", Phys. Rev. Lett. **20**, 491–493 (1968).

[215] S. W. Brown, T. A. Kennedy, D. Gammon, and E. S. Snow, "Spectrally resolved overhauser shifts in single GaAs/$Al_xGa_{1-x}As$ as quantum dots", Phys. Rev. B **54**, R17339–R17342 (1996).

[216] F. Berski, J. Hübner, M. Oestreich, A. Ludwig, A. D. Wieck, and M. Glazov, "Interplay of electron and nuclear spin noise in n-type GaAs", Phys. Rev. Lett. **115**, 176601 (2015).

[217] D. S. Smirnov, "Spin noise of localized electrons interacting with optically cooled nuclei", Phys. Rev. B **91**, 205301 (2015).

[218] I. I. Ryzhov, S. V. Poltavtsev, K. V. Kavokin, M. M. Glazov, G. G. Kozlov, M. Vladimirova, D. Scalbert, S. Cronenberger, A. V. Kavokin, A. Lemaître, J. Bloch, and V. S. Zapasskii, "Measurements of nuclear spin dynamics by spin-noise spectroscopy", Applied Physics Letters **106**, 242405 (2015).

[219] C. Rittmann, M. Y. Petrov, A. N. Kamenskii, K. V. Kavokin, A. Y. Kuntsevich, Y. P. Efimov, S. A. Eliseev, M. Bayer, and A. Greilich, "Unveiling the electron-nuclear spin dynamics in an n-doped InGaAs epilayer by spin noise spectroscopy", Phys. Rev. B **106**, 035202 (2022).

[220] T. Sleator, E. L. Hahn, C. Hilbert, and J. Clarke, "Nuclear-spin noise", Phys. Rev. Lett. **55**, 1742–1745 (1985).

[221] A. I. Ekimov and V. I. Safarov, "Optical electron-nuclear resonance in semiconductors", JETP Letters **15**, 453 (1972).

[222] V. K. Kalevich, "Optically induced nuclear magnetic resonance in semiconductors", Fiz. Tverd. Tela **28**, 3462–3465 (1986).

[223] V. K. Kalevich and V. G. Fleisher, "Optical detection of NMR with dynamic cooling of the nuclear spin system of a semiconductor by polarized light", Bull. Acad. Sci. USSR Phys. Ser **47** (1983).

[224] G. Burkard, T. D. Ladd, A. Pan, J. M. Nichol, and J. R. Petta, "Semiconductor spin qubits", Rev. Mod. Phys. **95**, 025003 (2023).

[225] D. D. Awschalom, L. C. Bassett, A. S. Dzurak, E. L. Hu, and J. R. Petta, "Quantum spintronics: Engineering and manipulating atom-like spins in semiconductors", Science **339**, 1174–1179 (2013).

[226] X. Sun, M. Gobbi, A. Bedoya-Pinto, O. Txoperena, F. Golmar, R. Llopis, A. Chuvilin, F. Casanova, and L. E. Hueso, "Room-temperature air-stable spin transport in bathocuproine-based spin valves", Nature Communications **4**, 2794 (2013).

[227] M. H. D. Guimarães, J. J. van den Berg, I. J. Vera-Marun, P. J. Zomer, and B. J. van Wees, "Spin transport in graphene nanostructures", Phys. Rev. B **90**, 235428 (2014).

[228] A. Greilich, A. Pawlis, F. Liu, O. A. Yugov, D. R. Yakovlev, K. Lischka, Y. Yamamoto, and M. Bayer, "Spin dephasing of fluorine-bound electrons in ZnSe", Phys. Rev. B **85**, 121303 (2012).

[229] F. Heisterkamp, E. A. Zhukov, A. Greilich, D. R. Yakovlev, V. L. Korenev, A. Pawlis, and M. Bayer, "Longitudinal and transverse spin dynamics of donor-bound electrons in fluorine-doped ZnSe: Spin inertia versus Hanle effect", Phys. Rev. B **91**, 235432 (2015).

[230] A. Carvalho and A. H. C. Neto, "Donor and acceptor levels in semiconducting transition-metal dichalcogenides", Phys. Rev. B **89**, 081406 (2014).

[231] M. Y. Petrov, A. N. Kamenskii, V. S. Zapasskii, M. Bayer, and A. Greilich, "Increased sensitivity of spin noise spectroscopy using homodyne detection in n-doped GaAs", Phys. Rev. B **97**, 125202 (2018).

[232] P. Sterin, J. Wiegand, J. Hübner, and M. Oestreich, "Optical amplification of spin noise spectroscopy via homodyne detection", Phys. Rev. Appl. **9**, 034003 (2018).

[233] G. G. Kozlov, I. I. Ryzhov, and V. S. Zapasskii, "Spin-noise spectroscopy of randomly moving spins in the model of light scattering: Two-beam arrangement", Phys. Rev. A **97**, 013848 (2018).

[234] M. M. Glazov, "Coherent spin dynamics in semiconductor quantum dots", Journal of Applied Physics **113**, 136503 (2013).

[235] D. S. Smirnov, V. N. Mantsevich, and M. M. Glazov, "Theory of optically detected spin noise in nanosystems", Physics-Uspekhi **64**, 923 (2021).

[236] P. L. Hall and D. K. Ross, "Incoherent neutron scattering function for molecular diffusion in lamellar systems", Mol. Phys. **36**, 1549–1554 (1978).

[237] K. S. Singwi and A. Sjölander, "Diffusive motions in water and cold neutron scattering", Phys. Rev. **119**, 863–871 (1960).

[238] C. T. Chudley and R. J. Elliott, "Neutron scattering from a liquid on a jump diffusion model", Proc. Phys. Soc. **77**, 353–361 (1961).

[239] K. W. Kehr, D. Richter, and G. Honig, "Stochastic theory of spin depolarization of muons diffusing in the presence of traps", Hyperfine Interact. **6**, 219–222 (1979).

[240] N. J. Harmon and M. E. Flatté, "Distinguishing spin relaxation mechanisms in organic semiconductors", Phys. Rev. Lett. **110**, 176602 (2013).

[241] A. V. Khaetskii and Y. V. Nazarov, "Spin relaxation in semiconductor quantum dots", Phys. Rev. B **61**, 12639–12642 (2000).

[242] C. Herring and M. Flicker, "Asymptotic exchange coupling of two hydrogen atoms", Phys. Rev. **134**, A362–A366 (1964).

[243] A. Miller and E. Abrahams, "Impurity conduction at low concentrations", Phys. Rev. **120**, 745–755 (1960).

[244] D. Chattopadhyay and H. J. Queisser, "Electron scattering by ionized impurities in semiconductors", Rev. Mod. Phys. **53**, 745–768 (1981).

[245] P. P. Debye and E. M. Conwell, "Electrical properties of N-type germanium", Phys. Rev. **93**, 693–706 (1954).

[246] L. Marton, *Advances in electronics and electron physics*, Vol. 7, ISSN (Academic Press, New York, 1955), pp. 85–182.

[247] A. Tadjine, Y.-M. Niquet, and C. Delerue, "Universal behavior of electron g-factors in semiconductor nanostructures", Phys. Rev. B **95**, 235437 (2017).

[248] A. V. Poshakinskiy and S. A. Tarasenko, "Spatiotemporal spin fluctuations caused by spin-orbit-coupled brownian motion", Phys. Rev. B **92**, 045308 (2015).

[249] D. Sprinzl, P. Horodyská, N. Tesa řová, E. Rozkotová, E. Belas, R. Grill, P. Malý, and P. N ěmec, "Influence of n-type doping on electron spin dephasing in CdTe", Phys. Rev. B **82**, 153201 (2010).

[250] S. Cronenberger, C. Abbas, D. Scalbert, and H. Boukari, *Spatiotemporal electronic spin fluctuations in random nuclear fields in n-CdTe*, arXiv:1910.11805, 2019.

[251] S. A. Crooker, L. Cheng, and D. L. Smith, "Spin noise of conduction electrons in n-type bulk GaAs", Phys. Rev. B **79**, 035208 (2009).

[252] D. T. Marple, "Effective electron mass in CdTe", Phys. Rev. **129**, 2466–2470 (1963).

[253] S. Perkowitz and R. H. Thorland, "Far-infrared study of free carriers and the plasmon-phonon interaction in CdTe", Phys. Rev. B **9**, 545–550 (1974).

[254] G. Fonthal, L. Tirado-Mejía, J. I. Marín-Hurtado, H. Ariza-Calderón, and J. G. Mendoza-Alvarez, "Temperature dependence of the band gap energy of crystalline CdTe", J. Phys. Chem. Solids **61**, 579–583 (2000).

[255] J. M. Francou, K. Saminadayar, and J. L. Pautrat, "Shallow donors in CdTe", Phys. Rev. B **41**, 12035–12046 (1990).

[256] A. N. Chantis, M. van Schilfgaarde, and T. Kotani, "Ab initio prediction of conduction band spin splitting in zinc blende semiconductors", Phys. Rev. Lett. **96**, 086405 (2006).

[257] M. Cardona, N. E. Christensen, and G. Fasol, "Relativistic band structure and spin-orbit splitting of zinc-blende-type semiconductors", Phys. Rev. B **38**, 1806–1827 (1988).

[258] J. Kainz, U. Rössler, and R. Winkler, "Temperature dependence of Dyakonov-Perel spin relaxation in zinc-blende semiconductor quantum structures", Phys. Rev. B **70**, 195322 (2004).

[259] J. Serre and A. Ghazali, "From band tailing to impurity-band formation and discussion of localization in doped semiconductors: A multiple-scattering approach", Phys. Rev. B **28**, 4704–4715 (1983).

[260] J. Monecke, W. Siegel, E. Ziegler, and G. Kühnel, "On the concentration dependence of the thermal impurity-to-band activation energies in semiconductors", Phys. Status Solidi **103**, 269–279 (1981).

[261] J. H. De Boer and W. C. Von Geel, Physica (Utrecht) **2**, 286 (1935).

[262] R. Levitt and A. Honig, "Low temperature electron trapping lifetimes and extrinsic photoconductivity in n-type silicon doped with shallow impurities", Journal of Physics and Chemistry of Solids **22**, 269–284 (1961).

[263] Palma, A., Jiménez-Tejada, J. A., Godoy, A., and Cartujo, P., "Capture process by shallow donors in silicon at low temperatures", J. Phys. IV France **06**, C3-105-C3–110 (1996).

[264] G. M. Müller, M. Oestreich, M. Römer, and J. Hübner, "Semiconductor spin noise spectroscopy: fundamentals, accomplishments, and challenges", Physica E: Low-dimensional Systems and Nanostructures **43**, 569–587 (2010).

[265] G. A. Intronati, P. I. Tamborenea, D. Weinmann, and R. A. Jalabert, "Spin relaxation near the metal-insulator transition: dominance of the Dresselhaus spin-orbit coupling", Phys. Rev. Lett. **108**, 016601 (2012).

[266] D. Roy, L. Yang, S. A. Crooker, and N. A. Sinitsyn, "Cross-correlation spin noise spectroscopy of heterogeneous interacting spin systems", Scientific Reports **5**, 9573 (2015).

[267] E. G. LeBlanc, M. Edirisooriya, O. S. Ogedengbe, O. C. Noriega, P. A. R. D. Jayathilaka, S. Rab, C. H. Swartz, D. R. Diercks, G. L. Burton, B. P. Gorman, A. Wang, T. M. Barnes, and T. H. Myers, "Determining and controlling the magnesium composition in CdTe/CdMgTe heterostructures", Journal of Electronic Materials **46**, 5379–5385 (2017).

[268] A. W. Overhauser, "Polarization of nuclei in metals", Phys. Rev. **92**, 411–415 (1953).

[269] A. L. Falk, P. V. Klimov, V. Ivády, K. Szász, D. J. Christle, W. F. Koehl, Á. Gali, and D. D. Awschalom, "Optical polarization of nuclear spins in silicon carbide", Phys. Rev. Lett. **114**, 247603 (2015).

[270] D. R. McCamey, J. van Tol, G. W. Morley, and C. Boehme, "Fast nuclear spin hyperpolarization of phosphorus in silicon", Phys. Rev. Lett. **102**, 027601 (2009).

[271] I. J. H. Leung and C. A. Michal, "Optical enhancement of NMR signals in CdTe", Phys. Rev. B **70**, 035213 (2004).

[272] D. A. Varshalovich, A. N. Moskalev, and V. K. Khersonskii, *Quantum theory of angular momentum* (World Scientific, Singapore, 1988).

[273] V. N. Faddeeva and N. N. Terent'ev, *Tables of values of the error function for complex arguments* (Gosud. Izdat. Teh.-Teor. Lit., Moscow, 1954).